Femtosecond Spectroscopy on Technically and Pharmaceutically Relevant Organic Molecules

Dissertation

von

Katrin Elisabeth Oberhofer

TUM

Fakultät für Physik
Lehrstuhl für Laser- und Röntgenphysik

Femtosecond Spectroscopy on Technically and Pharmaceutically Relevant Organic Molecules

Katrin Elisabeth Oberhofer

Vollständiger Abdruck der von der Fakultät für Physik der Technischen Universität München zur Erlangung des akademischen Grades eines
Doktors der Naturwissenschaften
genehmigten Dissertation.

Vorsitzender: Prof. Dr. Martin Zacharias
Prüfer der Dissertation:
1. Prof. Dr. Reinhard Kienberger
2. Prof. Dr. Ulrich K. Heiz

Zusammenfassung

Die Erzeugung von Laserpulsen mit einer Dauer von wenigen Femtosekunden ermöglicht die Erforschung ultrakurzer Prozesse in Molekülen direkt nach Absorption eines Photons. Mittels breitbandiger transienter Absorptionsspektroskopie untersuchen wir die Dynamik des angeregten Zustands neuartiger pharmazeutisch und technisch relevanter organischer Moleküle in Lösung. Durch Kombination mit quantenchemischen Rechnungen entschlüsseln wir die Ursprünge eines anomalen Schweratomeffekts in 3-Diethylphosphono-Cumarinen und Cumarin-3-Phosphonsäure. Halogensubstitution führt nach Anregung der primären Absorptionsbande zu zwei sich überlagernden Effekten. Durch verschiedene Substituenten lassen sich photochemische Schlüsselparameter wie Singulettlebensdauer und Triplettausbeute unabhängig voneinander kontrollieren. Das ist von großem Interesse für pharmazeutische Anwendungen, insbesondere da Phosphonogruppen und Phosphonsäure für ihre enzymhemmenden Eigenschaften bekannt sind. Im einem zweiten Projekt entflechten wir die Vorgänge während der photochemischen Umwandlung einer Chromonverbindung, die einen vielversprechenden Kandidaten für die Anwendung als nicht überschreibbarer (WORM-type) organischer Informationsspeicher darstellt. Breitbandige transiente Absorptionsspektroskopie deutet auf einen ultrakurzen zweistufigen Prozess hin, dem wir eine Ringöffnungs- und eine Ringschlussreaktion zuordnen können. Die gewonnenen Resultate ermöglichen die Optimierung der Molekülstruktur in Richtung höherer Quantenausbeute des Photoprodukts und Verbesserung der Speichereffizienz. Darüber hinaus führen wir Fluoreszenzaufkonversionsmessungen an Naphthalimid-Isoquinolin-Derivaten durch.

Die Experimente im zweiten Teil dieser Arbeit haben die Entwicklung einer neuen Methode zur Enantiomerenanreicherung von Filmen chiraler Moleküle zum Ziel. Mittels Zweite-Harmonische Zirkulardichroismus- und optischer Rotationsdispersionsspektroskopie erforschen wir die optische Aktivität und ihre Entwicklung während laserinduzierter Desorption von BINOL-Filmen. Die Versuche ergeben reproduzierbare Erzeugung substanzieller und wohldefinierter optischer Aktivität in einem ursprünglich razemischen kristallinen BINOL-Film durch resonante Zweiphotonenabsorption und gleichzeitige Desorption. Unsere Ergebnisse sprechen für die Erzeugung eines substanziellen Enantiomerenüberschusses im verbliebenen BINOL-Film. Enantiomerenanreicherung wird vermutlich durch bevorzugte direkte Desorption eines der beiden Enantiomere erreicht. Eine ausführliche Diskussion verschiedener Photoresolutionsprozesse ist Teil dieser Arbeit. Numerische Modellierung bestätigt qualitativ ein vereinfachtes Modell, das darüber hinaus noch thermisch aktivierte Prozesse wie Diffusion und Razemisierung beinhaltet. Dies ist die erste Demonstration einer definierten laserinduzierten Enantiomerenanreicherung eines auf einem achiralen Substrat aufgebrachten razemischen Films und eröffnet somit unvorhergegangene Möglichkeiten für die asymmetrische Katalyse.

Abstract

Femtosecond laser pulses allow the investigation of ultrafast processes in molecules directly upon absorption of a photon. We apply broadband transient absorption spectroscopy to examine the excited state dynamics in novel organic molecules in solution, which are relevant for pharmaceutical or technical applications. By combination with quantum chemical calculations, we unravel the origins of an anomalous heavy-atom effect in 3-diethylphosphonocoumarins and coumarin-3-phosphonic acid. Halogen-substitution upon excitation of the primary absorption band gives rise to two superimposing effects. Different substituents allow the individual control of photochemical key parameters such as singlet lifetime and triplet yield. This is of great interest for pharmaceutical applications, in particular, because phosphono groups and phosphonic acid are known for their enzyme inhibiting properties. In a second project, we disentangle the processes during the photochemical transformation of a chromone compound, which is an interesting candidate for the application as organic WORM-type (write once read many) information storage. Broadband transient absorption spectroscopy reveals strong indication for an ultrafast two-step process, which we can attribute to a ring-opening and a ring-closure reaction. The obtained results allow to optimise the molecular design towards larger quantum yield of the photoproduct and higher storage efficiency. Furthermore, we perform fluorescence upconversion spectroscopy on naphthalimide-isoquinoline derivatives.

The experiments presented in the second part aim at developing a new method for enantio-enrichment of films of chiral molecules using circularly polarised femtosecond pulses. We apply second-harmonic circular dichroism and optical rotation dispersion spectroscopy to investigate the optical activity and its evolution during laser-induced desorption of BINOL films. The experiments yield reproducible generation of substantial and well-defined optical activity in an initially racemic crystalline BINOL film upon resonant two-photon absorption and simultaneous desorption. Our results strongly support the generation of a substantial enantiomeric excess in the remaining BINOL film. Enantioenrichment is presumably achieved by preferential direct desorption of one of the two enantiomers. A detailed discussion of different photoresolution effects is included in this thesis. Numerical modelling qualitatively confirms a simplified model, which additionally comprises thermally activated processes such as diffusion and racemisation. This is the first demonstration of a defined laser-stimulated enantioenrichment of a racemic film deposited on an achiral substrate, and thus, opens up unprecedented opportunities for asymmetric catalysis.

List of Publications

Directly related to this thesis

Enantiospecific Desorption Triggered by Circularly Polarized Light

F. Mortaheb, K. Oberhofer, J. Riemensberger, F. Ristow, R. Kienberger, U. Heiz, H. Iglev, A. Kartouzian

Enantioenrichment of racemic films using circularly polarized femtosecond pulses

K. Oberhofer, F. Mortaheb, J. Riemensberger, F. Ristow, R. Kienberger, U. Heiz, H. Iglev, A. Kartouzian

Investigation of Transient State and Dynamics of Photochemical Transformations of Chromone Molecules

S. V. Gagarskiy, E. P. Grebennikov, V. V. Kiyko, K. S. Levchenko, A. N. Sergeev, Ya. Yu. Fomicheva, K. Oberhofer, H. Iglev

Individual control of singlet lifetime and triplet yield in halogen-substituted coumarin derivatives

K. E. Oberhofer, M. Musheghyan, S. Wegscheider, M. Wörle, E. D. Iglev, R. D. Nikolova, R. Kienberger, P. St. Petkov, H. Iglev

Understanding laser desorption with circularly polarized light

F. Ristow, J. Scheffel, X. Xu, N. Fehn, K. E. Oberhofer, J. Riemensberger, F. Mortaheb, R. Kienberger, U. Heiz, A. Kartouzian, H. Iglev

Other

Coulomb Mediated Hybridization of Excitons in Coupled Quantum Dots

P.-L. Ardelt, K. Gawarecki, K. Müller, A. M. Waeber, A. Bechtold, K. Oberhofer, J. M. Daniels, F. Klotz, M. Bichler, T. Kuhn, H. J. Krenner, P. Machnikowski, J. J. Finley

Physical Review Letters 116, 7, pp. 007401, 2016

Patents

Verfahren zur Enantiomerenanreicherung

A. Kartouzian, U. Heiz, F. Mortaheb, K. Oberhofer, J. Riemensberger, H. Iglev, R. Kienberger

Deutsches Patent- und Markenamt, DE 10 2018 117 346, 2018

List of presented conference and invited seminar talks

Enantioenrichment of Racemic Films Using Circularly Polarized Femtosecond Pulses
K. Oberhofer, F. Mortaheb, J. Riemensberger, F. Ristow, R. Kienberger, U. Heiz, H. Iglev, and
A. Kartouzian

CONFERENCE ON LASERS AND ELECTRO OPTICS (CLEO) 2019, San Jose

Transient Phototransformation of Chromone Molecules
K. Oberhofer, Ya. Yu. Fomicheva, A. N. Sergeev, C. Brunner, V. V. Kiyko, K. S. Levchenko,
R. Kienberger, H. Iglev, and S. V. Gagarskiy

DPG Frühjahrstagung 2019, München

Generating Enantiomeric Excess in Thin Films of Chiral Molecules with Femtosecond Pulses
K. Oberhofer, F. Mortaheb, J. Riemensberger, F. Ristow, R. Kienberger, U. Heiz, H. Iglev,
A. Kartouzian

DPG Frühjahrstagung 2019, München

Ultrafast Spectroscopy of the Phototransformation of Chromone Molecules
K. Oberhofer, Ya. Yu. Fomicheva, A. N. Sergeev, C. Brunner, K. Stallhofer, S. Roth, P. Scigalla,
V. V. Kiyko, K. S. Levchenko, R. Kienberger, H. Iglev, and S. V. Gagarskiy

Invited Talk, 2018, ITMO University, St. Petersburg

Individual control of lifetime and triplet yield in halogen-substituted coumarin derivatives
K. Oberhofer, M. Musheghyan, S. Wegscheider, M. Wörle, E. D. Iglev, R. D. Nikolova, R. Kienberger, and H. Iglev

DPG Frühjahrstagung 2017, Mainz

Individual control of lifetime and triplet yield in halogen-substituted coumarin derivatives
K. Oberhofer, M. Musheghyan, S. Wegscheider, M. Wörle, E. D. Iglev, R. D. Nikolova, R. Kienberger, and H. Iglev

Invited Talk, 2017, Lehrstuhl für Biomolekulare Optik, LMU München

Contents

List of Figures

List of Tables

List of Symbols and Abbreviations

E	electric filed
H	magnetic field
D	electric displacement
B	magnetic induction
ω	angular frequency
ν	frequency
λ	wavelength
P	polarisation
I	intensity
n	refractive index
N	number density
m	electron mass
χ	electric susceptibility
α	absorption coefficient
σ_a	absorption cross-section
σ_{TPA}	cross-section for two-photon absorption
α_{ij}	linear polarisability tensor
β_{ijk}	second order polarisability tensor
A	absorbance
ε	molar absorption coefficient
R^{fg}	optical rotation strength
δ	optical rotation
g	anisotropy factor
Φ_F	fluorescence quantum yield

Φ_T	triplet (quantum) yield
k_i	relaxation rate for process i
f	oscillator strength
μ	dipole moment
r_{ab}	correlation coefficient (of parameters a and b)

UV	ultraviolet
VIS	visible
(N)IR	(near) infrared
SHG	second-harmonic generation
SFG	sum-frequency generation
DFG	difference-frequency generation
OR	optical rectification
SF	self-focusing
SPM	self-phase modulation
TPA	two-photon absorption
(S)RS	(stimulated) Raman scattering
OD	optical density
RCP	right circularly polarized
LCP	left circularly polarized
(SHG-)ORD	(second-harmonic generation) optical rotation dispersion
(SHG-)CD	(second-harmonic generation) circular dichroism
ee	enantiomeric excess
SSHG	surface second-harmonic generation
HOMO	highest-energy occupied molecular orbital
LUMO	lowest-energy unoccupied molecular orbital

IC	internal conversion
ISC	intersystem crossing
CI	conical intersection
PES	potential energy surface
HAE	heavy-atom effect
FWHM	full width at half maximum
GVD	group velocity dispersion
TA	transient absorption
XPM	cross-phase modulation
ACN	acetonitrile
EOH	ethanol
CYH	cyclohexane
ESA	excited state absorption
SE	stimulated emission
TTA	triplet-triplet absorption
PP	pump-probe
PREP	pump-repump-probe
PREF	pump-repump-fluorescence
DA(D)S	decay associated (difference) spectra
EADS	evolution associated difference spectra
(TD)DFT	(time-dependent) density functional theory
CP(L)	circularly polarized (light)
LPP	linearly polarized light parallel to the plane of incidence
QM	quantum mechanical
DIET	desorption induced by electronic transitions
DIMET	desorption induced by multiple electronic transitions

Part I

Introduction

1. Introduction

The interaction of sunlight with matter is one of the most fundamental processes on earth [1, 2]. Absorption of a photon occurs in less than one femtosecond (1 fs = 10^{-15}s) and gives rise to perturbation of the molecular electron distribution, which triggers electronic and nuclear motions. One of the fastest nuclear vibrations, found in water molecules, oscillates with a periodicity of approximately nine femtoseconds. Because one oscillation of a light wave from the ultraviolet to visible spectral range takes one to two femtoseconds, the resolution of the primary photophysical processes in a molecule requires the use of few-cycle laser pulses. Since the demonstration of the first sub-pico- and few-femtosecond laser pulses in the 1970s and 1980s [3, 4], the field of femtosecond spectroscopy was rapidly emerging. The importance of the research field was honoured not least by the award of the Nobel Prize to Ahmed Zewail in 1999 for his contributions to the examination of the break of the chemical bond [5]. A few years later, femtosecond pulses were used to generate the first isolated attosecond pulses (1 as = 10^{-18}s) [6]. This opened up the way of studying sub-fs electronic processes in solids such as the photoemission of electrons from the valence band [7].

The femtosecond studies within this work comprise two major parts: broadband transient absorption spectroscopy (part III) and nonlinear examinations on enantioenrichment with circularly polarised laser pulses (part IV). Both parts include an introduction into the respective research field and complete the results with suggestions on continuative experiments. An introduction into the theoretical principles of light-matter interaction is outlined in part II. Finally, in part V, the results of both experimental parts are summarised and an outlook to future perspectives is given.

Since the early days of femtosecond spectroscopy, pump-probe experiments proofed to be a powerful tool for directly monitoring real-time electron and nuclear dynamics in molecules and solids upon absorption of a photon. This method enabled to elucidate the primary processes in photochemical reactions (see e.g. [8, 9, 10, 11]). When expanding the pulses to the infrared spectral range, processes such as structural changes and phase transitions can be observed (see e.g. [12, 13]). The impact of photophysics and photochemistry to (bio)chemical, pharmaceutical and medical sciences and also (nano)technologies is still growing. Detailed knowledge of the excited state dynamics allows to optimise the processes and molecular design towards the desired effects. Up to now, broadband transient absorption spectroscopy (introduced in chapter 3) has evolved to an indispensable standard tool for disentangling highly complex photophysical and photochemical processes in large biomolecules such as DNA or proteins [14, 15, 16, 17, 18]. Within this thesis, we apply this method to characterise the excited state dynamics in novel organic molecules for potential use in pharmaceuticals or for technical applications. Chapter 4 presents the examinations on coumarins 3-substituted

with diethylphosphono groups and phosphonic acid, which are known for their therapeutic effects concerning inhibition of enzymatic and viral processes. The synthesis of chemically or pharmaceutically relevant molecules points towards the control of molecular key parameters such as lifetimes and triplet yields because of their direct impact on photochemical reactions. In particular, substitution of halogens has shown to have an influence on both parameters via the heavy-atom effect. Hence, we compare the photophysical properties of Br- and Cl-6-substituted coumarin compounds to their unsubstituted analogue in different solvents. The experiments are complemented by time-dependent density functional theory calculations. Broadband transient absorption spectroscopy is further applied to examine the photochemical transformation of chromone derivatives (chapter 5). These molecules undergo an irreversible photochemical transformation and are suitable candidates for applications in optical information recording and storage.

The experiments reported in part IV aim at developing a new method for enantioenrichment of films of chiral molecules using circularly polarised femtosecond pulses. Enantioenrichment and enantioseparation play a crucial role in pharmaceutical chemistry. Many biomolecules, such as enzymes or amino acids are chiral. Hence, the majority of pharmaceutically active substances is chiral as well. However, the desired therapeutic effect is usually provided only by one of the enantiomers (chiral isomers), whereas in common chemical synthesis both enantiomers are produced in equal amounts. The other enantiomer often exhibits different effects, which can lead to unexpected complications [19, 20]. The most prominent case of unwanted side effects was probably the Contergan scandal in the 1960s [21]. Contergan was the name of a sedative in Germany with the active ingredient Thalidomide. Use of the drug during pregnancy caused severe deformities (dysmelia) in foetuses. Thalidomide, which is chiral, was delivered as a racemate. The sedative effect could be attributed to the R-enantiomer, while the S-enantiomer exhibits the teratogenic effects [22, 23]. This terrible incident emphasises the necessity of fundamental in vitro research on both enantiomers and their interactions. Likewise, the development of methods for enantioseparation and enantioenrichment, which in particular do not require the use of chemical additives in order to avoid additional side effects, is of great interest for the pharmaceutical industry. In chapter 6, experiments towards a new method for contaminant free enantioenrichment using circularly polarised femtosecond laser pulses are presented. The idea is to preferentially desorb one of the enantiomers of a film of racemic BINOL (1,1'-bi-2-naphthol) from an achiral surface. The highly sensitive technique of second-harmonic circular dichroism spectroscopy is utilised to measure the generated anisotropy factor in the remaining film. In combination with measurements on enantiopure films, this is expected to give information about the enantiomeric excess. Furthermore, numerical simulations are performed in order to identify and quantify the underlying processes on the irradiated surface.

Moreover, we examined naphthalimide-isoquinoline derivatives in solution using fluorescence upconversion spectroscopy with a femtosecond-long-cavitiy-oscillator.

Part II

Principles of light-matter interaction

2. Light-matter interaction

2.1. Introduction

The following chapter provides an overview of the theoretical background, which is required for a deeper understanding of the experiments and results discussed in this thesis. Beginning with the principles of light-matter interaction, section 2.2 focuses on nonlinear optical interactions for high power and/or ultrashort pulsed laser irradiation. Beside a presentation of nonresonant second- and third-order nonlinear effects, as far as relevant, an abstract on the derivation of resonant nonlinear processes leads to expressions for two-photon resonant susceptibilities. Further, nonlinear properties of chiral molecules are discussed. Moreover, in section 2.3 the fundamentals of the interaction of light with organic molecules are explained. Via basic principles such as the Born-Oppenheimer approximation and the Franck-Condon principle, Fermi's Golden rule is derived. Special attention is put on the theoretical concepts of the primary photophysical properties of organic molecules, while photochemical processes are only introduced as far as they are related to the experiments in this thesis. Finally, an introduction to femtosecond pulse propagation and polarisation is given in section 2.4.

2.2. Nonlinear optics

2.2.1. Nonlinear polarisation and electric susceptibility

In the classical limit of a quantum-mechanical notation, the interaction of an electromagnetic field with matter is described by the macroscopic Maxwell equations [24]:

$$\nabla \times \vec{E} = -\frac{\partial \vec{B}}{\partial t}, \tag{2.1}$$

$$\nabla \times \vec{H} = \vec{j} + \frac{\partial \vec{D}}{\partial t}, \tag{2.2}$$

$$\nabla \cdot \vec{D} = \rho, \tag{2.3}$$

$$\nabla \cdot \vec{B} = 0, \tag{2.4}$$

whereas the symbols $\vec{E}$ and $\vec{H}$ denote the electric and the magnetic field vector, $\vec{D}$ presents the electric displacement. The quantities $\vec{j}$ and ρ describe electric currents and free charge

densities. The magnetic flux density (or magnetic induction) $\vec{B}$ is related to the magnetic field strength $\vec{H}$ via

$$\vec{B} = \mu_0\mu\vec{H} = \mu_0(\vec{H} + \vec{M}) = \mu_0\vec{H}(1 + \chi_m), \tag{2.5}$$

using the permeability of free-space μ_0, the magnetic permeability μ and the magnetisation $\vec{M}$, which is the magnetic dipole moment $\vec{m}$ per unit volume. The quantity χ_m is referred to as the magnetic susceptibility. In general, magnetisation of the medium can be neglected for optical frequencies. Thus, the magnetic permeability $\mu = 1 + \chi_m$ is approximately 1. However, in chiral media, magnetisation has to be considered (see section 2.2.7). The classical treatment is valid for phenomena with high flux densities of photons, such as appear with the application of lasers. The interaction of the electric field $\vec{E}$ of an incoming laser pulse gives rise to displacement of electrons and ions in the material. The electric displacement $\vec{D}$ is given by the material equation

$$\vec{D} = \epsilon_0\epsilon\vec{E}. \tag{2.6}$$

The quantities ϵ_0 and ϵ display the dielectric constant and the absolute permittivity, respectively. In a dielectric medium, the generated polarisation $\vec{P}$, which is the dipole moment per unit volume, can be understood as response to the electric field $\vec{E}$. In the linear regime, $\vec{P}$ is given by the equation

$$\vec{P} = \epsilon_0\chi^{(1)}\vec{E}. \tag{2.7}$$

Herein, the dielectric properties of a medium are described by the linear electric susceptibility

$$\chi^{(1)}(\omega) = \epsilon(\omega) - 1, \tag{2.8}$$

which - like ϵ - is usually a frequency dependent second-rank tensor. Combining equations 2.6 - 2.8 gives

$$\vec{D} = \epsilon_0\vec{E} + \vec{P}. \tag{2.9}$$

For optical frequencies the linear polarisation can be approximated with a harmonic oscillator which includes a restoring force $F_r = -m\omega_0^2 z$. The equation of electron motion can be written according to the Lorentz-Drude model as

$$\ddot{z} + 2\gamma\dot{z} + \omega_0^2 z = -\frac{e}{m}E(t), \tag{2.10}$$

wherein ω_0 denotes the resonance frequency of the oscillator, $-e$ the charge of an electron, m the electron mass, and γ the damping constant. The displacement z of a single electron induces the dipole moment $\vec{p} = -ez$. The macroscopic polarisation $\vec{P}$ is equal to $N \cdot \vec{p}$. Hence, the complex susceptibility can be derived from the solution of the equation of motion to

$$\chi^{(1)}(\omega) = \chi' + j\chi'' = \frac{Ne^2}{\epsilon_0 m}\frac{1}{(\omega_0^2 - \omega^2) + 2j\omega\gamma}, \tag{2.11}$$

with N representing the number density of electrons with unit cm^{-3}. For nonresonant processes, the imaginary part χ'' approaches zero and only the real part χ' contributes. Quantum mechanical calculations of the linear susceptibility via perturbation solution to the density matrix equations of motion confirm the above shown result (equation 2.11) only differing in allowing multiple resonance frequencies ω_0 [25]. Using the relation $\epsilon = 1 + \chi$, the refractive index n can be calculated to

$$n(\omega) = \sqrt{\epsilon(\omega)} = \sqrt{1 + \chi^{(1)}(\omega)} \simeq 1 + \frac{1}{2}\chi^{(1)}(\omega) \tag{2.12}$$

for media with sufficiently small N. Thus, the refractive index is also a complex quantity, which can be written as $n' + in''$ with its real and imaginary parts n' and n''. Assuming the propagation of a plane wave $\tilde{E}(z,t) = Ae^{-i(kz-\omega t)} + c.c.$ (see equation 2.25) through a medium with wavevector $k(\omega) = n(\omega)\omega/c$ (c denotes the vacuum speed of light) and neglecting scattering effects, the intensity varies with position according to the Beer-Lambert law

$$I = nc\epsilon_0 \left\langle \tilde{E}(z,t)^2 \right\rangle = I_0 e^{-\alpha z}. \tag{2.13}$$

The angle brackets indicate a temporal average. The absorption coefficient α (in units of m^{-1}) is connected to the imaginary parts of n and $\chi^{(1)}$ by

$$\alpha = 2n''\frac{\omega}{c} = \chi''\frac{\omega}{c}. \tag{2.14}$$

Moreover, the absorption coefficient is proportional to the absorption cross-section σ_a:

$$\alpha = N_a \cdot \sigma_a, \tag{2.15}$$

with the number density N_a of absorbing particles (e.g. molecules).

For intense applied electric fields, i.e. the amplitude of $\vec{E}$ approaches the order of the atomic electric field strength $E_{at} = 5.14 \cdot 10^{11} \frac{V}{m}$, the movement of the electrons in the Coulomb potential of the atoms cannot be approximated with the harmonic oscillator model anymore. Therefore, nonlinear effects have to be considered. The below summarised fundamentals of nonlinear optics - as far as they are related to this thesis - follow the notation of R. W. Boyd [25]. The polarisation can be split into a linear and a nonlinear part

$$\vec{P} = \vec{P^{(1)}} + \vec{P^{NL}}. \tag{2.16}$$

Accordingly, equation 2.9 can be written as

$$\vec{D} = \vec{D^{(1)}} + \vec{P^{NL}} \tag{2.17}$$

with

$$\vec{D^{(1)}} = \epsilon_0\epsilon\vec{E} + \vec{P^{(1)}} = \epsilon_0\epsilon^{(1)}\vec{E}. \tag{2.18}$$

Assuming nonresonant excitation, the polarisation can be written as a power series

$$P(t) = \sum_i P^{(i)}(t) = (P^{(0)}) + \epsilon_0[\chi^{(1)}E(t) + \chi^{(2)}E^2(t) + \chi^{(3)}E^3(t) + ...], \qquad (2.19)$$

wherein $\chi^{(i)}$ ($i \geq 2$) denote the i-th-order nonlinear optical susceptibilities, which generally are tensors of the order of $(i + 1)$. The same accounts for the absolute permittivity $\epsilon = 1 + \chi$. The field-independent term $P^{(0)}$ describes the static polarisation. This only has to be considered in special cases, e.g. in some crystals, and is therefore omitted in most descriptions [26]. In case of nonresonant excitation, $\epsilon_0\chi^{(i)}E_{at}^i \approx \epsilon_0\chi^{(1)}E_{at}$. As $\chi^{(1)} \approx 1$ for condensed matter, $\chi^{(i)}$ is of the order of $1/E_{at}^{i-1}$. The influence of the single components to the generation of nonlinear polarisation, and hence, the occurrence of nonlinear effects, depends strongly on the symmetry properties of the material. Thus, the components of the susceptibility tensor can be simplified according to contraction rules [27, 25].

2.2.2. Microscopic formulation

Considering microscopic quantities, the molecular (or atomic) dipole moment p_i can be expanded in a power series similar to the macroscopic case (see equation 2.19) using the $n-$th-order molecular (or atomic) (hyper-)polarisabilities $\gamma^{(n)}$:

$$p_i(\omega) = p_i^{(0)}(\omega) + \sum_j \gamma_{ij}^{(1)}(\omega)E_j + \sum_{j \leq k} \gamma_{ijk}^{(2)}(\omega)E_jE_k + \sum_{j \leq k \leq l} \gamma_{ijkl}^{(3)}(\omega)E_jE_kE_l + ..., \qquad (2.20)$$

wherein i, j, k, l represent the internal molecular coordinates. Again, $p_i^{(0)}$ denotes the permanent dipole moment [26]. The first three $n-$th-order hyperpolarisabilities $\gamma^{(n)}$ are often referred to as the (linear) polarisability $\alpha_{ij} := \gamma^{(1)}$, and the second- and third-order hyperpolarisabilities $\beta_{ijk} := \gamma_{ijk}^{(2)}$ and $\gamma_{ijkl} := \gamma_{ijkl}^{(3)}$. The linear polarisability α_{ij} is defined as the expectation value of the dipole moment $\langle p(\omega) \rangle$ in the atom or molecule respectively, which is induced by an external electric field $E(\omega)$ [28, 25], via

$$\langle p(\omega) \rangle = \alpha_{ij}(\omega)E(\omega). \qquad (2.21)$$

Moreover, $\chi^{(1)}$ is defined over the atomic or molecular polarisability according to

$$\chi_{ij}^{(1)} = N\alpha_{ij}(\omega). \qquad (2.22)$$

Analogously, $\chi^{(2)}$ and $\chi^{(3)}$ can be expressed with the second and third order hyperpolarisabilities as

$$\chi_{ijk}^{(2)} = N\beta_{ijk}(\omega), \quad \chi_{ijkl}^{(3)} = N\gamma_{ijkl}(\omega), \qquad (2.23)$$

with the number density N of atoms or molecules.

2.2.3. Nonlinear wave equation

Assuming the absence of free charges and electrical currents, the nonlinear wave equation can be derived from the Maxwell equations for isotropic, dispersionless materials [25]:

$$\nabla^2 \vec{E}(\vec{r},t) - \frac{n^2}{c^2}\frac{\partial^2 \vec{E}(\vec{r},t)}{\partial t^2} = \frac{1}{\epsilon_0 c^2}\frac{\partial^2 \vec{P}(\vec{r},t)}{\partial t^2}. \tag{2.24}$$

Herein, the vacuum speed of light $c = 1/\sqrt{\epsilon_0 \mu_0}$ and the refractive index $n = \sqrt{\epsilon}$ are used. In case nonlinear effects can be neglected, the simplest solution of the wave equation 2.24 are plane waves, which are described in terms of the electric field of amplitude $\vec{A}$ oscillating with the angular frequency ω and propagating with the phase velocity $v_{ph} = \frac{c}{n}$ in direction of the wavevector $\vec{k}$ according to

$$\vec{E}(\vec{r},t) = \vec{A}e^{-i(\vec{k}\vec{r}-\omega t)} + c.c.. \tag{2.25}$$

The term c.c. denotes the complex conjugate, as the electric field is a real quantity, depending on the position in space $\vec{r}$ and the time t. Further following the notation of R. W. Boyd [25], the nonlinear case will be derived. The solution to equation 2.24 will be of similar type, subject to the condition that the nonlinear source term $\frac{1}{\epsilon_0 c^2}\frac{\partial^2 \vec{P}^{NL}(\vec{r})}{\partial t^2}$ is not too large. For simplicity, we presume the scalar field approximation with the light wave travelling in z-direction in the following. According to the slowly varying amplitude approximation, i.e.

$$\left|\frac{\partial^2 A(z)}{\partial z^2}\right| << \left|k\frac{\partial A(z)}{\partial z}\right|, \tag{2.26}$$

the amplitude A of the electric field is now a quantity which is slowly varying with z. Thus, the solution to equation 2.24 can be written as

$$\tilde{E}(z,t) = Ee^{-i\omega t} + c.c. \tag{2.27}$$

with $E = Ae^{ikz}$. The intensity of this wave is further obtained as

$$I = 2n\epsilon_0 c |A|^2. \tag{2.28}$$

Due to the resonant nature of light-matter interactions, the tensors of the electric susceptibility, and hence, the absolute permittivity, depend on frequency. We can express the electric field as a discrete sum of its frequency components ω_n

$$\tilde{E}(z,t) = \sum_n E_n e^{-i\omega_n t} + c.c.. \tag{2.29}$$

Analogue expressions can be derived for $\tilde{D}(z,t)$ and $\tilde{P}^{NL}(z,t)$. Incorporating equation 2.18, we can write

$$\tilde{D}_n^{(1)}(z,t) = \epsilon_0 \epsilon^{(1)}(\omega_n)\tilde{E}_n(z,t). \tag{2.30}$$

Hence, the nonlinear wave equation (equation 2.24) can be rewritten according to

$$\nabla^2 \tilde{E}_n - \frac{\epsilon^{(1)}(\omega_n)}{c^2} \frac{\partial^2 \tilde{E}_n}{\partial t^2} = \frac{1}{\epsilon_0 c^2} \frac{\partial^2 \tilde{P}_n^{\mathrm{NL}}}{\partial t^2}. \tag{2.31}$$

This results in a system of coupled wave equations, one for each frequency component ω_n. Mixing of fields with different frequency components in nonlinear media leads to a series of nonlinear effects. Thereby, output fields with new frequencies are generated. The expressions wherein newly generated frequencies fall close to material resonances, i.e. eigenfrequencies of the electronic and vibrational motions, contribute stronger to the outcoming field. Analogue considerations are valid for higher order susceptibilities. Below, the focus is laid on second-order and third-order nonlinear effects, which are relevant for the experiments presented in this thesis.

2.2.4. Second-order nonlinear effects

Within the electric-dipole approximation, second-order nonlinear effects arise upon three-wave mixing in a non-centrosymmetric medium. For our considerations, we assume the interaction of incoming plane waves of fundamental frequencies ω_1 and ω_2 with lossless materials which exhibit full permutation symmetry. Thus, the driving electric field according to

$$\tilde{E}_{in}(z, t) = E_1 e^{-i\omega_1 t} + E_2 e^{-i\omega_2 t} + c.c., \ \text{ with } E_i = A_i e^{ikz_i} \ \ (i = 1, 2), \tag{2.32}$$

generates a second-order polarisation which is represented by

$$\begin{aligned} \tilde{P}^{(2)}(z, t) = {} & P^{(2)}(2\omega_1) e^{i2\omega_1 t} + P^{(2)}(2\omega_2) e^{i2\omega_2 t} \\ & + P^{(2)}(\omega_1 + \omega_2) e^{i(\omega_1 + \omega_2)t} + P^{(2)}(\omega_1 - \omega_2) e^{i(\omega_1 - \omega_2)t} + P^{(2)}(0) \\ & + c.c.. \end{aligned} \tag{2.33}$$

Herein, each component can be associated with a physical process, such as second-harmonic generation (SHG), sum-frequency generation (SFG), difference frequency generation (DFG), and optical rectifictaion (OR)

$$\begin{aligned} P^{(2)}(2\omega_1) &= \epsilon_0 \chi^{(2)} E_1^2 \ \ \text{(SHG)}, \\ P^{(2)}(2\omega_2) &= \epsilon_0 \chi^{(2)} E_2^2 \ \ \text{(SHG)}, \\ P^{(2)}(\omega_1 + \omega_2) &= 2\epsilon_0 \chi^{(2)} E_1 E_2 \ \ \text{(SFG)}, \\ P^{(2)}(\omega_1 - \omega_2) &= 2\epsilon_0 \chi^{(2)} E_1 E_2^* \ \ \text{(DFG)}, \\ P^{(2)}(0) &= 2\epsilon_0 \chi^{(2)} (E_1 E_1^* + E_2 E_2^*) \ \ \text{(OR)}. \end{aligned} \tag{2.34}$$

The induced output field with the new frequency ω_3 can be written in the form

$$\tilde{E}_{out}(z, t) = A_3 e^{-i(-k_3 z_3 + \omega_3 t)} + c.c. \tag{2.35}$$

Using Einstein summation convention and defining $E_n(\omega_n)^* = E_n(-\omega_n)$, the induced polarisation can be written as

$$P_i^{(2)}(\omega_o; \omega_n, \omega_m) = \epsilon_0 D \sum_{jk} \chi_{ijk}^{(2)}(\omega_o; \omega_n, \omega_m) E_j(\omega_n) E_k(\omega_m). \tag{2.36}$$

Here the indices ijk are used for the Cartesian components of the field, whereas the components with indices onm represent the output frequency, which above refers to ω_3, and the two input frequencies (above ω_1, ω_2). The symbol D denotes the degeneracy factor for the permutations of the different input frequencies.

Three-wave mixing further requires momentum and energy conservation. Hence, usually only one of these processes is dominant depending on the phase matching of the wavevectors k_1 and k_2. In case of SFG (DFG), the outcoming wave oscillates with frequency $\omega_3 = \omega_1 + \omega_2$ ($\omega_3 = \omega_1 - \omega_2$) and travels with the wavevector $k_3 = k_1 + k_2$ ($k_3 = k_1 - k_2$.). Second-harmonic generation is a particular case of SFG for $\omega_1 = \omega_2$ and $k_1 = k_2$. Thus, $\omega_3 = 2\omega_1$, and $k_3 = 2k_1$. Optical rectification produces an electric field with $\omega_3 = \omega_1 + \omega_1 = 0$ and $k_3 = 0$.

Furthermore, optical parametric amplification allows the amplification of a weak input signal $E_1(\omega_1)$ by interaction with a strong pump field $E_2(\omega_2)$ ($\omega_2 > \omega_1$) through the parametric process of DFG. During this process the total energy is conserved by generation of idler photons at the difference frequecny $\omega_3 = \omega_2 - \omega_1$. The achieved gain depends on phase matching, interaction length in the nonlinear medium, the strenght of second-order nonlinearity of this medium and the pump intensity.

Perfect phase matching is achieved for

$$\Delta k = 0, \tag{2.37}$$

whereas $\Delta k = k_1 + k_2 - k_3$ for SFG and $\Delta k = k_1 - k_2 - k_3$ for DFG. In this case, the energy transfer from the incoming waves to the outcoming wave is most efficient. Deviations from perfect phase matching lead to a decrease of the output intensity.

Physically, the nonlinear generation of new frequencies in the output field can be explained according to the model of an anharmonic oscillator, i.e. by adding an additional anharmonic term to the equation of motion in the Lorentz-Drude model (equation 2.10), for instance. The solution of this anharmonic equation contains terms of the form $(\omega_0^2 - \omega_i^2) + 2j\omega_i\gamma$ (with $i = 1, 2, 3$) in the denominator of $\chi^{(2)}$ for each of the output and input frequencies. A comparison with equation 2.11 shows that the second-order nonlinear susceptibility can be expressed and experimentally

realised as a product of first-order, i.e. linear, susceptibilities

$$\chi^{(2)}(\omega_3; \omega_1, \omega_2) = \frac{\epsilon_0^2 ma}{n_e^2 e^3} \chi^{(1)}(\omega_1) \chi^{(1)}(\omega_2) \chi^{(1)}(\omega_3).$$ (2.38)

The same accounts for higher order susceptibilities. For instance, $\chi^{(3)}$ can also be described as a product of $\chi^{(1)}$ processes. Furthermore, due to the phenomenon of cascaded optical nonlinearities, $\chi^{(3)}$ can be expressed by a combination of $\chi^{(2)}$ processes [29].

It has to be noted that the discussion of second-order nonlinear effects in this section was restricted to the electric-dipole approximation, which is generally applied for the case of $\vec{k}\vec{r} << 1$ (with $\vec{r}$ the vector from the nucleus to the electron), i.e. the wavelength of the excitation pulse is much larger than the size of the atom or molecule, as it is the case for the experiments presented within this work. It has been shown experimentally and theoretically that SHG is also possible in isotropic media when taking into account electric quadrupole effects and magnetic dipole effects [30, 31, 32]. However, the intensities are many orders of magnitude smaller than electric-dipole allowed SHG-intensities [32]. Only at surfaces, where the symmetry is broken, the SHG intensity is enhanced due to a surface term arising from the first few atomic layers of the medium, which is at least as large as the so-called nonlocal nonlinear bulk response [32, 33].

2.2.5. Third-order nonlinear effects

Applying the model of the anharmonic oscillator to centrosymmetric media, the equation of motion contains terms, which are proportional to an odd power of z. Deriving the polarisation from its solution, P contains odd-order nonlinear susceptibilities $\chi^{(1)}$, $\chi^{(3)}$, ..., while $\chi^{(2)}$, $\chi^{(4)}$, ..., are zero. Typical third order effects include i. a. third-harmonic generation, the optical Kerr effect, self-focusing (SF), and self-phase modulation (SPM). In general, the third-order polarisation $P_i^{(3)}(\omega_p)$ with output frequency ω_p can be written analogously for the three input frequencies ω_n, ω_m and ω_o

$$P_i^{(3)}(\omega_p; \omega_n, \omega_m, \omega_o) = \epsilon_0 D \sum_{jkl} \chi_{ijkl}^{(3)}(\omega_p; \omega_n, \omega_m, \omega_o) E_j(\omega_n) E_k(\omega_m) E_l(\omega_o).$$ (2.39)

Again, the permutations of the input frequencies are represented by the degeneracy factor D. Considering positive and negative signs for the input frequencies, the output field consists of 44 different frequency components [25]. Therefore, we want to limit ourselves to the simple example of a monochromatic input field $E(\omega)$. The generated nonlinear polarisation gives rise to output fields with frequencies at ω and 3ω:

$$\tilde{P}^{(3)}(z, t) = \frac{1}{4}\epsilon_0 \chi^{(3)} E(\omega)^3 e^{i3\omega t} + \frac{3}{4}\epsilon_0 \chi^{(3)} E(\omega)^3 e^{i\omega t}.$$ (2.40)

The first term describes the generation of the third harmonic at frequency 3ω. The second term leads to effects like SF or SPM. In this case, the refractive index of many materials is

intensity-dependent and can be written as

$$n = n_0 + n_2 I = n_0 + 2n_2\epsilon_0 c \left| E(\omega) \right|^2. \tag{2.41}$$

This relation is called the optical Kerr effect. The linear and the nonlinear refractive indices n_0 and n_2 can be expressed in terms of the linear and nonlinear susceptibilities according to

$$n_0 = \sqrt{1 + \chi^{(1)}}, \quad n_2 = \frac{3\chi^{(3)}}{4n_0^2\epsilon_0 c}. \tag{2.42}$$

The optical Kerr effect gives rise to several processes with applications in ultrafast physics. In the Gaussian shaped profile of a collimated laser beam, which propagates through a medium with positive n_2, the refractive index at the centre of the beam is larger than at the periphery. Therefore, the material has the effect of a lens, the so-called Kerr lens, which causes self-focusing of the laser beam above a critical peak power. For much larger laser powers, subsequent ionisation and filamentation lead to a breakup of the beam. Self-focusing is an important process to achieve mode-locking in laser oscillators.

As a further effect, self-phase modulation can be related to the intensity dependence of the refractive index. The change of the phase of a laser pulse with central frequency ω_0, when propagating through a thin nonlinear medium with length L, is given by

$$\Phi_{\text{NL}}^{\text{L}}(t) = -n_2 I(t)\omega_0 \frac{L}{c}. \tag{2.43}$$

Within the slowly varying amplitude approximation we can define the instantaneous frequency $\omega(t)$ of the transmitted pulse

$$\omega(t) = \omega_0 + \delta\omega(t) \ \text{ with } \ \delta\omega(t) = \frac{d}{dt}\Phi_{\text{NL}}^{\text{L}}(t). \tag{2.44}$$

The variation of the instantaneous frequency $\delta\omega(t)$ causes spectral broadening and hence, produces new frequency components. Self-phase modulation is, thus, the dominant process in white-light and supercontinuum generation, which underlies the broadband probe generation in our transient absorption spectrometer.

2.2.6. Resonant nonlinear susceptibility

As mentioned above, the Lorentz-Drude model and its extension to an anharmonic oscillator constitutes a sufficiently good approximation for the nonresonant nonlinear effects as presented in sections 2.2.4 and 2.2.5. However, the nonlinear susceptibility becomes extremely large, when the frequencies of the incoming laser pulse are in resonance with an optical transition frequency of the material. In order to be able to treat effects such as collisional broadening of these resonances, a quantum mechanical approach is required, such as it is given in density matrix perturbation theory (see i.a. R. W. Boyd, chapter 3.3 [25]). Accordingly, the statistical

state of a system is expressed by the density matrix. The probability amplitudes C_n^s of the eigenstates u_n of the atom are summarised in the wave function of the system in state s

$$\psi_s(\vec{r}, t) = \sum_n C_n^s(t) u_n(\vec{r}). \tag{2.45}$$

This wavefunction has to satisfy the Schrödinger equation

$$i\hbar \frac{\partial \psi_s(\vec{r}, t)}{\partial t} = \hat{H} \psi_s(\vec{r}, t). \tag{2.46}$$

The interaction energy of the atom and the incoming laser field can be written as $\hat{V}(t) = -\hat{\mu}\hat{E}(t)$ using the dipole moment operator $\hat{\mu}$. Applying a perturbation ansatz, the different terms $\chi^{(i)}$ of the electric susceptibility can be derived. Hence, the first term, i.e. the linear susceptibility $\chi^{(1)}$, can be written as

$$\chi^{(1)}(\omega) = \frac{N}{\epsilon_0 \hbar} \sum_n \frac{1}{3} |\mu_{ng}|^2 \left[\frac{1}{(\omega_{ng} - \omega) - i\gamma_{ng}} + \frac{1}{(\omega_{ng} + \omega) + i\gamma_{ng}} \right] \tag{2.47}$$

for an isotropic material. The indices ng denote the optical electronic transition from the ground state g to higher lying states n. Thus, the quantities μ_{ng} and ω_{ng} represent the associated dipole moments and transition frequencies, and γ_{ng} the damping rates. The nonlinear susceptibilities exhibit an equivalent form, however, contain multiple terms for all possible permutations (expressed by the permutation operator P) of transitions $n_1 \to n_2$ and input frequencies ω_i

$$\chi^{(m)}(\omega) \propto P \left[\frac{1}{(\omega_{n_1 n_2} - \sum_i \omega_i) - i\gamma_{n_1 n_2}} + \frac{1}{(\omega_{n_1 n_2} + \sum_i \omega_i) + i\gamma_{n_1 n_2}} \right]. \tag{2.48}$$

If one or a combination of input frequencies approaches one of the resonance frequencies $\omega_{n_1 n_2}$ for optical electronic transitions, singularities occur in the susceptibility. This leads to a "resonant enhancement" of the susceptibility. It has to be noted that close to resonances the small-perturbation approximation made in the calculation becomes invalid, because the transition frequencies in the denominator of equation 2.48 become field-dependent and thus, have to be treated as strong perturbations. Taking this fact into account, the susceptibility is limited to a finite value [26]. Moreover, the interaction between different atoms or molecules has been neglected so far, and the electric field has been considered as the macroscopic field described in the Maxwell equations. However, for a more realistic description of dense media, local field effects have to be considered. The Lorentz local field can be expressed as

$$E_{\text{loc}} = E + \frac{N}{3\epsilon_0} p, \tag{2.49}$$

wherein p is the dipole moment per molecule. Taking these into account, the second-order susceptibility for second-harmonic generation, for instance, can be derived to

$$\chi^{(2)}(2\omega;\omega,\omega) = \left(\frac{\chi^{(1)}(\omega)+3}{3}\right)^2 \left(\frac{\chi^{(1)}(2\omega)+3}{3}\right) N\beta(2\omega;\omega,\omega). \qquad (2.50)$$

Here the quantity β represents the second-order hyperpolarisability of the target molecule.
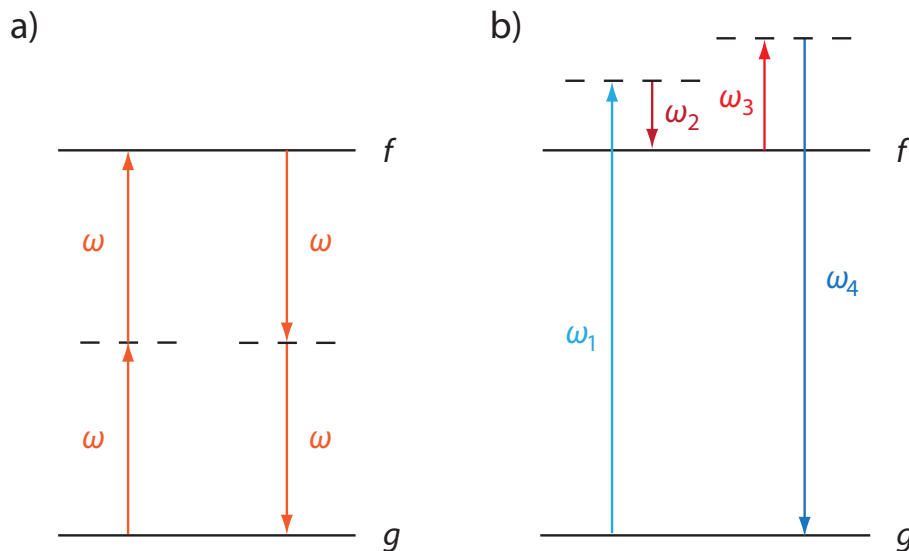
Figure 1 Molecular energy-level diagrams of the resonant third-order nonlinear processes a) two-photon absorption (TPA), and b) Raman scattering (RS). a) In TPA, two photons with frequency ω are absorbed simultaneously according to a resonant transition with energy $2\hbar\omega$ from the molecule's ground state g to the excited state f. b) The case $\omega_1 = \omega_4 = \omega_p$ and $\omega_2 = \omega_3 = \omega_s$ applies to stimulated Raman scattering (SRS) with pump frequency ω_p and Stokes frequency ω_s. If $\omega_1 = \omega_3$, the process is called coherent anti-Stokes Raman scattering (CARS) with anti-Stokes frequency ω_4. Dashed lines refer to virtual levels (adapted from [26]).

In many spectroscopic techniques the $\chi^{(3)}$-processes of two-photon absorption (TPA) and Raman scattering (RS) play a significant role. Figure 1 illustrates respective molecular energy level diagrams for the two processes. In TPA two photons with energy $\hbar\omega$ are absorbed simultaneously when 2ω is equal to the frequency of an optical transition, while the frequency ω of only one photon need not be equal to a transition. Hence, the dashed line refers to a virtual level. The first theoretical description of TPA was given by Maria Göppert-Mayer [34]. For spontaneous Raman scattering, the nonlinear medium is assumed to oscillate at a vibrational frequency Ω_v. Hence, interaction with an incoming field of frequency ω_p generates Stokes- and anti-Stokes-frequencies $\omega_{S,AS} = \omega_p \mp \Omega_v$. Even more important is the effect of stimulated Raman scattering (SRS), particularly in microscopy [35, 36]. In SRS two incoming laser fields, a pump field with frequency ω_p and a second field with the Stokes-shifted frequency ω_s, induce the emission of photons with the so-called Stokes or Raman frequency ω_s. The Stokes-shift $\Omega_v = \omega_p - \omega_s$ is usually in the infrared spectral range. For strong pump fields at frequency ω_p this effect can be very efficient.

According to P. N. Butcher and D. Cotter [26], expressions for the third-order nonlinear susceptibility of two two-photon-resonant $\chi^{(3)}$-processes can be derived from the general case (see equation 2.48). By defining the first-order (TPA-resonant) transition hyperpolarisibility tensors α_{fg} as

$$\alpha_{fg}(\omega_1; \omega_2) = \frac{e^2}{\hbar} \sum_i \left[\frac{\mu_{fi}\,\mu_{ig}}{(\omega_{ig} - \omega_2)} + \frac{\mu_{fi}\,\mu_{ig}}{(\omega_{ig} - \omega_1)} \right], \tag{2.51}$$

and using the relation $\alpha_{fg}(\omega_1; \omega_2) = \alpha_{fg}(\omega_2; \omega_1)$, the third-order nonlinear susceptibility for TPA follows as

$$\chi_{\mathrm{TPA}}^{(3)}(\omega; \omega, \omega, -\omega) = \frac{N}{6\hbar\epsilon_0} \frac{1}{\omega_{fg} - i\Gamma - 2\omega} \sum_{\{g,f\}} [\rho_0(g) - \rho_o(f)] \langle \alpha_{fg}(\omega; \omega)^* \alpha_{fg}(\omega; \omega) \rangle, \tag{2.52}$$

Here, $\rho_0(g)$ and $\rho_0(f)$ denote the fractional populations of the degenerate states g and f, and Γ is the damping factor. For simplicity, local field effects are neglected in above equations. However, they can be included without altering the discussion according to [26]. The products of first-order transition hyperpolarisability tensors α_{fg} in angle brackets indicate an orientation average of these quantities. These tensors describe, analogously to the transition matrix moments μ_i (see section 2.3.2), the transition from ground state g to final state f in the linear regime for TPA-resonant processes [34, 26].

The cross-section σ_{TPA} for TPA is linearly depending on intensity:

$$\sigma_{\mathrm{TPA}} = \sigma_2 I. \tag{2.53}$$

The coefficient σ_2 describes the strength of the TPA process [25].

The experiments using SHG spectroscopy described in chapter 6 are concerned with the case of SHG resonant or near resonant with a one-photon transition frequency ω_f at the second harmonic frequency. According to A. Moad and G. Simpson [37], the second-order hyperpolarisability tensor for this case can be written as

$$\beta^{ijk}(2\omega; \omega, \omega) = \frac{-1}{4\hbar} \sum_f \frac{\mu_{fg}^i (\alpha_{fg}^{jk})_{\mathrm{TPA}}}{(\omega_f - 2\omega - i\Gamma_f)}. \tag{2.54}$$

The matrix elements for the (one-photon) transitions from ground state g to final state f are herein denoted as μ_{fg}, whereas $(\alpha_{fg}^{jk})_{\mathrm{TPA}}$ denotes the tensor elements describing TPA from the states g to f with applied electric fields polarised along the directions j and k [38, 34]. Recalling expression 2.23, equation 2.54 links the second-order nonlinear susceptibility to TPA, which is actually a $\chi^{(3)}$-process.

2.2.7. Resonant nonlinear optical properties of chiral molecules

Chiral molecules have isomers, called enantiomers, which are not superimposable with their mirror image. Assuming a mixture of two enantiomers with amount concentrations S and R, the enantiomeric excess (ee) of the mixture is defined as

$$\text{ee} = \frac{|R - S|}{R + S}.\tag{2.55}$$

A mixture with ee = 0.5 is termed a racemic mixture or racemate.

Linear optical activity

Chiral molecules do not posses an axis of rotary inversion (or improper rotation). This results in different refractive indices for interaction with left and right circularly polarised light, thus, giving rise to optical activity. Assuming a circularly polarized plane wave with frequency ω propagating in z-direction through a medium which is isotropic in the xy-plane, the complex electric field vector for right (+) and left circular polarisation (-) is given by (see equation 2.25)

$$\begin{aligned}\vec{E}_+(z) &= \vec{A}e^{-i(n_+\frac{z}{c}-\omega t)}(-\vec{e}_x + i\vec{e}_y),\\\vec{E}_-(z) &= \vec{A}e^{-i(n_-\frac{z}{c}-\omega t)}(\vec{e}_x - i\vec{e}_y),\end{aligned}\tag{2.56}$$

wherein $\vec{e}_x$ and $\vec{e}_y$ are unit vectors in x- and y-direction. The complex refractive index can be written as $n_\pm = n'_\pm + in''_\pm = n'_\pm + i\frac{\alpha_\pm c}{2\omega}$ (see equation 2.14). In a chiral medium, $n'_+ \neq n'_-$ and $n''_+ \neq n''_-$. Starting with a linearly polarized wave at $z = 0$, the different interaction of the circular components of $\vec{E}$ with the medium causes a relative phase delay. Thus, the electromagnetic wave is elliptically polarised after transmission through the chiral medium.

In most theoretical descriptions, a proper explanation of linear optical activity extends beyond the electric-dipole approximation [39, 40, 41]. Beside the induced electric-dipole moment $\vec{\mu}$, the induced magnetic dipole moment $\vec{m}$ (which exhibits different signs for the enantiomers [42]), and for a medium consisting of oriented chiral molecules, the induced electric-quadrupole moment have to be considered. The optical rotation strength R^{fg} is defined as [43, 44, 45]

$$R^{fg} = \Im\mathfrak{m}(\vec{\mu}_{gf} \cdot \vec{m}_{fg})\tag{2.57}$$

Accordingly, the optical rotation over a path l is given by [43, 45, 39, 40]

$$\delta = (n'_- - n'_+)\frac{\omega l}{2c} \propto -\frac{\omega l}{c}R^{fg}\tag{2.58}$$

Measuring the optical rotation is the basis of the important spectroscopic technique of optical rotation dispersion (ORD) measurements, whereby the rotation of a monochromatic, linearly polarised laser beam in a chiral medium is detected. The ellipticity angle can be written as [39]

$$\theta = (n''_- - n''_+)\frac{\omega l}{2c}(\propto R^{fg}).$$

(2.59)

Furthermore, the imaginary part of the phase delay gives rise to different absorption of the electromagnetic wave in the chiral medium. This effect is referred to as circular dichroism (CD) and is defined as the difference of absorbance $A = \mathrm{OD}$ (or optical density OD) of a solution containing chiral molecules for excitation with left (LCP) and right circularly polarised (RCP) light [46]:

$$\mathrm{CD} = A_{\mathrm{LCP}} - A_{\mathrm{RCP}} = (\varepsilon_{\mathrm{LCP}} - \varepsilon_{\mathrm{RCP}})Cl.$$

(2.60)

The quantity C denotes the amount concentration (with unit mol L^{-1}), and l is the path length through the solution. The difference of the molar absorption coefficients $\varepsilon_{\mathrm{LCP}} - \varepsilon_{\mathrm{RCP}}$ for LCP and RCP light, respectively, is termed as the molar CD. The molar absorption coefficient [46] (formerly also known as molar extinction coefficient) can be derived from the (linear) absorption coefficient α (see equation 2.13 (Napierian definition) and equation 2.88 (decadic definition)) by $\varepsilon = \frac{\alpha}{C} = \frac{A}{Cl}$. Moreover, the circular dichroism is also proportional to the optical rotation strength (see equation 2.57) [45]:

$$\mathrm{CD} \propto R^{fg}.$$

(2.61)

Normalising the quantity CD gives the anisotropy factor ("g-Factor"):

$$g = \frac{\Delta\varepsilon}{\varepsilon} = \frac{\varepsilon_{\mathrm{LCP}} - \varepsilon_{\mathrm{RCP}}}{\frac{1}{2}(\varepsilon_{\mathrm{LCP}} + \varepsilon_{\mathrm{RCP}})}$$

(2.62)

While the above given description applies well for isotropic media, the occurrence of ORD and CD in systems of oriented molecules can be explained solely within the electric-dipole approximation [47, 48, 49].

Second-order nonlinear optical properties of chiral molecules

Chiral molecules are intrinsicly non-centrosymmetric. Thus, second-order nonlinear processes can be observed [50, 51, 52, 53] and explained within the electric-dipole approximation, even in isotropic chiral solutions and liquids [50, 54]. Assuming three-wave mixing in a chiral medium, the induced polarisation includes components, which oscillate at the sum-frequency and the difference frequency polarisation (see section 2.2.4). In 1965 J. A. Giordmaine showed theoretically that SFG- and DFG-effects are possible in optically active liquids, although excluding SHG [54]. The second-order susceptibility tensor $\chi^{(2)}_{ijk}$ can be written as the sum of a symmetric tensor $S_{ijk} = S_{ikj}$ and an antisymmetric tensor $A_{ijk} = -A_{ikj}$. In isotropic liquids, the symmetric tensor is equal to zero. Using contracted notation ($a_{14} = A_{123} - A_{132} = \chi^{(2)}_{123} - \chi^{(2)}_{132}, a_{25} =$

$\chi^{(2)}_{231} - \chi^{(2)}_{213}, a_{36} = \chi^{(2)}_{312} - \chi^{(2)}_{321}$), the antisymmetric tensor can be reduced to

$$
A_{ijk} = \begin{pmatrix} 0 & 0 & 0 & a_{14} & 0 & 0 \\ 0 & 0 & 0 & 0 & a_{25} & 0 \\ 0 & 0 & 0 & 0 & 0 & a_{36} \end{pmatrix}, \tag{2.63}
$$

wherein a_{14}, a_{25}, and a_{36} are the only non-vanishing elements. The totally antisymmetric tensor A_{ijk} changes sign under reflection on a mirror plane, but does not vary under rotational transformations, thus violating Kleinmann symmetry, which is a requirement for the occurrence of SHG [27, 55]. Averaging over all orientations of the molecule, the polarisation for sum-frequency in a liquid can be written as [54, 56]

$$
\vec{P}(\omega_1 + \omega_2) = \chi^{(2)}_{chiral}\vec{E}(\omega_1) \times \vec{E}(\omega_2) = \frac{1}{6}(a_{14} + a_{25} + a_{36})\vec{E}(\omega_1) \times \vec{E}(\omega_2). \tag{2.64}
$$

For chiral molecules the sum of these "chiral" elements, $a_{14} + a_{25} + a_{36}$, which is a pseudoscalar, is nonzero. It follows further, that non-collinear arrangement of the incoming fields $\vec{E}(\omega_1)$ and $\vec{E}(\omega_2)$ is required in order to generate a sum-frequency signal. A quantum-mechanical description yields that $\chi^{(2)}_{\text{chiral}}$ gets proportional to $(\omega_1 - \omega_2)$, when ω_1 approaches ω_2 [54, 55, 56]. If further, the sum-frequency ω_{sum} is in resonance with an electronic transition $g \to f$, it follows [56]

$$
\chi^{(2)}_{\text{chiral}} \propto N \sum_f \frac{(\omega_1 - \omega_2)}{(\omega_{\text{sum}} - \omega_{fg} + i\Gamma_{fg})} \times \sum_m \frac{\vec{\mu}_{gf}(\vec{\mu}_{fm} \times \vec{\mu}_{mg})}{(\omega_1 - \omega_{mg})(\omega_2 - \omega_{mg})}. \tag{2.65}
$$

Therefore, no second-harmonic can be generated in an isotropic ensemble of (enantiopure or racemic mixtures of) chiral molecules. Because $\chi^{(2)}_{\text{chiral}}$ is a pseudoscalar, it changes sign under reflection on a mirror plane, as it would be the case for the other enantiomer. Hence, second-order nonlinear processes are not possible in racemic solutions. In fact, in a solution which is a mixture of two enantiomers, the SFG-intensity, which is proportional to $|\chi^{(2)}|^2$, depends on the difference in concentration of the two enantiomers, hence, the enantiomeric excess [40]. Furthermore, for a proper alignment of the polarisations of the incoming beams, i.e. the incoming fields being either both parallel or one parallel and the other one perpendicular to the incident plane, SFG is an almost background-free spectroscopy technique for probing only the chiral-specific elements of an isotropic medium [55, 56, 40]. However, the strength of the SFG-signal is quite small. Due to similarities in the expressions of χ_{NL} and the optical rotation ρ, Giordmaine estimated $\chi^{(2)}_{\text{chiral}}$ to be at least two orders of magnitude smaller than ρ, even close to resonances [54]. Distinct alignment of the polarisations of the incoming and outcoming beams even allows to distinguish between the enantiomers [56]. However, this can be achieved much simpler with SHG-spectroscopy on surfaces of thin films of chiral molecules (see below).

Recalling the notation from Moad and Simpson [37] (see equations 2.54 and 2.51) the second-

order hyperpolarisability tensor for SFG in an isotropic chiral medium can be written as [57]

$$\beta^{ijk}(\omega_1 + \omega_2; \omega_1, \omega_2) \propto \frac{\mu_{gf}^z \left[(\alpha_{xy}^{fg})_{\text{TPA}} - (\alpha_{yx}^{fg})_{\text{TPA}} \right]}{(\omega_f - (\omega_1 + \omega_2) - i\Gamma_f)}. \qquad (2.66)$$

Herein, the TPA-tensor α_{TPA}^{fg} is only asymmetric, i.e. $\alpha_{xy} \neq \alpha_{yx}$, for $\omega_1 - \omega_2 \neq 0$. Therefore, from this notation also follows that SHG is not possible in isotropic chiral media within the electric-dipole approximation. Only the many orders of magnitude weaker SHG-effects arising from electric quadrupole and magnetic-dipole transitions can occur as mentioned in section 2.2.4.

However, sum-frequency and second-harmonic frequency signals can be generated at surfaces of oriented systems of molecules [58, 51, 52, 53, 41, 40, 59]. Because of the symmetry breaking at the interface, certain chiral and achiral second-order nonlinear effects are allowed. The common models, which explain these effects, depend on the structure of the molecule [60, 40]. Hence, second-harmonic optical activity of chiral molecules has been described either using a one-electron mechanism, in which one electron is bound to a helical path, or by a model of two coupled anharmonic oscillators. The one-electron model attributes the second-harmonic optical activity to the superposition of chiral $\chi^{(2)}$-elements arising from magnetic dipolar transitions and achiral elements representing electric dipolar transitions [61, 60, 40]. Chiroptical SHG-effects in films of polythiophene [62] and chiral stilbene [63], for instance, could only be theoretically described including magnetic contributions. On the other hand, the second-harmonic optical activity of molecules described with the coupled-oscillator model attributes the effect to chiral $\chi^{(2)}$-elements representing electric-dipole transitions, and achiral elements due to electric-dipole, electric-quadrupole, and magnetic-dipole transitions [40, 57]. In general, the contribution of magnetic-dipole moments to the chiroptical response is, however, limited to at most a few per cent (in contrast to predictions of early studies) of the response of electric-dipole effects [57, 64, 65]. Generation of second-harmonic nonlinear effects of a monolayer of BINOL (1,1'-bi-2-naphthol) is in agreement with the coupled-oscillator model and can be described solely within the electric dipole approximation [40, 66, 67, 56]. Beside the above-described optical activity of chiral molecules, structural chirality, i.e. the alignment of chiral or even achiral molecules in macromolecular chiral structures like helical or propeller-like assemblies or crystals, for instance, can give rise to strong second-harmonic optical activity effects or enhance existent chiral effects [68, 69, 70, 57, 71]. Even anisotropic surfaces of achiral molecules or racemic mixtures can exhibit properties like surfaces of chiral molecules [72, 73, 74].

The second-order nonlinear susceptibility tensor $\chi^{(2)}$ consists of the orientational average of coherent contributions of N_m individual molecules [57],

$$\chi_{ijk}^{(2)} = N_m \sum_{xyz} \langle R_{ix} R_{jy} R_{kz} \rangle \beta_{xyz}, \qquad (2.67)$$

where the transformation from molecular coordinates x, y, z to laboratory coordinates i, j, k is

expressed by the vectors R_{mn}. Generally, orientational ordering of molecules on a surface can, additionally to resonant excitation, strongly enhance the second-order intensity and optical activity [75, 76].

In analogy to the effects of linear optical activity (see equations 2.58, 2.60, 2.62), second-harmonic generation circular dichroism (SHG-CD) is defined as [61, 40, 41, 51]

$$\mathrm{SHG-CD} = I_{\mathrm{LCP}}(2\omega) - I_{\mathrm{RCP}}(2\omega), \tag{2.68}$$

with the second-harmonic intensity $I_{\mathrm{LCP,RCP}}(2\omega)$. The corresponding anisotropy factor can be written as

$$g(2\omega) = \frac{I_{\mathrm{LCP}}(2\omega) - I_{\mathrm{RCP}}(2\omega)}{\frac{1}{2}(I_{\mathrm{LCP}}(2\omega) + I_{\mathrm{RCP}}(2\omega))}. \tag{2.69}$$

As in ORD, in second-harmonic optical rotation dispersion (SHG-ORD) the linear or elliptical polarisation of the generated light is rotated by an angle δ with respect to the polarisation of the incoming linearly polarised fundamental beam [53, 77].
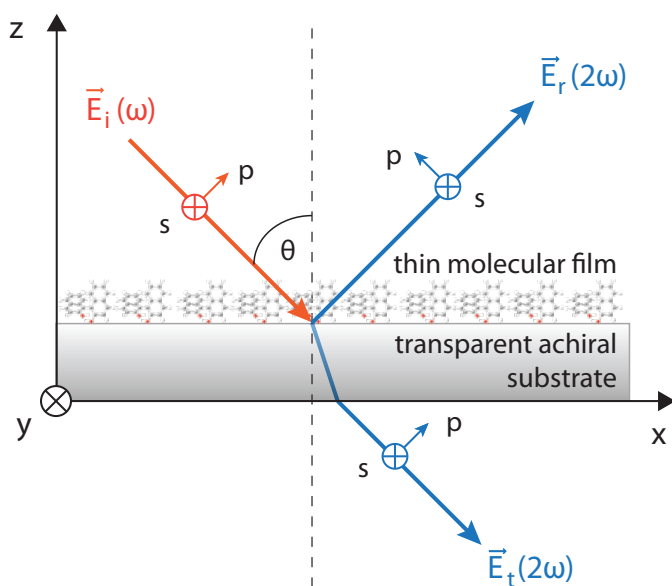
Figure 2 Geometry of SHG at a surface of a thin (chiral or achiral) molecular film (with thickness smaller than the wavelength of the incoming beam) deposited on a transparent achiral substrate. The second-harmonic is generated by the incoming fundamental electric field $\vec{E}_i(\omega)$, which is incident at an angle θ with respect to the surface normal, at the molecule-substrate interface and can be detected in reflection ($\vec{E}_r(2\omega)$) and transmission ($\vec{E}_t(2\omega)$). The molecular axis in this example is parallel to the surface normal.

In figure 2 the basic geometry for the process of SHG on a surface of a thin film of oriented molecules on an isolating substrate is depicted. The surface is supposed to be symmetric about its normal, i.e. C_∞-symmetry for a chiral surface or $C_{\infty\nu}$-symmetry for an achiral surface. Further, the fundamental beam hits the surface at an angle θ. The nonlinear polarisation P and magnetisation M in the medium, which are induced by the interaction with the incoming

fundamental electromagnetic field (E and B), can be written as [30, 78, 41]

$$P_i(2\omega) = \epsilon_0 \chi^{eee}_{ijk}(2\omega; \omega, \omega) E_j(\omega) E_k(\omega) + \epsilon_0 \chi^{eem}_{ijk}(2\omega; \omega, \omega) E_j(\omega) B_k(\omega)$$
$$M_i(2\omega) = \epsilon_0 \chi^{mee}_{ijk}(2\omega; \omega, \omega) E_j(\omega) E_k(\omega)$$

(2.70)

The superscripts e and m of the second-order susceptibility tensors $\chi^{(2)}_{ijk}$ refer to the respective electric- (e) and magnetic- (m) dipole transitions of the involved fields with frequencies 2ω, ω, and ω. It has to be noted that the electric second-order susceptibility χ^{eee} is a real quantity. The second-order chiral (or magnetic) susceptibilities χ^{eem} and χ^{mee} are imaginary and only occur in chiral media. Electric-quadrupolar effects are left out here, as they are much weaker than electric- and magnetic-dipole effects. The following discussion will be restricted to electric-dipole effects, like in common models for BINOL, for instance. Further, the film is assumed to consist of a monolayer of molecules in an orientation of their molecular axes parallel to the surface normal. The electric field vector $\vec{E} = \vec{E}_p + \vec{E}_s$ is split into a component E_p parallel to the plane of incidence, and a component E_s perpendicular to this plane. Hence, for isotropic surfaces there exist four non-vanishing tensor components of $\chi^{(2)}$. These include three achiral elements $a_1 = \chi^{(2)}_{ZZZ}$, $a_2 = \chi^{(2)}_{ZXX} = \chi^{(2)}_{ZYY}$, $a_3 = \chi^{(2)}_{XXZ} = \chi^{(2)}_{XZX} = \chi^{(2)}_{YYZ} = \chi^{(2)}_{YZY}$, and one chiral element $a_4 = \chi^{(2)}_{XYZ} = \chi^{(2)}_{XZY} = -\chi^{(2)}_{YXZ} = -\chi^{(2)}_{YZX}$. In analogy to SFG in isotropic chiral media, the chiral $\chi^{(2)}$-element a_4 changes sign for the enantiomers. Thus, $a_4 = 0$ for racemic mixtures as well as for achiral media [57]. Combining linear combinations of the non-vanishing $\chi^{(2)}$-elements in the nonlinear expansion coefficients f, g, and h, the SHG-field components can be written as [42, 79, 78, 41, 40]

$$E_i(2\omega) = f_i E_p^2(\omega) + g_i E_s^2(\omega) + h_i E_p(\omega) E_s(\omega), \quad (i = s, p).$$

(2.71)

The according parallel (p) and perpendicular (s) expansion coefficients for the transmitted SHG-signal are [77]

$$f_s = 2a_4 \sin\theta \cos\theta$$
$$g_s = 0$$
$$h_s = 2a_3 \sin\theta$$
$$f_p = (a_1 \sin^2\theta + a_2 \cos^2\theta + 2a_3 \cos^2\theta)\sin\theta$$
$$g_p = a_2 \sin\theta$$
$$h_p = -2a_4 \sin\theta \cos\theta.$$

(2.72)

The expansion coefficients including the terms for magnetic-dipole transitions for SHG-fields in reflection and transmission can be found elsewhere [78, 41, 40, 77]. From equations 2.72 follows that a SHG-signal can only occur, if the angle between the incoming laser beam and the molecular axis of the molecules or the symmetry axis of a macromolecular arrangement or crystal, respectively, is greater than zero (see figure 3b). Moreover, as the chiral element a_4 changes sign for different enantiomers, whereas the achiral components do not change, the

SHG-CD changes sign for different enantiomers. However, for a change of the orientation of the arrangement, i.e. an exchange or reversal of the surfaces, the chiral element will be the same, but the achiral elements change sign (cf. equation 2.67), and thus, the SHG-CD changes sign.
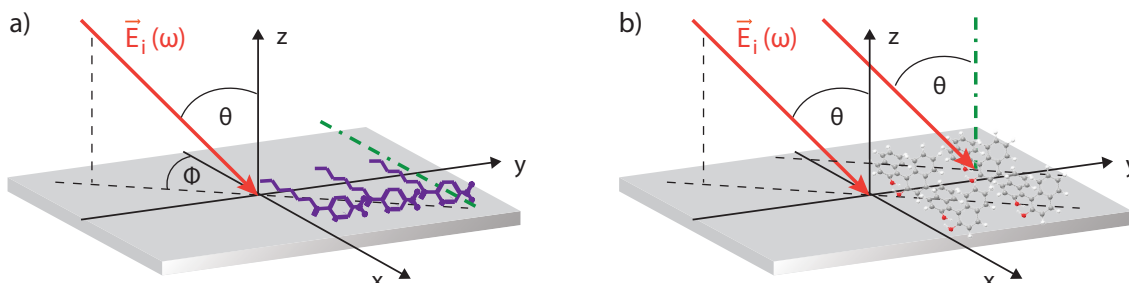
Figure 3 SHG at an interface of an achiral substrate, and an oriented a) achiral and b) chiral molecular film. The incoming fundamental laser beam (with electric field $\vec{E}_i(\omega)$) is tilted by an angle θ with respect to the surface normal (z-axis). a) Achiral molecules are oriented with their molecular axis (dot-dashed green line) along the x-axis. Thus, $\vec{E}_i(\omega)$ exhibits an azimuthal angle Φ with respect to the molecular axis, giving rise to an in-plane anisotropy and the generation of a second-harmonic signal. b) Chiral molecules are aligned with their molecular axis (dot-dashed green line) parallel to the surface normal, i.e. at an angle θ with respect to the incoming laser beam. In this case, SHG is possible even for in-plane isotropy [72].)

Assuming an incoming circularly polarised beam, the phase difference between E_s and E_p is equal to $\pm\frac{\pi}{2}$, and $E_p(\omega) = \pm iE_s(\omega)$ with $+$ for RCP-light and $-$ for LCP-light. Thus, the SHG-intensity can be expressed as

$$I_i(2\omega) = |-f_i + g_i \pm ih_i|^2 |E_s(\omega)|^4 . \tag{2.73}$$

Hence, the SHG-intensity depends strongly on the pump intensity. Moreover, the occurrence of SHG-CD requires a non-vanishing coefficient h. This is given at surfaces of chiral molecules, and at achiral surfaces which exhibit an anisotropy axis at an angle $\Phi > 0$ with respect to the plane of incidence (see figure 3a) [72]. As a further requirement, there has to exist a phase difference between $g - f$ and h. Close to resonances, this phase difference occurs within the electric-dipole approximation. However for nonresonant excitation, magnetic dipole effects have to be considered [41]. The second-harmonic can also be generated at the interface of achiral molecules and a chiral surface [42]. Furthermore, achiral molecules which assemble in macroscopic chiral structures on surfaces exhibit nonzero chiral $\chi^{(2)}$-elements, and thus a non-vanishing coefficient h leading to significant SHG-CD [70, 73, 40]. Structural chirality, i.e. macromolecular chiroptical activity, of chiral or achiral molecules plays an important, if not dominant role in the contribution to the effects of second-harmonic optical activity [72, 68, 69, 70, 57].

2.3. Interaction of light with molecules

2.3.1. Molecular electronic states within the Born-Oppenheimer approximation

The quantum-mechanical description of a molecule of energy E is given by the Schrödinger equation

$$\hat{H}\Psi = E\Psi. \tag{2.74}$$

Here, the Hamilton operator $\hat{H} = \hat{T} + \hat{V}$ consists of the sum of the kinetic energy $\hat{T}$ and the potential energy $\hat{V} = V(\vec{r}, \vec{R})$ of all N_e electrons and K nuclei with their respective coordinates $\vec{r}$ and $\vec{R}$, and masses m and M [80]. Hence, equation 2.74 can be written as

$$\left(-\frac{\hbar^2}{2m} \sum_{i=1}^{N_e} \nabla_i^2 - \frac{\hbar^2}{2} \sum_{k=1}^{K} \frac{1}{M_k} \nabla_k^2 + V(\vec{r}, \vec{R}) \right) \Psi(\vec{r}, \vec{R}) = E\Psi((\vec{r}, \vec{R}). \tag{2.75}$$

The potential energy includes the Coulomb repulsion of the nuclei and of the electrons, respectively, and the nucleus-electron attractions. Further corrections due to spin interactions of electrons and nuclei can be determined using a relativistic ansatz, or approximated using perturbation theory.

Because of the large energy (and mass) differences of electrons and nuclei, the electron wavefunction depends only weakly on $\vec{R}$ for small deviations from the equilibrium position $\vec{R}_0$ [81]. Hence, one of the basic principles in molecular physics is the separation of the Schrödinger equation into an electronic and a nuclear part. In the adiabatic approximation, the total wavefunction $\Psi(\vec{r}, \vec{R})$ can be written as the sum of products of nuclear and electronic wavefunctions $\chi(\vec{R})$ and $\phi(\vec{r})$, respectively [80],

$$\Psi(\vec{r}, \vec{R}) = \sum_m \chi_m(\vec{R})\phi_m(\vec{r}, \vec{R}). \tag{2.76}$$

Using a perturbation ansatz, $\hat{H} = \hat{H}_0 + \hat{H}'$, with the unperturbed Hamilton operator $\hat{H}_0 = \hat{T}_{el} + \hat{V}$ describing the electron potential for distinct nuclear positions $\vec{R}$, the kinetic energy of the nuclei represents a small perturbation $\hat{H}' = \hat{T}_{nu}$. This ansatz results in two coupled equations

$$\hat{H}_0\phi(\vec{r}, \vec{R}) = E^0(\vec{R})\phi(r, R) \ \ (I),$$
$$\hat{H}'\chi_n(\vec{R}) + \sum_m c_{nm}\chi_m(\vec{R}) = (E - E_n^0(\vec{R}))\chi_n(R) \ \ (II). \tag{2.77}$$

The coefficients c_{nm} represent the coupling of electronic states n and m. In the adiabatic approximation, only the diagonal elements c_{nn} are considered. Treating $\vec{R}$ as constant during the motion of electrons, thus assuming no coupling between nuclear and electronic motion, all coefficients c_{nm} are set to zero. This is valid as long as the energy difference of unperturbed

electronic states, $E_n^0(\vec{R}) - E_m^0(\vec{R})$, is large with respect to the perturbation by the nuclear motions [80]. Equations 2.77 become then

$$\hat{H}_0 \phi_n^{el}(\vec{r}) = E_n^0 \phi^{el}\vec{r}) \;\; (I),$$
$$(\hat{T}_{nu} + E_n^0)\chi_n(\vec{R}) = E_{n,i}\chi_{n,i}(R) \;\; (II).$$

(2.78)

Thus, the energy of the $n-$th electronic state is represented by an energy surface as function of nuclear coordinates $\vec{R}$ for a nuclear state i. This is known as the Born-Oppenheimer approximation [80].

In general, the total energy of a molecule in state n is given by the sum of the electronic, vibrational and rotational energy, i.e. for each electronic state (typically in the deep ultraviolet (UV) to UV spectral range) there exist several vibrational states (near infrared (NIR) and IR spectral range), and for each vibrational state many rotational (IR to far IR) sub-levels. In large molecules, these different vibrational (and rotational levels) are very close in energy, such as they cannot be resolved with conventional spectroscopy. Thus, they do not exhibit line spectra like atoms or small molecules, but rather broad bands. Furthermore, a complete characterisation of the state of a molecule comprises the coupling of the electrons. Most important is the coupling of the orbital angular momenta of the electrons to the nuclear field along the molecular axis, and the projection of the total electronic spin Σ to this axis. Hence, the complete electronic angular momentum of a molecule is expressed by $\Omega = \Gamma + \Sigma$, with Γ denoting the projection of the complete electronic orbital angular momentum to the molecular axis. Moreover, the complete wavefunction,

$$\Psi = \chi(\vec{R})\phi(\vec{r}, \vec{R})\zeta,$$

(2.79)

also includes a spin function ζ and has to be antisymmetric according to the Pauli principle [82]. Most molecules exhibit only paired electron spins in their ground state configuration, thus have singlet multiplicity.

Molecular orbitals can be calculated according to different approximations, as for instance, the MO- (molecular orbital theory), the LCAO-(linear combination of atomic orbitals) method, density functional theory (DFT), or for more accurate calculations of many-electron systems, the Hartree-Fock method [82]. The most important molecular orbitals for most photophysical and photochemical processes are the highest-energy occupied molecular orbital (HOMO) and the lowest-energy unoccupied molecular orbital (LUMO). In aromatic molecules, such as those discussed in this work, conjugated π-systems formed by the overlap of the p_z-orbitals of the sp^2-hybridised carbon atoms constitute the nature of HOMO (bonding π-orbitals) and LUMO (antibonding π-orbitals).

2.3.2. Electronic transitions

For an adequate description of the absorption or emission of light, one can make use of time-dependent perturbation theory. Hence, the Schrödinger equation can be written as [83]

$$i\hbar\dot{\Psi} = (\hat{H}_0 + \hat{H}^S)\Psi,$$ (2.80)

with the time-independent Hamilton operator $\hat{H}_0$ and the perturbation operator $\hat{H}^S$. The solution $\psi_\nu^0(t) = exp(-\frac{i}{\hbar}E_\nu t)\varphi_\nu$ of the unperturbed Schrödinger equation includes the time-independent wave equations φ_ν and their respective eigenenergies E_ν. Hence, the solution for equation 2.80 is represented as the sum of the unperturbed wave equations $\psi_\nu^0(t)$:

$$\Psi(t) = \sum_{\nu=1}^{\infty} a_\nu(t)\psi_\nu^0.$$ (2.81)

Here, the coefficients $a_\nu(t)$ are time-dependent. Their square $|a_\nu(t)|^2$ denotes the probability of the molecule to be in state ν due to the perturbation. The probability of a transition from state κ to state μ is equal to $w_{\mu\kappa} = \frac{d|a_\mu(t)|^2}{dt}$. If the final states μ are part of a continuous energy spectrum Ω, the transition probability W is given by $W = \sum_{\mu\in\Omega} w_{\mu\kappa}$, and can be written as [83]

$$W = \frac{2\pi}{\hbar} \sum_{\mu\in\Omega} \delta(E_\mu - E_\kappa) \left|\left\langle \varphi_\mu^* |\hat{H}^S|\varphi_\kappa \right\rangle\right|^2,$$ (2.82)

with $\left\langle \varphi_\mu^* |\hat{H}^S|\varphi_\kappa \right\rangle = \int \varphi_\mu^* \hat{H}^S \varphi_\kappa dV$. Hence, the energy of the absorbed or emitted photon, $E_{ph} = \hbar\omega_{\mu\kappa} = \frac{h}{\lambda_{\mu\kappa}}$, has to match the energy difference $\delta(E_\mu - E_\kappa)$ for reasons of energy conservation. Equation 2.82 is also known as Fermi's golden rule [84]. If the wavelength $\lambda_{\mu\kappa}$ is large with respect to the diameter of the molecule, the transition probability from an initial state i to a final state f can be expressed within the dipole approximation by

$$W_{fi} = \frac{2\pi}{\hbar}|\theta_{fi}|^2\delta(E_f - E_i).$$ (2.83)

This notation makes use of the transition moment

$$\theta_{fi} = \left|\left\langle \varphi_f^*|\hat{\mu}|\varphi_i \right\rangle\right|^2,$$ (2.84)

with the dipole-moment operator $\hat{\mu} = e\sum_j \vec{r}_j$. The vector $\vec{r}_j$ denotes the position of the j-th electron with charge e with respect to the charge centre of the molecule [83] . Moreover, the classical description for transition probabilities by the Einstein-coefficients for absorption B_{12}, spontaneous emission A_{12}, and stimulated emission B_{21}, can be related to the transition moment [83], however will not be discussed further here. A further quantity for the description of optical transitions is given by the oscillator strength f

$$f = \frac{8\pi^2 m_e}{3he^2}\nu|\theta_{fi}|^2.$$ (2.85)

The oscillator strength can also be determined from the absorption spectrum by calculating the frequency integral of the (decadic) molar absorption coefficient in dependency of the frequency ν (here with unit cm^{-1} and $\Delta\bar{\nu}_{1/2}$ as full-width half maximum [85, 86, 87]):

$$f = \frac{4.39}{n} \cdot 10^{-9} \int \varepsilon(\nu)d\nu \approx \frac{4.39}{n} \cdot 10^{-9} \varepsilon_{max}\Delta\bar{\nu}_{1/2}, \tag{2.86}$$

From equations 2.83, and 2.85 follows that the probability as well as the strength of the transition depend on the transition moments. Within the Born-Oppenheimer approximation, the wavefunction can be separated into an electronic $\phi(\vec{r}, \vec{R})$, a nuclear $\chi(\vec{R})$ and a spin function ζ (see equations 2.76 and 2.79). Thus, the transition moment can be written as [86, 83]

$$\theta_{fi} \propto \left|\left\langle \phi_f^*(\vec{r}, \vec{R})|\hat{\mu}|\phi_i(\vec{r}, \vec{R})\right\rangle\right|^2 |\langle\zeta_f^*|\zeta_i\rangle|^2 \left|\left\langle \chi_f^*(\vec{R})|\chi_i(\vec{R})\right\rangle\right|^2. \tag{2.87}$$

The electronic term depends on the symmetry of the initial and final state. Group theory allows to deduce predictions about allowed and forbidden transitions. The $\pi \to \pi^*$ transition is symmetry-allowed, for instance. The transition from a non-bonding orbital n to an excited π^*-orbital is symmetry-forbidden, thus, resulting in a low oscillator strength. Furthermore, the spin-wavefunctions for singlet and triplet states are orthogonal. Therefore, the factor $\left\langle\zeta_f^*|\zeta_i\right\rangle$ becomes zero for transitions comprising a change in multiplicity, which leads to the spin selection rule $\Delta S = 0$ [86, 83].

Franck [88] and Condon [89] showed that an electronic transition occurs independently of the phase of the vibrational motion of the nuclei. The most probable final state, which is referred to as the Franck-Condon state, exhibits the same nuclear position $\vec{R}$ as the initial state. This is expressed by the vertical arrows representing the electronic excitation in figure 4. The vibrational term, $\left|\left\langle\chi_f^*|\chi_i\right\rangle\right|^2$, represents the Franck-Condon factor. As the integral over all vibrational states is always equal to one for each initial vibrational state, the transition moment, and thus, the oscillator strength is independent of this term [82]. However, the Franck-Condon factor determines the intensity distribution of the excited vibrational modes in the final state, hence the shape of the absorption spectrum (and emission spectrum). Because the excited electronic state usually has a different equilibrium position, the transition is accompanied with vibrational excitation. Immediately after excitation, the electron starts to thermalise to the lowest vibrational level at the new nuclear equilibrium position. Therefore, emission spectra are usually red-shifted by the so-called Stokes-shift with respect to their corresponding absorption spectra (see figure 4).

2.3.3. Primary photophysical and photochemical processes

The intensity decrease caused by absorption of a monochromatic light wave with initial intensity I_0 travelling a distance of x (in cm) through a solution of organic molecules with an amount
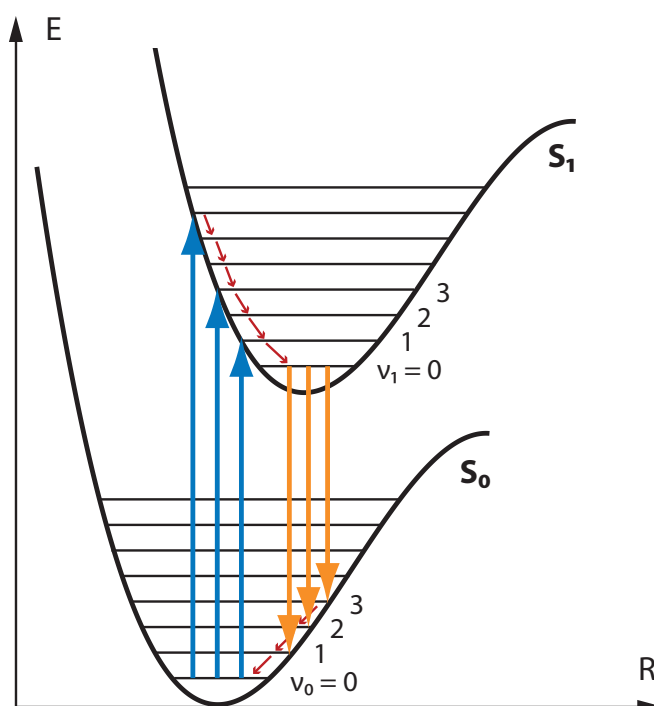
Figure 4 Schematic illustration of the Franck-Condon principle. The potential energy of electronic ground state S_0 and first excited singlet state S_1 is depicted as a function of the nuclear coordinate R. The horizontal lines indicate the according vibrational levels $\nu_i = 0, 1, 2...; \; i = 0, 1$. Vertical blue arrows represent the excitation from the relaxed ground state to higher vibrational levels of S_1 upon absorption of photons. Small red arrows denote the vibrational relaxation to the lowest vibrational level $\nu_1 = 0$ of S_1. The subsequent deactivation by fluorescence is depicted as vertical orange arrows, followed by vibrational relaxation to the ν_0-level of S_0.

concentration of C (with unit mol L^{-1}) is given by the Lambert-Beer law (see equation 2.13)

$$I = I(0) \cdot 10^{-\varepsilon C x}. \tag{2.88}$$

The quantity ε denotes the molar absorption coefficient (in decadic definition [46]). Accordingly, the absorbance A or optical density OD is defined as

$$A = \mathrm{OD} = log\left(\frac{I(0)}{I(x)}\right) = \varepsilon C x. \tag{2.89}$$

The absorption of a photon excites the molecule from state A to a Franck-Condon state of the excited state A$^*_{\mathrm{FC}}$. The following deactivation can occur by radiative, or nonradiative relaxation or by a photoreaction. Figure 5 depicts the primary photophysical and photochemical processes in a molecule. The competing deactivation processes over different channels are described according to the corresponding rate constants k_j. Thus, the lifetime of the excited state (A*) is given by

$$\tau(A^*) = \frac{1}{\sum_j k_j}. \tag{2.90}$$
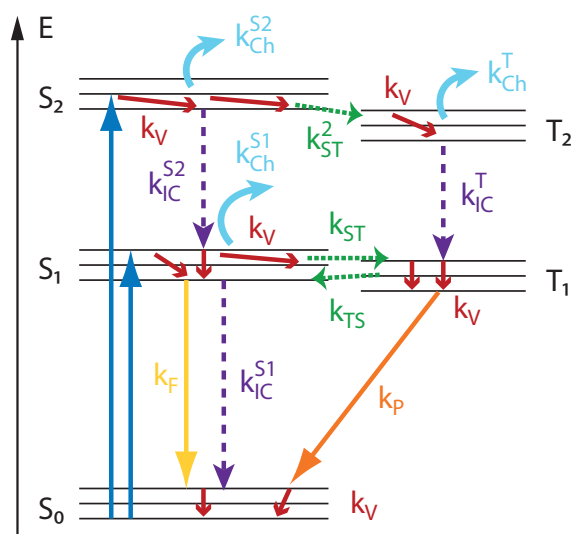
Figure 5 State energy diagram of an organic molecule including primary photophysical and photochemical processes. Vertical blue arrows indicate absorption from the ground state (S_0) to the first (S_1) or second (S_2) excited singlet states. The first and second triplet states are represented by T_1 and T_2, respectively. The different deactivation processes are depicted as arrows together with their respective decay rates: vibrational relaxation (k_V, red, solid arrow), fluorescence (k_F, yellow, solid), internal conversion (k_{IC}, violet, dashed), intersystem crossing (k_{ST}, k_{TS}, green, dotted), phosphorescence (k_P, orange, solid), and photochemical singlet and triplet reactions (k_{Ch}^S, k_{Ch}^T, light blue, curved arrows).

Accordingly, the quantum yield of a process i deactivating the excited state A^*, when directly excited by absorption, is defined as

$$\Phi_i = \frac{k_i}{\sum_j k_j}. \tag{2.91}$$

In solution, the fastest, and thus, most probable, deactivation process is vibrational relaxation (or thermalisation) from the hot Franck-Condon state to the lowest vibrational level of the excited state by collisions with surrounding molecules. This occurs, depending on the molecule and the solvent, typically in a few picoseconds.

For a strongly allowed transition from the singlet ground state to the first excited singlet state $S_0 \rightarrow S_1$ by absorption of a photon, the most probable deactivation from the lowest vibrational level of the (relaxed) excited state to the ground state $S_1 \rightarrow S_0$ will be by fluorescence. Although the emission of photons starts immediately after excitation, this early fluorescence is competing with the faster thermalisation. The radiative decay rate, i.e. the decay rate by fluorescence in absence of any other relaxation processes, is defined as [90, 91, 85]

$$k_r \cong 2.88 \cdot 10^9 n^2 \frac{\int F(\nu) d\nu}{\int \frac{F(\nu)}{\nu^3} d\nu} \int \frac{\varepsilon(\nu)}{\nu} d\nu. \tag{2.92}$$

Here, $F(\nu)$ is the fluorescence spectrum in dependence of frequency ν, which is given in wavenumbers (cm^{-1}). Ranging in the nanosecond region, the radiative (or natural) lifetime,

$\tau_r = 1/k_r$, gives a theoretical upper limit for the expected lifetime of the first excited singlet state S_1. Accordingly, the fluorescence quantum yield is related to the S_1-lifetime by [85]

$$\Phi_{\mathrm{F}} = k_r \cdot \tau_{S_1} = \frac{\tau_{S_1}}{\tau_r}. \tag{2.93}$$

Photoluminescence from the lowest triplet state to the singlet ground state is referred to as phosphorescence. As this process is spin-forbidden, the respective rate k_{P} is very low resulting in long triplet lifetimes up to seconds. The same accounts for the spin-forbidden process of intersystem crossing (ISC) between singlet and triplet states with rate k_{ISC}. However, if atoms with large atomic weight, such as halogens, are involved in the transition, both rates, k_{P} and k_{ISC}, can be strongly enhanced. The same accounts for the triplet (quantum) yield Φ_{T}, i.e. the quantum yield for triplet formation.

Internal conversion (IC) denotes radiationless relaxation between different electronic states of the same multiplicity. Hence, this process is symmetry-forbidden, and significantly fast rates (k_{IC}) for $S_1 \rightarrow S_0$-transitions are only possible for constellations of overlapping energy levels which allow an isoenergetic transition (see figure 6 a) [86]. However, because of the larger overlap between the electronic potentials of higher excited states, internal conversion from a higher excited singlet or triplet state to S_1 or T_1, respectively, is much more probable, and thus, even faster than the emission of a photon (<1 ps). Therefore, with few exceptions, fluorescence usually occurs from the S_1-state (Kasha's rule [92]).

As indicated in figure 5, an excited singlet or triplet state can also be the origin of a photoreaction [93, 87, 94]. In this case, the molecule does not relax to its original ground state nuclear geometry.

2.3.4. Influence of the solvent

Absorption and emission spectra in solution depend on the interaction of solvent and solute. The process of solvation involves the rearrangement of solvent molecules around the solute, i.e. the formation of a solvation shell, and is typically completed prior to fluorescence, depending on temperature and solvent viscosity. The most important solvatochromatic parameters are polarity and hydrogen-bonding ability, resulting in the observation of effects on the solute, such as spectral shifts, different intensities and variations in lifetime and quantum yields. Very strong solvatochromatic effects can be observed in molecules which exhibit large changes in their dipole moments of ground and excited state due to intramolecular charge transfer or twisted intramolecular charge transfer (TICT) involving the rotation of a group on the molecule. For a charge transfer to occur during excitation, it is necessary that the molecule has electron donating and electron accepting groups, which enhance the π-conjugation. Polar solvents tend to stabilize such charge transfer excited states, whereas local excited states are favoured in apolar solvents. Furthermore, depending on the choice of the solvent, different states are contributing with

various oscillator strengths to a HOMO→LUMO-transition. Particularly, $n \rightarrow \pi^*$-transitions are solvent sensitive. Hence, their energies can be solvatochromically shifted with respect to $\pi \rightarrow \pi^*$-states in a way that the nature of the lowest energy transitions can vary between $n \rightarrow \pi^*$- and $\pi \rightarrow \pi^*$-transitions. Moreover, solvent viscosity influences rotational diffusion and the formation of TICT states [95, 85, 86].

2.3.5. Non-adiabatic effects

If the coupling of electronic and nuclear motion cannot be neglected anymore, i.e. the coefficients c_{mn} in equation 2.77 cannot be set to zero anymore, different electronic states, or electronic and vibrational states are mixed, and the Born-Oppenheimer approximation breaks down. This coupling of wavefunctions has to obey selection rules, such as the conservation of their total angular momentum and their parity. Internal conversion is such an example. According to the Born-Oppenheimer approximation, the transition moment between different electronic states of the same multiplicity becomes zero. Hence, IC can only be described for the vibronic coupling between electron and nuclear wavefunctions of the same symmetry (see figure 6 a).
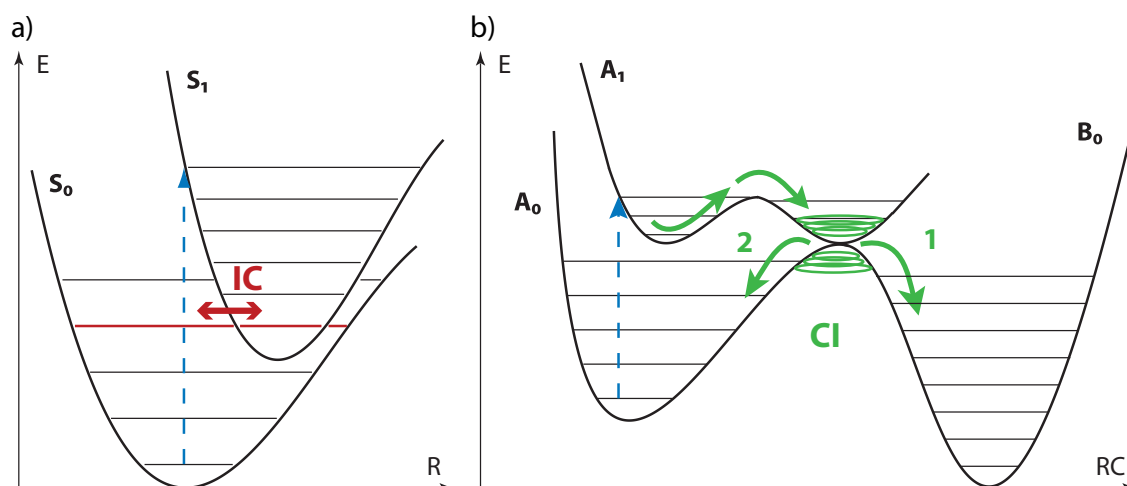
Figure 6 Examples of nonadiabatic processes. a) Internal conversion (IC) between isoenergetic energy levels of the states S_1 and S_0, mediated by vibronic coupling (red double arrow). b) Conical intersection (CI, green double cone) between the PES of the excited state A_1 and the ground state of the photoproduct B_0 of a photochemical reaction with reaction coordinate RC. Deactivation through the CI (green arrows) can either lead along pathway 1 to B_0, or along pathway 2 back to the original ground state A_0. Dashed blue arrows indicate the preceding excitation of the molecule by absorption of a photon, followed by vibrational relaxation (not shown here).

Another case are crossings of the potential energy surfaces. In the limit of the energy difference of two electronic potential energy surfaces (PES) approaching zero, their wavefunctions are degenerate, and the "crossing point" can become a conical intersection, which allows the transition or "jump" between the two states. This process is usually described in terms of PES plotted over the reaction coordinate. Figure 6b depicts an example for a conical intersection (CI). The pathway through the conical intersection can either lead to the ground

state (photophysical process) or to a photoproduct (photochemical reaction). The initial state of a primary photoreaction can be either an excited singlet state or a triplet state. Hence, the final state will be an excited singlet, a ground state singlet, or a triplet state of the photoproduct, respectively. Whenever two PES come close to each other, they can also form an avoided crossing (or anticrossing). However, this usually occurs only in highly symmetric molecules, like axially symmetric diatomic molecules, for instance [87]. In general, radiationless transitions between PES at a critical point $(\vec{R}_c)$ become probable in the limit of vanishing energy (E) difference and large differences in their slopes $\frac{dE}{d\vec{R}}(\vec{R} \to \vec{R}_c)$.

The same accounts for intersystem crossings (ISC), i.e. radiationless transitions between states of different multiplicity. In this case the spin-orbit operator $\hat{H}_{\mathrm{SO}}$ constitutes the perturbation operator $\hat{H}'$ in equations 2.77. Commonly, $\hat{H}_{\mathrm{SO}}$ for molecules is written in the form [96, 97]

$$\hat{H}_{\mathrm{SO}} = \frac{e^2}{2m^2c^2} \sum_{\mu} \sum_{i} \frac{Z_{\mu}^{\mathrm{eff}}}{r_{i\mu}^3} (\vec{l}_i \vec{s}_i), \tag{2.94}$$

with summation over all electrons i and nuclei μ and the assumption of an effective atomic number Z_{μ}^{eff} in order to account for the screening of the nucleus by the inner-shell electrons. The quantities $\vec{l}_i$ and $\vec{s}_i$ denote orbital and spin angular momenta, respectively. Thus, the mixing of states with different multiplicity increases with atomic number Z. In the absence of heavy atoms, i.e. atoms with large atomic weight Z, the ISC-rates are usually very low. However, if $n \to \pi^*$-transitions exist, spin-orbit coupling may be enhanced according to the El-Sayed rules [98, 86]. Hence, symmetry-allowed ISC are $(n \to \pi^*)_1 \leftrightarrow (\pi \to \pi^*)_3$ and $(n \to \pi^*)_3 \leftrightarrow (\pi \to \pi^*)_1$, whereas the subscripts 1 and 3 refer to singlet and triplet multiplicity, respectively. On the other hand, ISC between transitions of the same symmetry, $(\pi \to \pi^*)_1 \leftrightarrow (\pi \to \pi^*)_3$ and $(n \to \pi^*)_1 \leftrightarrow (n \to \pi^*)_3$, are forbidden. However, when the molecule exhibits heavy atoms, the spin-orbit operator is dominated by their contribution resulting in high ISC-rates and large phosphorescence quantum yields Φ_{P} and triplet yields Φ_{T}, accompanied by reduced fluorescence lifetimes and quantum yields Φ_{F} [99, 100, 97]. The heavy atom can be part of the molecule, then the effect is referred to as intramolecular or internal heavy-atom effect (HAE) [100, 101], or part of the solvent in case of external HAE [102, 103, 104]. In case of intramolecular HAE, based on the analysis of M. EL-Sayed and A. Albrecht [105, 96], three additional contributions except of first-order (of perturbation theory) spin-orbit coupling could be extracted to be relevant for the HAE: first-order spin-orbit-vibronic coupling, i.e. the interaction of $\hat{H}_{\mathrm{SO}}$ with vibrational states, and second-order singlet and triplet vibronic coupling, mixing with spin-orbit-coupling. Hence, either case describes a mixing of singlet and triplet states, enhancing the ISC-rate. Further, singlet $\sigma \to \pi^*$- and $\pi \to \sigma^*$-states are involved [97]. However, the particular contributions of the different mixing states depend on symmetry properties, and also on the position of the halogen in the molecule [106, 107]. Therefore a proper choice of type and position of heavy-atom substituents allows to make use of the HAE for specific applications in molecular photonics [108, 109, 97]. Moreover, the HAE influences not only photophysical

quantities like Φ_T, but also enhances photochemical reactions, when the reaction involves triplet states [110, 111, 112].

2.4. Femtosecond laser pulses

2.4.1. Pulse propagation

The experiments in the scope of this thesis were performed using femtosecond laser pules. Assuming propagation along the z-direction, the electric field of these pulses in the time-domain can be written as

$$\vec{E}_{\mathrm{L}}(z,t) = \frac{1}{2}\vec{e} \cdot E_{\mathrm{L}}(z,t) \cdot e^{i\Phi^{\mathrm{L}}(z,t)} + c.c., \tag{2.95}$$

with the polarisation vector $\vec{e}$, the field envelope $E_{\mathrm{L}}(z,t)$, and the phase $\Phi^{\mathrm{L}}(z,t)$. The field envelope can often be approximated as a Gaussian function,

$$E_{\mathrm{L}}(z,t) = E_{0,\mathrm{L}}(z) \cdot e^{-\frac{4\ln 2}{\Delta\tau^2}t^2}. \tag{2.96}$$

Herein, the full width at half maximum (FWHM) of the pulse duration is denoted as $\Delta\tau$. The amplitude $E_{0,\mathrm{L}}$ is further assumed to exhibit a spatial envelope of a Gaussian intensity profile. Within the slowly varying amplitude approximation in space and time, i.e. $E_{\mathrm{L}}(z,t) \approx \tilde{a}(z,t)$, and $\left|\frac{\partial^2 \tilde{a}(z)}{\partial z^2}\right| << \left|k\frac{\partial \tilde{a}(z)}{\partial z}\right|$ (see equation 2.26), and $\left|\frac{\partial^2 \tilde{a}(t)}{\partial t^2}\right| << \left|\omega\frac{\partial \tilde{a}(t)}{\partial t}\right|$, the propagation of a laser pulse in dispersive nonlinear media is described by the nonlinear Schrödinger equation,

$$\frac{\partial a(z,\tau)}{\partial z} = -i\frac{k_2}{2}\frac{\partial^2 a}{\partial t^2} + i\delta|a|^2 a. \tag{2.97}$$

Here, we use a coordinate transformation $a(z,\tau) = \tilde{a}(z,t)$ by substituting $\tau = 1 - \frac{z}{v_g}$. The quantity $v_g = \left(\frac{\partial \omega}{\partial k}\right)_{\omega_{\mathrm{L}}}$ denotes the group velocity, which is the velocity of the wavepacket, i.e. the pulse envelope with central angular frequency ω_{L}. Moreover, group velocity dispersion (GVD) is defined as

$$\mathrm{GVD} = k_2 = \left(\frac{\partial^2 k}{\partial \omega^2}\right)_{\omega_{\mathrm{L}}} = \frac{\partial}{\partial \omega}\left(\frac{1}{v_g}\right)_{\omega_{\mathrm{L}}}. \tag{2.98}$$

The nonlinearity of the propagation is represented by the parameter $\delta = 2n_0\epsilon_0 n_2\omega_0$ (with the linear and nonlinear refractive indices n_0 and n_2, see equation 2.42) [25].

Furthermore, we reconsider pulse propagation in a linear dispersive medium, i.e. $\delta = 0, k_2 \neq 0$, as described by equation 2.95. The phase is represented by

$$\Phi^{\mathrm{L}}(z,t) = -\omega_{\mathrm{L}}t - \beta_{\mathrm{L}}t^2 + \Phi^{\mathrm{L}}_{\mathrm{CE}}, \tag{2.99}$$

whereas the quantity $\Phi^{\mathrm{L}}_{\mathrm{CE}}$ denotes the carrier-envelope-phase (CEP), i.e. the phase delay of the field maximum of $\vec{E}_{\mathrm{L}}(z,t)$ with respect to the maximum of the envelope $E_{\mathrm{L}}(z,t)$. The quantity

β_{L} represents the chirp of the laser field, which is caused by GVD in the medium. For a linear positive chirp, $\beta_{\mathrm{L}} > 0$, the instantaneous carrier frequency ω_i of the pulse,

$$\omega_i = \omega_{\mathrm{L}} - \frac{d}{\omega_{\mathrm{L}}} dt(-\beta_{\mathrm{L}} t^2) = \omega_{\mathrm{L}} + 2\beta_{\mathrm{L}} t, \tag{2.100}$$

increases linearly with time. A Fourier transformation of equation 2.95 leads to the equivalent description of pulse propagation in the frequency domain:

$$\vec{E}_{\mathrm{L}}(z, \omega) = \int_{-\infty}^{\infty} dt \int_{-\infty}^{\infty} dz E_{\mathrm{L}}(z, t) \cdot e^{-i(\omega t - kz)} = \frac{1}{2}\tilde{E}_{\mathrm{L}}(z, \omega) \cdot e^{i\varphi^{\mathrm{L}}(\omega)}, \tag{2.101}$$

with the spectral phase $\varphi^{\mathrm{L}}(\omega)$, and neglecting the polarisation. In analogy to the intensity $I(t) = |E_{\mathrm{L}}(t)|^2$, the spectrum of the pulse is expressed by $S(\omega) = |\tilde{E}_{\mathrm{L}}\omega)|^2$. Further, the FWHM spectral bandwidth of the pulse is denoted in terms of the FWHM pulse duration $\Delta\omega = \frac{4\ln 2}{\Delta\tau}$. Hence, the time-bandwidth-product of a Gaussian pulse cannot be smaller than

$$\Delta\tau \cdot \Delta\nu = \Delta\tau \frac{\Delta\omega}{2\pi} \approx 0.441. \tag{2.102}$$

A pulse satisfying this relation is referred to as Fourier-limited or time-bandwidth-limited.

2.4.2. Polarisation

The polarisation of the laser pulses, which propagate along z-direction, is described by means of the polarisation vector $\vec{e}$ in the x-y-plane, which is normalised to unity. A general description is given by the Jones formalism. Here, $\vec{e}$ is equal to the Jones vector. Assuming linear polarisation along the x- or y-direction, $\vec{e}$ can be written as $\vec{e}_x = (1, 0)^T$ or $\vec{e}_y = i(0, 1)^T$, respectively. Circularly polarised light exhibits a phase difference of $\pm\pi/2$ between $\vec{e}_x$ and $\vec{e}_y$ and is expressed in its two basis vectors $\sigma^+ = -\frac{1}{\sqrt{2}}(1, i)^T$ and $\sigma^- = \frac{1}{\sqrt{2}}(1, -i)^T$. Circularly polarised light can be generated from linearly polarised light by a quarter-wave plate. Assuming a light wave, which is linearly polarised along the y-axis, travelling through a quarter-wave plate with its fast axis aligned at an angle of $+45°$ with respect to the x-axis, the Jones formalism can be written as

$$\vec{e}_f = \frac{1}{\sqrt{2}} \begin{pmatrix} -1 & i \\ i & -1 \end{pmatrix} \begin{pmatrix} 0 \\ i \end{pmatrix} = \frac{1}{\sqrt{2}} \begin{pmatrix} -1 \\ -i \end{pmatrix} = \sigma^+. \tag{2.103}$$

The most general case of elliptical polarisation is written as

$$\vec{e}_{el}(z, t) = e^{-i\delta}(\cos\epsilon\, \vec{\sigma}_+ - \sin\epsilon\, \vec{\sigma}_-). \tag{2.104}$$

Here, the quantity ϵ denotes the ellipticity angle, and δ the alignment angle with respect to $\vec{e}_x$ [82]. The ellipticity is defined as

$$\tan\epsilon = \frac{b}{a}, \tag{2.105}$$

with the long (a) and short (b) axes of the ellipse (see figure 7).
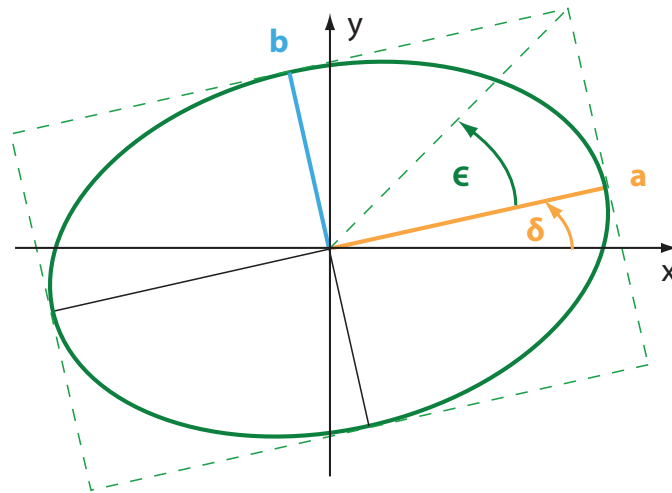
Figure 7 Elliptical polarisation. Definition of ellipticity ϵ and azimuthal rotation angle δ with respect to the x-axis.

Handedness of polarisation

For the definition of left (LCP) (or anti-clockwise) and right (RCP) (or clockwise) circularly polarised light exist two different conventions. In optics, particularly in older textbooks, and in chemistry, the handedness is defined from the view of the receiver. Accordingly, the electric field vector describes a clockwise or right-handed circle when looking against the direction of propagation. The second convention follows the definition of helicity. Thus, for a right-handed light wave, the electric field vector of the light wave travels clockwise (right-handed) from the point of view of the source (confer to right-hand rule). This convention is often used in electrodynamics, astrophysics, electrical engineering etc..

In chapter 6, the definition of RCP and LCP is defined according to the second convention, hence, from the view of the source. The respective alignment of the waveplate is shown in appendix A.2.

The degree of circular polarisation is given by the Stokes parameter P_3:

$$P_3 = \frac{I(\mathrm{RCP}) - I(\mathrm{LCP})}{I(\mathrm{RCP}) + I(\mathrm{LCP})},\tag{2.106}$$

and describes the relative intensities of a light beam with respect to the vectors σ_+ and σ_- [82].

Part III

Broadband transient absorption spectroscopy

3. Experimental setup and spectroscopic technique of broadband transient absorption spectroscopy

3.1. Introduction and statement of contributions

In this chapter, the experimental setup and the technique of broadband transient absorption spectroscopy are presented. Both were used for the following two projects. In chapter 4, anomalous photophysical effects in pharmaceutically relevant coumarin derivatives are unscrambled with this method, whereas in chapter 5, first insights into the photochemical transformation of molecules intended for organic information recording are given.

The pump-probe setup was assembled by Martin Wörle in the course of his Master's thesis [113] under the supervision of Dr. Daniel Hutzler. The measurements are controlled by a Labview program, which was originally written by Martin Fischer and later optimised by M. Wörle. For data post-processing, we used a MATLAB program written by the author.

3.2. Experimental setup

Figure 8 shows a sketch of the experimental setup. Femtosecond pulse generation is realised by means of a commercial Ti:Sapphire-laser system (CPA-2010, Clark MXR), which is based on chirped pulse amplification, a method awarded with the Nobel prize to Donna Strickland and Gerard Mourou in 2018 [114], and two non-collinear optical parametric amplifiers (NOPA-ultra, ag-Riedle, E. Riedle and coworkers). The CPA-2010 uses an Erbium doped "Stretched Pulse" fibre oscillator (SErF) as seed source. The SErF is passively mode-locked via polarisation rotation and generates 1550 nm seed-pulses. These are frequency-doubled, stretched, and injected into a Ti:Sapphire-based regenerative amplifier. The latter is pumped by a Q-switched Nd:YAG laser, which is frequency-doubled to 532 nm. After compression, the CPA-2010 provides 150 fs pulses with an energy of 1 mJ and a central wavelength of 775 nm at a repetition rate of 1 kHz. Fractions of 30 % and 42 % of these pulses are used to pump two identical, but differently aligned, non-collinear optical parametric amplifiers (NOPA), NOPA I and NOPA II, respectively. The remaining light is used for an independent experiment. Both NOPAs consist of two stages, whereof the signal generated in the first NOPA-stage is amplified in the second stage [115, 116, 117], resulting in pulse energies up to 15 μJ. A white-light continuum generated
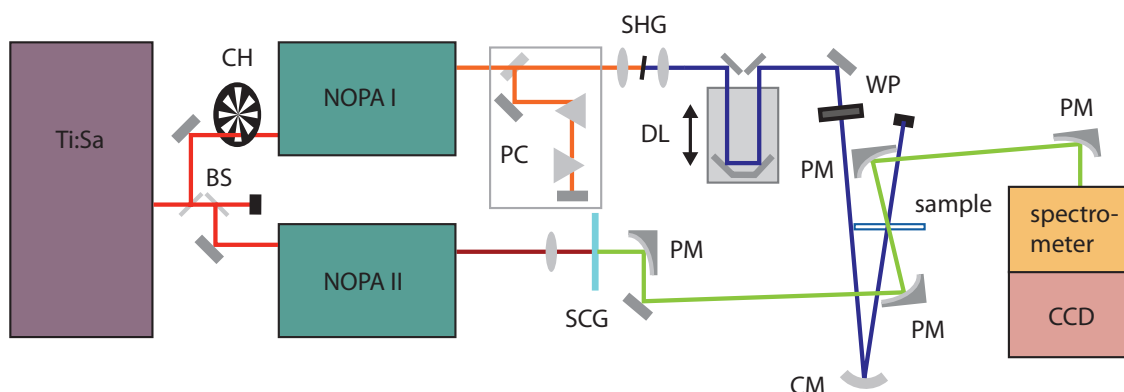
Figure 8 Sketch of the femtosecond pump-probe spectrometer. A commercial Ti:Sa-laser system (CPA-2010, Clark MXR) provides $1\ mJ$ 150-fs-pulses at a central wavelength of $775\ nm$. Fractions of $30\ \%$ and $42\ \%$ are split off these pulses by beam splitters (BS) and pump two identical non-collinear optical parametric amplifiers (NOPA I and NOPA II). The visible output of NOPA I is further compressed to < 50 fs with a prism compressor (PC) and frequency-doubled by SHG in a BBO-crystal (SHG). This pulse serves as the pump-pulse and is focused onto the sample by a curved mirror (CM). Measuring the pump-induced change of the optical density $\Delta OD(\lambda, t)$ is realised by white-light probe pulses, which are generated from the output of NOPA II by SCG in a Ca_2F-plate. A pair of off-axis parabolic mirrors (PM) is used to focus and re-collimate the probe pulse before focussing the transmitted probe pulses into the detector (spectrometer and CCD). Temporal delay of pump and probe pulses is provided by a linear translation stage (DL). A half-waveplate allows the alignment of the polarization between pump and probe pulses (WP).

in a Sapphire-crystal, which is focused into a 1 mm thick beta barium borate crystal (BBO, type I) serves as the seed for parametric amplification (see section 2.2.4) in the first stage. Pumping is realised by a fraction of the frequency-doubled laser fundamental. The wavelength and bandwidth of the output signal are controlled by adjusting the temporal delay of the chirped seed and the pump pulses, and aligning the angle between their wavevectors in order to minimize the group velocity mismatch. The output spectrum for standard alignment (NOPA I) lies in the range from 450 nm to 760 nm [117]. Amplification of these signal pulses in the second stage is realised py pumping a second BBO (type I, 2 mm) with the remaining fraction of the second harmonic. The chirped output pulses of the NOPA are further compressed to Fourier limits well below 50 fs by means of a prism compressor consisting of two sequential fused silica Brewster prisms. Pulse durations are characterised with an SHG-autocorrelation setup. A pulse duration of 14 fs can be obtained from the autocorrelation trace of the pump pulse (see figure 9a). In NOPA II, the idler of the DFG-process in the first stage is used as seed for the second stage allowing the generation of pulses in the near-infrared (NIR) spectral range beyond 865 nm [116].

The outputs of the NOPAs serve as excitation sources for the state-of-the-art pump-probe setup depicted in the right half of figure 8. The design roughly conforms to the pump-probe setup pioneered by Megerle et al. in the group of Eberhard Riedle [117]. Because organic molecules usually exhibit absorption spectra in the ultraviolet (UV) spectral range, the second harmonic of the output of NOPA I is generated in a BBO crystal (type I, 38.8°, 200 μm) acting as the pump pulse. Further, the pump pulse is delayed with respect to the probe pulse by reflection on a
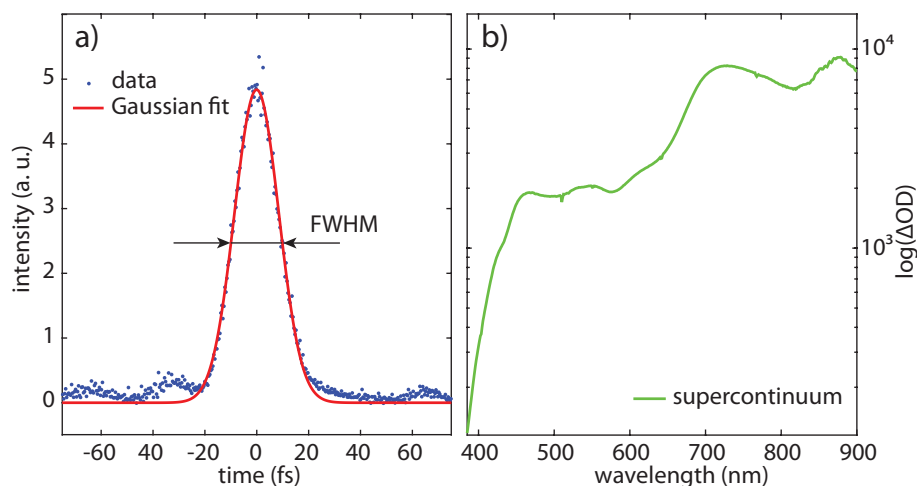
Figure 9 Properties of exemplary pump and probe pulses. a) SHG-autocorrelation result of the pump pulse (see also figure 53). The pulse duration can be determined to 13.8 fs by dividing the FWHM by $\sqrt{2}$. Assuming a non-collinear arrangement with an angle of 10° between pump and probe, the effective cross-correlation increases to ∼50 fs. b) Visible spectral range of the supercontinuum used for probing.

retro-reflector, which is mounted on a computer controlled linear translation stage (M-531.DD, Physik Instrumente GmbH). A half-wave plate (B.Halle) is used to align the polarisation between the linearly polarised pump and probe pulses. Then, the pump beam is focused by means of a curved silver mirror (focal length f = 150 mm) onto the sample. Probe pulses are provided by supercontinuum generation (SCG) when focussing the NIR output of NOPA II onto a Ca_2F-plate with a lens (focal length f = 100 mm). SCG is a nonlinear $\chi^{(3)}$-process mediated mainly by self-phase modulation and self-focusing (see section 2.2.5). Group velocity dispersion in bulk Ca_2F causes a chirp of the supercontinuum. An exemplary spectrum of the visible part of the generated supercontinuum is shown in figure 9b. The white-light probe pulses are collected and re-collimated with an off-axis parabolic mirror (protected silver, f = 50.8 mm, diameter d = 25.4 mm). Subsequently, the probe pulses are focussed onto the sample at an angle of less than 10° with respect to the pump-pulses. Focussing of the incoming probe-pulses and re-collimation of the transmitted pulses is achieved by two off-axis parabolic mirrors (protected silver, f = 50.8 mm, d=25.4 mm). For detection of the transmitted light, we use a Czerny-Turner spectrometer (Micro HR Imaging, Horiba, 150 lines/mm, refraction optimised for 500 nm) and a CCD camera (Series 2000, Stresing GmbH) with a 512×122-pixel sensor (S7030-0907, Hamamatsu) allowing single pulse detection. In order to measure the pump induced change of the optical density of the sample, every second pump pulse is blocked with a chopper wheel. As a reference, small fractions are splitted off the probe and pump beams before focussing onto the sample, and reflected onto boundary pixels of the CCD sensor without passing through the sample.

The time resolution of the setup can be determined by measuring the cross-correlation of pump and probe pulses. The non-collinear pump-probe geometry with an angle of about 10° reduces

the temporal resolution from 14 fs to 50 fs. But we need this geometry in order to separate both beams. M. Wörle confirmed this estimation by extracting the FWHM of the transient absorption (TA) signal of TPA in ultra-pure water [113]. As M. Rasmusson et al. showed, this Gaussian-like signal can be used as a measure for the pump-probe cross-correlation, if other processes like impulsive stimulated Raman scattering or cross-phase modulation are suppressed, as it is the case in a non-collinear pump-probe alignment, for instance [118]. The influence of the temporal chirp of the white-light probe pulse on the time resolution of the setup can be compensated by an accurate determination of the time zero of each spectral component (see section 3.4) [117]. Furthermore, the spectral resolution is determined by the spectrometer grating, and can be estimated to $\simeq 3$ nm [113].

The samples in this work consist of solutions of organic molecules in 1 mm thick glass cuvettes (Suprasil, Hellma). The sample-holder is mounted on a motorised linear x-y-z-translation stage, which allows to move the cuvette after each acquisition point in order to avoid photobleaching of the molecules.

For the experiments described in chapter 5, NOPA II was exchanged by a commercial optical parametric oscillator (TOPAS, Light Conversion), and instead of the Czerny-Turner spectrometer, we used a prism-based polychromator as described by Megerle et al. [117].

3.3. Transient absorption spectroscopy

Pump-probe spectroscopy is a powerful method to study ultrafast phenomena below the temporal resolution limit of electronic devices. In 1999, Ahmed H. Zewail was honoured with the Nobel prize for his examinations on transition states in photophysical and photochemical molecular dynamics with sub-picosecond time resolution [5]. Applying broadband transient absorption spectroscopy [11, 119], we examine the change in absorbance A, which is equal to the change in optical density OD, of a molecule upon excitation with an UV laser pulse. This process can be described mathematically according to

$$\Delta A(\lambda, t_d) = \Delta \text{OD}(\lambda, t) = -\log\left(\frac{I(\lambda, t_d)}{I_0(\lambda)}\right).$$ (3.1)

Here, I_0 and I are the spectral intensity of the probe pulse after transmission through the sample without and with prior excitation by the pump pulse, i.e. pump blocked or not blocked by the chopper wheel. Both spectra are measured for delay times t_d of probe pulses arriving before ($t_d < 0$) and after the pump pulses ($t_d > 0$) for a temporal range from about -5 ps up to maximum 1.3 ns. Time steps are chosen to be $\Delta t_d = 12$ fs for a small interval from -0.5 ps to 0.5 ps, $\Delta t_d = 24$ fs from -1 ps to -0.5 ps and 0.5 ps to 1 ps, and increase exponentially for larger absolute values of t_d. A scheme of the pulse sequence is shown in figure 10b.
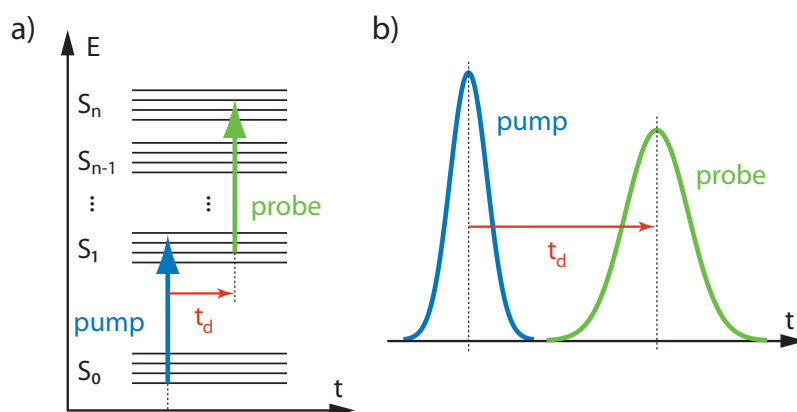
Figure 10 Pump-probe principle. a) Excitation of the molecule by the pump pulse from S_0 to S_1. The probe pulse, which is delayed according to delay time t_d, excites the molecule to a higher-energy state S_n. b) Pulse sequence of pump and probe.

In terms of potential energies, the pump-probe process can be described according to the scheme depicted in figure 10a. The pump pulse is usually tuned in resonance for excitation of the molecule from its ground state S_0 to an excited electronic state, which in our case is the first excited electronic state S_1. The probe gives rise to further excitation to a state of higher energy. Thus, the initial state for the probe can be any pump-induced electronic or vibrational state during the absorption and relaxation process of the molecule (cf. section 2.3.3). In our studies, the probe spectrum does not contain any frequencies higher than the pump frequency. Therefore, the measured ΔOD-spectrum is zero for negative delay times and exhibits positive values for the spectral range, where excited state absorption occurs in case of positive delays. Negative signals can be detected due to fluorescence and stimulated emission. If the probe spectrum covers also the pump frequency, a negative signal is observed at this frequency caused by the depletion of the ground state, which is termed as ground state bleaching.

The coherent interaction of an intense pump pulse and a weaker probe pulse with the molecules in the sample can be described best according to a $\chi^{(3)}$-process such as cross-phase modulation and two-photon absorption [120, 121]. For delays smaller than the pump pulse duration, the transmitted signal can exhibit a coherent artifact [122, 123]. The shape of the coherent artifact depends strongly on the duration of the pump pulse and the chirp of the probe pulse. The main origins of coherent artifacts are TPA and cross-phase modulation [123]. The latter process is generated by the change of spectral probe components due to the varying pump-induced polarisation of the medium [120, 121].

3.4. Data post-processing

Wavelength calibration is realised by placing a narrow bandgap filter (BG36, Schott) in front of the detector and comparing the pixel number of the peaks in the transmission spectra of

the white light with the according wavelength values from literature. When using the Czerny-Turner spectrometer, a polynomial fit of these values in a wavelength-versus-pixel diagram allows to extract a linear calibration function [113]. The calibration function of the prism-based polychromator was obtained according to Megerle et al. [117]. Deviations in the transient data due to variations in pump intensity were corrected according to the relative change in intensity of the recorded reference signal.

Furthermore, the chirp originating from group velocity dispersion during SCG in the bulk glass leads to different zero delay times t_0 for each wavelength component of the ΔOD-spectrum. Hence, the chirp needs to be corrected in order to obtain a common time zero and transient time axis for the whole spectrum. A common method uses coherent artifacts [124, 117]. The centre of the coherent artifact, deduced from a Gaussian fit, of each wavelength component is extracted and fitted with a polynomial function. Subsequently, the transient data is interpolated and corrected to a chosen time axis with common zero time. Chirp correction is essential for a global analysis based on transient spectral evolution. Due to the absence of significant coherent artifacts in the experiments presented in this thesis, we determined the point in time $t_{0,i}$ for closely spaced wavelength components i, i.e. kinetic traces, over the examined spectral range, when ΔOD(λ_i, t) has reached 50% of its maximum absolute value. Figure 11a depicts a contour plot of the chirped transient data including a polynomial fit of fifth order on the extracted t_0-trace serving as a basis for the transformation to a common time-delay axis. The residua of the fit are shown in figure 11b. The fit matches the data well beyond 510 nm and between 430 nm and 490 nm with residuals below 5 fs. Larger residuals only appear around 500 nm due to an isosbestic point around 500 nm in the transient spectra (see figure 14b), and below 430 nm, where the stimulated emission band of the data approaches zero. Below 470 nm, the zero time points $t_{0,i}$ are below a measurement time of -0.5 ps (see figure 11a). Since below -0.5 ps the time steps increase (see section 3.3), temporal discontinuities appear as an interference-like pattern around $t_d = 0$ below 470 nm in the spectrum in figure 14b.

In order to obtain quantitative information (e.g. relaxation mechanism and decay rates) from the data, the involved transitions and decay mechanisms are fitted according to a kinetic rate equation model [125, 126]. The fitting software was developed by Andreas Brodschelm and Andy Thaller, former members of the "Chair for Laser and X-Ray Physics" at TU Munich [127, 128]. The multi-exponential fit allows to obtain different time constants τ_i and the spectral amplitudes of the respective transitions a_i for the primary photophysical processes upon relaxation from the Franck-Condon state (see section 2.3.3) and describes the decay according to

$$\Delta\text{OD}(\lambda, t) = I_0 e^{-4\ln 2(\frac{t}{t_{pp}})^2} \otimes \theta(t) \cdot \sum_i (a_i e^{-\frac{t}{\tau_i}}) + a_\infty. \tag{3.2}$$

Herein, the symbol $\otimes$ denotes the convolution operator, $\theta(t)$ is the step function, and τ_{pp} the FWHM of the pump-probe cross-correlation. The expression $I_0 e^{-4\ln 2(\frac{t}{t_{pp}})^2}$ represents the
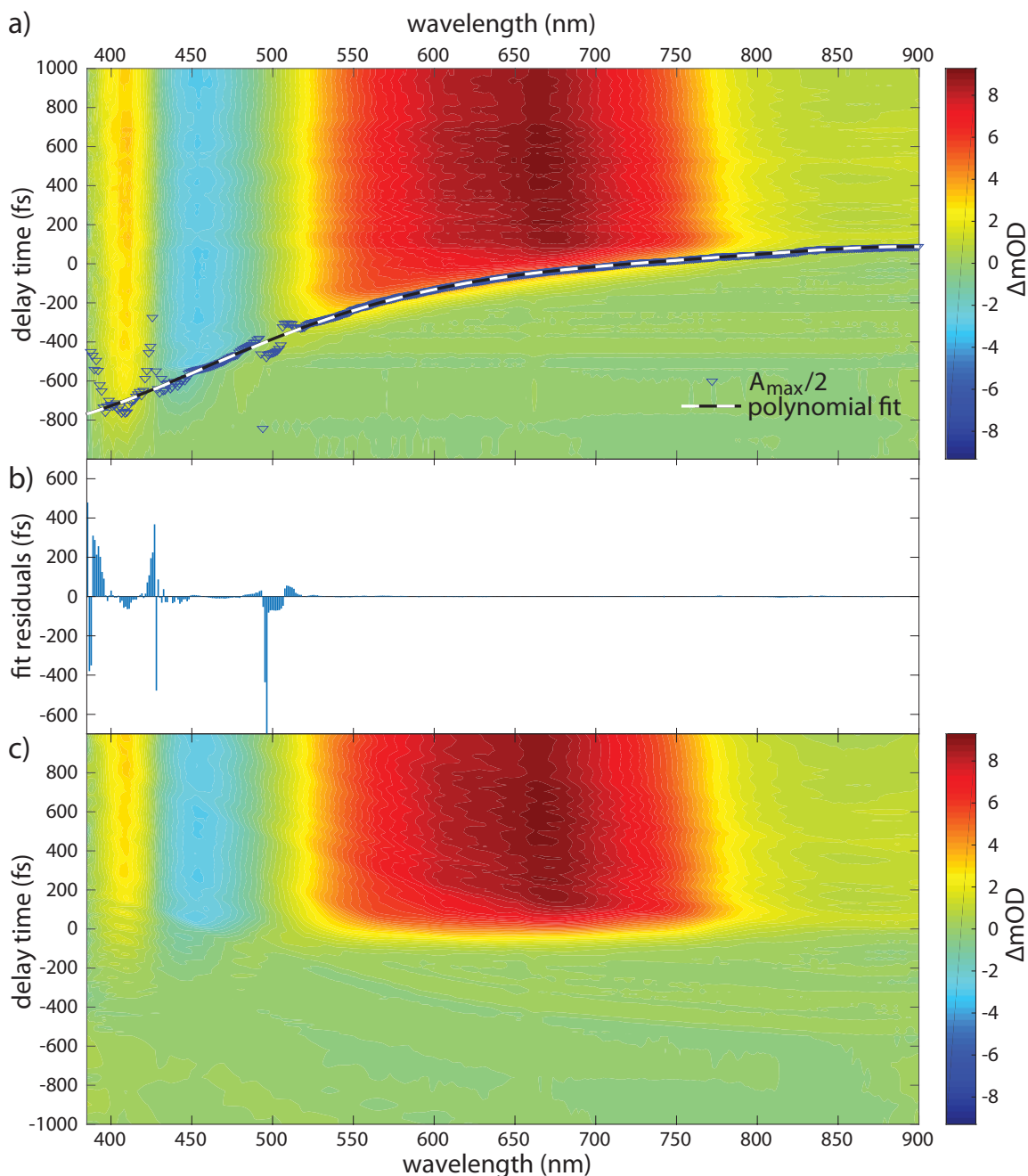
Figure 11 Chirp correction procedure. a) Chirped transient absorption data for -1000 fs < t_d < 1000 fs. Blue triangles indicate the data points, where $\Delta\mathrm{OD}$ is equal to half of its maximum absolute value ($A_{\mathrm{max}}/2$) for the kinetic trace of each recorded wavelength. The black-white dashed line denotes a polynomial fit of fifth order to the $A_{\mathrm{max}}/2$-points. b) Residua of the fit. Around 500 nm and below 430 nm the transient absorption and stimulated emission bands approach zero causing large residuals. c) Chirp corrected transient data. Temporal discontinuities around $t_d = 0$ in the spectrum below ~470 nm can be attributed to lower temporal resolution (see text).

Gaussian instrument response function for transient absorption spectroscopy, and a_∞ is a constant. We modelled the transient absorption data by two different methods. In section 5.3, single-channel fits are performed, i.e. single kinetic traces from each representative wavelength of the spectrum are fitted with locally different time constants. In contrast, in a global analysis

all kinetic traces of the detected transient absorption spectrum are fitted with the same global time constants (see section 4.3) [125, 126]. From the corresponding fitting amplitudes for each time constant, decay associated difference spectra (DADS) for a parallel deactivation scheme and evolution associated difference spectra (EADS) according to a sequential scheme can be generated. In both cases, the rise-time of the signal reflecting the initial absorption to the excited state is given by the cross correlation of pump and probe pulse envelopes. From the fitting procedure the time zero of any spectral component can be extracted with high accuracy. However, we used the faster method of polynomial fitting, described above, for the chirp correction.

4. Broadband transient absorption spectroscopy on halogen-substituted coumarin derivatives

4.1. Introduction and statement of contributions

The present chapter presents studies on tunable photophysical properties observed in halogen-substituted coumarin derivatives. A summary of the most important results examined with broadband transient absorption spectroscopy and density functional theory (DFT) calculations in acetonitrile solutions are published in RSC Advances [129].

Coumarin is an aromatic molecule, which naturally occurs in various plants such as tonka beans, sweet grass, strawberries, black currants or cinammon. Its derivatives feature a broad spectrum of applications in diverse fields including pharmaceutical chemistry and medical sciences [130, 131, 132, 133, 134]. Of particular interest are their photochemical properties. As mentioned in section 2.3.3, triplet states are the origin of many photochemical processes [93, 94, 87]. In coumarins, triplet states play a significant role in their application as photosensitizers [135], molecular sensors [136, 137, 138], photolabile protecting groups [139, 111], photodynamic therapy of cancer [140, 141], or enantioselective photo-cycloaddition [142]. The efficiency of a triplet-mediated photoreaction depends strongly on the intersystem crossing (ISC) rate, thus, the triplet (quantum) yield Φ_T. Strong enhancement of triplet yields can be achieved by introducing atoms with large atomic numbers in the molecules due to the intramolecular heavy-atom effect (HAE, see section 2.3.5). This was shown in earlier studies by Furuta et al. and Takano et al. [143, 111], who managed to improve triplet-mediated photolytic efficiencies and reaction rates of coumarin-derivatives drastically by 6-substitution with halogens. In contrast, large Φ_T are usually accompanied with very low fluorescence quantum yields Φ_F, and thus, greatly reduced lifetimes of the first excited singlet state. Therefore, the HAE constitutes an effective method for controlling Φ_T and Φ_F, which are crucial parameters of organic molecules regarding their desired application (see section 2.3.5) [99, 100, 97, 107, 108, 109, 111]. Particularly coumarins are suitable molecules due to small energy spacings between triplet states and the lowest excited singlet states, which can be varied by substitutions [144, 145, 146, 147, 148, 149]. Moreover, the overall photophysical and photochemical properties are strongly influenced by the attached functional groups. Thus, small molecules like coumarin can either serve as backbones of pharmaceutical substances or as model systems for examinations on the effect of functional groups with respect to their chemical or pharmaceutical applications, for instance [150, 139, 140, 151]. However, not only the type of atom or functional group, which is

substituted to the coumarin moiety, but also the position of substitution contributes significantly to the photophysical properties. Combinations of electron-donating groups at the 7-position of coumarin and electron-accepting substitutions at the 3-position favour charge-transfer transitions resulting in large Φ_F (see section 2.3.4). Hence, coumarins of this class have found manifold applications as laser dyes [152, 153, 154, 155, 156, 157] and organic light-emitting diodes (OLEDs) [158, 159].

The coumarins examined in our studies are 3-substituted either with a diethylphosphono group (PO(OEt)$_2$) or phosphonic acid (PO(OH)$_2$). Phoshphono groups and phsosphonic acid exhibit enzyme and viral inhibiting properties [160, 161, 162]. In order to avoid unnecessary elongation of this thesis and because the results from the experiments with coumarin-3-phosphonic acid qualitatively agree with the other results, we limit the discussion to the 3-diethylphosphonocoumarins. The experiments on coumarin-3-phosphonic acid are summarised in Sebastian Wegscheider's Master's thesis [163].

Position 6 is either not-substituted, or substituted with a halogen, Cl and Br, respectively. The diethylphosphono group exhibits an electron-withdrawing effect with a stronger influence on the 7-position than on the 6-position due to symmetry reasons. Therefore, the 6-substituent would be expected to influence the photophysical properties only weakly and seems to be ideal for fine-tuning of the properties of the 3-diethylphosphonocoumarins. According to the HAE, we would expect slightly enhanced Φ_T and reduced Φ_F upon 6-substitution of Cl and Br, while the influence of Br would be supposed to be stronger. However, the observed effect resembles an anomalous HAE. Thus, in the following sections, this anomaly in the HAE is examined with broadband transient absorption spectroscopy in combination with conventional absorption and fluorescence spectroscopy, and the experimental findings are interpreted with and corroborated by TDDFT simulations.

All presented experiments as well as data post-processing and analysis were performed by the author. Martin Wörle, who constructed the femtosecond pump-probe spectrometer [113] supported the transient measurements. Mikayel Musheghyan performed preliminary absorption and fluorescence spectroscopy in various solvents and helped with measuring and data post-processing of previous time-resolved experiments on the 3-diethylphosphonocoumarins in the course of his Master's thesis [164]. Likewise, during his Master's studies, Sebastian Wegscheider analysed the set of 6-substituted coumarin-3-phosphonic acid [163]. (TD)DFT calculations were performed by Dr. Petko Petkov, and the molecules were synthesised by the group of Prof. Dr. Rositca Nikolova [165], both from the Faculty of Chemistry and Pharmacy at University of Sofia, Bulgaria. Results and conclusions were discussed in collaboration with PD Dr. Hristo Iglev, Dr. Petko Petkov, Dr. Eleonora Iglev and Prof. Dr. Reinhard Kienberger. The publication comprises the measurements and (TD)DFT calculations in acetonitrile solutions [129]. In this work, more details are added and additional data measured in further solvents is

presented and discussed.

4.2. Absorption and fluorescence properties
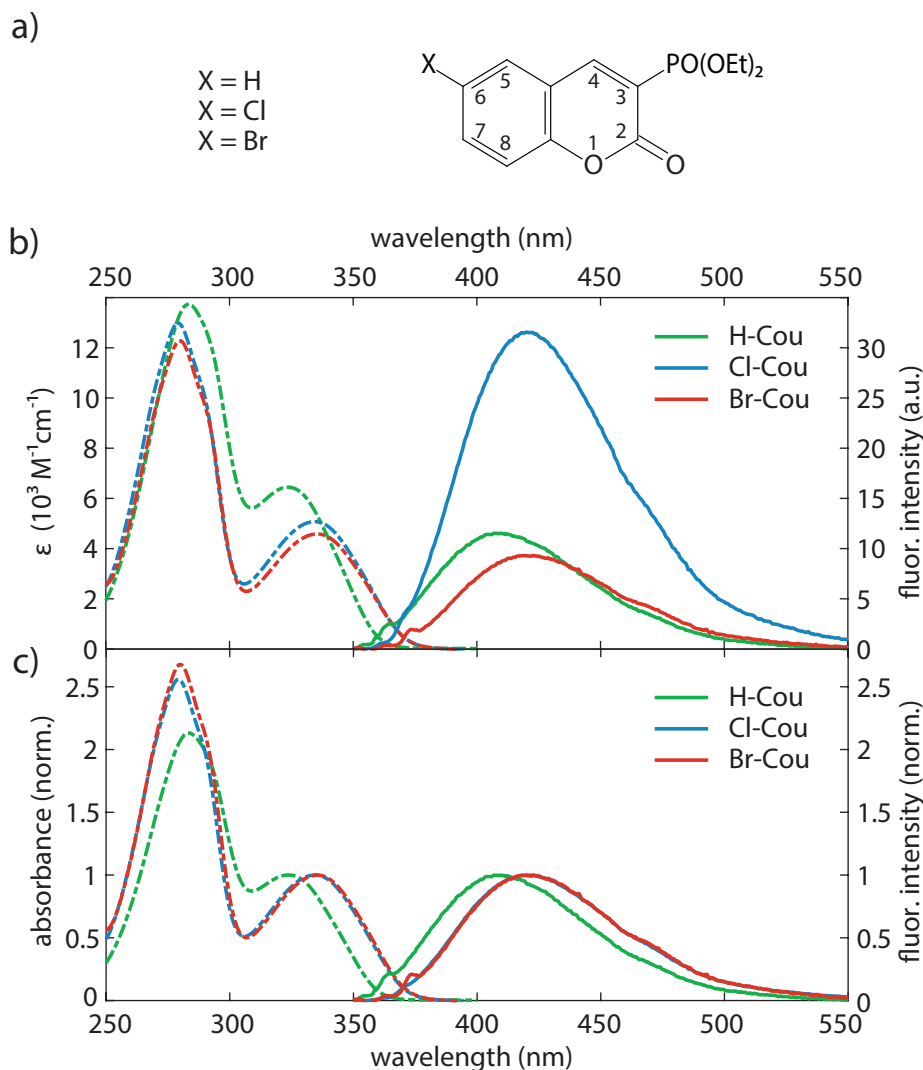
Figure 12 a) Chemical structure of the examined coumarin derivatives: X = H (H-Cou), X = Cl (Cl-Cou), X = Br (Br-Cou). b) Molar absorption coefficient ε (left ordinate scale, dashed lines) and fluorescence intensities (right ordinate scale, solid lines) of H-Cou (green), Cl-Cou (blue) and Br-Cou (red) in ACN (C = 80 μmol/l). c) Normalised absorption and fluorescence spectra of the respective compounds. Absorption normalised to the maximum of the primary absorption band.

The chemical structure of the examined molecules is depicted in figure 12a. The compound H-Cou is derived from the coumarin molecule by 3-substituting a diethylphosphono group $PO(OEt)_2$ (Et = $-CH_2-CH_3$). Cl-Cou and Br-Cou are additionally 6-substituted with Cl and Br, respectively. Conventional absorption spectroscopy was carried out on a commercial absorption spectrometer (Lambda 19, Perkin-Elmer). Fluorescence spectra were recorded with a spectrofluorometer (FP-6500, Jasco) upon setting the excitation wavelength to the respective absorption maximum

of each molecule and applying a photo-multiplier voltage of 400 V. The corresponding spectra of the three molecules in acetonitrile (ACN) solutions (99.5%, Sigma-Aldrich) at a concentration of $C = 80\frac{\mu mol}{l} = 80\ \mu M$ are shown in figure 12b and c. Further measurements in other solvents are discussed below. In the left half of figure 12b the first two absorption bands of the three compounds are depicted in units of their molar absorption coefficient ε. Commonly, different orbitals contribute and superimpose to the respective transitions between ground state S_0 and excited states S_n. To their right, the respective fluorescence spectra are shown. In order to determine molar absorption coefficient and fluorescence intensity, the depicted spectra represent each an average over several individually prepared solutions. Hence, the largest molar absorption coefficient was measured for H-Cou ($\varepsilon = 6.4 \cdot 10^3$ M^{-1}cm^{-1}), followed by slightly smaller values of Cl-Cou ($5.1 \cdot 10^3$ M^{-1}cm^{-1}) and Br-Cou ($4.6 \cdot 10^3$ M^{-1}cm^{-1}) (see figure 12b and table 1). All three values are extracted from the absorption maximum of the respective primary absorption band, i.e. the lowest excited state. The corresponding oscillator strengths f (see table 1), which are determined from theses values according to equation 2.86, reflect the relative behaviour of the molar absorption coefficients. Because of the spectral overlap of the first two absorption bands, these values serve only as a rough estimation. Much larger differences between the molecules can be found in the fluorescence spectra in the right part of figure 12b. The fluorescence intensity of Cl-Cou is enhanced threefold with respect to H-Cou, and even fourfold compared to Br-Cou. The same accounts for the fluorescence quantum yield of the samples, Φ_F^s. Using a reference sample such as the commercially available Coumarin-120 with known fluorescence quantum yield, the new samples' unknown fluorescence quantum yield Φ_F^s can be calculated according to following equation [166]:

$$\Phi_F^s = \frac{F^s a_r n_s^2}{F^r a_s n_r^2} \Phi_F^r. \tag{4.1}$$

The reference quantum yield $\Phi_F^r = 63\%$ (coumarin-120 in ACN) was taken from the studies of H. Pal et al. [167]. The parameters F^s and F^r are the integrated measured fluorescence intensities of sample (s) and reference (r) in ACN, respectively, and n_s and n_r the respective refractive indices. The quantities a_s and a_r denote the respective absorption factors $a_i = 1 - 10^{-A_i}$ ($i = s, r$) with the absorbance A. Thus, a value of $\Phi_F = 1.01\%$ is deduced for Cl-Cou, and the lower values of $\Phi_F = 0.34\%$ and $\Phi_F = 0.32\%$ belong to H-Cou and Br-Cou, respectively (table 1). Figure 12c shows the respective normalised spectra of the molecules. Absorption maxima of the first excited state can be extracted to 324 nm for H-Cou (see table 2). The electron-withdrawing inductive effect leads to a redshift of the respective maxima of Cl-Cou (334 nm) and Br-Cou (336 nm) [168, 111, 144]. The same redshift upon halogen-substitution can be found in the fluorescence spectra. H-Cou shows its fluorescence maximum at 410 nm, Cl-Cou at 420 nm, and Br-Cou at 423 nm. Thus, nearly identical Stokes-shifts of 86 nm and 87 nm are determined for all three samples. Stokes-shifts, absorption and fluorescence maxima lie in a for coumarins typical spectral range [169, 144, 170, 151]. Further differences between H-Cou and the halogenated compounds can be found in the growing distance between the first

and second absorption maximum. Because the photophysical properties are dominated by HOMO $\rightarrow$ LUMO transitions, i.e. transitions between ground and first excited state, the second absorption band will not be discussed further.

compound	H-Cou	Cl-Cou	Br-Cou
ε $(10^3 M^{-1} cm^{-1})$	6.4 ± 0.1	5.1 ± 0.4	4.6 ± 0.4
f (10^{-2})	7.0	6.6	5.9
Φ_{F} (%)	0.34 ± 0.02	1.01 ± 0.05	0.32 ± 0.03

Table 1 Molar absorption coefficient ε, oscillator strength f (according to equation 2.86) and fluorescence quantum yield Φ_{F} of samples H-Cou, Cl-Cou and Br-Cou in ACN (C = 80 μmol/l).

maxima (nm) (± 0.5)	abs. (ACN)	fluo. (ACN)	abs. (EOH)	fluo. (EOH)	abs. (CYH)
H-Cou	324	410	326	417	325
Cl-Cou	334	420	338	420	337
Br-Cou	336	423	339	420	337

Table 2 Absorption and fluorescence maxima of samples H-Cou, Cl-Cou and Br-Cou in ACN, EOH and CYH.

While the shape of absorbance and fluorescence bands of all three coumarins is very similar, the strongly enhanced fluorescence intensity and quantum yield of the Cl-substituted compound is remarkable. A "normal" HAE influence would be expected to quench not only the Br-Cou fluorescence, which is at least slightly weaker than fluorescence from the unsubstituted molecule, but also Cl-Cou fluorescence. The overall low fluorescence quantum yields of $\Phi_{\mathrm{F}} \leq 1\%$ indicate fast nonradiative relaxation [171].

The three compounds were further studied in solvents with strongly varying solvatochromatic parameters: acetonitrile (ACN), which is polar (dipole moment μ = 3.5 D) and aprotic, ethanol (EOH), which is polar (dipole moment μ =1.7 D) and protic, thus has the ability to donate hydrogen bonds, and cyclohexane (CYH), which is nonpolar (dipole moment μ =0.0 D) and aprotic. DFT calculations determined the dipole moments of the compounds to 2.7 D for Cl-Cou and Br-Cou, and 5.1 D for H-Cou (see section 4.4). Polar molecules, such as the examined compounds, often exhibit a redshift in polar solvents compared to nonpolar solvents [144, 145, 169, 172]. However, the absorption and emission spectra of each molecule, show only minor changes regarding the respective maxima when changing the solvent (see figure13 and table 2). The absorption maximum of H-Cou redshifts merely from 324 nm in ACN to 326 nm in the less polar solvent EOH and to 325 nm in nonpolar CYH. Because the PO(OEt)$_2$-group can accept hydrogen bonds, the redshift in protic EOH with respect to the more polar ACN can be attributed to the formation of hydrogen bonds. The fluorescence maximum exhibits a slight

redshift of 7 nm in EOH, presumably due to the lower polarity and the formation of hydrogen bonds. Upon halogen substitution, the redshift of the absorption becomes slightly larger. Again, the value in CYH lies between the maxima of the other solvents. Fluorescence spectra are nearly equal in ACN and EOH. Fluorescence of the molecules dissolved in cyclohexane is very low, the fluorescence quantum yield is approximately zero. Therefore, the spectra are strongly dominated by fluorescence of the pure solvent and not shown here. These measurements were also performed in a couple of other solvents [164]. However, no drastic differences could be observed, and therefore, this data is not shown here.
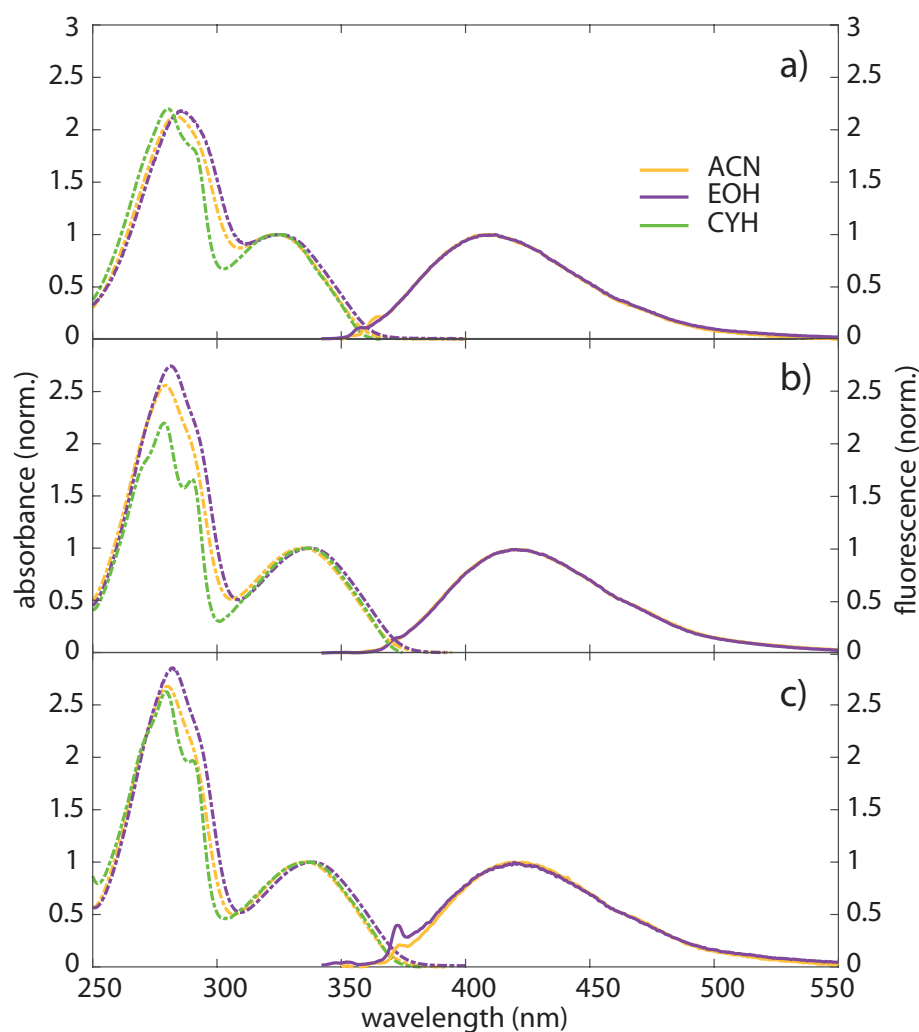
Figure 13 Normalised absorption (dashed lines) and fluorescence (solid lines) spectra in ACN (orange), EOH (purple) and CYH (green, only absorption) for a) H-Cou, b) Cl-Cou and c) Br-Cou. Absorption normalised to the maximum of the primary absorption band.

In summary, changing the 6-substitution leads to much larger effects than changing the solvent. The lack of significant solvatochromic shifts despite the existing polarity of the molecules is unusual. The same accounts for the slight redshift observed in CYH, where a blueshift would be expected. These results are an indication for a complex composition of the first excited state.

4.3. Transient spectra and temporal evolution of the excited state dynamics
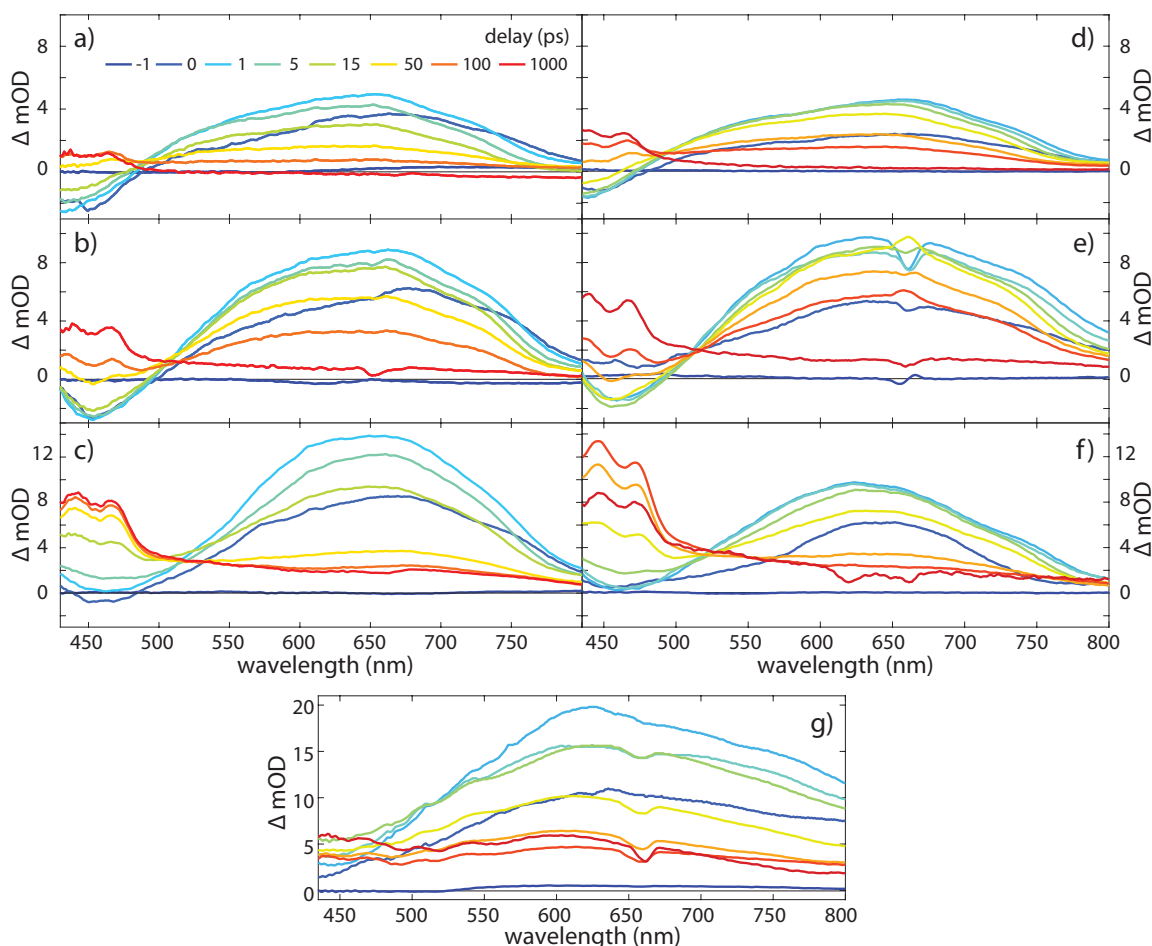
Figure 14 Chirp-corrected transient absorption spectra for selected time delays (see legend) measured in ACN (a-c), EOH (d-f), and CYH (g) solutions upon excitation at 330 nm. a, d) H-Cou, b, e) Cl-Cou, and c, f, g) Br-Cou. Concentrations in ACN are 0.1 mol/l, in EOH: 0.15 mol/l for H-Cou, and 0.0925 mol/l for Cl-Cou and Br-Cou; in CYH a saturated solution of 0.1 mol/l was used. The transient data is smoothed over seven data points spectrally and three subsequent data points on the time axis. Little distortions at 660 nm in e), f) and g) are caused by stray-light of the pump-fundamental.

The pump-probe setup described in section 3.2 was used for time-resolved studies of the excited state dynamics of the three compounds. The pump pulse, which was generated from the frequency-doubled output of a NOPA, was set to a wavelength of 330 nm, close to the respective absorption maxima, and a pulse energy of 200 nJ. Broadband supercontinuum pulses, generated from the 1150 nm output of a second NOPA, allowed probing the samples over a spectral range from 430 nm to 800 nm. In order to measure isotropic signals, the pump polarization was adjusted with a half-wave plate to an angle of 54.7° with respect to the probe pulses. Measurements in pure solvent revealed no contribution to the $\Delta\mathrm{OD}(\lambda, t_d)$-signal. Therefore, we desisted from subtracting the solvent data. For negative delay times, i.e. probe

pulses arriving before pump pulses at the sample, $\Delta OD(\lambda)$ is theoretically zero. We correct the remaining background by subtracting the mean $\Delta OD(\lambda)$-value between -5 ps and -3 ps from the measured data.

In figure 14, the chirp-corrected transient spectra of H-Cou (a, d), Cl-Cou (b, e), and Br-Cou (c, f, g) in acetonitrile (a-c), ethanol (d-f), and cyclohexane (g) are plotted for delay times between -1 ps and 1 ns. The presented data is the mean of three measurement series and shows similar dynamics for the three compounds. Similar to the steady-state results, the transient spectra exhibit only minor differences when changing the solvent. Again, the discussion is based on the example of ACN (see figure 14a-c) and compared to the other solvents below. Upon excitation by the pump pulse to the first excited singlet state, the probe pulse gives rise to transitions into higher-energy excited electronic states resulting in a broad excited state absorption (ESA) band within the first picosecond. This ESA band, which exhibits a maximum at around 640 nm, starts around 500 nm and reaches beyond our detection limit at 800 nm. It decays almost completely within 1 ns. Considering the transient spectrum in acetonitrile after 1 ps, the ESA maximum grows from a value of 4.5 mOD for H-Cou, to values of 9 mOD for Cl-Cou and 13 mOD for Br-Cou (see figure 14a-c). Below 500 nm a negative signal appears and likewise reaches its maximal ΔOD within the first picosecond. As the exciting pump pulse is set to 330 nm, ground state bleaching can be ruled out. However, this wavelength range overlaps with the fluorescence spectrum (see figure 12). Hence, we can attribute this negative band to stimulated emission (SE) generated by the probe pulse. It should be noted that ESA and SE bands overlap spectrally. At the blue end of our detection range, the SE band approaches zero, although significant steady-state fluorescence can be detected for wavelengths below 400 nm. We assume that this effect is due to the low intensity of the probe below 450 nm. Comparing the three compounds, the absolute values of SE maxima correlate with the fluorescence intensities (see figure 12b), thus, largest for Cl-Cou, followed by H-Cou and Br-Cou.

For pump-probe delays above 1 ps, an isosbestic point occurs, indicating intramolecular relaxation from the excited singlet state into a different state with longer lifetime. Upon halogen substitution, the isosbestic point redshifts from 490 nm (H-Cou) to 505 nm (Cl-Cou) and 515 nm (Br-Cou). Beyond 50 ps, the SE band has vanished giving rise to a second spectrum with two distinct maxima at 440 nm and 465 nm and a flat side band ranging to wavelengths beyond our detection range of 800 nm. The results of the DFT calculations (see section 4.4) allow its assignment to triplet-triplet absorption (TTA), which is typically in the range of 350 nm to 700 nm for coumarins [173, 144, 147, 148, 149]. The spacing between the two peaks is in the order of 1200-1400 cm^{-1} and can be attributed to vibrational modes, in particular the C-C stretching mode, in agreement with earlier studies [147, 148]. Halogen-substitution causes a significant growth of the TTA signal. We extract maximum signal intensities of 1.5 mOD for H-Cou, 4 mOD for Cl-Cou, and 9 mOD for Br-Cou.
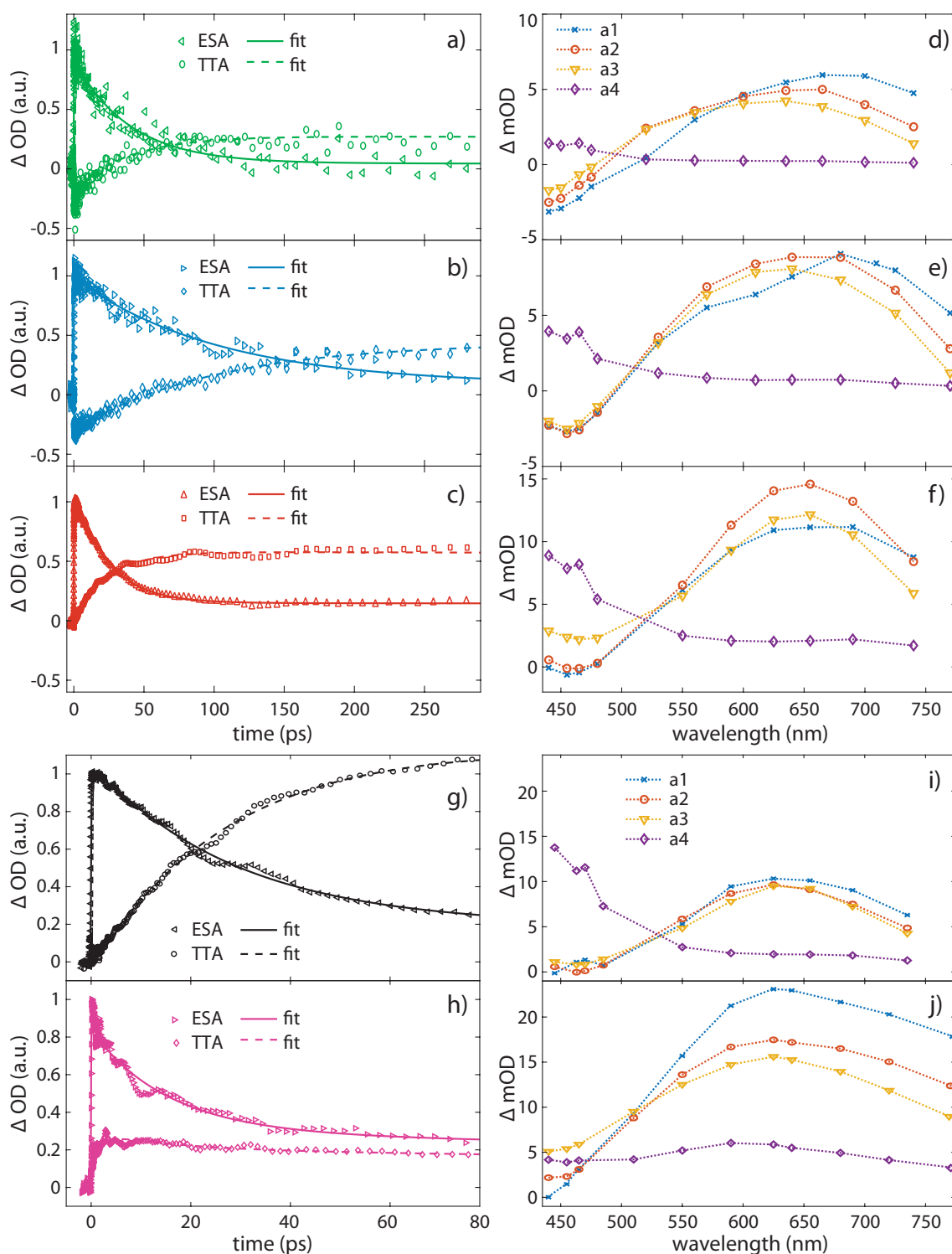
Figure 15 Temporal (left) and spectral evolution (right). a-c) Kinetic traces of H-Cou (a, green), Cl-Cou (b, blue), and Br-Cou (c, red) in ACN recorded at the ESA maximum and the lower energy maximum of the respective TTA, normalised to the respective ESA maximum for delay times up to 290 ps. Solid and dashed lines represent a fit according to a global rate equation model with four time constants. d-f) EADS of H-Cou (d), Cl-Cou (e), and Br-Cou (f) in ACN constructed from the fitted amplitudes $a_i(\lambda)$ according to the respective time constants τ_i. The spectra of a_1, a_2, and a_3 denote subsequent intermediate states of S_1. The triplet state T_1 is represented by a_4. g, h) Respective kinetic traces of Br-Cou in EOH (g, black) and CYH (h, pink) for delay times up to 80 ps. Corresponding EADS of Br-Cou in EOH (i) and CYH (j). Fit residuals are all well below 10% and therefore not shown here.

A comparison of the transient data in EOH to the ACN data reveals largely similar positions for ESA maxima, isosbestic point, and TTA-maxima (see figure 14d-f). H-Cou exhibits similar ΔOD-values as in ACN, although the concentration in EOH is 1.5-fold. The poor solubility of our polar molecules in nonpolar solvents such as CYH caused difficulties in achieving reliable TA data. Only the measurements of transient spectra of Br-Cou in CYH succeeded with acceptable signal to noise ratio. Therefore, we abandoned to analyse the spectra of the other molecules. The ESA strength is significantly larger than in EOH and ACN and exhibits a slight blueshift. In contrast, TTA is lower compared to Br-Cou in the other solvents. The isosbestic point is less pronounced and blueshifted to 470 nm. No indication of SE is visible in our detection range in agreement with the observed very low fluorescence quantum yield. Differences regarding lifetimes and triplet yields are discussed below.

The ultrafast temporal dynamics of the singlet-triplet relaxation is shown in figure 15. On the left side of the figure the kinetic traces measured at the ESA maximum and at the lower energy maximum of the respective TTA are depicted. Figures 15a-c illustrate the transient results of the three compounds in ACN, and figures 15g-h the results of the Br-substituted compound in EOH and CYH. The scans are normalised to the respective ESA maxima for each molecule. In order to obtain quantitative information from the dynamics of the involved decay mechanisms, we analysed the data with a global fitting procedure according to a sequential rate equation model (see section 3.4, equation 3.2). A scheme of the kinetic model is shown in figure 16a. Considering the above discussed temporal evolution, at least three time constants are necessary. However, for an adequate fit of the experimental data, we identify four subsequent relaxation steps of the broadband transient absorption data. The corresponding evolution associated difference spectra (EADS) are described below. Each intermediate state i ($i = 1 - 4$) contributes to the signal with a term $a_i(\lambda) \cdot e^{-t/\tau_i}$, wherein $a_i(\lambda)$ represents the spectral intensity of the probed transition amplitude and τ_i the respective decay constant of the associated state.

The ESA kinetic trace of H-Cou in ACN (see figure 15a) exhibits a fast rise in about 130 fs to its maximal value according to the cross correlation time of the pump and probe pulses, which is equal for all three molecules. Subsequently, the signal decreases with complex multi-exponential behaviour. We obtain time constants of $\tau_1 \approx 0.2$ ps, $\tau_2 \approx 4$ ps, $\tau_3 \approx 40$ ps, and $\tau_4 > 1$ ns from the fit (see table 3). The value of τ_1 is typical for the ultrafast solvation of coumarins from the Franck-Condon state to a "hot" excited singlet state in acetonitrile [169]. The following relaxation in the time τ_2 is indicative of vibrational cooling [174, 175]. The pronounced isosbestic point in figure 14 confirms the intramolecular transition of the relaxed excited singlet state population to a nearby triplet state via intersystem crossing represented by the second data set (TTA-scan) in figure 15a. The corresponding time-constant τ_3 for ISC represents the lifetime of the excited state S_1. Moreover, the first three time-constants include contributions of radiative decay, i.e. SE and fluorescence, and nonradiative decay such as IC. In order to keep our model simple, we desisted from introducing multiple parallel minor deactivation pathways.
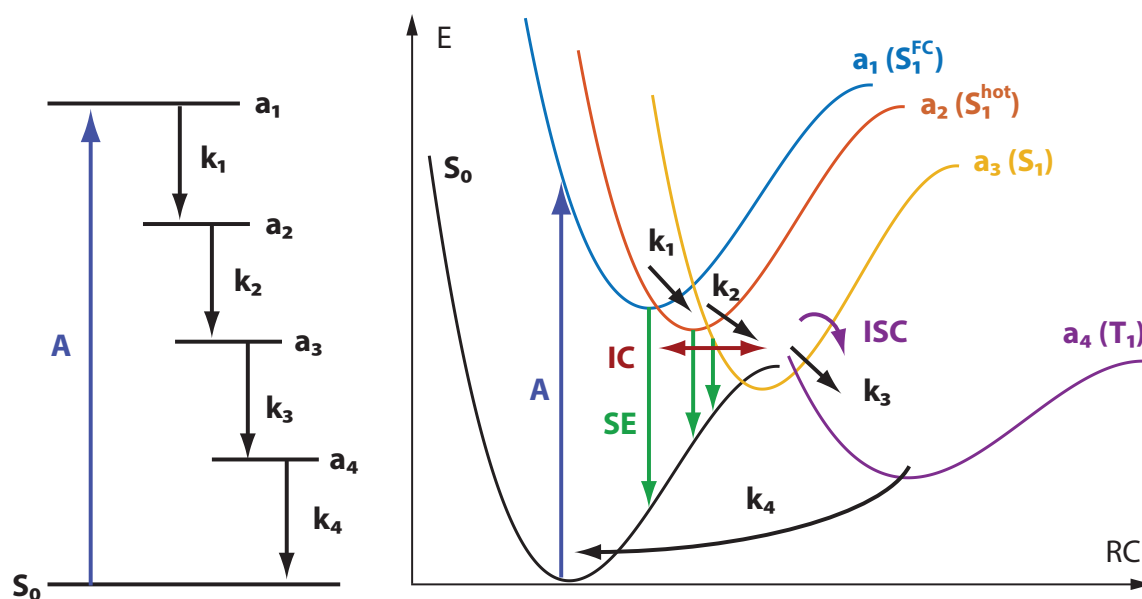
Figure 16 a) Sequential kinetic model and b) reaction scheme as energy diagram (E: potential energy, RC: reaction coordinate) according to the singlet-triplet relaxation of the three coumarin compounds after $S_0 \rightarrow S_1$-excitation. $k_i = 1/\tau_i$ $(i = 1 - 4)$ denote the corresponding decay rates for relaxation from the respective Franck-Condon state (a_1) over a hot S_1-state (a_2) to the relaxed S_1-state (a_3), and the following ISC to T_1 (a_4). k_1 - k_3 include nonradiative decay by internal conversion (IC) and radiative decay by stimulated emission (SE).

The TTA-scan drops in about 130 fs to a negative value, in correlation with the negative SE signal (see figure 14). The decrease is followed by a growth to positive values in agreement with the increase of the TTA peak at 465 nm in figure 14. The decay time of the excited triplet state (τ_4) exceeds our measurement range of 1 ns.

Substitution of Cl at the 6-position leads to a slowdown of the relaxation dynamics (figure 15b). While the fit shows only slightly enhanced values for solvation (τ_1 = 0.2 ps) and vibrational cooling (τ_2 = 7 ps) with respect to H-Cou, a much larger lifetime of $\tau_3 \approx$ 100 ps can be extracted. The dynamics including relaxation of the SE and increase of the TTA is also drastically slower. On the other hand, Br-Cou shows qualitatively analogue, however, even faster relaxation dynamics than H-Cou (figure 15c). Accordingly, the lifetime can be extracted to $\tau_3 \approx$ 24 ps, which is the shortest lifetime of the three coumarin derivatives. Values of τ_1 = 0.22 ps and τ_2 = 6 ps for the initial dynamics resemble again the values of H-Cou.

The slowest time constants τ_4 are all beyond our measurement range of 1 ns. All three compounds exhibit minor fluorescence quantum yields of equal to or less than 1% and S_1-lifetimes much shorter than the theoretical radiative lifetime $\tau_r = 1/k_r$ of coumarins (see equation 2.92), which is in the few nanosecond range [144]. This correlation is in agreement with formula 2.93. Taking into account the clearly pronounced TTA-spectra of the three compounds, this indicates large rates for ISC.

Evolution associated difference spectra (EADS) allow an analysis of the spectral dynamics [125]. The spectra of the transition amplitudes $a_i(\lambda)$ according to the respective global decay constants τ_i in ACN are extracted from the fit and depicted in figures 15d-f. The first three amplitude-spectra represent sequential intermediate states of the first excited singlet state S_1. Thus, a_1 represents the Franck-Condon state following the excitation by the pump pulse, which relaxes with constant τ_1 to a "hot" excited singlet state a_2. Subsequently, the signal decreases to the "relaxed" excited singlet state a_3 according to time constant τ_2. Figure 16b illustrates the reaction scheme of the sequential relaxation dynamics according to the applied rate equation model.

The unsubstituted compound H-Cou (see figure 15d) exhibits a decrease of the spectral intensity and a blueshift due to the energetically lowering of the initial state of the ESA within these first two relaxation steps. Additionally, the second step is accompanied by the observation of a decrease of the spectral width indicative of vibrational cooling. The first three Cl-Cou spectra also reveal a blueshift (see figure 15e), however the blue side of the spectra does not shift. Moreover, the intensities decrease more slowly. Br-Cou also shows a blueshift of the red edge of its spectra (see figure 15f). Here, the a_2-intensity is even stronger than a_1. The missing blueshift of the blue-edge of a_2- and a_3-EADS for the halogen-substituted compounds indicates the enhanced ISC-rate for the transition from S_1 to T_1. In H-Cou, a smaller fraction of the S_1-population undergoes this $S_1 \rightarrow T_1$ transition, and the remaining part shows a further relaxation within the singlet manifold. The negative amplitudes (EADS a_1 - a_3) below 500 nm can be attributed to transient SE. In agreement with fluorescence intensities (see figure 12) and lifetimes (see figure 15a-c), these spectra decrease faster in their absolute values for H-Cou and Br-Cou (see figure 15d and f) than for Cl-Cou (see figure 15e), where their intensities remain constant during the first two relaxation steps. Amplitude a_4 refers to the first excited triplet state T_1. These spectra resemble the TTA-transients beyond 100 ps (see figure 14a-c). The quotients of TTA-maxima over the respective ESA-maxima, i.e. in units of ΔOD, can serve as a relative measure for the triplet yields Φ_T. The determination of the absolute triplet quantum yields Φ_T from TA spectra would require the analysis (and observation) of a ground state bleaching [14]. We obtain TTA/ESA-quotients of 0.32 for H-Cou, 0.46 for Cl-Cou, and 0.77 for Br-Cou. Hence, the triplet yield increases for 6-substitution of a halogen, even more it increases with growing atomic number of the 6-substituted atom.

The lower panels of figure 15 show the kinetic traces for the first 80 ps and the corresponding EADS of Br-Cou in EOH (g,i) and CYH (h,j). The scans are fitted according to the same rate equation model as the kinetics measured in ACN. Kinetic analysis from earlier studies in organic molecules in ethanol attribute the first fast time constant in the femtosecond range to intramolecular vibrational redistribution, while the second time constant (in the 1-5 picosecond range) represents combinations of vibrational cooling, solvation and the formation of hydrogen bonds [175, 169]. Because our extracted first two time constants are in these time ranges, we

follow this interpretation. Furthermore, from a comparison of the kinetics and EADS of Br-Cou in EOH (figure 15g and i) with the same compound measured in ACN (figure 15c and f), some more differences can be obtained. Stimulated emission has almost vanished, however, the S_1-lifetime is slightly enhanced to 28 ps. The strong increase of the TTA-scan (see figure 15g) as well as the enhancement of the 440-nm- and 465-nm-maxima of a_4 confirm the observation from the transient spectra (see figure 14f) of an enhanced triplet yield in EOH. The TTA/ESA-quotient is even larger than 1. This indicates that the deactivation rate through the triplet state is favoured with respect to singlet relaxation. The analysis of the CYH-scans reveals larger differences to the ACN and EOH data. Only the ESA kinetics resembles the dynamics of Br-Cou in EOH and ACN (see figure 15j). Early dynamics in CYH up to the few picosecond range is reported to be similar, but faster, than in EOH [169]. Moreover, CYH is aprotic. Hence, we can refer τ_1 to intramolecular vibrational redistribution, and τ_2 to a combination of vibrational relaxation and solvation. Concerning the TTA-scans, the kinetic trace deviates from the measurements in EOH and ACN. It exhibits a fast increase in less than 5 ps to a comparably small maximum value. No indication of SE is observable. The corresponding TTA-spectrum (a_4, figure 15j) reveals a large overlap with the ESA band. The spectrum of a_4 shows a broad band centred at 600 nm. In contrast to the respective spectra in ACN and EOH, the a_4-values below 500 nm are very low and no significant indication of pronounced TTA-peaks are observed. Hence, the TTA/ESA-quotient in CYH is the lowest of the examined samples. Analogue to the fluorescence quantum yield of close to zero, a strongly reduced S_1-lifetime of 16 ps can be obtained from the fit on the CYH-data, which is shorter than the respective lifetimes of Br-Cou in EOH and ACN. These observations can be explained by an enhanced rate for internal conversion [144, 145]. Hence, the rate of nonradiative decay, $k_{nr} = k_{IC} + k_{ISC}$ decreases with increasing solvent polarity. Moreover, k_{IC} is much greater than k_{ISC} in nonpolar solvents [145], resulting in the low triplet yield, even in the Br-compound, and a reduced slowest time constant τ_4. All time constants and TTA/ESA-quotients, which serve as a relative measure for the triplet yields are summarised in table 3.

X(X-Cou)	H (ACN)	Cl (ACN)	Br (ACN)	H (EOH)	Cl (EOH)	Br (EOH)	Br (CYH)
τ_1 (ps)	0.22	0.23	0.34	0.10	0.10	0.10	0.28
τ_2 (ps)	4.3	6.6	5.6	6.3	5.7	2.9	2.0
τ_3 (ps)	39	103	24	68	160	28	16
τ_4 (ps)	>3000	>3000	>3000	>3000	2800	1400	510
Φ_T (rel.)	0.34	0.48	0.77	0.66	0.80	1.2	0.26

Table 3 Extracted fit parameters from global analysis: time constants τ_i, i = 1-4, and TTA/ESA-quotients Φ_T (rel.), which serve as a relative measure for Φ_T, of samples H-Cou, Cl-Cou and Br-Cou in ACN, EOH and CYH. τ_1, τ_2: solvation and vibrational relaxation (solvent dependent), τ_3: S_1-lifetime, τ_4: T_1-lifetime.

4.4. DFT calculations

The geometry of ground and excited state of the examined coumarin derivatives in ACN were calculated by Dr. Petko Petkov with the Gaussian09 suite [176] by means of density functional theory (DFT) and time-dependent DFT (TDDFT) [177, 178, 179], respectively. Results are published in RSC Advances [129]. (TD)DFT allows to compute the electronic structure of many-body systems such as molecules and their time-dependent response to an external potential such as an electromagnetic field by means of functionals of the electron density of the system. For our simulations the triple-ζ basis set 6-311+G(d,p) including polarisation and diffuse functions was employed and coupled to the hybrid range-separated exchange-correlation energy functional CAM-B3LYP as implemented in Gaussian09. This functional combines short-range and long-range orbital-orbital interactions using Hartree-Fock and Becke 1998 exchange integrals [180]. Earlier TDDFT simulations of charge transfer states of coumarins in different polar solvents achieved highly reliable results with this functional [181, 151]. Furthermore, the TDDFT formalism enabled the calculation of dipole moments and the respective vertical transition energies between the optimised geometrical structures of ground and excited state. The polarisable continuum model (PCM), also implemented in the Gaussian09 software, was applied for computing the interaction of the solute molecules with the solvent, which is considered as a homogeneous dielectric medium. Therein, a solute molecule causes a polarisation of the solvent [182, 183, 181].

	$\lambda_{\mathrm{abs}}^{\mathrm{sc}}$ (nm)	f (calc.)	$\mu(S_0)$ (D)	$\mu(S_1)$ (D)	$\Delta\mu$ (D)
H-Cou	324	0.305	5.10	7.10	+2.0
Cl-Cou	334	0.223	2.72	6.84	+4.12
Br-Cou	335	0.213	2.68	7.33	+4.65

Table 4 Results from (TD)DFT calculations: absorption maxima $\lambda_{\mathrm{abs}}^{\mathrm{sc}}$ scaled by a factor of 1.125, oscillator strengths f and ground state dipole moments $\mu(S_0)$ upon vertical $S_0 \rightarrow S_1$ excitation of samples H-Cou, Cl-Cou and Br-Cou in ACN. Excited state dipole moments $\mu(S_1)$ and changes of dipole moment $\Delta\mu$ are calculated with respect to the energy minimum of S_1.

Table 4 provides an overview of the DFT and TDDFT results. A typical scaling factor of 1.125 was determined from the ratio of experimental and vertical $S_0 \rightarrow S_1$ excitation energies of H-Cou and applied for computation of the respective absorption maxima of Cl-Cou and Br-Cou. The calculated and scaled absorption wavelengths match the respective experimentally measured values (see table 2) almost perfectly.

Figure 17 depicts the calculated HOMO and LUMO orbitals of the three studied compounds. Hereby, the LUMO represents the respective energy minimum of the (relaxed) first excited state S_1. The corresponding lowest excitation energies can be assigned primarily (94%) to a HOMO

$\rightarrow$ LUMO transition. The remaining 6% (of transition probability) can be attributed to higher energy transitions between orbitals contributing to the first absorption band such as HOMO-1 $\rightarrow$ LUMO or HOMO $\rightarrow$ LUMO+1 transitions.

LUMO

H-Cou   Cl-Cou   Br-Cou
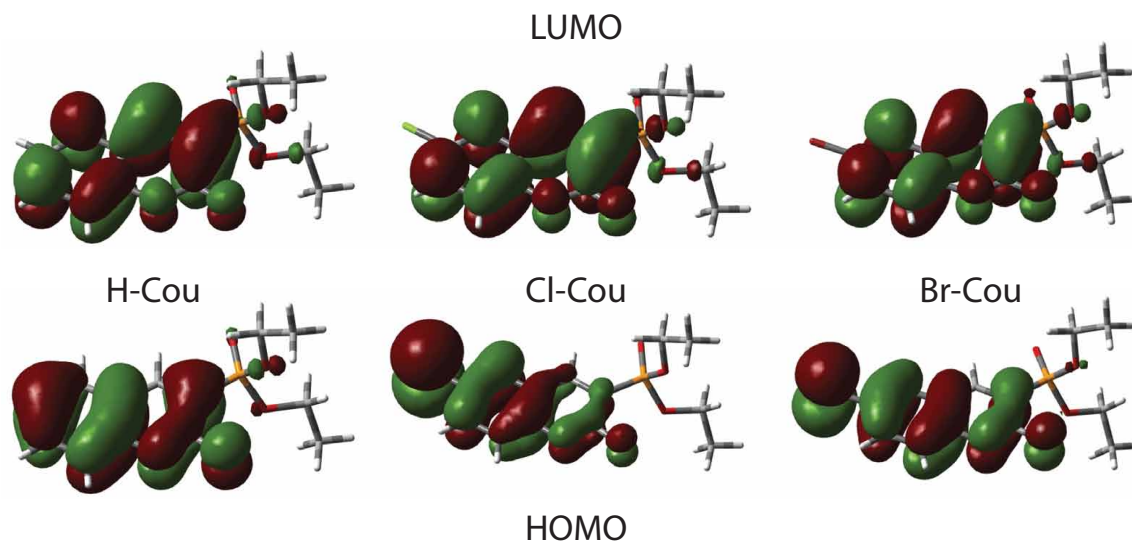
HOMO

Figure 17 HOMO and LUMO orbitals of H-Cou, Cl-Cou and Br-Cou (adapted from [129]).

The three simulated LUMO geometries show a high conformity (figure 17). The electron density is delocalised over the whole coumarin moiety indicating a significant contribution of π^*-orbitals. Only minor occupation of the orbitals located on the 3-substituted diethylphosphono group is observed. In contrast to the LUMO, the orbitals contributing to the HOMO reveal explicit differences between the unsubstituted and the two halogen-substituted molecules. H-Cou exhibits a uniformly delocalised electron density on the whole coumarin moiety corresponding to a HOMO $\rightarrow$ LUMO transition of mainly $\pi \rightarrow \pi^*$-character. The diethylphosphono group again exhibits only a very low fraction of total electron density. In the Cl-Cou and Br-Cou HOMO formations, the respective diethylphosphono groups are nearly free of charges. In contrast, part of the electron density is shifted towards the halogen lone pair orbitals, which are normal to the molecular plane, due to the inductive effect. The latter is stronger for Cl than for Br corresponding to the larger electronegativity of Cl. The participation of halogen lone pairs is reflected in the calculated oscillator strengths for vertical excitation, which are reduced by almost 30% for the halogenated coumarins (see table 4). The calculated values extend the estimated oscillator strengths determined from the molar absorption coefficients by a factor of about 4, not untypically of TDDFT results, yet reflect their descending order (see table 1) in good agreement. The different respective electron distribution of the HOMO further causes decreased ground state dipole moments of Cl-Cou (μ = 2.72 D) and Br-Cou (μ = 2.68 D) with respect to H-Cou (μ = 5.10 D) (see table 4). In agreement with the nearly uniform LUMO geometry (figure 17), the respective dipole moments of excited state energy minima of the three compounds are in the same range of close to 7 D (see table 4). Thus, the calculated change of the dipole moment ($\Delta\mu$) for the HOMO $\rightarrow$ LUMO transition increases by a factor of approximately 2 for the halogenated

compounds with respect to the unsubstituted molecule H-Cou. Furthermore, the absorption from first to second triplet state, which was calculated to exhibit scaled wavelengths of 444 nm (H-Cou), 447 nm (Cl-Cou), and 448 nm (Br-Cou), matches the lower energy TTA-peak in the TA data very well.

4.5. Discussion

Summarising the results described in the previous sections, the experimental analysis of the influence of 6-substitution of 3-diethylphosphonocoumarins with Cl and Br exhibits three superimposing effects. Most impressive is the observation of clearly enhanced values of lifetimes for the Cl-compound (see table 3, section 4.3). Taking into account the steady-state results (see table 1, section 4.2), a qualitative comparison of the lifetimes with the fluorescence quantum yields in ACN reveals a strong correlation, and thus manifests itself in an anomaly of the HAE. On the other hand, the triplet yields grow according to the atomic number of the 6-substituted atom, reflecting exactly the heavy-atom effect (see section 2.3.5). Moreover, molar absorption coefficients and the respective oscillator strengths in ACN decrease going from H-Cou over Cl-Cou to Br-Cou. DFT and TDDFT calculations carried out in ACN provide an explanation for this unusual behaviour (see section 4.4). While in the LUMO all three compounds show very similar π^*-like geometries, the simulated HOMO geometries exhibit differences between the unsubstituted and the halogen-substituted compounds. The electron-withdrawing inductive effect of the halogens leads to an occupation of their lone pair orbitals in the formation of the HOMO and causes a redshift of absorption and fluorescence spectra (see section 4.2). The participation of the halogen lone pairs reduces the oscillator strengths calculated for vertical excitation in agreement with our respective experimentally determined parameters and earlier studies on 6-substituted coumarin [184].

In order to explain the increase in fluorescence quantum yield and lifetime for the Cl-compound, the LUMO geometry has to be considered. In the LUMO, the nonbonding orbitals are not occupied. Accordingly, optical excitation causes a partial intramolecular charge transfer from the halogen lone pair orbitals in Cl-Cou and Br-Cou to their respective π^*-orbitals of the LUMO. Hence, the change of dipole moment $\Delta\mu$ between HOMO and LUMO doubles with respect to H-Cou. In coumarins, intramolecular charge transfer processes are often observed [151, 152, 185]. Earlier studies show a conjunction of intramolecular charge transfer with large $\Delta\mu$ for HOMO $\rightarrow$ LUMO transitions associated with large experimentally determined fluorescence quantum yields [185, 186]. For Cl-substitution, this is reflected in the enhanced fluorescence quantum yield. However, the HAE quenches the fluorescence due to the increase of the ISC-rate. For Br-6-substitution in the 3-diethylphosphonocoumarin, the influence of the HAE is stronger than for Cl or H at the 6-position, leading to a decrease of fluorescence quantum yield and lifetimes for Br-Cou.

In all three compounds, the diethylphosphono group presumably does not have any significant influence to the photophysical properties due to its minor orbital occupation in both HOMO and LUMO. This is in contrast to earlier studies by M. Wagner et al. on 7-Et$_2$N-substituted 3-diethylphosphonocoumarins, where the diethylphosphono group plays a significant role in the $7 \rightarrow 3$ charge transfer upon excitation [151]. This strong charge transfer character of the HOMO $\rightarrow$ LUMO transition is additionally strengthened by the formation of hydrogen bonds with the solvent molecules. The difference can be explained by the enhanced 3-7-conjugation, which favours charge transfer states. This is not the case for 3- and 6-position, as in our molecules.

Measurements in additional solvents reveal differences in lifetimes and triplet yields, which are of the same order of magnitude as for changing the 6-substituted atom. The first two decay constants describe solvent specific different contributions to ultrafast processes such as solvation, vibrational relaxation and redistribution as discussed in section 4.3. In ethanol, S_1-lifetimes and triplet yields are enhanced up to 1.6-fold (see table 3), thus, in a typical range for changing the solvent. The origin for these differences, and furthermore, the observation of no significant spectral shifts in steady-state absorption and fluorescence spectra, can presumably be explained with similar considerations as above. Unravelling the exact molecular origins would, however, require further TDDFT calculations. All three coumarin compounds exhibit minor fluorescence quantum yields in correlation with small S_1-lifetimes and significant triplet yields both in ACN and in EOH (see sections 4.3 and 4.2). This suggests a high rate of nonradiative decay with large contributions of ISC in polar solvents. On the other hand, strongly reduced values for S_1-lifetime, triplet yield and slowest time constant in nonpolar CYH are caused by an enhanced rate of internal conversion, typical for nonpolar solvents as reported by J. Seixas de Melo et al. [144, 145].

The sequential kinetic model, which is constructed to fit the transient absorption, is combined with the spectroscopic information into a full relaxation model, which is depicted in figure 16b, summarising the above discussed results. Upon excitation by the pump pulse, the molecule exhibits solvent specific nonradiative relaxation within the first excited singlet state represented by the decay rates k_1 and k_2. Because stimulated emission is observable from time zero on, it additionally contributes to the first two decay rates. The following decay k_3 from the relaxed state S_1 represents the rate for intersystem crossing and includes varying contributions from radiative relaxation such as stimulated emission and fluorescence, and nonradiative decay according to internal conversion. The respective contributions vary for different 6-substitutions and solvents as explained before. Relaxation from the triplet state occurs according to decay rate k_4.

4.6. Conclusion and outlook

Broadband transient absorption spectroscopy in combination with conventional absorption and fluorescence spectroscopy and TDDFT calculations was performed to disentangle the complex interplay between different intramolecular processes, which resulted in an anomalous heavy atom effect. We show that 6-substitution with the halogens Cl and Br of 3-diethylphosphonocoumarins allows fine-tuning of the photophysical parameters S_1-lifetime and intersystem crossing rate, and thus, fluorescence and triplet quantum yields. Taking into account the results from different solvents, the lifetime of 6-substituted 3-diethylphosphonocoumarins can be varied between 16 ps (Br-Cou in CYH) and 160 ps (Cl-Cou in EOH), whereas the triplet yield exhibits an almost five-fold enhancement going from Br-Cou in CYH to EOH. 6-substitution with F or I might lead to an even further increase of the triplet yield. Additional experiments on halogenated coumarin-3-phosphonic acid qualitatively confirm the results resulting in a similar distribution of lifetimes and triplet yields [163]. Accordingly, applications of coumarins in pharmaceutical chemistry and medical sciences, which are based on triplet-mediated processes, can be improved by 6-substitution of halogens. Normal HAE behaviour of 6-substituted coumarin derivatives was already shown in earlier studies [111, 187]. The special case of HAE-anomaly, which comes along with substitution of Cl in the 3-diethylphosphonocoumarins, can be of advantage, if both a large triplet yield and a sufficient fluorescence quantum yield are required. It allows examination of a triplet mediated reaction with a fluorescence microscope, for instance. Because coumarins are a crucial component of many pharmaceutical substances, the ability of controlling triplet yields and fluorescence quantum yields is of great interest for the research on and the structural design of new drugs. Moreover, these parameters can be determined fast and easily with a combination of conventional steady-state spectrometers and state-of-the-art pump-probe setups, as can be found in modern labs of most research institutes dealing with molecular physics or chemistry.

5. Transient absorption spectroscopy of the phototransformation of chromone compounds

5.1. Introduction and statement of contributions

Almost 100 years ago Fritz Weigert observed the effect of an irreversible photoinduced dichroism and colour changes when irradiating molecules in collodion with polarized monochromatic light [188, 189]. Many years later, this was pursued in the field of optical information recording and processing [190]. Molecules of the chromone class are promising photo-sensitive centres for WORM-type (write once read many) archive memory when embedded into a polymeric matrix [191, 192]. Upon excitation with light in the ultraviolet spectral range, 2-furyl-3-acetylchromones perform an irreversible photochemical transformation, causing a shift of the absorption spectrum from the ultraviolet to the visible range [193, 194]. Although the close similarity, the irreversible photochemical transformation of these molecules does strictly speaking not represent photochromism, which implicates a reversible transformation according to the definition of the International Union of Pure and Applied Chemistry (IUPAC) [195]. While the initial isomer of the molecule is non-fluorescent, the fluorescence of the stable photoisomer is used for information readout following excitation in the visible range. Recording is achieved by irradiating the molecule in its initial form with ultraviolet light. Compared to single-photon recording, two-photon recording with a visible laser pulse in the nanosecond to femtosecond range allows better spatial resolution and localization due to the contraction of nonlinear interaction in the tight focus [196], which is also the basis of two-photon excitation microscopy.

The measurements discussed in the following are part of a collaboration with the group of Dr. Sergey Gagarskiy at the Department of Laser Technologies and Bio-Medicine Optics at ITMO University in St. Petersburg, Russia. Research in this project aims at the development of materials and systems for optical information recording and storage [191, 192]. Possible applications are multilayer fluorescent discs (US Patent by V. Kiyko [197]), which can consist of several hundred information layers [198, 196]. In the course of experiments on 2-furyl-3-acetylchromones by the Gagarskiy group, fluorescence quantum yields measured on samples which were recorded using two-photon absorption revealed to be much lower compared to those on single-photon recorded samples. Furthermore, earlier investigations on the threshold for nonlinear recording showed a strong increase of recording power density threshold, when reducing the excitation pulse duration from a few nanoseconds to 120 fs [199]. However, for pulses below 100 fs, quantitative transformation of molecules was not

achieved. Analogue observations in photochromic diarylethene compounds have been linked with a two-step sequential excitation mechanism [200, 201]. Thus, time-resolved examinations of the chromone compounds became necessary to understand the complex dynamics of the phototransformation of 2-furyl-3-acetylchromones and their technically relevant derivatives.

Broadband transient absorption spectroscopy was performed on a thiophene containing 2-furyl-3-acetylchromone in toluene. In this chapter, examinations of the ultrafast irreversible photo-transformation of the chromone compound LHC480 are discussed. First, the absorption and fluorescence spectra of the initial and the transformed form are presented. Further, the transient spectra are shown and insight in the temporal evolution of the excited state dynamics is given, followed by a summarizing discussion of the molecular processes including the identification of a predicted short-lived intermediate state during the phototransformation. Broadband transient absorption spectroscopy and data analysis were conducted by the author. Christian Brunner assisted with fitting the data. Steady-state absorption and fluorescence measurements were performed in collaboration with Pascal Scigalla in the course of his Bachelor's thesis [202], while the samples were synthesized at the Russian Academy of Sciences [194] and selected and provided by our collaborators. Interpretations were discussed in cooperation with Dr. Sergey Gagarskiy, PD Dr. Hristo Iglev, Yana Fomicheva, Dr. Andrey Sergeev, Dr. Anton Ayt and the author. Results were published in the Russian Journal "Optika i Spektroskopiya", 2018, Vol. 125, 4, pp. 463-467 (English version online in "Optics and Spectroscopy" [203]) and presented at the 18th International Conference on Laser Optics (ICLO 2018) [204]. These publications comprise the steady state and transient results as presented in figures 18, 20, and 23, and the corresponding discussions and conclusions. Here, further details are given and discussed, in particular, results in connection with figures 19 and 21.

5.2. Optical properties of LHC480

Figure 18a shows the above mentioned irreversible photochemical transformation of the examined chromone compound. The chemical structure of 2-(furan-2-yl)-3-(thiophene-2-carbonyl)-chromen-4-one (LHC480) in its original form is depicted in figure 18a, structure A. UV radiation in the range between 250 nm and 350 nm initiates a ring-opening reaction in the furan ring. This short-lived intermediate state (see figure 18a, structure B) has been proposed earlier [193, 194], however verification of its importance for the phototransformation and information on its lifetime are still lacking. Finally, finishing the phototransformation, a new furan ring is formed between the chromone moiety and the thiophen group, resulting in the stable photoproduct (see figure 18a, structure C).

The corresponding absorption and fluorescence spectra in toluene solution are presented in figure 18b recorded with a commercial absorption spectrometer (Lambda 19, Perkin-Elmer)
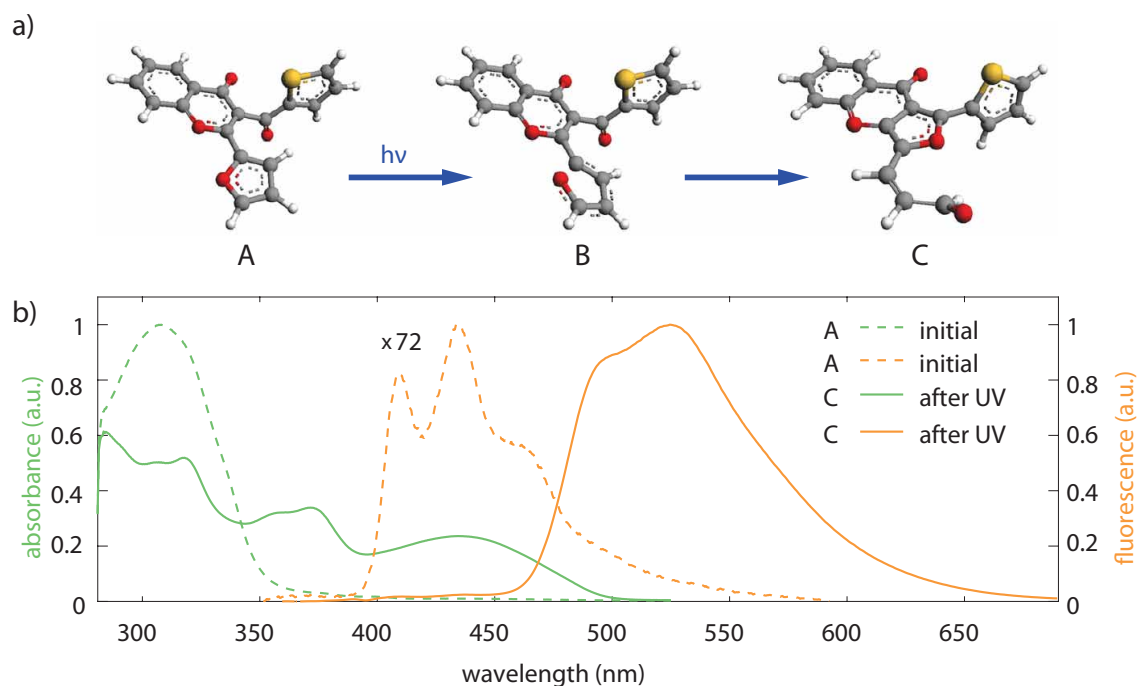
Figure 18 a) Photochemical transformation of LHC480. Chemical structure of the initial form A, the short-lived intermediate state B and the final form C (adapted from [203]). b) Absorption spectra of the initial (green, dashed line) and the final form (green, solid line) normalized to the absorption maximum of the initial form. Fluorescence spectrum of the initial (magnification 72x, orange, dashed line) and the final form (orange, solid line). LHC480 is dissolved in toluene at a concentration of 50 μmol/l. The final isomer was obtained after 6 h irradiation of the sample with 312 nm.

and a spectrofluorometer (FP-6500, Jasco). The initial isomer is characterized by a single absorption band in the spectral range beyond 280 nm with a maximum at 308 nm. Irradiation with UV light (UV lamp, Bioblock Scientific, Model VL6MC, 6 W) at a wavelength of 312 nm gives rise to a change and a redshift of the absorption spectrum due to the transformation of a part of the dissolved molecules. The new spectrum exhibits three absorption bands, whereas the energetically lowest maximum is located at 436 nm. The optical density of this band saturates after six hours of irradiation, which corresponds to 10.3 J/cm^2 of total UV irradiation [202]. The observed change of the absorption spectrum is typical for this kind of transformation including a ring-closure process [193, 194]. The initial isomer shows very weak fluorescence (magnified by a factor of 72 in figure 18b) upon excitation at 308 nm with a maximum at 434 nm and a fluorescence quantum yield far below 1 % and is usually referred to as "non-fluorescent" [203, 194]. In contrast, the photoproduct's fluorescence quantum yield can be estimated to 24 % in toluene solution [192]. This bright fluorescence with a red-shifted maximum at 525 nm allows easy detection without any perturbation by the weak photoluminescence of the molecules in their original form. Hence, optimal excitation wavelengths for the information recording, i.e. initiating a phototransformation, and the reading process can be extracted from the steady-state spectra. However, no information about the intermediate state is obtainable. Therefore, the excited state dynamics of the molecule upon initiating a phototransformation is studied with

transient absorption spectroscopy.

5.3. Transient spectra and temporal evolution of the phototransformation

The pump-probe setup described in chapter 3.2 was used for the measurements on the compound LHC480 dissolved in toluene. The excitation pulse was provided by the frequency-doubled output of the NOPA and was set to 320 nm, close to the absorption maximum of the molecule in its initial form. The supercontinuum generated by the 1250 nm output of the TOPAS allowed probing the pre-excited sample over a super-octave spectral range from below 430 nm up to 950 nm. For a rotation free signal, the polarizations of pump and probe pulses were aligned to 54.7°, i.e. magic angle configuration. In order to enhance the signal quality and ensure reproducibility, we measured three data series at different spots in the same cuvette (cf. section 4.3). One measurement was carried out over the whole 500 ps range, and two only up to 100 ps pump-probe delay, (in order to keep the irradiation time of the molecules as short as possible). The presented data is the mean of these three measurement series. Data analysis was performed according to section 3.4. In order to compensate for an overall low signal to noise ratio beyond pump-probe delays of 4 ps, the transient data is smoothed over seven data points spectrally and three subsequent data points on the time axis.
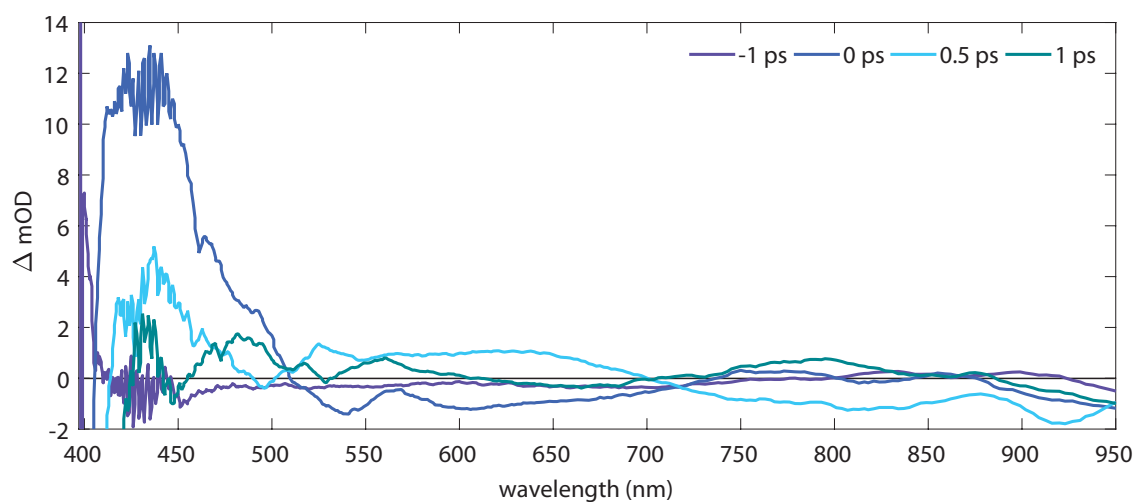
Figure 19 Chirp corrected transient absorption spectra of pure toluene for time delays from -1 to 1 ps plotted over the whole examined spectral range. The instantaneous rise of a strong signal in the spectral range below 500 nm can be assigned to a coherent artifact. For delay times longer than 1 ps the solvent does not contribute to any further absorbance changes.

The pure solvent was measured under the same conditions as the solution. The resulting change of optical density was subtracted from the results of the sample solution in order to exclude solvent contributions. In figure 19, the transient spectra of toluene are depicted for pump-probe time-delays up to 1 ps. The instantaneous rise of the signal up to 12 mOD and

following decay close to zero in the wavelength range between 400 nm and 500 nm can be attributed to a coherent artifact mainly caused by the cross-phase modulation between pump and probe pulses (see section 3.3). For probe wavelengths beyond 500 nm no further signals from the solvent or coherent artifacts were detected.
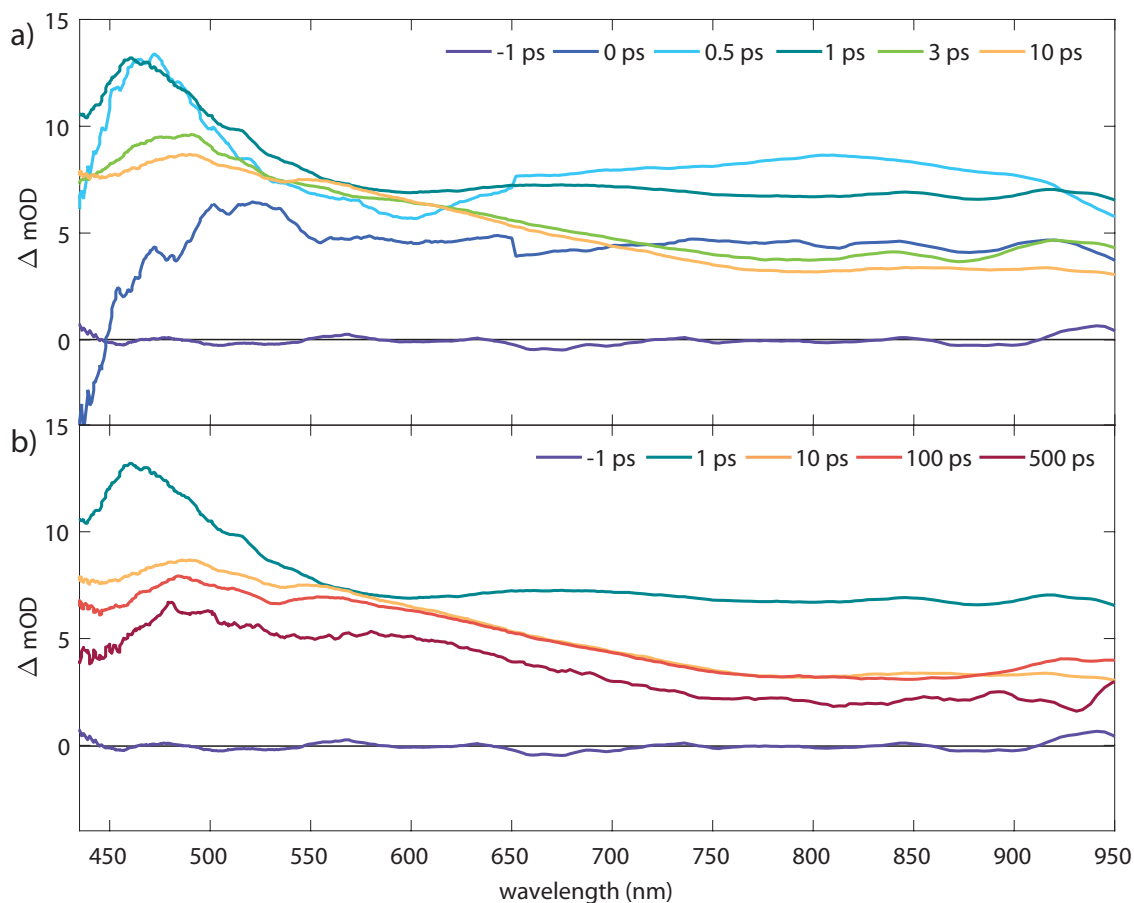
Figure 20 a) Transient absorption spectra of LHC480 for time delays from -1 ps to 10 ps following excitation at 320 nm. For the measurement 1 mol/l LHC480 was dissolved in toluene. b) Transient spectra of LHC480 for longer time delays up to 500 ps. All spectra are smoothed and chirp corrected. Solvent contribution is subtracted.

Transient spectra of LHC480 for pump-probe time delays from -1 ps up to 500 ps are shown over a wavelength range from 430 nm to 950 nm in figure 20. Again, negative times denote the probe pulse arriving before the pump pulse on the sample (cf. section 4.3). Earlier studies report that ring-opening and ring-closure processes occur on a timescale much shorter than our detection range of 500 ps [200, 205]. Thus, the measured transient spectra consist of a superposition of the signals originated from the different species which are involved in the phototransformation. In the following, the temporal evolution of these superimposed spectra is described. Straightforwardly, two excited state absorption (ESA) bands revealing ultrafast dynamics are observed in figure 20a, an intense band ranging from 430 nm to 550 nm (ESA1) and a second broad band from 650 nm up to the low-frequency detection limit of the transient spectrometer (ESA2). This kind of broad ESA is typical for molecules with large functional

groups as already observed in chapter 4.3. The negative signal on the blue side of the spectrum for a pump-probe delay of 0 ps can be attributed to an overestimation of the solvent contribution. After 0.5 ps, ESA has saturated giving rise to the characteristic spectrum with the two bands.

Subsequently, ESA2 decreases to less than half of its maximum signal strength within the first 3 ps. The relaxation of ESA1, however, seems to be significantly slower. Between 1 ps and 3 ps its maximum decreases from 13 mOD to 10 mOD combined with a slight redshift from 465 nm to 480 nm. Subsequently, the two bands merge into one single broad band with a pump-induced absorption maximum at 490 nm, which redshifts slightly within the following 100 ps (see figure 20b). The following slow decay evolves without any further pronounced spectral shifts within our detection limit. The fact that the two ESA maxima constitute a different relaxation dynamics indicates contributions to their signals from different states.
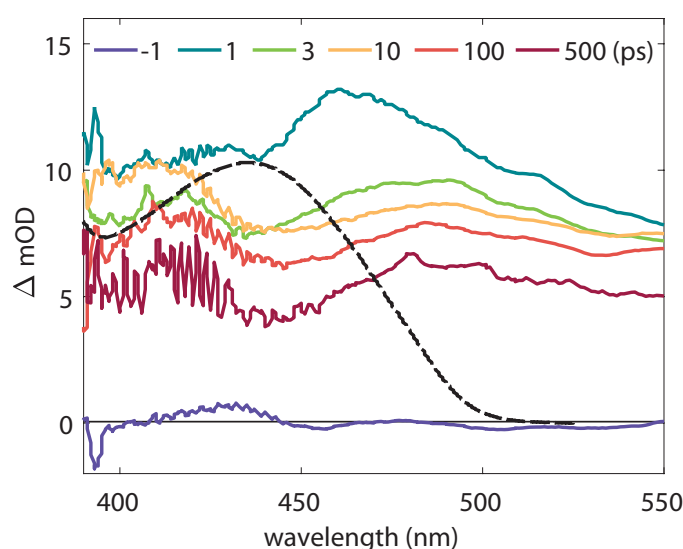
Figure 21 Transient spectra of LHC480 for the spectral range from 390 nm to 550 nm. The black dashed line represents the (magnified) absorption spectrum of the photoproduct upon irradiation at 312 nm. All spectra are smoothed and chirp corrected.

Below 430 nm, the intensity of the supercontinuum probe is very weak, which leads to low signal-to-noise ratios, as seen in the transient spectrum of 500 ps (see figure 21). Another issue results from the strong nonlinear response of the solvent (see figure 19). Although the solvent contribution is subtracted, the transient spectra for time delays up to 1 ps in this spectral range could be distorted by the large signal of toluene and are therefore not shown here. Nonetheless, focussing on the 3 ps-spectrum, a distinct absorption maximum can be located at around 415 nm (see figure 21). Increasing the time delay to 10 ps, this maximum grows by almost 2 mOD. We assume that the observed dynamics of the 415 nm-maximum stems from the absorption of transformed molecules, which, however, is superimposed with the neighbouring ESA1 similarly as shown in studies on photochromic molecules by Wilcken et al. [206]. For comparison, the steady state absorption spectrum of the photoproduct of the LHC480 transformation (see figure 18b) is added to the figure. Note, that the transient spectrum of the photoproduct does

not necessarily match the steady-state spectrum, but can be blueshifted instead. From 10 ps to 100 ps and 500 ps, the intensity of the transient photoproduct absorption decreases due to the reduction of the ESA1 background. Further relaxation would be expected to cause a spectral redshift, hence resulting in a better match with the steady state spectrum, which arises from the saturated absorption of transformed and fully relaxed molecules (see section 5.2). Additionally, the fluorescence generated by stimulated emission (SE) is expected to cause a reduction of the transient ESA intensity in the spectral range covering the fluorescence spectrum of the final form C (see figure 18b). However the uniform spectral relaxation of the ESA band beyond 4 ps does not show any clear features which could be attributed to SE. A possible explanation would be that the phototransformation evolves over triplet states as assumed elsewhere [193], thus, quenching fluorescence during the transformation.
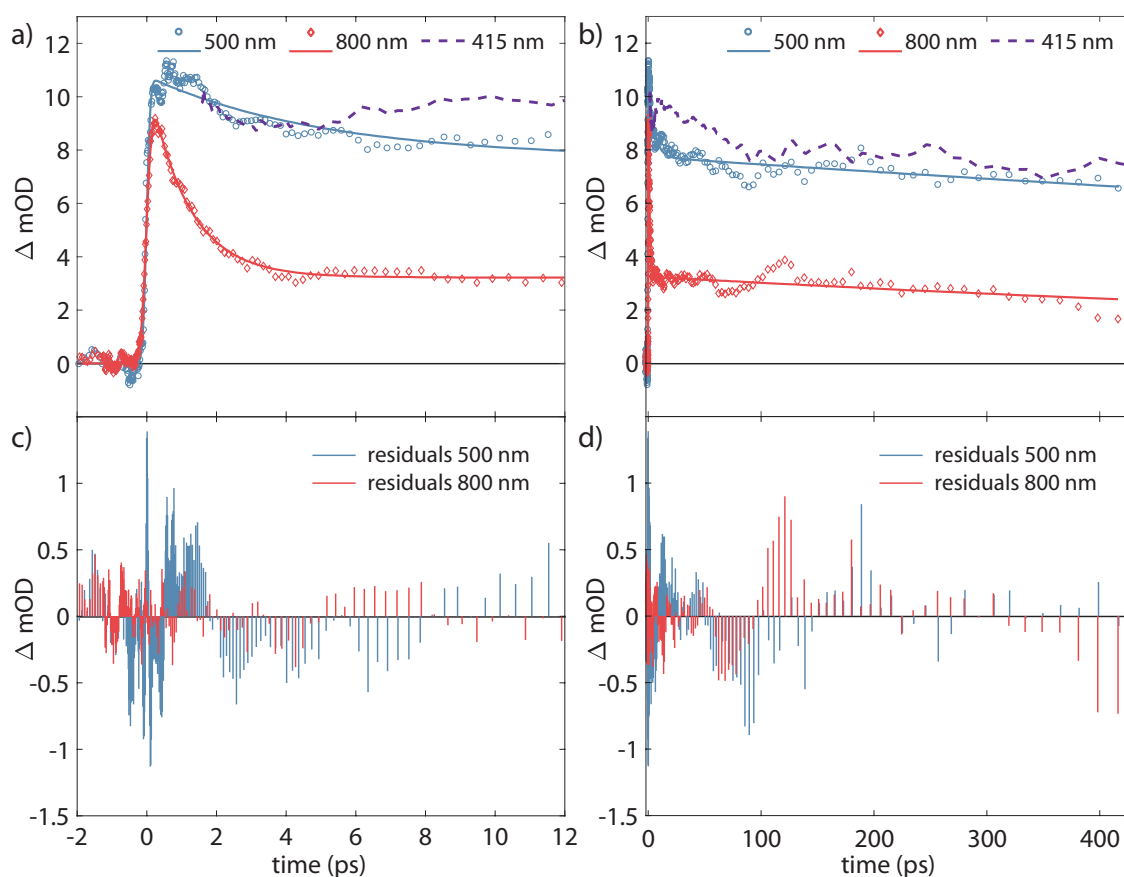
Figure 22 Temporal evolution of the excited state dynamics for selected kinetic data curves at 415 nm (violet, dashed line), 500 nm (blue) and 800 nm (red). Red and blue symbols denote measured data points, solid lines represent a fit according to a rate equation model with two decay constants τ_1 and τ_2. Vertical lines in c) and d) indicate the residuals given by the fit. The data curve at 415 nm, likely caused by the transient absorption of transformed molecules, is only given for time delays > 1 ps due to signal distortions by the solvent for shorter times. a), c) Time delay from -2 ps to 12 ps. b), d) Time delay from -2 ps to 430 ps. The time traces are smoothed over 7 and 3 data points spectrally and temporally, respectively.

Figure 22 shows the temporal evolution of the change of the optical density at two selected wavelengths representing the two ESA maxima at 500 nm and 800 nm. Excitation with the

pump-pulse causes a fast rise of both curves within the first 250 fs, which is followed by a bi-exponential decay. The kinetic data is fitted according to a simple rate-equation model (see section 3.4) with two local time constants τ_1 and τ_2, which describe the decay of the kinetic traces. Following the scan at 800 nm in figure 22a, we can see a fast decay from a maximum amplitude of 9 mOD to a value of less than 4 mOD within the first 4 ps. The fit matches the data well as indicated by the low residuals (see figure 22c). We extract a first time constant $\tau_1^{800} \approx 1.1$ ps from the fit on the 800 nm-kinetics. Remarkably, the 500 nm-scan is not only characterised by a higher maximal intensity of 11 mOD, but also exhibits a slower relaxation dynamics. This is in agreement with the observations in the transient spectra (see figure 20a). For the first picosecond, the time-trace deviates significantly from exponential decay due to its origin in the transient superposition of different states. The large residuals for this time range reflect this behaviour (see figure 22c). Then, after 2 ps, the time-scan decreases exponentially. The large residuals in the time-range beyond 100 ps (see figure 22d) can be attributed to the fact that the curves here are the result of one measurement, whereas up to 100 ps the spectra are averaged as mentioned earlier. Our simple fitting model does not reflect the exact evolution of the 500 nm-scan, however indicates an averaged first time constant of $\tau_1^{500} \approx 5$ ps. (This finding is yet sufficient for demonstrating a difference in the temporal evolution of ESA1 compared to ESA2.) A better matching fit would require including more than two time constants. However, due to the low signal to noise ratio, it is recommendable to use a model which is as simple as possible. Note that the depicted data is strongly smoothed.

In figure 22b, the temporal evolution is plotted for the total measurement range from -2 ps up to 430 ps. After 50 ps both the 800 nm and the 500 nm-scan relax with a similar time constant. Restricted by the measurement range of 500 ps, we can only estimate this second time constant τ_2 to be larger than about 1.5 ns in both curves. This time constant can be attributed to the lifetime of the first excited state of the molecule. Additionally, we fitted the kinetic traces of 600 nm, 650 nm, 700 nm and 750 nm at the blue side of the broad ESA2. Their decay constants are in agreement with the results from the 800 nm curve (see table 5), with the exception of a slight increase with decreasing wavelength. This can be attributed to the non-negligible overlap with ESA1 at wavelengths below 700 nm.

Furthermore, the transient absorption at 415 nm is added to figures 22a and b for time delays beyond 1 ps. Since we observe a strong solvent contribution below 1 ps, we abandoned to fit this data curve. From 1 ps to 4 ps, the 415 nm-kinetics is almost identical with the 500 nm-curve, hence, originating from the same excited state (see figure 22a). However, after 4 ps its intensity increases by about 1.5 mOD and remains constant for further 6 to 8 ps, presumably due to absorption of molecules which have already (partly) transformed to the form C (see figure 18a). The subsequent slower relaxation resembles the decay of the two ESA bands (see figure 22b). As the photoproduct's absorption superimposes the signal from ESA1, the measured curve does not reflect the real decay of ESA1.

wavelength (nm)	500	600	650	700	750	800
τ_1 (ps)	5.0 ± 0.5	1.4 ± 0.1	1.3 ± 0.1	1.3 ± 0.1	1.3 ± 0.1	1.1 ± 0.1

Table 5 Relaxation time constants τ_1 at different wavelengths (see [203]). The values are retrieved from fitting the respective kinetic traces according to a rate-equation model.

5.4. Discussion
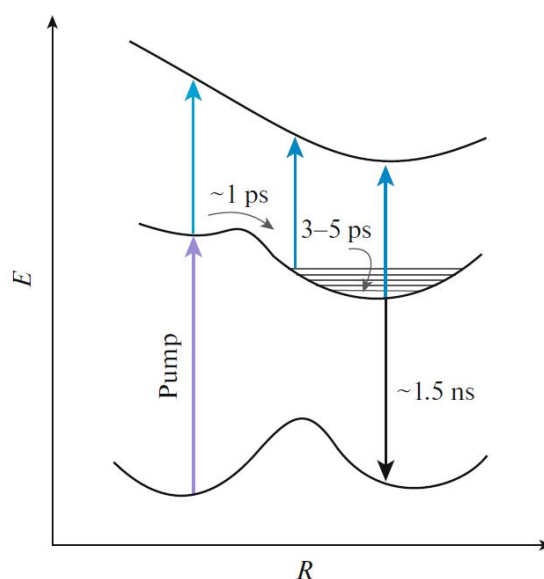
Figure 23 Proposed energy diagram visualising the transformation dynamics of LHC480 upon excitation with the pump-pulse at 320 nm. Adapted from [203].

Molecular dynamics after ultrafast photoexcitation are commonly explained in terms of potential energy surfaces (PES) of the examined chromone compound. Figure 23 presents the proposed energy diagram of the underlying molecular processes. The 320 nm pump pulse excites the molecule from its (singlet) ground state S_0^A of the initial isomer (form A in figure 18a) to the first excited singlet state S_1^A. Subsequently, the supercontinuum probe pulse gives rise to a rapid increase of two pronounced excited state absorption bands caused by the evolvement of the excited electronic state, followed by electronic redistribution and relaxation. This leads to a decrease of the intensity of the transient spectra. However, the spectral relaxation within the first picosecond is not accompanied by any significant spectral shift, in contrast to the subsequent decay for the following 2 ps (see figure 20a). This finding is indicative of the existence of a barrier on the S_1^A-PES, which has to be crossed. Further confirmation is given by the characteristics of the kinetic traces and the extracted decay constants. These resemble the observations for photo-induced ring-opening reactions in photochromic molecular switches described by Draxler et al. and Ward et al. [200, 205]. According to them, upon excitation to the Franck-Condon region, a barrier on the PES has to be overcome, which takes a time of a few ps. Subsequent movement on the PES and deactivation over a conical intersection leads to the open-ring

isomer in further few picoseconds. As the temporal evolution of the maximum at 465 nm (ESA1) matches these descriptions (see figure 20a), the transient dynamics reflected by this ESA can be associated to the occurrence of the predicted intermediate state (open-ring form B in figure 18a). As mentioned before, the initial rise of the two ESA bands proceeds from the initial form A of the molecule. Thus, the measured ESA is a superposition of signals from the excited form A and the evolving form B. Differentiation of their contributions to the transient spectra can not be sufficiently performed solely with these pump-probe results, although a phenomenological description is given in the following. While ESA1 exhibits characteristic signatures, which can be attributed to the intermediate state B, the faster relaxation dynamics of the broad ESA on the red side of the examined spectral range (ESA2) likely reflects the pure decay of form A. During the break of the bond in the furan ring, the electron distribution changes, thus, causing reorientation of the nuclei to new energy minima. As depicted in figure 18a, the chain of nuclei, which originally formed the furan ring, twists and unwinds. The electron distribution follows this movement and the subsequent relaxation to a new minimum on the PES leads to a redshift in the transient curves in the spectral range of ESA1 between 1 ps and 3 ps. After 3 ps ESA2 has either vanished or merged into ESA1 by a blueshift (see figure 20a). A decrease of the population of molecules in their original form and simultaneous increase of the number of molecules in the intermediate state could be the reason for this spectral evolution. More sufficient explanations would require further experimental measurements as suggested in section 5.5. Subsequently, the new furan ring at the chromone moiety closes (see figure 18a). Typically, ring-closure reactions occur on a time-scale below 1 ps [200, 207]. Thus, around 4 ps after excitation, a part of the molecules has either transformed from the intermediate state B to a hot (singlet) ground state of form C or has performed an intersystem crossing to a triplet state of form B. Probing gives rise to an absorption peak with a maximum at 415 nm superimposing ESA1 (see figure 21). Its maximum increases from 9 mOD to 10 mOD within the following 4 ps to 6 ps. As studies from Huffman et al. on 3-aroyl-2-(2-furyl)chromones indicate that "the photochemical transformation proceeds primarily via a triplet, or series of triplets" [193], this finding probably also affects our thiophene containing 2-furyl-3-acetylchromones, as they show very similar optical properties. However, no data about the spectral range of the triplet-triplet absorption for these molecules is available. Therefore, the above described absorbance peak at 415 nm likely involves contributions from photoproduct absorption and eventually absorption from a triplet state of form B as, for instance, reported by Wilcken et al. in experiments on different photochromic molecules [206]. Furthermore, the above mentioned single broad ESA band after 3 ps (see figure 20) can be associated with ESA of an early stage of form C. The further decrease of the absorbance intensity of this ESA band in combination with a redshift of its blue edge can be attributed to further redistribution of the electrons and relaxation by vibrational cooling and solvation processes. Directly after the ring-closure, the molecule in form C relaxes additionally by the emission of photons. The missing SE in the spectra indicates an evolution of the phototransformation over triplet states and an associated fluorescence quenching. Again, more sophisticated examinations including density functional theory (DFT) calculations would be

required for proving this. Finally, the different relaxation processes continue until the molecule reaches a new equilibrium state with a stable spectrum. Our measurements suggest that the phototransformation of the LHC480 molecules to their stable form C is completed after a few nanoseconds. The photoproduct C then exhibits the optical properties as shown in figure 18b.

5.5. Conclusion and outlook

In conclusion we have analysed the time and energy (wavelength) resolved relaxation dynamics of the first excited state of the chromone compound LHC480 from a few hundred fs to 500 ps upon excitation close to the absorption maximum of the initial state. Broadband transient absorption spectroscopy reveals two characteristic ESA bands, whereof the spectral evolution of the energetically higher ESA band is assumed to be related to an intermediate state. The observed dynamics comprises various spectrally and temporally superimposed states and their thermal relaxation, which are difficult to unscramble. Fitting the kinetic data with a rate equation model allows to limit the lifetime of the intermediate state to about 3-5 ps. Moreover, spectral features likely originated in the absorption of the photoproduct and triplet states can be observed after 4 ps. Thus, this pump-probe experiment provides a first time-resolved insight into the evolution of the photochemical transformation of this molecule. The determined ultrafast time-scales for the involved ring-opening and ring-closure processes make this molecule a promising candidate for the application as WORM-type information storage, although improvements on the mentioned low fluorescence quantum yields upon two-photon recording would be desirable. Hence, as a first step further time-resolved measurements in combination with (time-dependent) density functional theory ((TD)DFT) simulations are necessary in order to verify the assumed two-step process via an intermediate state. Other groups were able to resolve the complete photochemical transformation of photochromic molecules by combination of different spectroscopical and theoretical methods [206, 205]. Possible spectroscopic examinations include transient absorption and fluorescence spectroscopy both on the initial form and the transformed form of the molecule, pumping in their respective absorption maxima, using single-photon as well as two-photon excitation for initiation of the photoreaction. As fluorescence spectroscopy allows to exclusively study the emission dynamics, this method can help to disentangle the contributions of excited state absorption and stimulated emission in the transient data obtained with pump-probe spectroscopy. Both methods can be expanded to pump-repump-probe (PREP) and pump-repump-fluorescence (PREF) measurements in order to unravel the time scales and the required excitation wavelengths for the two-step process by varying the time-delay and wavelength of the second excitation pulse, as shown in [200, 201, 207] with PREP, for instance. Global analysis of the results including decay associated spectra (DAS) [208], decay associated difference spectra (DADS) [126, 209] or species associated spectra (SAS) [210, 211] provide information about the temporal evolution and the spectra of the different involved states as well as reaction yields [206]. Furthermore, transient IR spectroscopy constitutes a different approach

to study the phototransformation. Excitation of the sample in the UV range, hence initiating the transformation, and probing in the IR fingerprint range provides information on structural changes including identification of different species [212] and presumably the intermediate state. As preparation for these experiments, Sebastian Roth performed FTIR (Fourier-transform infrared spectroscopy) measurements and DFT calculations for LHC480 and a new chromone compound in the course of his Bachelor's thesis [213]. The results are promising for identification and characterization of the intermediate state with UV-pump-IR-probe spectroscopy, and provide a pathway to further understanding of technically relevant chromophores and their (multi-photon) fluorescence.

The obtained results can help to tune particular properties like switching rate and efficiency of the chromone compound by adding different substitutions to the functional groups as, for instance, has been done according to fluorescence properties by Martynov et al. [192]. Moreover, proper selection of solvents, and likely also the ambient polymetric matrices, with different polarity and structure can additionally influence the reaction parameters [214, 215]. As triplet states are involved in the phototransformation [193], using the heavy-atom effect by substituting halogens into the functional groups (internal HAE) or in the surrounding polymeric matrix (external HAE) might also have an impact on the reaction parameters or yields (cf. chapter 4). Hence, pump-probe spectroscopy of chromone compounds guides to enhancement of transformation yields as well as fluorescence quantum yields, thus, improving the suitability concerning the desired application for information recording and reading.

Part IV

Nonlinear studies on enantioenrichment using circularly polarized laser pulses

6. Nonlinear studies on enantioenrichment using circularly polarized laser pulses

6.1. Introduction and statement of contributions

Chiral molecules have enantiomers, which are not superimposable with their mirror image. In the 19th century Louis Pasteur was the first to relate optical activity, earlier described by Jean-Babtiste Biot [216], to two different, i.e. enantiomorphous, isomers and separated them manually [217, 218]. Beside their natural occurrence, e.g. in glucose, amino acids, or enzymes, chiral substances play a major role in the chemical and pharmaceutical industry. More than 50% of pharmaceutically active substances currently in use are chiral [219]. Although most of them are synthesised as racemates, usually only one of the enantiomers shows the desired effect in pharmaceuticals or agrochemicals [220]. The other enantiomer has the same atomic composition, however often produces even toxic or carcinogenic side effects [19, 20, 220, 221]. Because the existing methods for enantioselective catalysis from absolute asymmetric catalysis are not applicable to all chiral molecules, affordable techniques of enantioseparation and -purification are pivotal for pharmaceutical industry and clinical analysis. Moreover, both enantioselective catalysis and purification generally require the use of chiral seeds or phases [222, 223]. Therefore, we present by proof-of-principle a new method for enantioenrichment by the different interaction of the enantiomers with polarised light, thus, without the risk of chemical contamination. Our aim is to preferentially desorb one enantiomer of a film of racemic BINOL (1,1'-bi-2-naphthol) from an achiral surface using circularly polarised (CP) femtosecond laser pulses. The main results of our studies are published in "Enantiospecific Desorption Triggered by Circularly Polarized Light" in the International and German Edition of Angewandte Chemie [224], and were presented at the Conference for Lasers and Electro-Optics in 2019 [225].

Because of its true chiral nature, circularly polarised light (CPL) has been shown theoretically and experimentally to induce enantiospecific synthesis or separation [226]. Ben L. Feringa et al. report on three different types using CPL for enantioselective catalysis: photodestruction, photoresolution and asymmetric photosynthesis [223]. In the latter method chiral substances are synthesised by inducing a photochemical reaction on prochiral educts by CPL [227, 228, 229]. In enantioselective photodestruction, one enantiomer is preferentially decomposed by illumination with strong CP UV light, leading to high purities of up to an enantiomeric excess (ee) of 30%. However, this high ee usually comes along with a destruction of more than 99% of the complete racemic substance [230, 231, 232]. Photoresolution provides a reversible method for converting a small fraction of a mixture of two enantiomers in solution into one specific enantiomer by excitation with CPL [227, 233, 234]. Due to competition with thermal racemisation, i.e. the

process of interconverting enantiomers in order to form a racemic mixture, however only small enantiomeric excesses of up to a few percent can be achieved. Applying to bistable molecules, photoresolution is a promising method for inducing crystallisation in specific chiral phases or designing the morphology of surfaces, e.g. for applications in optical data storage [235, 236]. Separation of enantiomers with CPL has been achieved with different recent approaches based on deflection or microfluidic sorting caused by the enantiospecific interaction of chiral microparticles with two interfering CP laser pulses with opposite handedness of the light [237, 238]. However, these methods are not applicable yet for particles of molecular size.

Laser desorption is used to study fast surface processes and reactions in surface science [239, 240, 241, 242]. Furthermore, in the field of chemical analysis, laser desorption provides a suitable non-destructive instrument for the examination of non-volatile molecules in the gas phase with high resolution [243, 244, 245], particularly in combination with mass spectrometry and resonant enhanced multi-photon ionisation (REMPI) as was shown in numerous studies [246, 247, 248, 249, 250]. The latter two methods are also used for high resolution discrimination of enantiomers as well as techniques employing photoelectron angular distribution, Coulomb explosion or microwave spectroscopy, for instance [251, 252, 253]. Using its ability to remove molecules under controlled conditions without destroying them, laser desorption provides the possibility of resonant interaction of CPL with surface molecules, and thus, to induce quantum mechanical effects [254, 255]. The optical activity of our BINOL films is determined with surface second harmonic generation spectroscopy (SSHG). Because SHG-CD at a surface of an ordered system of chiral molecules is mainly induced by electric-dipole transitions, in contrast to the much weaker linear CD effect, SSHG spectroscopy provides a very sensitive tool for the detection of small chiroptical responses (see section 2.2.7). BINOL is an organic molecule, which exhibits axial chirality and occurs in the two enantiomers R-BINOL and S-BINOL. Due to its high stability against thermal racemisation, it serves as a model system in numerous studies about SHG-CD. Further applications can be found in asymmetric catalysis [256, 257].

In this chapter, the experiments on enantioenrichment and enantiospecific desorption are presented. While enantiospecific thermal desorption from chiral surfaces was already reported by J. D. Horvath and J. Gellman [258], our objective is to probe enantiospecific laser desorption from an achiral surface. We use circularly polarised laser pulses to test, whether we can preferentially desorb one of the two enantiomers, and thus, generate an enantioenrichment of the remaining film. An overview of the experimental setup and the applied methods is given in section 6.2. The SHG-CD and SHG-ORD experiments (see sections 6.3 and 6.4) and further measurements under vacuum conditions (see section 6.5) are combined with microscope examinations (sections 6.2.4 and 6.3) and discussed in detail. Furthermore, different approaches for phenomenological models and numerical simulations are developed (section 6.6).

The presented SSHG experiments were performed under guidance of PD Dr. Hristo Iglev within

a collaboration with the group of Dr. Aras Kartouzian from the Chair of Physical Chemistry at the Department of Chemistry at TU Munich, who also initiated the project. The proof-of-pinciple setup was developed by the author. Moreover, all SSHG-spectroscopy and data post-processing was performed by the author (sections 6.2, 6.3, 6.4) or with major contribution from the author (section 6.5). The data was analysed with a MATLAB program written by the author. Dr. Johann Riemensberger supported with suggestions for the experimental setup design and data analysis. Measurement control was realised by a Labview program, which was joint written by J. R. and the author. The samples were prepared by Dr. Farinaz Mortaheb from our collaborating group (section 6.2.3). She further examined BINOL with conventional spectroscopy (see section 6.3), and performed preliminary experiments. Those are shown in her doctoral thesis as well as a summary of our proof-of-principle results [250]. The high-vacuum setup (section 6.5) was designed by J. R. and Florian Ristow during the course of his Master's thesis [259]. F. R. also assisted with measurements and data analysis of the vacuum experiments and examined the BINOL films by microscopy in cooperation with the author (see sections 6.5 and 6.3). Furthermore, F. R. and Xuqiang Xu performed measurements on samples with 10% ee, and recorded images with a confocal microscope (see sections 6.3 and 6.2.4). The fit model (section 6.4.4) and the simulations (section 6.6) were developed by the author in cooperation with J. R. and H. I. The fit model was also recently presented in F. M.'s doctoral thesis [250]. All results were discussed and interpreted in cooperation with H. I., A. K.,F. M., J. R., Prof. Dr. Reinhard Kienberger, Prof. Dr. Ulrich Heiz and F. R.. This work gives an extended version of the results and corresponding discussions recently published in Angewandte Chemie [224] and F.M.'s doctoral thesis [250] by adding more details and presenting additional data. In particular, the information given in sections 6.2.1 and 6.2.3, and the results in connection with figures 29, 59, 33, 34, 35b, 38a and b, 39, and 44a are presented in both above mentioned works. Results in connection with figures 25b, 31b, 32, 36 and 35d are published in Angewandte Chemie [224]. Figures, which are reprinted with permission of Wiley-VCH Verlag GmbH & Co. KGaA., are correspondingly labelled.

6.2. Experimental setup and methods

6.2.1. SHG-setup

For proof-of-principle of enantiospecific desorption, we developed a simple setup (see figure 24) based on the UHV-SSHG-setup pioneered by Dr. A. Kartouzian using nanosecond laser pulses [77]. This setup was used for all experiments described in the above mentioned publication [224]. Sub-50-fs excitation pulses with a central wavelength of 600 nm and 650 nm were provided by the Ti:Sa-based laser system in combination with a noncollinear optical parametric amplifier (NOPA I) and a prism compressor as described in section 3.2. The sample consists of a 1.5 μm thick film of BINOL, which was evaporated and deposited onto thin borosilicate glass (BK7) substrates (thickness: < 0.2 mm, side-lengths: 1 cm). The laser pulses are focused by a lens (fused silica, f = 100 mm) onto the sample surface generating a second-harmonic (SH) signal and causing desorption of BINOL molecules. The co-propagating transmitted SH and fundamental laser light are recollimated by a second lens (fused silica, f = 40 mm), separated by refraction in two Brewster prisms and focused onto the entrance slit of the detector by another lens (fused silica, f = 100 mm). As detector we used the Czerny-Turner spectrometer (MircoHR, Horiba) described in section 3.2, and a liquid nitrogen cooled CCD (LN/CCD-1340x400, Controller ST-133, Princeton Instruments). Remaining fundamental light is blocked by bandpass filters (Schott 2UG11, 1UG5) before detection. A quarter-wave plate (achromatic retarder, 460-680 nm, B. Halle), which is controlled by a stepper motor (RDM 545, Berger Lahr), enables the control of left and right circular polarisation after ensuring incoming linear polarisation with a wire grid polariser (ProFlux PFU04C Ultra contrast 420-700 nm, MOXTEK Nanowire Technology). Definition and characterisation of the circular polarisation are given in appendix A.2. A second identical wire grid polariser, which the light has to pass first, allows fine-tuning the excitation pulse energy from below 0.1 μJ up to more than 3 μJ by twisting its optical axis with respect to the following polariser. The sample-holder carrying the BINOL-covered glass substrates is rotatably mounted on an x-y-z-translation stage, which allows adjusting the angle of incidence of the excitation pulse as well as horizontal and vertical positioning with respect to the impinging pulse. By moving the sample in direction of the beam, the distance to the focus of the beam, and therefore, the size of the illuminated spot can be controlled. For SHG-ORD experiments a motorised UV Glan-Thompson polariser can be placed after the collimating lens (see figure 54). During the movements of the stepper motors the beam is blocked with an external shutter (SH05, Controller SC10, Thorlabs). In order to ensure a stable excitation pulse energy, the part of the laser output, which is not used for pumping NOPA I, is measured with a powermeter (LabMax, Coherent). Data and power recording as well as the stepper motors are controlled by a self-written Labview programme.
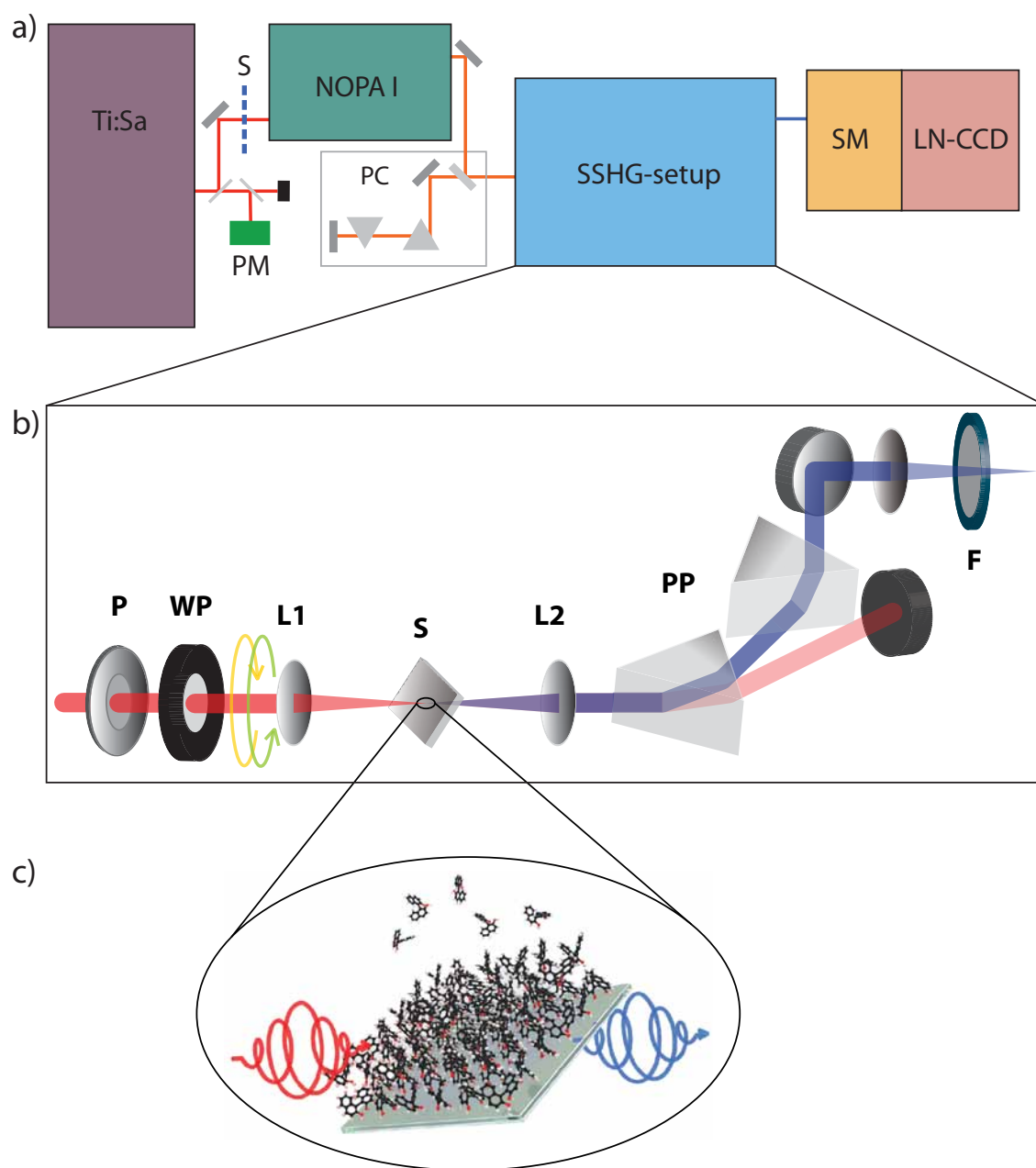
Figure 24 a) Experimental setup for SSHG-spectroscopy and enantiospecific laser desorption. Generation of femtosecond excitation pulses using the Ti:Sa-based laser system, NOPA I and the prism compressor (PC) is described in section 3.2. An external shutter (S) allows blocking the beam. Stability of pulse energy is measured with a power meter (PM). b) Details of the SSHG-setup used for the proof-of-principle experiments. The NOPA output pulses compressed to sub-50 fs with a central wavelength of 600 and 650 nm (red) are focused by lens L1 onto the sample, causing desorption of BINOL molecules. The polarisation is controlled by a polariser (P) and a quarter-wave plate (WP), which alters the original linear polarisation of the laser light to RCP (orange) or LCP (green). SHG in the BINOL film and on its surface is first co-propagating with the fundamental laser light through the collimating lens L2, then separated from the latter in the prism pair PP and band pass filters F. Subsequently, the beam is focused into the detector, consisting of a Czerny-Turner spectrometer (SM) and a liquid nitrogen cooled CCD camera (LN-CCD). c) Magnification of SHG and desorption of BINOL molecules.

6.2.2. SHG-spectroscopy

Second-harmonic frequency signals can be generated at surfaces, where the symmetry is broken. In section 2.2.7 the theoretical details for surface second harmonic generation (SSHG) at surfaces of chiral molecules adsorbed on an achiral subtsrate are explained. The first SSHG experiments on sub-monolayers of BINOL were performed by the group of J. Hicks in 1993, who reported on SHG-CD values close to unity [51]. This strong chiroptical response can be explained by the generation of SHG-CD mainly by electric-dipole transitions in contrast to linear CD, which is caused by much weaker magnetic-dipole transitions (see section 2.2.7). A monolayer of BINOL molecules, which are adsorbed to a glass substrate, i.e. an achiral surface, is now a well understood system [40, 66]. In our experiments we measured the SHG signal in transmission as depicted in figure 25a, and applied the methods of SHG-CD (second-harmonic generation circular dichroism) spectroscopy and SHG-ORD (second-harmonic generation optical rotatory dispersion) spectroscopy to examine the optical anisotropy of BINOL films. According to equations 2.71, 2.72, and 2.73, the SSHG intensity is proportional to $|E_i(\omega)|^4$, thus depends strongly on the pump intensity. When the latter is kept constant, the SSHG intensity grows almost linearly with increasing thickness of the BINOL film during evaporation as was shown in earlier studies [77] and confirmed by measurements in our high-vacuum setup (see figure 25b).
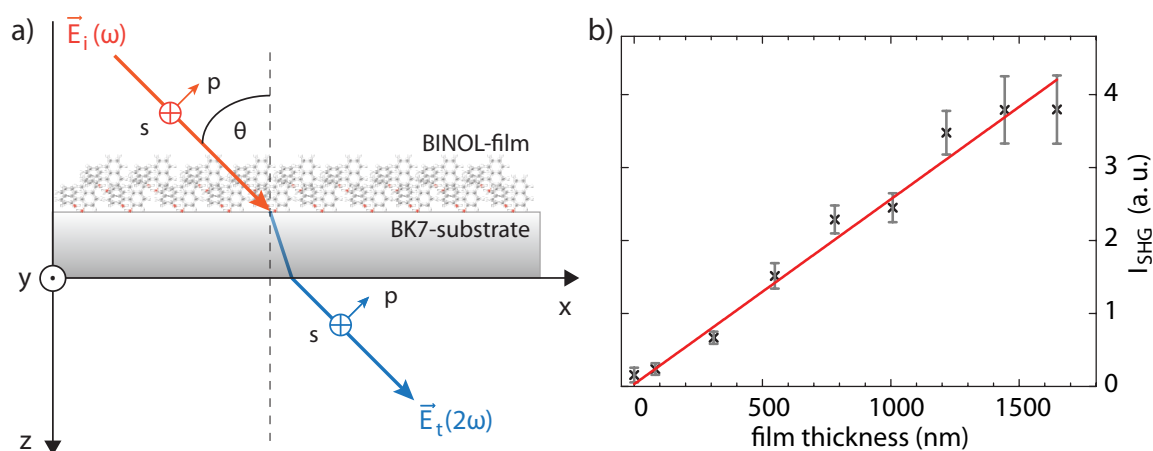
Figure 25 a) Geometry of SSHG spectroscopy. The incoming fundamental beam $\vec{E}_i$, which is incident at an angle θ, generates the second harmonic at the BINOL-BK7 surface, which is measured in transmission. The polarisation of fundamental and SSHG beams can be parallel (p) or perpendicular (s) with respect to the plane of incidence, or circular ($\vec{E}_{i,p} = \pm i\vec{E}_{i,s}$). b) SSHG intensity of a BINOL film measured during the evaporation process in the vacuum chamber (see figure 47). The quantity I_{SHG} is the mean of the SHG-response upon excitation with RCP and LCP pulses (650 nm). The red line denotes a linear fit. Adapted from [224].

Specifications of the SSHG setup

For all measurements the CCD camera was cooled to -100°C and the exposure time was set to 1 s. The data was saved as spectra over the full 1340-pixel-width of the sensor, whereas the 400-pixel-columns were binned. Alignment and wavelength calibration was realised in a first step using the SHG from a BBO-crystal (type I, 10 μm), and in a second step with a BINOL

sample (see figure 26). The known wavelengths of the signals from exciting fundamental beam and SHG allowed to translate pixel numbers to wavelengths with a linear calibration function. Although much care was taken of detector housing and screening stray light, the signal from the fundamental beam could not be eliminated fully, however, can be well distinguished from the SSHG-peak (see figure 26). The SSHG from the BINOL sample was further checked to be a real nonlinear response by means of bandpass filters and its sensitivity with respect to variations of the excitation pulse length.
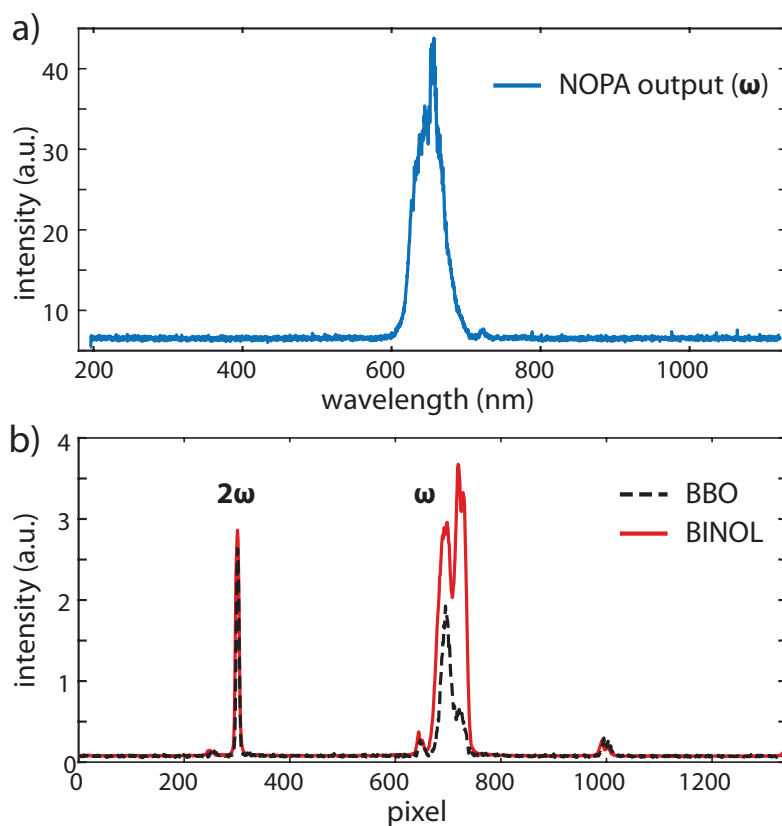
Figure 26 SSHG calibration. a) Spectrum of the NOPA output measured with a commercial spectrometer (HR4000, Ocean Optics). b) Spectrum of a BINOL-sample and a BBO-crystal, which was mounted at the position of the sample, recorded with the Czerny-Turner spectrometer in combination with the LN-CCD (see section 6.2.1). Excitation pulse energy was adjusted to 1.5 μJ for the BINOL-sample and to < 0.1 μJ for the BBO-crystal. The second-harmonic (2ω) and fundamental (ω) signals were identified by blocking the respective other peak with UV and VIS bandpass filters.

The incoming visible laser beam was characterised with a commercial beam camera (CinCam CMOS-1202, CINOGY Technologies). It shows a slightly elliptical shape (see figure 27). In order to determine an optimum position of the sample with respect to the laser focus, in a first step, the FWHM of the beam was measured along the z-axis, which is parallel to the direction of pulse propagation (see figure 25a), in the vicinity of its focus. Close to the focus, the beam profile approaches a circle with a minimum diameter of about 20 μm (see figure 27).

Furthermore, the surface-second-harmonic signal was recorded by moving a BINOL sample
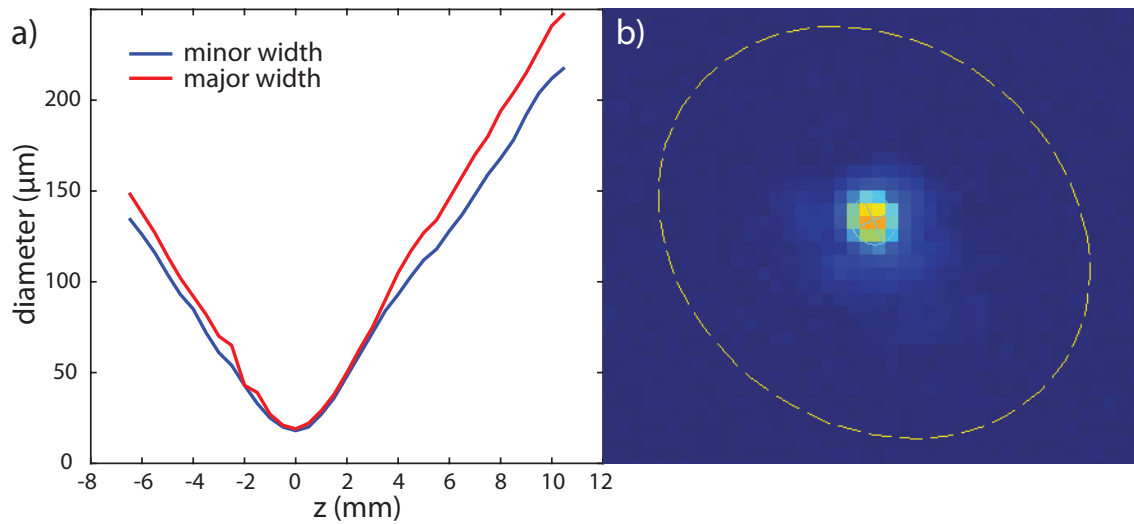
Figure 27 Characterisation of exitation beam. a) FWHM of the slightly elliptic beam profile with major axis (red) and minor axis (blue) depending on propagation direction z. b) Beam profile in the focus z = 0 measured with a CinCam beam camera and a neutral density filter (Schott OD3). The major and minor width are 20.4 μm and 18.1 μm, according to an area of 1160 μm^2.
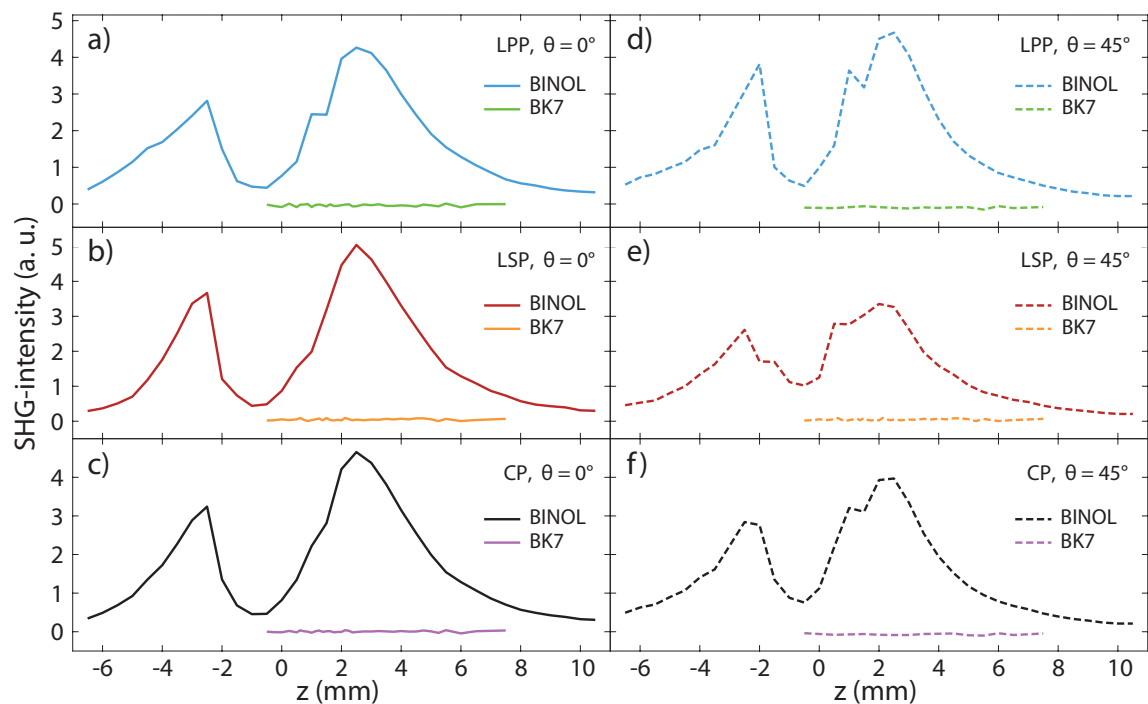
Figure 28 SSHG intensity (integrated over the spectral range from 300 nm to 355 nm) of a BINOL sample and an uncoated BK7 substrate measured along the z-axis in the vicinity of the focus of the excitation beam, which was adjusted to an energy of 1.25 μJ at a central wavelength of 650 nm. a-c) Angle of incidence $\theta = 0°$. d-f) Angle of incidence $\theta = 45°$. Polarisation of the excitation beam: a,d) LPP (linear, parallel), c,e) LSP (linear, "senkrecht"), and c,f) CP = (LPP + LSP)/2.

through the focus of the beam along the z-axis for normal incidence ($\theta = 0°$) and $\theta = 45°$ incidence (see figure 28). The energy of the excitation pulse was set to 1.25 μJ at a central

wavelength of 650 nm, typical for our experiments. In order to examine any anisotropies arising from the setup, these SHG-z-scans were carried out for two perpendicular linear polarisations, parallel (LPP) and normal ("senkrecht", LSP) with respect to the plane of incidence. Additionally, the case of circular polarisation (CP) was constructed from the mean of both curves. The overall progression of the SSHG intensity is very similar for all 6 cases. When approaching the focus in beam direction, the intensity first increases. Then, about 2 mm before the focus, the signal drops close to zero, and starts growing fast from the position of the focus at z = 0. At 2.5 mm behind the focus, when the sample is in the diverging beam, the second-harmonic reaches its maximum intensity, before it decreases again. The drop of the signal is presumably caused by destruction of molecules at the surface due to intensities above the destruction threshold and the unfavourable orientation of the wavefronts in the focussing beam. Hence, for our experiments we placed the sample 3.5-4.5 mm behind the focus, according to a FWHM beam diameter of about 90-120 μm. Repeating the SHG-z-scans for an uncoated BK7 substrate, no signal could be detected in the range behind the focus up to a pulse energy of 3 μJ. The spectrum of one of these measurements on a BK7 substrate in comparison to the SSHG-spectrum of a BINOL sample is depicted in figure 29.
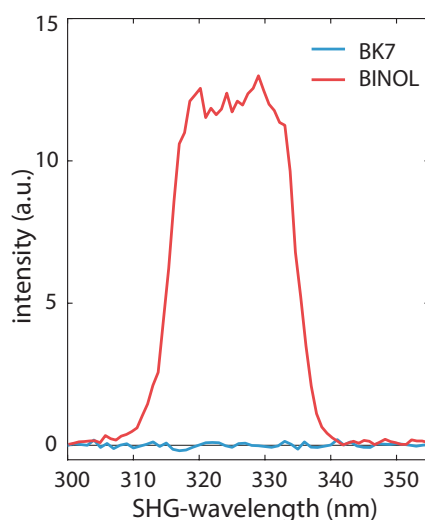
Figure 29 SSHG-spectra of a BINOL sample (red) and an uncoated BK7 substrate (blue) measured at a z-position of 3.5 mm and with $45°$-incidence for linear polarisation parallel to the plane of incidence.

Excitation of the BINOL sample with pulse energies of more than around 2.5 μJ leads to white light generation, when the sample is placed close to the focus, thus, a large background signal obscures the SSHG.

The desorption experiments (see section 6.4) were performed with the SSHG-geometry shown in figure 25a, whereas the angle of incidence was nonzero according to earlier SSHG-experiments from our collaborators [77, 260]. They showed, that for a coverage of only a few monolayers of BINOL, the signal intensity for normal incidence is zero, however, increases for larger angles of incidence. In thicker layers the SSHG intensity grows with increasing film thickness due to

random orientation of the molecules. For our 1.5 μm thick films, we thus expect no significant dependency of the SSHG intensity on the angle of incidence. However, SSHG can occur on surfaces, which exhibit in-plane anisotropy (see section 2.2.7).

In order to avoid this effect, we carried out the SHG-z-scans additionally at normal incidence of the excitation pulse with respect to the sample surface as suggested by Huttunen et al. [59]. Table 6 shows the intensity ratios for normal incidence (figures 28a-c) and 45°-incidence (figures 28d-f) of the excitation pulse with respect to the surface normal. First, the sum of all intensity values at normal incidence along the z-axis was calculated and compared to the sum of intensities at 45°-incidence: ratio sum $:= \sum_i I^{0°}(z_i) / \sum_i I^{45°}(z_i)$. Further, the ratio was taken from the respective maximum intensities: ratio max $:= max(I^{0°}(z_i))/max(I^{45°}(z_i))$. For incident beams with linear polarisation parallel to the plane of incidence (LPP) or circular polarisation (here constructed from the sum of parallel and normal linear polarisations, LPP+LSP), both ratios are close to 1, reflecting that the SHG-signal arises from the (microscopic or macroscopic) chirality of the BINOL film. For linear polarisation normal to the plane of incidence, the SHG-intensities are larger at normal incidence, confirming at least that we do not generate a second-harmonic signal due to in-plane anisotropy. Measurements in the scope of these thesis were all conducted with circular polarisation or linear polarisation parallel to the plane of incidence.

polarisation	LPP	LSP	LPP+LSP
ratio sum	1.03	1.27	1.14
ratio max	0.91	1.50	1.16

Table 6 Intensity ratios of $\theta = 0°$ and $\theta = 45°$ incidence for linear parallel (with respect to the plane of incidence) polarisation (LPP), linear perpendicular polarisation (LSP) of the excitation pulse, and the sum of LPP and LSP. First, the sum over z of the integrated intensities are compared (ratio sum), then, the respective intensity maxima (ratio max).

SHG-CD and SHG-ORD measurement scheme

For our studies, we applied two different SSHG methods, SHG-CD (second-harmonic generation circular dichrosim, equation 2.68) and SHG-ORD (second-harmonic generation optical rotation dispersion, section 2.2.7). The corresponding results are presented in sections 6.3 and 6.4.

The anisotropy factor $g(2\omega) = 2(I^{\mathrm{LCP}}(2\omega) - I^{\mathrm{RCP}}(2\omega))/(I^{\mathrm{LCP}}(2\omega) + I^{\mathrm{RCP}}(2\omega))$ (equation 2.69) of the BINOL films was determined by means of SHG-CD. Therefore, the SSHG-intensity at one specific spot on the sample surface is measured using LCP and RCP light. Excitation intensities were chosen to a condition of constant SSHG-intensity in order to suppress effects such as desorption or bleaching. In order to keep the random error low, we took the mean of a series of n = 12-20 spectra (depending on the actual laser stability), which were recorded at each polarisation. During the movement of the stepper motors, which rotate quarter-wave plate and UV-polariser, the beam is blocked with an external shutter in order to avoid desorption. The

SSHG-intensity ($I_{\mathrm{SHG}}^{\mathrm{RCP/LCP}}$) was obtained by integrating the mean spectral SSHG-amplitude ($S^{\mathrm{RCP/LCP}}(\lambda)$),

$$I_{\mathrm{SHG}}^{j} = I^{j}(2\omega) = \int S^{j}(\lambda)d\lambda, \ \ j = LCP, RCP, \tag{6.1}$$

with

$$S^{j}(\lambda) = \frac{1}{n}\sum_{k=1}^{n} S_{k}^{j}(\lambda). \tag{6.2}$$

The order of LCP and RCP, however, was altered when examining a new spot or for the next g-value measurement in the desorption experiments to further minimise systematic errors.

For SHG-ORD experiments, the excitation beam was linearly polarised parallel to the plane of incidence (LPP). Therefore, the fast axis of the waveplate was aligned parallel to the direction of linear polarisation. An UV-polariser was placed behind the collimating lens in order to record polarisation dependent SSHG intensity (I^{polar}). Similarly to SHG-CD, 10-15 SSHG spectra ($S_{l}^{\mathrm{polar}}(\lambda)$) were measured for each azimuthal angle $\varphi_{l} = 360°/(l-1)$ of the polariser. In analogy to SHG-CD, the angle dependent integrated SSHG intensity is given by

$$I_{l}^{\mathrm{polar}}(\varphi_{l}) = \int S_{l}^{\mathrm{polar}}(\lambda)d\lambda, \ \ l = 1, 2, ..., 25. \tag{6.3}$$

In addition to the determination of I^{polar}, the g-value was measured directly afterwards with LCP and RCP incoming light by rotating the waveplate to the respective positions. Because we could not remove the polariser during an automated measurement, the SSHG response was detected in dependence of the polariser angle and added up over all angles according to

$$I_{\mathrm{SHG}}^{j} = \sum_{l} I_{l}^{\mathrm{polar,j}}(\varphi_{l}), \ \ j = LCP, RCP. \tag{6.4}$$

By means of SHG in a BBO-crystal (type I, 10 μm) the symmetry properties of the extended setup were characterised. As shown in figure 30a, the spectrally integrated SHG intensities were plotted in polar coordinates. The angle dependent SHG was fitted according to the the polar form of an ellipse

$$I^{\mathrm{polar}}(\varphi) = r(\varphi) = \frac{ab}{\sqrt{a^{2}\sin^{2}(\varphi - \delta) + b^{2}\cos^{2}(\varphi - \delta)}}. \tag{6.5}$$

Herein, the parameter φ denotes the azimuthal angle of the polariser (for direction of φ see figure 54). The major and minor axes of the ellipse are represented by a and b, and δ denotes the initial rotation from the x-axis, which is aligned with the polarisation of the incoming beam (see figure 30b). The parameters a, b, and δ are extracted from the fit. Due to its characteristic form of an oscillating dipole, the angle dependent SHG was additionally fitted in analogy to polarisation resolved photoelectron spectra with the formula for atomic subshell photoionization
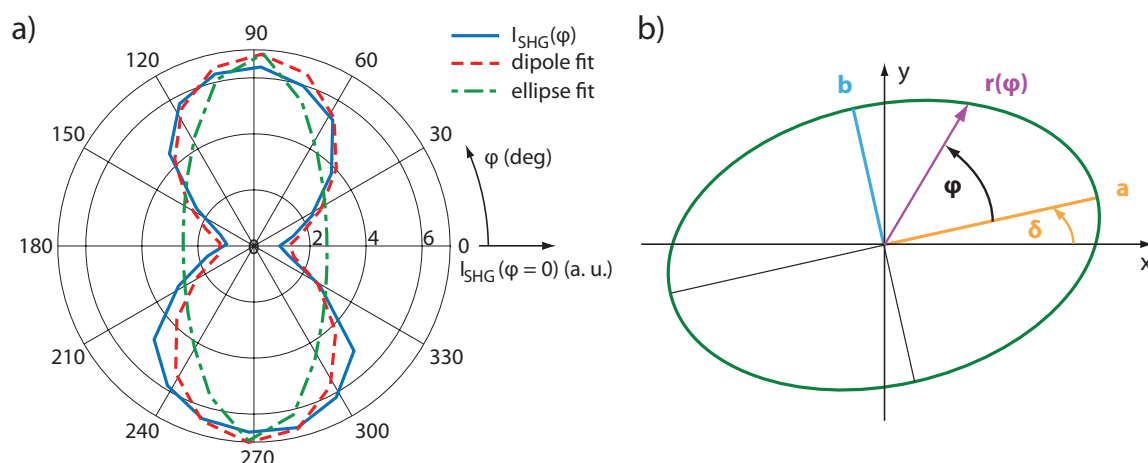
Figure 30 a) Polarisation dependence of SHG intensity (blue, solid) measured on a BBO-crystal placed 3.5 mm behind the focus of the excitation beam (LPP, < 1 μJ, 650 nm). The data was fitted according to equations 6.5 (green, dot-dashed) and 6.6 (red, dashed). The rotation angle with respect to LPP is extracted from the fit to 91.54°. b) Ellipse with the respective parameters used for the polar fit: major axis a (orange) and minor axis b (blue), angular coordinate φ and rotation angle δ with respect to the x-axis. The vector r(φ), defining the ellipse, has its origin in the centre of the ellipse.

cross sections [261]

$$I^{\mathrm{polar}}(\varphi) = a(1 + \frac{b}{2}(3 \cdot \cos^2(\varphi - \delta) - 1)). \tag{6.6}$$

This plot represents the response of our detector to a linear polarised SSHG signal, which is rotated by 90° to LPP. The fit, i.e. the ellipse fit as well as the dipole fit, allow to determine the optical rotation δ of the SSHG signal.

6.2.3. Sample preparation

Samples with thin molecular films were prepared by thermal evaporation of BINOL molecules (Aldrich, 99%) and subsequent adsorption onto BK7 substrates in a high-vacuum setup at pressures of 10^{-7} mbar and room temperature [250]. The BK7 substrates were cleaned with iso-propanol and lint-free tissues afore. Evaporation of one full crucible containing 40 mg BINOL enabled deposition of a 1.5 μm thick film after 20 min [262]. Determination of the film thickness was performed by means of a pre-calibrated quartz micro balance (QMB) (INFICON SL-A1E40) using the Sauerbrey equation

$$\frac{\Delta f}{f_0} = -\frac{\Delta m_f}{m_q}. \tag{6.7}$$

Deposition of an additional mass Δm_f to the quartz crystal mass m_q causes a change Δf in the resonance frequency of the crystal. The quantity f_0 denotes the initial resonance frequency of the crystal. The film thickness of a racemic film can be calculated using the molar mass of BINOL (M = 286.32 g/mol) and the density of racemic BINOL (ρ = 1.303 g/cm^3) [263, 264].

6.2.4. Laser desorption

Photodesorption is one of the most fundamental processes at a surface. Thereby, the laser beam can cause desorption by direct electronic excitation in single atoms or molecules, or indirectly, i.e. substrate-mediated, by initial absorption in the substrate and subsequent transfer of energy and charge to the adsorbed molecule [265, 241]. Both direct and indirect processes involve a quantum mechanical (QM) interaction of the impinging photons or electrons and the adsorbate or adsorbate-substrate complex, respectively. Direct desorption of weakly-bound surface adsorbates by UV to visible light is favoured at insulating or semiconducting surfaces. Desorption yields depend on excitation intensity, frequency and polarisation of the incoming laser pulse. Polarisation along the transition dipole moment of the adsorbate enhances the desorption cross-section. Indirect desorption plays a major role on metal surfaces and is referred to as DIET (desorption induced by electronic transitions), or as DIMET (desorption induced by multiple electronic transitions), when using intense light sources such as femtosecond pulses. Most studies describe the desorption process by means of a monolayer or sub-monolayer of atoms or molecules adsorbed to a substrate [254, 265, 266, 267]. Assuming sufficiently large excitation energy, the system is excited by a Franck-Condon transition and evolves along the excited-state PES to a repulsive electronic state, e.g. by a crossing with a PES of a nonbonding state or through conical intersections, leading to dissociation of the adsorbate-substrate bond. The probability of this process depends mainly on the coupling strength of the excited adsorbate to the substrate. Another possible process is photodissociation of the adsorbed molecules. Which reaction, desorption or dissociation, is favoured, depends on the excitation frequency, fluence, coupling and bond strengths. Nonetheless, laser desorption can provide intact neutral molecules in the gas phase as was shown in several high-resolution mass spectrometric studies (see section 6.1). On metal surfaces, desorption rates are generally lower than on insulating surfaces. Already in 1964, D. Menzel, R. Gomer and P. Redhead published a semi-classical description of the corresponding processes, commonly known as Menzel-Gomer-Redhead mechanism (MGR) [268, 269]. Upon electronic excitation of the adsorbate-substrate complex, motion along the excited PES of a repulsive state leading to desorption competes with energy transfer away from the system resulting in recapture of the adsorbate. In the experiments underlying the MGR, electrons were used to induce desorption (ESD, electron stimulated desorption). However, a similar description for photodesorption was given by R. Adams and E. Donaldson [270], and a few years later by P. Antoniewicz. He proposed a similar mechanism, assuming an ionized excited state, causing acceleration of the adsorbate to the surface, which is followed by neutralisation and relaxation to the nonbonding branch of the ground state [271]. Since then, many quantum mechanical simulations based on a first-principle treatment have lead to a better understanding of the desorption process of small adsorbates [267, 265, 242]. Furthermore, time-resolved experiments could limit the process of desorption to a sub-picosecond timescale [272].

Desorption induced by thermal heating of the material is known as thermal desorption and

is always present [273]. Thermal desorption yields depend mainly on the temperature of the medium, hence, on the energy deposited by the incoming laser beam. In order to realise large contribution of direct photodesorption to the desorption yield, the incoming laser fluence should be as low as possible.

Within this work, the term "laser desorption" always refers to the definition of laser-induced desorption as given by R. Haglund: " laser-induced desorption results in the emission of ions, atoms and molecules without any substantial disturbance in the surrounding surface", in contrast to " laser ablation", which "is associated with large-scale disruption of surface and near-surface geometrical and electronic structure, and under some conditions of the stoichiometry as well." [266]. Strictly speaking, desorption is usually used for heterogeneous processes, i.e. molecules leaving a surface, which consists of a different material than the desorbed adsorbate molecules. Nonetheless, we use the term desorption instead of sublimation, because the process, which we describe, is highly non-adiabatic in contrast to sublimation, which occurs in thermal equilibrium conditions. Besides, the term was used for similar processes for REMPI and MALDI (matrix assisted laser desorption ionisation) studies.

Characterisation of desorption parameters
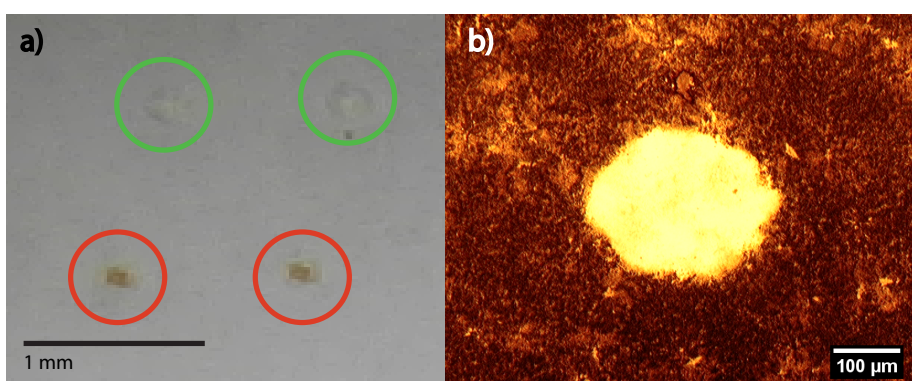
Figure 31 a) Magnified picture of four desorption spots on a sample after irradiation for 2 h. The spots in the upper row (marked with green circles) do not show any indications of photodestruction. The spots in the lower row (red circles) exhibit brown spots in their centre pointing to possible photodestruction. b) Reflected light microscope image of a desorption spot after 2 h irradiation with sub-50 fs pulses. Adapted and modified from [224].

Amongst examination of QM effects our experiments aim to show enantioenrichment of racemic BINOL films by means of laser desorption. Therefore, the irradiation intensity of the impinging pulses had to be adjusted to a value above the threshold for desorption of BINOL molecules, but below the destruction threshold. In order to assure intactness of the remaining BINOL molecules on the irradiated surface we examined the desorbed areas by microscopy. Furthermore, the mass spectrum of BINOL molecules, which were desorbed from an identical sample using a nanosecond-laser (607 nm, 5 mJ, 30 Hz), confirms that desorption of intact and neutral BINOL molecules is generally favoured (see appendix A.5). For our desorption experiments,

we used sub-50-fs excitation pulses with central wavelengths of 600 and 650 nm. Figure 31b shows the image of a desorbed spot after 2 h irradiation with 1 μJ at 1 kHz pulse repetition rate (4 mm behind the focus) examined with a reflected light microscope (Axiolab, Carl Zeiss). The area of the spot is determined from the image to $5.4\pm0.12\cdot10^4$ μm^2 corresponding to a mean diameter of 263 ± 15 μm indicating that the region of influence of the laser beam is much larger than the FWHM-area of the Gaussian shaped pulse profile. Assuming a 13.8 ± 1.6 fs excitation pulse (for estimation of the pulse duration see A.1), the intensity is calculated to 134.1 ± 0.1 GW/cm^2 according to a fluence of 1.85 ± 0.041 mJ/cm^2 per pulse. According to the results from section 6.2.2, the BINOL sample was placed at positions 3.5-4.5 mm behind the focus corresponding to FWHM-diameters of 90 to 120 μm. Hence, we assume desorption spot areas in the range from approximately 4.9 to $6.5\cdot10^4$ μm^2. Irradiating the samples with pulse energies between 0.8 and 1.8 μJ results in intensities spreading from 90 to 270 ± 40 GW/cm^2 and fluences from 1.2 to 3.7 ± 0.7 mJ/cm^2 per pulse. No desorption was observable for pulse energies below 0.7 μJ, whereas significant desorption could be measured for energies above 0.8 μJ. Therefore, the desorption threshold can roughly be estimated to 90 GW/cm^2 and 0.8 μJ pulse energy deposited into the BINOL film. The threshold for direct desorption is expected to depend on intensity, as the cross-section for TPA is intensity dependent. An exact estimation of the threshold intensity for desorption requires a detailed systematic study on intensity and fluence dependent desorption rates, which was beyond the scope of this work.

The desorbed area in figure 31b exhibits a structure similar to its environment, only more transparent, indicating an intact remaining BINOL film. Figure 31a shows four desorption spots at lower magnification, whereas irradiation of the spots in the upper row was performed according to the above mentioned parameters. The spots in the lower row were desorbed using laser pulses with energies beyond 2 μJ leading to higher intensities (> 270 GW/cm^2). They exhibit brown spots in their centre, indicative of carbon accumulation from molecules dissociated by excess multi-photon absorption, in contrast to the intact spots in the upper row. Therefore, no features, which point to destruction, are visible under our experimental conditions below intensities of 270 GW/cm^2.

In order to test potential photodegradation, a small volume of BINOL in ethanol solution was irradiated at high intensities of >420 GW/cm^2 for 30 - 60 min. After dilution and spectroscopic examination, we could not observe any significant changes of the spectrum. In contrast, irradiation of a similar BINOL solution with UV light for 30 min exhibited pronounced indication of photodegradation (see appendix A.6).

Earlier studies on degradation and racemisation of BINOL using UV (248 nm) ns-pulses report thresholds of 22 mJ/cm^2 for both processes. This is above the fluence used for our desorption experiments, however, lower than the fluence underlying the results in figure 59 showing intact desorbed molecules. Generally, the photodegradation threshold in the visible spectral range is

assumed to be at much higher intensities and fluences as in the UV range, as shown in other studies using 80 fs visible pulses, for instance [274]. Another question, which arises, is, whether the fluence or the intensity is the critical parameter for photodegradation. Moreover, reports on desorption yields show different dependence on fluence for ns-pulse and fs-pulse excitation due to a change of the mechanism from single (DIET) to multiple photon excitation (DIMET) [275, 276]. Hence, further examinations of BINOL films after fs-pulse desorption would be an asset.
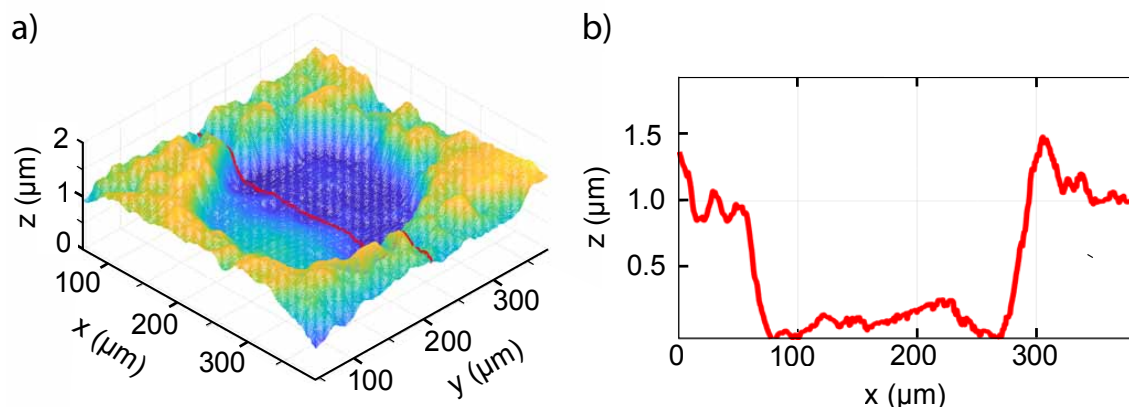
Figure 32 a) Confocal microscopy image of desorption spot. b) Depth profile along the x-axis. The distance of the z = 0 level to the BK7-substrate could not be measured exactly.

Figure 32a is an image of a desorption spot examined with a confocal microscope (Confocal Sp5, Leica, Objective: 40x, oil, lens NA = 1.25; Acquisition Program: Leica Application Suite – Advanced Fluorescence). The occurrence of a hole in the surface confirms that the decrease of SSHG-intensity and the accompanying chiroptical effects (see section 6.4) are connected to the removal of material.

6.3. Optical and structural properties of BINOL

BINOL (1,1'-bi-2-naphthol) is composed of two 2-naphthol monomers. The steric hindrance around the C-C bond, which connects the naphthyl groups, allows the existence of two stable enantiomers, R-BINOL and S-BINOL (see figure 33c) [264]. BINOL can form two types of crystals, ennatiopure R-BINOL and S-BINOL crystals and racemic crystals. At room temperature, enantiomeric pure BINOL crystallises into chiral three-fold screw structures with clockwise and anti-clockwise axes. Inside the helical structure, the molecules are hydrogen-bonded with one of its hydroxy groups to the neighbouring molecule. The helical structures are connected by van der Waals interactions. Mixing of powders or crystallites from both enantiomers induces a molecular movement into racemic crystals within 48 h [263]. The racemic crystals are composed of two alternate clockwise and anti-clockwise arranged forms of two-fold screw axes. In these achiral crystals two molecules of the same enantiomer are connected by two hydrogen bonds each. Thus, the racemic crystal is the more stable form and exhibits a slightly larger density with respect to the enantiopure crystal. It belongs to a different crystal class (racemic: 1.303 g/cm^3, orthorhombic; enantiopure: 1.301 g/cm^3, trigonal), which is further reflected in smaller dihedral angles between the planes of the naphthyl groups (racemic: 90.6°, enantiopure: 101.7°) [264, 263]. Accordingly, the racemic crystal exhibits a higher melting temperature of 215°C compared to the enantiopure crystals with 210°C. The lowest melting temperatures of 197°C can be found at the eutectic points in binary mixtures of R- and S-BINOL with R-BINOL mole fractions of 0.155 and 0.845 [277].
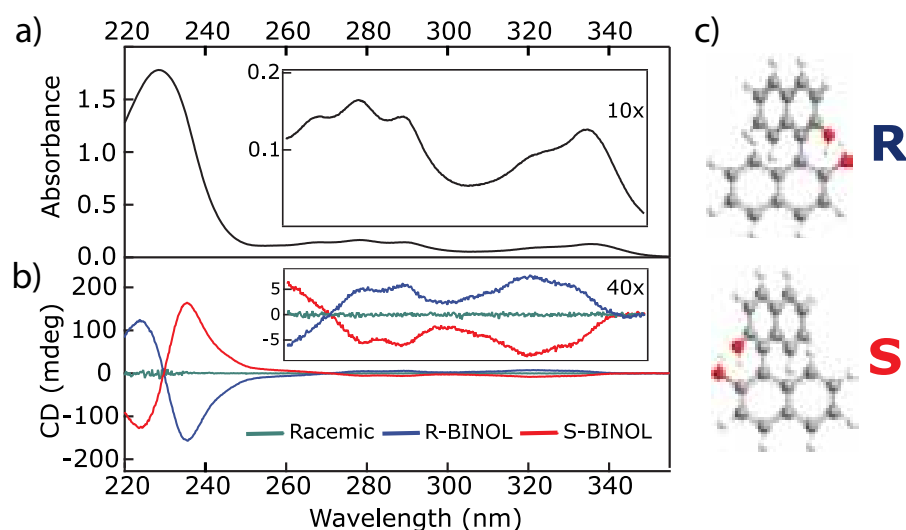
Figure 33 a) Absorption spectrum of BINOL in ethanol solution. The inset shows the absorbance between 260 nm and 350 nm at 10-fold magnification. b) CD spectrum of racemic BINOL (green), R-BINOL (blue) and S-BINOL (red). 40-fold magnified spectra for 260-350 nm are depicted in the inset. c) Chemical structure of R-BINOL and S-BINOL. Adapted and modified from [224]. Copyright Wiley-VCH Verlag GmbH & Co. KGaA. Reproduced with permission.

Absorption and circular dichroism (CD) spectra of BINOL dissolved in ethanol with a concentration of 3.4 mg/l are presented in figure 33a and b. The spectra were recorded with a commercial CD spectrometer from JASCO (J-815). The absorption spectrum in units of OD features an intense peak at 230 nm, which can be assigned to $\pi \rightarrow \pi^*$-transitions polarised along the long axis of the 2-naphthol monomers. Short-axis and off-axis transitions give rise to two broad and structured bands with maxima at 275 nm and 335 nm, respectively [278]. It has to be noted, that absorbance is nearly the same for enantiopure R- and S-BINOL and racemic BINOL (for CP and LP light). Therefore, CD is often given in units of ellipticity θ (see equation 2.59) in mdeg [279, 250] and can be written as

$$\mathrm{CD} = A_{\mathrm{LCP}} - A_{\mathrm{RCP}} = \frac{4\pi\theta(\mathrm{deg})}{180 \cdot ln10} = \frac{\theta(\mathrm{mdeg})}{30.3}. \tag{6.8}$$

As shown in section 2.2.7, CD is proportional to the optical rotation strenght R (see equations 2.58 and 2.60), which is equal to the imaginary part of the product of induced electric- and magnetic-dipole moments. Hence, sign as well as strength of the CD depend on the respective transition. The CD spectra of R-Binol and S-BINOL are depicted in figure 33b. For a wavelength range from approximately 270 nm up to 340 nm, the CD spectrum exhibits maximum absolute values below 10 mdeg, whereas its sign is positive for R-BINOL and negative for S-BINOL. The definition of CD in units of mdeg (see equation 6.8) reflects the low strength of linear CD with respect to SHG-CD and SHG g-factors. The latter are up to 100-fold enhanced, because SHG-CD is electric-dipole allowed, whereas linear CD is caused by the weaker magnetic-dipole transitions (see section 2.2.7). However, CD spectra differ also depending on the method of excitation and detection. When recording CD upon two-photon absorption (TPA) in the TPA range from 220 nm to 330 nm, the sign of TPA-CD is negative for S-BINOL and positive for R-BINOL [280]. For SHG-CD values on R-BINOL monolayers, J. D. Byers et al. report positive values of SHG-CD in the spectral range of 318-345 nm and 288-298 nm, and negative values for 300-319 nm. In contrast, our collaborators recently showed positive values for thin films of S-BINOL and negative values for R-BINOL in the spectral range beyond 270 nm [262].

The sign of SHG-CD (see equation 2.68) or the related anisotropy factor (equation 2.69) further depends on the definition of LCP and RCP (see section 2.4.2). For our experiments, we defined the handedness according to the alignment of the waveplate (see appendix A.2.1).

Figure 34 shows the SSHG-spectrum of BINOL, which was measured with a picosecond-laser system in the setup of our collaborators, in comparison to the absorption spectrum [281, 262]. Although significant SSHG-intensity is detectable up to 340 nm, the spectral shape in the range of the two lowest absorption bands does not exhibit two distinct bands but resembles rather a single broad band with some minor structure.
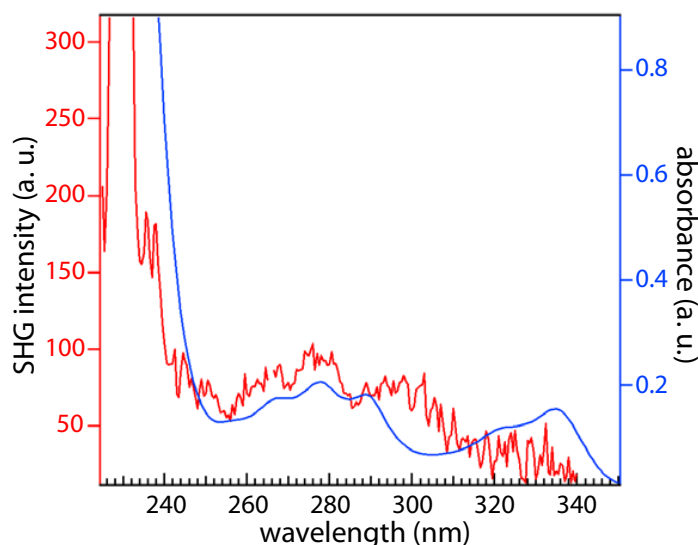
Figure 34 SSHG spectrum of a BINOL film (prepared according to section 6.2.3) measured with a picosecond-laser system in the setup of our collaborators [262] is shown in red. The blue line refers to the absorption spectrum of BINOL. Adapted from [281]. Copyright Wiley-VCH Verlag GmbH & Co. KGaA. Reproduced with permission.

SHG-CD results of enantiopure and racemic BINOL films

With regard to experiments on enantiospecific desorption, a characterisation of the prepared BINOL films (see section 6.2.3) with the same spectroscopic method is essential. The anisotropy factors g of thin films of enantiopure and racemic BINOL were determined by means of resonant SHG-CD spectroscopy using 600 nm and 650 nm excitation pulses at intensities below the desorption threshold (see section 6.2.2). The order of LCP and RCP was altered when examining a new spot to further minimise systematic errors.

Fig. 35	g-values	mean g	σ
a)	S-BINOL (all)	-0.091	0.305
a)	R-BINOL (all)	0.198	0.451
b)	S-BINOL (large cryst.)	-0.491	0.274
b)	R-BINOL (large cryst.)	0.924	0.423
c)	Racemic BINOL	0.007	0.090
d)	10%-ee S-BINOL	-0.045	0.072
d)	10%-ee R-BINOL	0.092	0.082

Table 7 Mean g-values and standard deviations σ of enantiopure (S-BINOL and R-BINOL), racemic BINOL, 10%-ee S-BINOL and 10%-ee R-BINOL films extracted from figure 35.
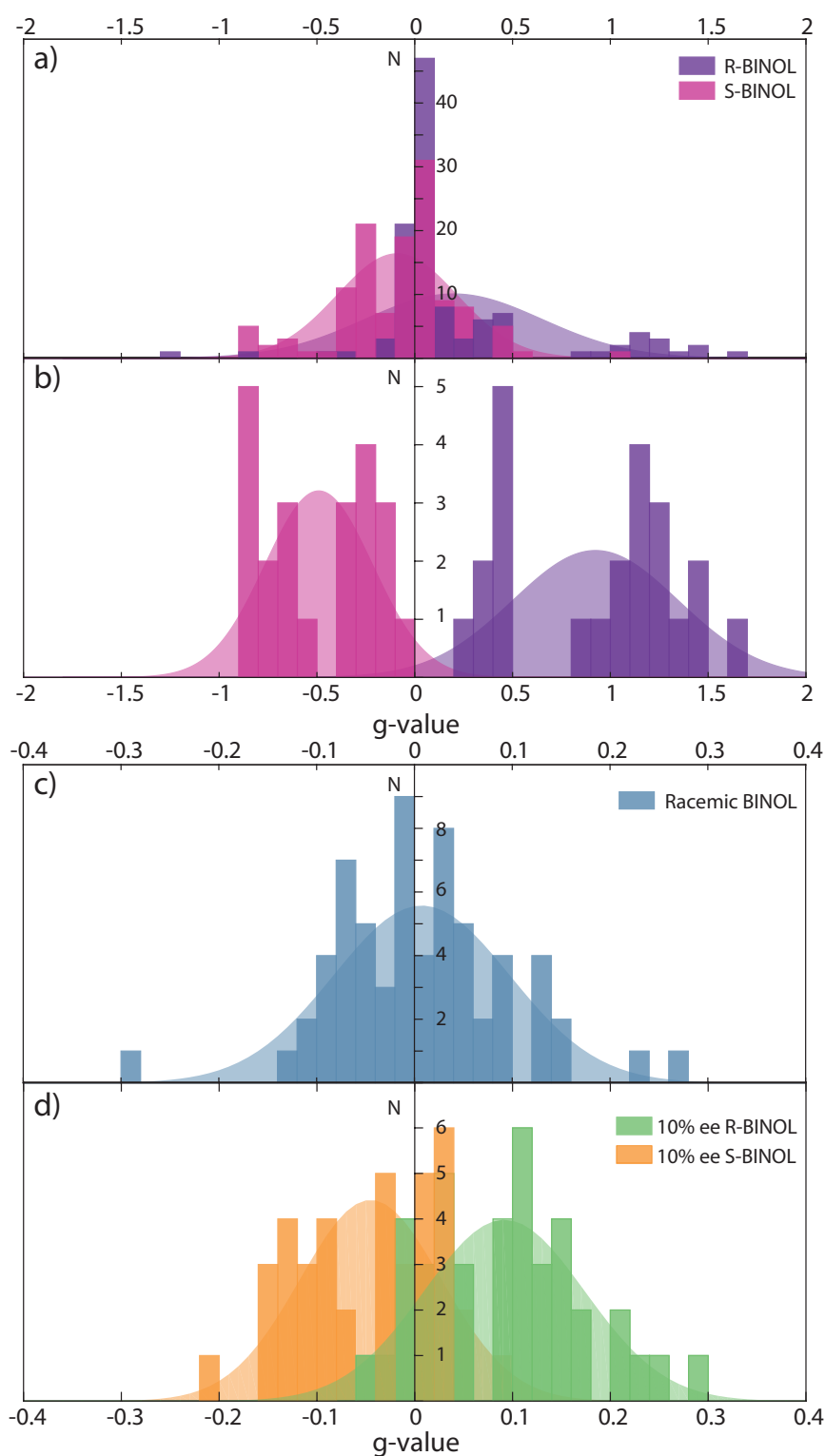
Figure 35 Distribution of anisotropy factors of enantiopure, 10% ee and racemic BINOL (N stands for the number of results with the respective value of g). The curves over the light shaded areas denote normal distributions. a) Anisotropy factors of S-BINOL (pink) and R-BINOL (violet) including samples with crystals of sizes in the range of the exciting laser spot, resulting in a variety of g-values close to zero with large standard deviations. b) Anisotropy factors from enantiopure samples with crystals larger than the laser spot. The mean g-values of S-BINOL (22 spots on 3 samples, pink) and R-BINOL (23 spots on 5 samples, violet) deviate significantly from zero. c) Anisotropy factors of racemic BINOL (blue) with a mean close to zero. d) Anisotropy factors of samples with 10% ee of S-BINOL (orange) and R-BINOL (green).
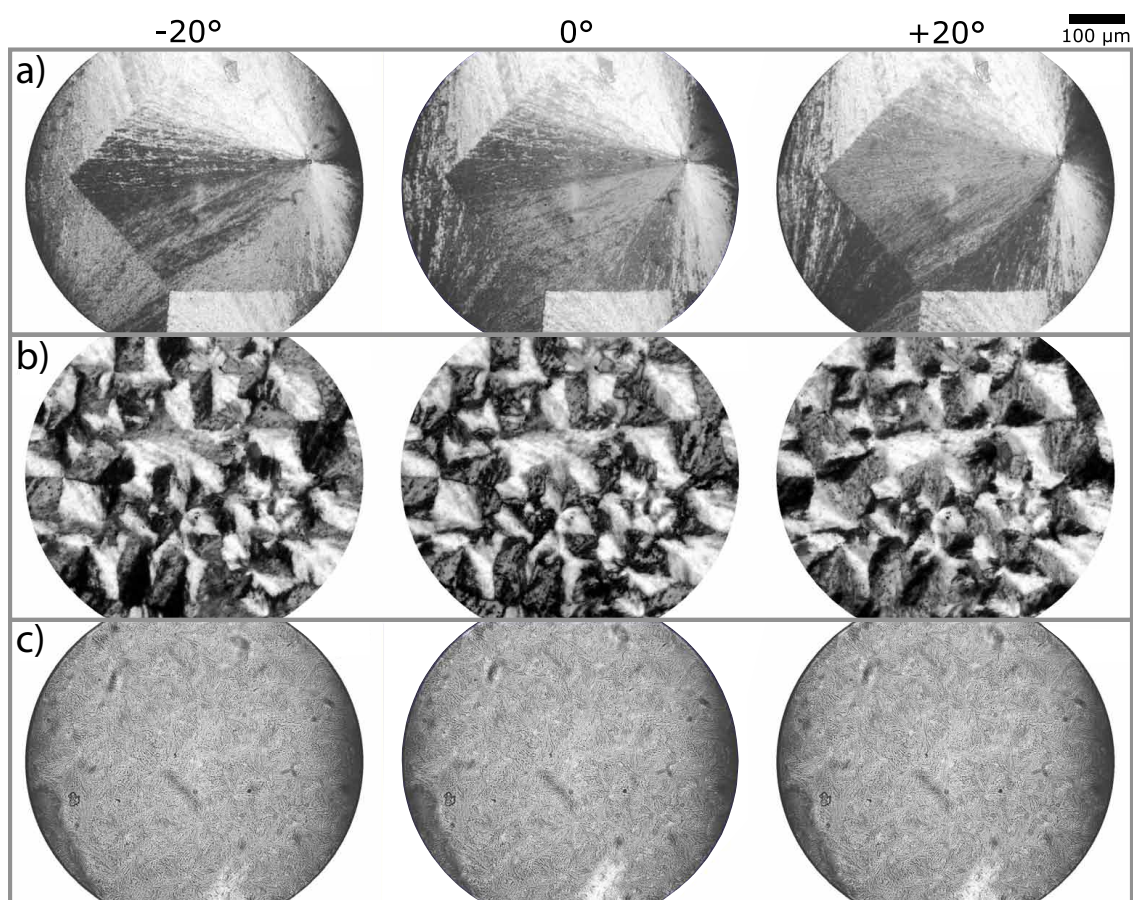
Figure 36 Images of thin films of R-BINOL (a), S-BINOL (b) and racemic BINOL (c) on BK7 glass substrates examined in a polarized light microscope (40x magnification). The analyser is rotated by an angle of -20° (left), 0° (centre) and +20° (right), with 0° being the position of minimum transmission. Adapted from [281]. Copyright Wiley-VCH Verlag GmbH & Co. KGaA. Reproduced with permission.

Figure 35a illustrates the detected anisotropy factors in films of S-BINOL and R-BINOL. The data indicate a strong variation of the g-values obtained in different samples and at different positions in the same sample. The origin of this phenomenon can be elucidated by examination of BINOL films with a polarised light microscope (Leica DMI 6000 B) (see figure 36a, b). The microscope images reveal the formation of large crystals with an optical active macrostructure, which make a reliable determination of anisotropy factors very difficult. Alternating bright and dark areas on the films of both S- and R-BINOL observed for the crossed polariser and analyser pair are indicative of the formation of chiral domains. Rotating the analyser around its normal axis with respect to the polariser leads to a change of the pattern. While some of the domains brighten, when turning the analyser from -20° to +20°, others darken, demonstrating the existence of the opposite chirality on the surface of the same enantiopure R-BINOL sample (see figure 36a). The corresponding data on S-BINOL measured with the same magnification is shown in figure 36b. Obviously, S-BINOL film also forms a crystal structure with complex chirality, however, both the crystals and crystal domains are significantly smaller than those observed on R-BINOL in agreement with other reports [282]. The existence of crystal domains with opposing chirality

illustrates the challenge of measuring reliable g-values on pure-enantiomer R- and S-BINOL films, as the relation of the diameter of the laser spot and the crystal has to be considered. If the exciting laser spot covers mostly a single crystal, the anisotropy factor will not reflect the microscopic g-value from a single molecule. The majority of samples in our study shows g-values $|g| < 0.1$ for both R- and S-BINOL measured at different spots across the surface. Determination of crystal diameters on the microscope images leads to values of 150-300 μm and 100-200 μm for the majority of R-BINOL and S-BINOL samples, respectively, i.e. in the range of the laser spot diameter (90-120 μm at FWHM, see section 6.2.2). This confirms the assumption that the laser is exciting different domains of one crystal simultaneously leading to an average value of g close to zero (see table 7).

Usually, the generated enantiomeric excess (ee) upon enantiospecific desorption of racemic BINOL should be directly provided by comparison with the g-values of the enantiopure samples, measured by SHG-CD with the same setup. Therefore, leaving the size of the laser focus constant, sufficiently large crystals on enantiopure samples are essential to determine reliable g-values in single domains of enantiopure samples. Eight of our samples exhibit large crystals with diameter of >1 mm for R-BINOL and >200 μm for S-BINOL, i.e. much larger than the average laser spot diameter. Hence, the g-value of single domains with the same chirality can be obtained. The distribution of the g-values from these samples is presented in figure 35b. In case of R-BINOL a mean g-value of 0.92 can be extracted, while the mean g-value for S-BINOL is -0.49 (see table 7), leading to an absolute mean value of g_p = 0.71, which was used as reference for the determination of ee. While the absolute value agrees with earlier SHG-CD measurements [52], no difference between R- and S-BINOL is reported. This asymmetry, i.e. smaller absolute values for S-BINOL, may be related to the smaller size of the S-BINOL crystals. Commercially available enantiomers often contain small amounts of impurities. We believe this to be the major cause of the observed differences of the crystal size and g-values.

In contrast to the enantiopure samples, polarisation-resolved microscopy on films of racemic BINOL (figure 36c) does not indicate the formation of large optically active crystals. The detected anisotropy factors for racemic films show a normal distribution of g-values around zero with a standard deviation of 0.09, much smaller than for enantiopure samples (see figure 35c and table 7). Similar statistical distributions for racemic samples of binaphthyl have been shown before. Pincock et al. report on spontaneous optical resolution when inducing crystallisation by supercooling of binaphthyl melt [283]. In the binaphthyl melt at high temperatures, the formation of enantiopure crystals is favoured with respect to racemic crystals in contrast to the solid phase at room temperature. Moreover, racemisation is very rapid in the melt. Thus, random nucleation into a specific crystallite and further growth to an enantiopure crystal can result in optical resolution [283, 284]. A similar process could occur in our racemic films. Although the energy deposited by the laser pulses is not sufficient for melting, random nucleation into enantiopure crystallites may also occur in our films during the proceeding crystallisation process under

atmospheric conditions. Because the racemic phase is favoured, these crystallites are probably too small for the formation of a macrostructure. Another issue is a possible measurement error. Desorption, which occurs during the time for recording 15-20 spectra at each polarisation, can give rise to a small error err_{des}, which is usually below 0.01 (see appendix A.3). Although we tried to adjust the excitation intensity during the g-factor measurement below the desorption threshold, we can not completely exclude the occurrence of this error, which can also explain partly the statistical distribution.

In summary, both enantiopure and racemic films show statistical distributions around a central value, whereas their width is much smaller in racemic films. In expectation of getting more reliable results from samples with a very similar composition as racemic BINOL, we examined films with an ee of only 10% of either R- or S-BINOL. The normal distributions of 10%-ee S-BINOL and 10%-ee R-BINOL are centred around g-values of -0.045 and 0.092, respectively (see figure 35d and table 7). Standard deviations from this value are much smaller than in enantiopure sample. Hence, the 10%-ee samples allow an exacter estimation of generated ee in enantiospecific desorption experiments.

It has to be noted that in the supporting information to our publication [281], S-BINOL and R-BINOL were accidentally exchanged, hence, leading to different signs than in the main paper and in this work.

SHG-ORD results of enantiopure and racemic BINOL films and correlation with g-values

Furthermore, we examined our BINOL films with SHG-ORD spectroscopy as described in section 6.2.2. SHG-ORD is the nonlinear analogue to optical rotation dispersion (ORD) (see section 2.2.7). The specific rotation $[\alpha]_D^T$ is defined as the angle, by which linear polarised light with a wavelength of 589 nm is rotated upon passing a path of 1 dm through the solution at temperature T. Dissolved in THF (tetrahydrofuran) with a concentration of 1 g/ml, S-(R-)BINOL has a specific rotation of $[\alpha]_D^{22}$= -(+)34° [285]. Racemic BINOL does not cause an ORD effect. Recent SHG-ORD experiments by P. Heister et al. show rotation angles of more than -(+)30° for films of less than 10 monolayers of S-(R-)BINOL, and zero rotation for racemic films, at an incidence angle of 25° of the incoming 674 nm laser pulse [77]. Hence, analogue to SHG-CD, the effects measured by SHG-ORD are much larger than effects from linear ORD measurements.

Figure 37a shows the rotation angles δ of S-BINOL and R-BINOL films, which are obtained from an ellipse fit (see equation 6.5), in dependence of the g-value measured at the same position. Because specific rotation is defined as positive or negative rotation with respect to 0°, rotation angles 181° to 360° (cf. figure 30) are translated to the angles -179° to 0° in figure 37. The positive direction of the azimuthal angle φ is illustrated in figure 54c. Both S-BINOL and R-BINOL
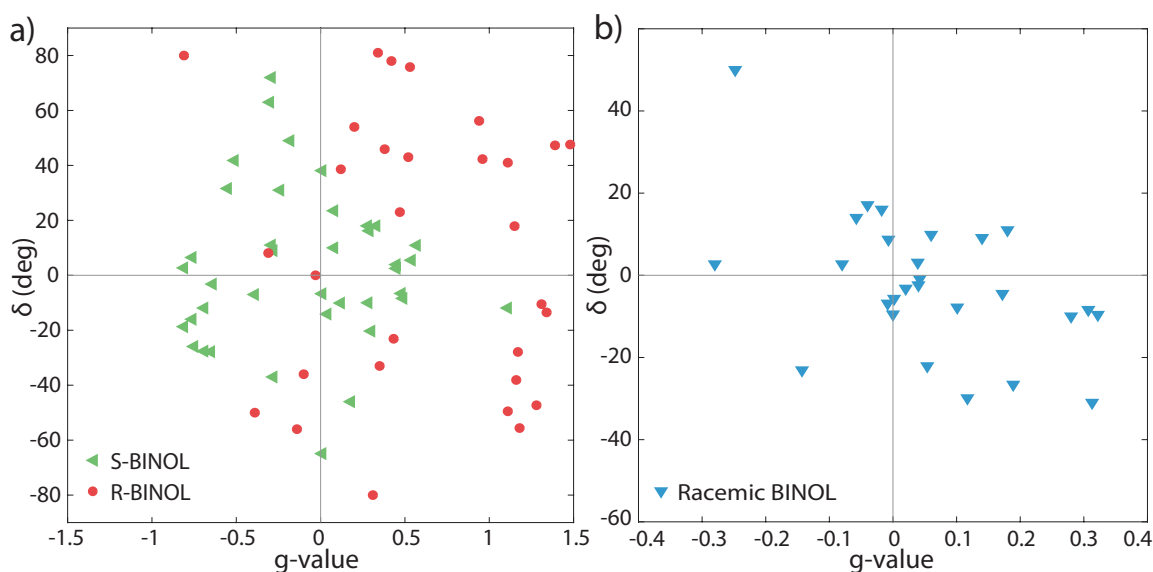
Figure 37 Rotation angles δ of BINOL films as a function of g-value. a) S-BINOL (green triangles), R-BINOL (red circles). b) Racemic BINOL (blue triangles).

	mean δ	$\sigma(\delta)$	mean g	$\sigma(g)$	$r_{\delta g}$
S-BINOL	2.3	28.2	-0.097	0.484	-0.002
R-BINOL	8.6	48.5	0.596	0.614	-0.075
Racemic	-2.1	17.1	0.055	0.154	-0.501

Table 8 Mean rotation angles and their standard deviations $\sigma(\delta)$, mean g-values of the shown subset and their standard deviations $\sigma(g)$, and the corresponding correlation coefficients $r_{\delta g}$ of enantiopure S-BINOL and R-BINOL, and racemic films extracted from figure 37.

reveal a large spreading of rotation angles between -90° and 90° (see table 8). Therefore, it was not possible to assign the enantiomers to specific rotation angles. We determine mean values of 2.3° for S-BINOL and 8.6° for R-BINOL. Additionally to the determination of the rotation angle, the g-value was measured at the same spot. In order to examine a possible linear dependence of these two parameters, we calculated the corresponding correlation coefficients. The correlation coefficient is a measure for the statistical correlation of two parameters a and b and their mean values $\bar{a}$ and $\bar{b}$, and is defined as:

$$r_{ab} = \frac{\sum (a - \bar{a})(b - \bar{b})}{\sqrt{\sum (a - \bar{a})^2 \sum (b - \bar{b})^2}}.$$ (6.9)

We obtain values of $r_{\delta g}$ = -0.002 for S-BINOL, and $r_{\delta g}$ = -0.075 for R-BINOL. Correlation coefficients close to zero indicate that there does not exist any significant correlation. The large spreading of rotation angles is presumably caused by the chiral macrostructure of different size and handedness as shown in figure 36. The missing correlation indicates that the crystalline structure has a different effect on SHG-ORD as on SHG-CD. This finding emphasises the

assumption that the results from both spectroscopic methods do not reflect the molecular composition of our enantiopure films.

Rotation angles determined in racemic films are distributed between -31° and 50° with a mean of -2.1° (see figure 37b). Similar to the g-values, the width of the distribution is smaller than for enantiopure films (see table 8). Hence, random nucleation into enantiopure crystallites can be a possible origin for this phenomenon. Similar to the enantiopure samples, we can not observe any significant linear relation between the two parameters. However, the correlation coefficient of -0.501 is larger. Because our racemic films do not show an optically active macrostructure, we assume a larger contribution of the molecular composition to the occurrence of SHG-ORD and SHG-CD effects than in our enantiopure samples.

6.4. Enantiospecific desorption using circularly polarised laser pulses

The objective of our experiments is to test, whether resonant irradiation of a racemic film of chiral molecules, deposited on an achiral surface, with circularly polarised laser pulses can induce preferential desorption of one of the two enantiomers, and thus, generate an enantiomeric excess (ee) in the remaining film. The experiments on enantiospecific desorption are carried out by irradiation of a spot on the BINOL film with CPL of one specific handedness (LCP or RCP). The enantiospecific character of desorption is examined by measuring the anisotropy factor before and during the desorption process. In order to determine the generated ee, the anisotropy factor of enantiopure samples was measured under similar experimental conditions (see section 6.3). Pulse energy and focus position were adjusted according to sections 6.2.2 and 6.2.4 below the thresholds for self-focusing, supercontinuum generation, nonlinear optical responses from BK7 and photodamage of the molecules, however above the threshold of photodesorption. Based on the above described optical properties, we used excitation pulses at central wavelengths of 600 nm and 650 nm to irradiate the samples with pulse energies of 0.8 - 1.8 μJ according to intensities in the range of 90 - 270$\pm$40 GW/cm^2 (see section 6.2.4) for the following SSHG-spectroscopy experiments. This allows stable and easily reproducible excitation above the onset of TPA as well as detection in a spectral range with sufficient quantum efficiency of our detector. The experiments were performed ex-situ under atmospheric conditions. Due to the fast crystallisation process under these conditions, the examined films can be considered to exhibit a crystalline structure.

6.4.1. Second-harmonic generation circular dichroism spectroscopy

The measurement principle of the desorption experiment is illustrated in figure 38. The figure on the left side (a) shows an experiment, where the sample, i.e. a spot of $\sim$250 μm diameter on the surface of the racemic film, was irradiated for a desorption time t_d of 150 min with LCP pulses. The figure on the right side (b) shows the desorption of another spot on the sample for a desorption time t_d of 120 min with RCP pulses. In the beginning (t_d = 0) and after distinct time steps during the experiment, desorption was interrupted and the anisotropy factor was determined by detection of the chiroptical response upon excitation with RCP and LCP light as described in section 6.4.1. Figures 38a and b show the respective normalised spectra of the SSHG response $S^{n,L}(\lambda)$ and $S^{n,R}(\lambda)$ (L = LCP, R = RCP) after each time step t_d, and the corresponding (normalised) integrated intensities $I_{SHG}^{n,L/R} = \int S^{n,L/R}(\lambda)d\lambda$, which decay to less than 40% of their initial value during the experiments. Already in the second pair of LCP and RCP spectra in figure 38a, after t_d = 10 min irradiation, the intensity for LCP excitation is significantly reduced with respect to the RCP spectrum. This difference in intensity persists until

103
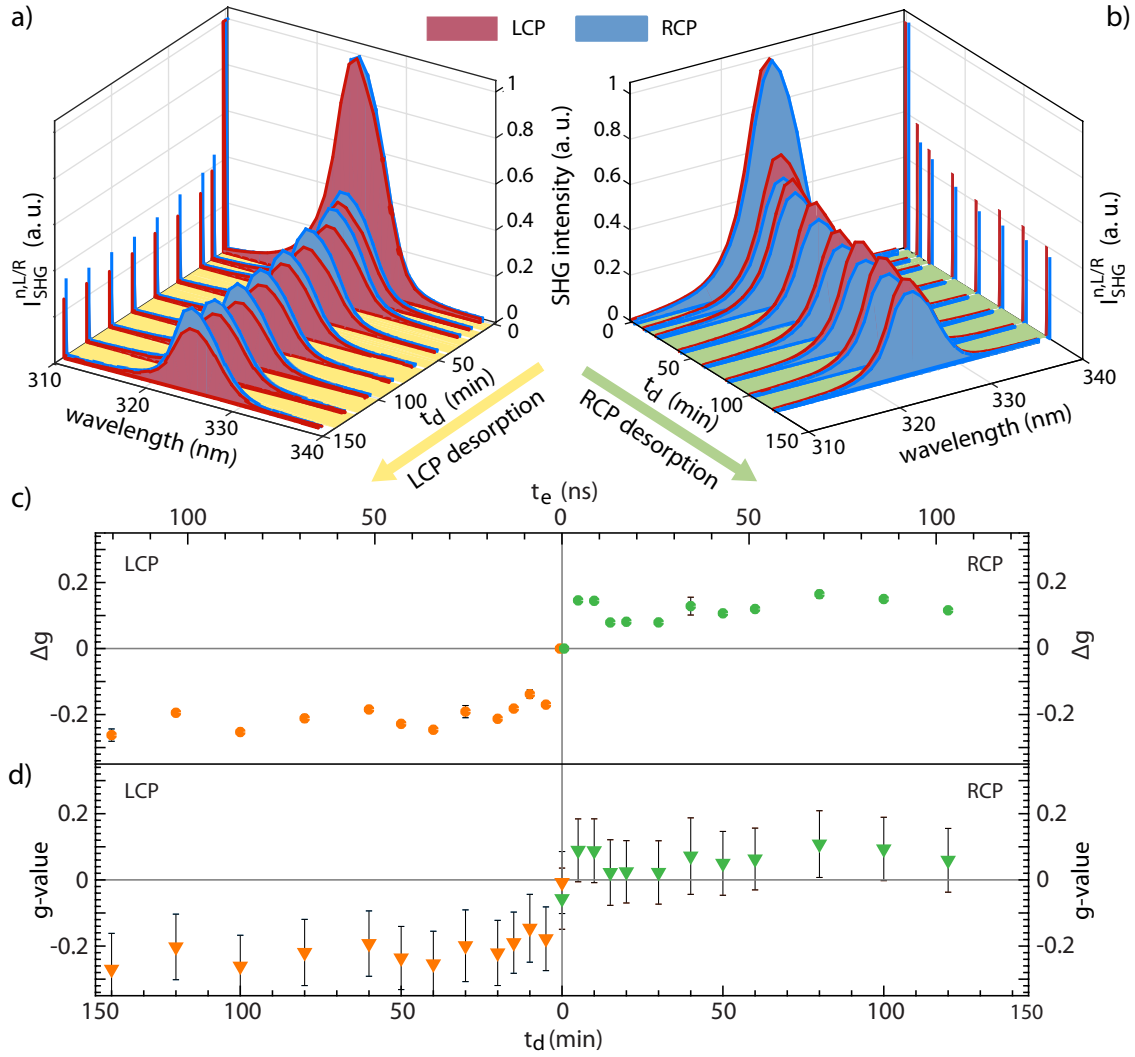
Figure 38 Enantiospecific desorption experiment. a, b) Measurement principle. Irradiation of a racemic sample with LCP (a, yellow) and RCP (b, green) pulses above the desorption threshold. Normalised mean spectra $S^{n,L}(\lambda)$ (red) and $S^{n,R}(\lambda)$ (blue) (L = LCP, R = RCP) are recorded at distinct time steps of t_d during the desorption process. The red (LCP) and blue (RCP) vertical bars to the left (a) and to the right (b) of the spectra represent the respective intensities integrated over the depicted wavelength range: $I^{n,L}_{SHG}(t_d)$ and $I^{n,R}_{SHG}(t_d)$. Spectra and intensities for t_d = 5, 15, 30, 50 min are left out for clearness. c, d) Corresponding induced anisotropy factors $\Delta g(t_d)$ (equation 6.10) (c), and g-values $g(t_d)$ (equation 6.11)(d) with the respective random and systematic measurement errors. Errors below 0.03 are not plotted for clarity reasons. $err_{surf} = 0.09$ for both $g^{LCP}(t_d)$ and $g^{RCP}(t_d)$, $err^{LCP}_{stat}(t_d) \leq 0.02$, $err^{RCP}_{stat}(t_d) \leq 0.026$, $err^{LCP}_{des}(t_d) \leq 0.000$, and $err^{RCP}_{des}(t_d) \leq 0.001$ for all data points.

the end of the measurement at t_d = 150 min. The intensities $I^{n,L/R}_{SHG}$ reflect this observation. The spectra in figure 38b exhibit the opposite effect upon desorption with RCP pulses. Figures 38c and d show the corresponding induced change in g-value $\Delta g(t_d)$ and the absolute anisotropy factors $g(t_d)$, which are calculated according to

$$\Delta g(t_d) = 2\frac{I^{n,L}_{SHG}(t_d) - I^{n,R}_{SHG}(t_d)}{I^{n,L}_{SHG}(t_d) + I^{n,R}_{SHG}(t_d)}, \tag{6.10}$$

and

$$g(t_d) = 2\frac{I_{\mathrm{SHG}}^{\mathrm{LCP}}(t_d) - I_{\mathrm{SHG}}^{\mathrm{RCP}}(t_d)}{I_{\mathrm{SHG}}^{\mathrm{LCP}}(t_d) + I_{\mathrm{SHG}}^{\mathrm{RCP}}(t_d)}. \tag{6.11}$$

Herein, $I_{\mathrm{SHG}}^{\mathrm{LCP/RCP}}(t_d)$ are the integrated intensities over the measured SSHG spectra, and

$$I_{\mathrm{SHG}}^{\mathrm{n,L/R}}(t_d) = \frac{I_{\mathrm{SHG}}^{\mathrm{LCP/RCP}}(t_d)}{I_{\mathrm{SHG}}^{\mathrm{LCP/RCP}}(0)}, \tag{6.12}$$

represent their normalised values. The composition of the measurement errors $err(t_d) = err_{\mathrm{stat}}(t_d) + err_{\mathrm{des}}(t_d) + err_{\mathrm{surf}}(t_d)$ is described in appendix A.3. Standard deviations of $I_{\mathrm{SHG}}^{\mathrm{LCP}}$ and $I_{\mathrm{SHG}}^{\mathrm{RCP}}$ could be reduced to below 1% by sequential recording and averaging of multiple spectra. Hence, propagation of errors resulted in uncertainties err_{stat} of well below 0.03 for the g-values and Δg. Desorption during the duration of the g-value measurement, which is 1 s for each of the 15-20 spectra, leads to a small systematic error err_{des}. In order to keep err_{des} small, i.e. below 0.01, the intensity was adjusted to ensure low desorption rates and the order of LCP and RCP measurements was alternated for each g-value determination in a desorption series. Maximum errors occurred in the initial values at $t_{\mathrm{d}} = 0$, as the desorption rate is largest in the beginning. Hence, for a conservative error estimation the first set of spectra is used for determination of err_{des} (see appendix A.3). The inhomogeneity of the BINOL films causes an additional random error err_{surf} to g. Its exact determination is difficult because of entanglement with err_{des}. As reference, we apply the standard deviation of 0.090, which is extracted from the distribution in figure 35c. This error does not appear in Δg, since the use of normalised intensities in the calculation of Δg leads to an initial value of $\Delta g(0) = 0$. Whereas the desorption time t_{d} denotes the time passing during the experiment, the sample is only exposed to laser light for the 13.8 fs duration of a pulse at a repetition rate of 1 kHz (for estimation of the pulse duration see appendix A.1). Hence, a desorption time of 150 min corresponds to a light exposure time t_{e} of 124 ns (see figure 38b top axis). It has to be noted that relaxation and thermalisation processes in the BINOL film have not completed after the duration of the laser pulse. Therefore, t_e is not a suitable parameter when describing the observed phenomena and is not considered further.

The induced changes in g-value $\Delta g(t_{\mathrm{d}})$ exhibit negative signs for LCP desorption with a maximum absolute value of 0.262 after a desorption time $t_{\mathrm{d}} = 150$ min (see figure 38c, left panel). Negative signs also occur for the g-values $g(t_{\mathrm{d}})$ calculated from the measured intensities, whereas the values are only shifted by the initial g-value $g(0) = -0.008$ (see figure 38d, left panel). In contrast, we observe positive $\Delta g(t_{\mathrm{d}})$ and $g(t_{\mathrm{d}})$ upon desorption with RCP pulses. The maximum Δg of 0.165 and corresponding g of 0.108 is measured after 80 min desorption (see figures 38c and d, right panel). Unlike the smooth exponential decay of the intensities $I_{\mathrm{SHG}}^{\mathrm{n,L/R}}$ with desorption time, the induced g-values $\Delta g(t_{\mathrm{d}})$ rise very fast to nearly maximum values within the first 5 min, and further vary around a constant value of -0.206 (LCP) and 0.120 (RCP). This unevenness can not be explained with the measurement errors. A possible explanation is

given in section 6.4.5. Differences in the maximum absolute values of $\Delta g(t_{\mathrm{d}})$ for LCP and RCP desorption are presumably caused by slightly different irradiation and desorption intensities, and thus, desorption rates (see figure 39).
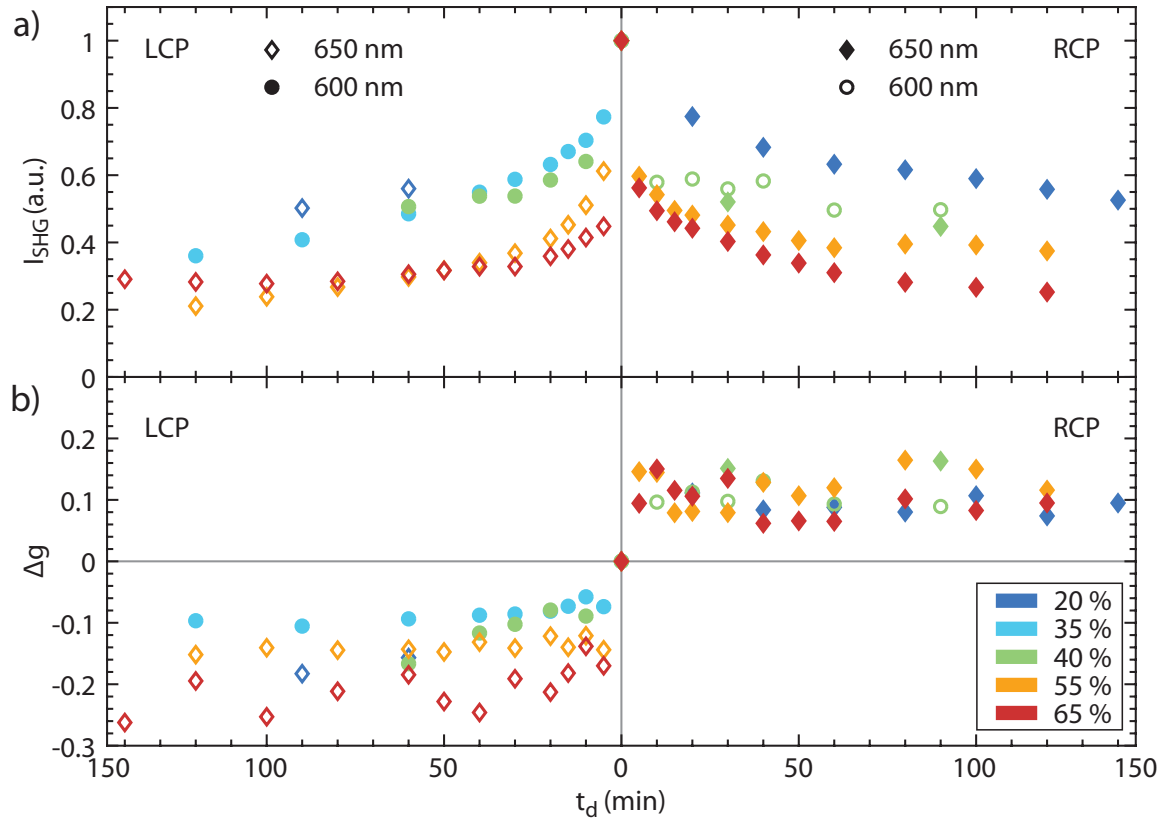
Figure 39 Overview of all desorption scans, satisfying the requirement $|g(0)| < 0.1$, for irradiation with LCP pulses (left panel) and RCP pulses (right panel) at 20° incidence at central wavelengths of 600 nm (circles) and 650 nm (diamonds). a) SSHG intensity $I_{\mathrm{SHG}} = (I_{\mathrm{SHG}}^{\mathrm{LCP}} + I_{\mathrm{SHG}}^{\mathrm{RCP}})/2$ for proceeding desorption time t_d. b) Corresponding values for the induced change of anisotropy factor Δg. The colours represent the percental decay of I_{SHG} within the first 20 min.

Figure 39 gives an overview of ten desorption scans for irradiation with LCP pulses (left panel) and RCP pulses (right panel) including the two data sets from figure 38. In figure 39a, the mean normalised SSHG intensity for LCP and RCP excitation,

$$I_{\mathrm{SHG}} = \frac{1}{2}(I_{\mathrm{SHG}}^{\mathrm{n,L}} + I_{\mathrm{SHG}}^{\mathrm{n,R}}), \tag{6.13}$$

is shown in dependency of desorption time t_{d}. Desorption of BINOL molecules leads to a removal of material in the irradiation spot (see figures 31 and 32). The SSHG intensity serves as a measure for the thickness of the remaining film and the desorption yield. Empirically, we determined a linear dependence of I_{SHG} on the film thickness in the studied range of 0 - 1.5 μm during evaporation (see figure 25). However, the exact dependency in the crystallised film may deviate from linear and still has to be determined (see section 6.4.5). We observe symmetric decay behaviour for LCP and RCP desorption with proceeding desorption time t_d. The spreading

of the data is mainly due to different excitation intensities resulting in different desorption rates. The colour code reflects the strength of the desorption by sorting the data according to the percental decay of the initial SSHG intensity within the first 20 min. The corresponding values of $\Delta g(t_{\mathrm{d}})$ are depicted in 39b and clearly exhibit antisymmetric evolution for LCP and RCP irradiation. Following a fast rise within the initial 30% decay of I_{SHG}, i.e. during the first 10 to 20 min, the induced anisotropy factors of all data sets exhibit a saturation around a medium value until the end of the measurement range. The largest absolute values of Δg (LCP: -0.260, RCP: 0.165) can be obtained from the two data sets from figure 38, here shown as red (LCP) and orange (RCP) 650 nm traces. Whereas the intensities decay smoothly (with the only exception of the green 600 nm scan from the RCP data), some of the Δg kinetics exhibit unevenness as observed in figure 38. The data convey the impression that larger desorption strengths result in larger Δg. Besides, Δg seem to be smaller for 600 nm desorption than for 650 nm desorption. However, for obtaining a general dependency of $\Delta g(t_{\mathrm{d}})$ on desorption strength or rate and on the excitation wavelength, a systematic examination of this relation is required, which was not the aim of this proof-of-principle study.

In order to ensure an initially racemic, i.e. achiral, sample material, the data presented in figure 39 is limited to desorption series on spots, where we determined an initial anisotropy factor close to zero: $|g(0)| < 0.1$. It has to be noted that in most of the desorption series, the g-value measurement started with the same polarisation as was applied for desorption. Despite adjustment of excitation intensities low enough to keep err_{des} below 0.01, this leads to a weak anti-correlation of $g(0)$ and Δg. A complete overview of all measured desorption series is shown in figure 40 (for excitation and irradiation with 600 nm and 650 nm pulses). Maximum measured values of Δg are given as a function of $g(0)$. The correlation coefficient (equation 6.9) r_g = -0.640 for the correlation of $g(0)$ and Δg confirms the necessity of introducing a criterium for significant change in g-value during irradiation. Therefore, the data in figure 39 is further limited to desorption series with $|\Delta g| > |g(0)|$. Nevertheless, the overview in figure 40 emphasizes the preference for generating positive Δg upon irradiation with RCP pulses and negative Δg upon irradiation with LCP pulses, as only less than 10% of all data points deviate from this result.

Desorption at irradiation intensities close to the presumed desorption threshold did neither lead to significant decay of $I_{\mathrm{SHG}}(t_d)$, i.e. less than 5% within the first 10 min, nor induce a significant change in $\Delta g(t_{\mathrm{d}})$ (see figure 41a). This supports the hypothesis that substantial desorption is required in order to induce a significant change in g-value.

Moreover, samples measured within the first two days after preparation, which is the time scale for complete crystallisation at room temperature [263], did not show any decay of SSHG intensity either. Instead, the SSHG signal increased under irradiation (see appendix A.4). Presumably, irradiation with laser pulses induces or enforces the completion of forming crystals. Because highly ordered structures [75, 76] enhance the SSHG intensity, we assume that the
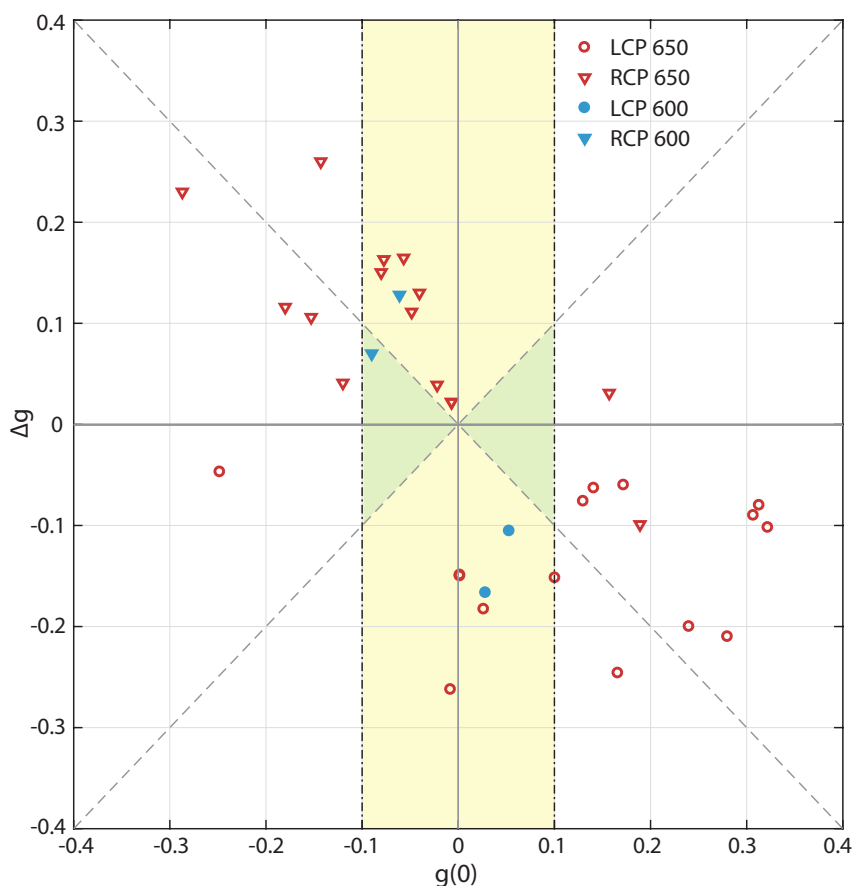
Figure 40 Correlations of initial g-value and maximum Δg for desorption series irradiated with LCP (circles) and RCP (triangles) pulses at central wavelengths of 600 nm (blue) and 650 nm (red). The dashed lines denote $\Delta g = g(0)$ and $\Delta g = -g(0)$. The limits of our criterium $|g(0)| < 0.1$ are depicted as vertical dot-dashed lines. The domain with $|\Delta g| > |g(0)| < 0.1$, satisfying both criteria, is shaded in yellow colour. The green shaded area comprises desorption series with $|g(0)| < 0.1$, but $|\Delta g| < |g(0)|$. Correlation coefficient of all data: $r_g(g(0), \Delta g)$ = -0.640.
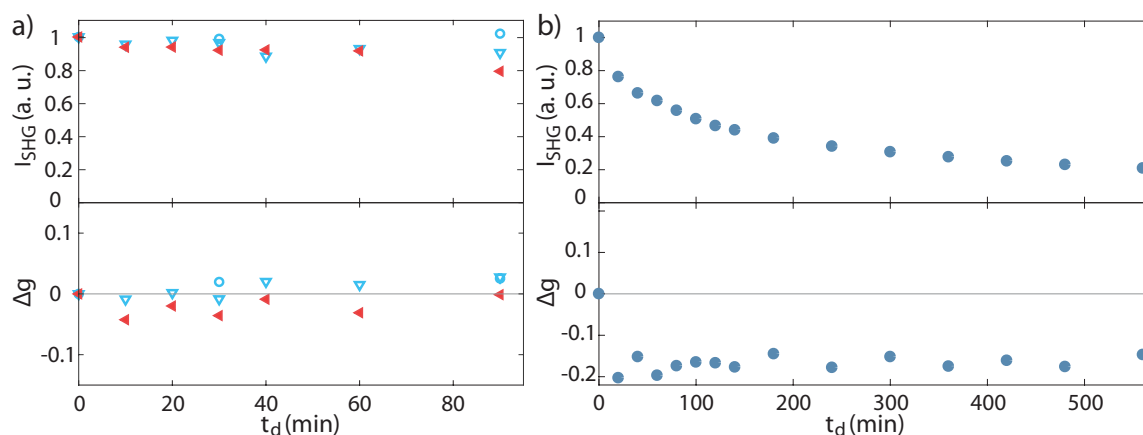
Figure 41 a) Racemic samples irradiated with RCP (red) and LCP (blue) pulses (650 nm) close to the desorption threshold. b) Same sample, different spot, irradiated with LCP pulses (650 nm) at higher intensities for 9 h.

observed effect of intensity increase can be related to the larger degree of orientation during the crystallisation process. Whether desorption occurred additionally to crystallisation during this process, cannot be deduced from these desorption series. It has to be noted that crystallisation may further proceed beyond two days. Observation of significant decrease of the SSHG signal during irradiation, however, indicates that the contribution of crystallisation plays a minor role to the evolution of $I_{\mathrm{SHG}}(t_d)$.

In order to examine the long-time behaviour of the evolution of induced changes in g-value, we recorded the SSHG response for 9 h (see figure 41b). Within this time, the intensity decays to 0.2, i.e. the BINOL film within the irradiated spot is still not desorbed completely. The change of anisotropy factor, Δg, does not exceed a value of -0.21 reflecting the observed saturation effect from figure 39b. We further observe that Δg decreases slowly from its maximum after 10 min to lower values with proceeding desorption time.

In summary, symmetric decay of SSHG intensity and simultaneous antisymmetric evolution of Δg during desorption unambiguously demonstrates that we generate significant chirality or anisotropy in the remaining film. The most intuitive explanation would be an enantiomeric enrichment in the film, which we assume to be generated by enantiospecific desorption as will be discussed in section 6.4.5.

6.4.2. Second-harmonic generation optical rotation dispersion spectroscopy

For a complementary examination of the observed SHG-CD effects, we studied the SHG-ORD response of the BINOL film during desorption with CPL (see section 6.2.2).

The measurements protocol is the same as shown in the previous section with exception of an additional SHG-ORD measurement after each desorption time step. Thus, additionally to the determination of the g-value (by excitation with LCP and RCP pulses), the SSHG intensity $I_{\mathrm{SHG}}^{\mathrm{polar}}(\varphi, t_d)$ upon excitation with LPP light was measured in dependence of the angle of a polariser placed behind the sample as described in section 6.2.2. It has to be noted that the measurement started with a polariser angle of 272°. The last data point was measured after a full 360° rotation of the polariser. Desorption during the measurement leads to a slightly reduced intensity at the last data point, which corresponds to err_{des} (see appendix A.3). Figure 42 depicts a data set obtained from SHG-ORD measurements on a racemic BINOL sample irradiated with RCP pulses for 90 min. Interaction of an incoming linearly polarised beam with a chiral molecule does not only cause a rotation of the polarisation, but also a phase delay between the two circular components of the laser beam, which results in an elliptically polarised beam. The data is fitted according to equation 6.5, allowing to extract the rotation angles $\delta(t_d)$ and the ellipticity $b/a(t_d)$. The rotation angles start with a value of $\delta(0) = 2.8°$, close to zero, which would be the expected value of racemic BINOL. Upon desorption of BINOL molecules,
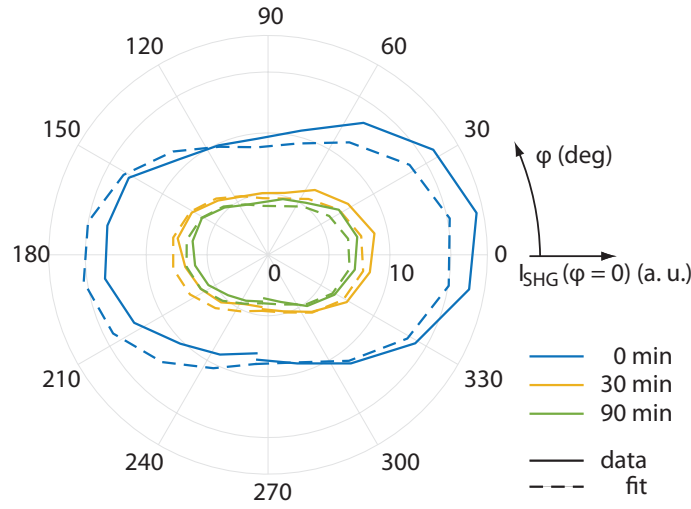
Figure 42 Results of SHG-ORD spectroscopy for RCP desorption. The SSHG intensity $I_{\mathrm{SHG}}^{\mathrm{polar}}(\varphi, t_d)$ upon excitation with LPP light was measured in dependence of the polariser angle φ (view in direction of beam propagation) after desorption for 0 min (blue, solid), 30 min (yellow, solid) and 90 min (green, solid). The data was fitted according to the polar form of an ellipse (equation 6.5) shown as dashed lines. From the fit, rotation angles of $\delta(0\,\text{min}) = 2.8°$, $\delta(30\,\text{min}) = 358°$ and $\delta(90\,\text{min}) = 358°$ could be extracted. The corresponding values for ellipticity b/a can be obtained to 0.597, 0.597 nad 0.605.

indicated by reduced $I_{\mathrm{SHG}}^{\mathrm{polar}}$ after 30 min and 90 min, the rotation angle changes to $358°$, whereas $358°$ corresponds to $-2°$. Defining the induced change of rotation angle $\Delta\delta$ to

$$\Delta\delta(t_d) = \delta(t_\mathrm{d}) - \delta(0), \tag{6.14}$$

we can deduce changes of $\Delta\delta(30\,\text{min}) = \Delta\delta(90\,\text{min}) = -4.8°$. Note, that the positive direction of rotation is defined anti-clockwise in the direction of beam propagation as depicted in figures 42 and 54c. The ellipticity increases from 0.597 at $t_d = 0$ min and 30 min to 0.605 after 90 min. However, ellipticity is not expected to be enantiospecific, and therefore, is not considered further.

An overview of all SHG-ORD results for LCP and RCP irradiation, which satisfy the requirement $|g(t_d = 0)| < 0.1$, is given in figure 43. For each of the four data sets, the SSHG intensity I_{SHG} (a), the induced changes of anisotropy factor Δg (b), the induced changes of rotation angle $\Delta\delta$ (c) and the rotation angles δ (d) are shown for proceeding desorption time. The data was fitted according to equation 6.5 at every measured time t_d. The rotation angle is extracted from the fit, and $\Delta\delta$ is determined according to equation 6.14. The overview includes the data set from figure 42, here shown as green circles. The data depicted in figures 43a and b are part of the overview shown in figure 39. Hence, only the corresponding results from figures 43c and d are discussed in the following. LCP desorption, causing large negative values of Δg, generates a positive change of rotation angles with a maximum of $\Delta\delta = 5.4°$ after 60 min. Correspondingly, irradiation with RCP light induces a maximum (negative) $\Delta\delta = -4.8°$ after 30 min. Thus, we observe antisymmetric evolution of $\Delta\delta$ with desorption time. Here,
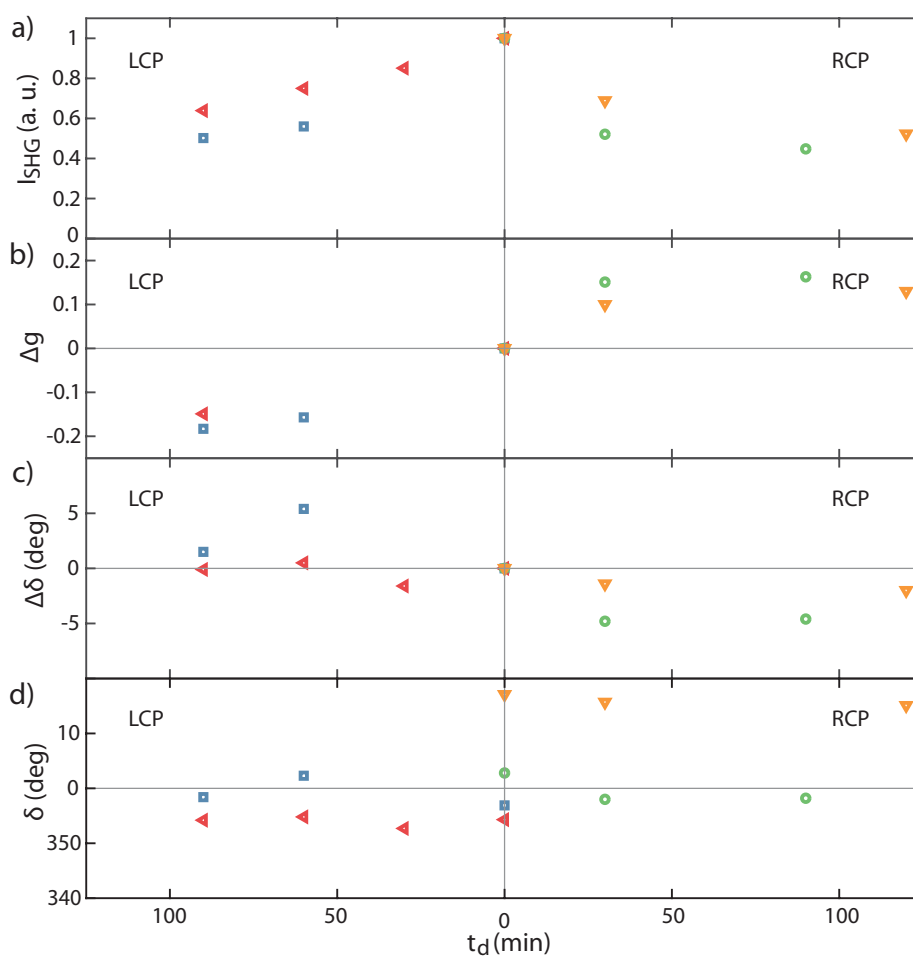
Figure 43 Overview of SHG-ORD results for LCP (left panel) and RCP (right panel) irradiation as a function of t_d. Only desorption scans satisfying the requirement $|g(t_d = 0)| < 0.1$ are shown. a) SSHG intensities $I_{\mathrm{SHG}}(t_d)$. b) Induced changes of anisotropy factor $\Delta g(t_\mathrm{d})$. c) Induced change of rotation angle $\Delta\delta(t_\mathrm{d}) = \delta(t_\mathrm{d}) - \delta(0)$. d) Rotation angles $\delta(t_d)$ extracted from the fit. $360°$ corresponds to $0°$.

$\Delta\delta$ is positive for anticlockwise rotation. Figure 43d depicts the corresponding rotation angles extracted from the fit. The initial values $\delta(0)$, which vary between $-5.7°$ and $17.1°$, reflect the deviation from the expected racemic response.

Although the number of SHG-ORD data sets is very low, the observed antisymmetric evolution of $\Delta\delta$ indicates that desorption with CPL and simultaneous generation of anisotropy, i.e. the generation of $|\Delta g| > 0$, induces a rotation of incoming linearly polarised light with a preferred handedness. A comparison of figures 43c and d reveals that two of four data sets (red and orange desorption series), although satisfying the requirement $|g(0)| < 0.1$, exhibit larger initial rotation angles $\delta(0)$ than their induced maximum changes $\Delta\delta$. Despite the observation of an antisymmetric evolution, the results obtained from SHG-ORD can not reliably confirm enantiospecific desorption and the generation of an enantiomeric excess under these conditions. Repeating these examinations in situ and on much thinner films may allow a directed control of the rotation angle with CPL. Taking into account the observation of a large spreading of rotation

angles from SHG-ORD on various racemic and enantiopure samples (see figure 37), we assume that the SHG-ORD response arising from macroscopic chiral structures influences strongly our detected SHG-ORD signals (see section 6.3).

6.4.3. Reference measurements

SHG-CD spectroscopy using linearly polarised pulses for desorption
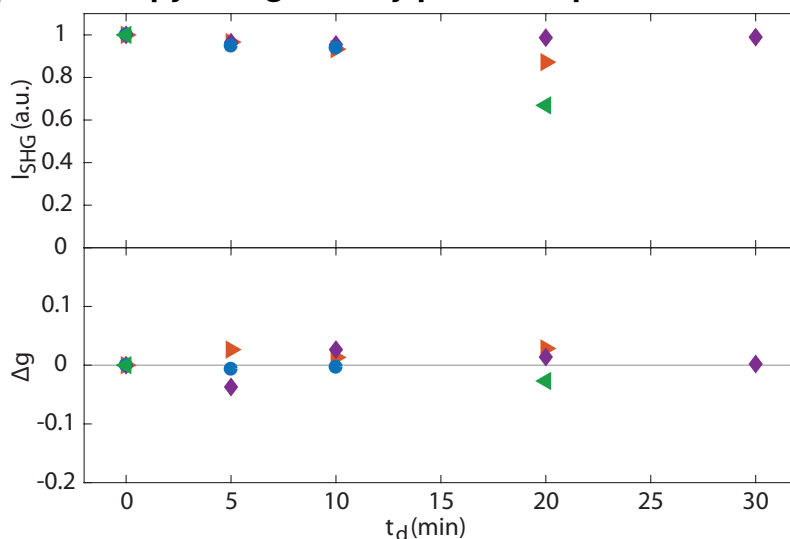
Figure 44 Racemic samples irradiated with LPP pulses (650 nm). Only desorption scans satisfying the requirement $|g(t_d = 0)| < 0.1$ are shown. The data set represented by green triangles exhibits an intensity (I_{SHG}) decay of 33% in 20 min (upper panel). The corresponding value for Δg can be obtained to -0.027 (lower panel).

In order to examine, if the antisymmetric evolution of Δg is triggered by the circular polarisation of the light, experiments using linear polarisation (parallel to the plane of incidence, LPP) were performed (see figue 44).

The induced changes in anisotropy factor vary slightly around zero with both positive and negative signs. Hence, a significant and controlled generation of Δg presumably can not be generated by linearly polarised pulses. However, the data set represented by green triangles is the only one, which exhibits a significant decay (33% in 20 min, see upper panel) of the SSHG intensity due to desorption. A comparison with figure 41a might arise the assumption that the other three data sets in figure 44 are not convincing. Therefore, for verification of the result, further experiments are required.

Nonresonant SHG-CD spectroscopy

Furthermore, we examined the evolution of the anisotropy factor upon irradiation with CP pulses at a central wavelength of 900 nm, i.e. below the photon energy required for TPA. Most of the desorption series exhibit significant decay of the SSHG intensities with desorption time indicating that off-resonant desorption is generally possible (see figure 45 upper panel). The corresponding
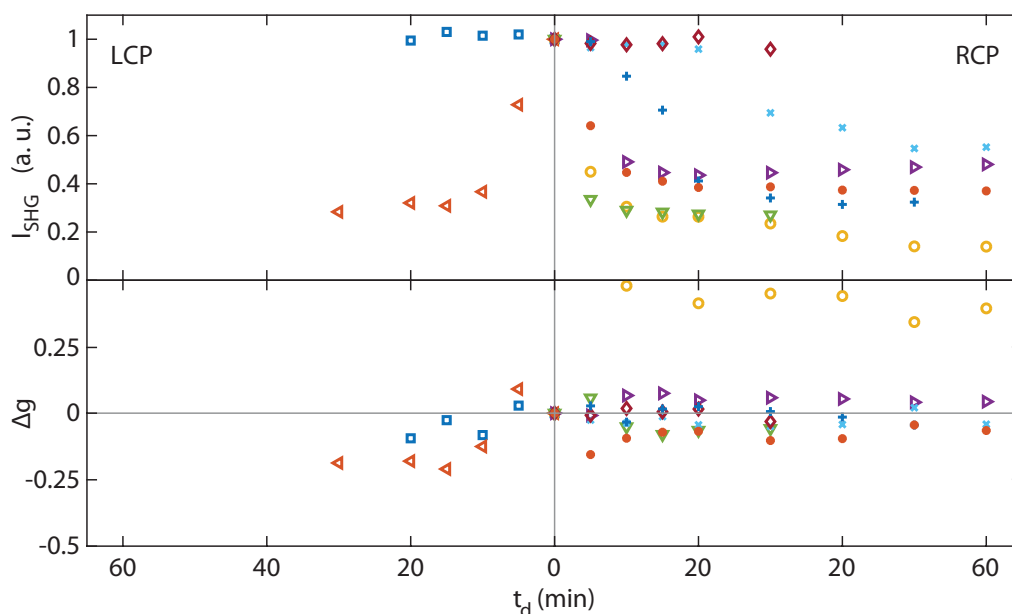
**Figure 45** Racemic samples irradiated with LCP (left panel) and RCP (right panel) pulses at a central wavelength of 900 nm. Only desorption scans satisfying the requirement $|g(t_d = 0)| < 0.1$ are shown.

traces of Δg vary between -0.21 and 0.09 for LCP desorption, and between -0.18 and 0.49 for RCP desorption (see figure 45 lower panel). Although resulting in an asymmetric evolution for left and right CP, both positive and negative signs are measured for each polarisation. However, the number of data sets is not sufficient for a general conclusion, particularly for LCP desorption.

6.4.4. Quantitative description of generated anisotropy and enantiomeric excess

For a quantitative description of the observed phenomena, we fitted the data according to a simple phenomenological rate equation model. We assume that the illumination with circular polarised light leads to simultaneous desorption of both enantiomers, but with different desorption rates. Hence, d_1 and d_2 are defined as the rates for desorption of S-BINOL and R-BINOL molecules upon interaction with LCP light. Both rates include thermal as well as quantum mechanical (QM) contributions. Because S- and R-BINOL are mirror images of each other, the rates are exchanged for interaction with RCP pulses. Accordingly, d_2 describes desorption of S-BINOL and d_1 the desorption of R-BINOL molecules. Note that these desorption rates are extremely sensitive to the used experimental conditions, as laser intensity, experimental geometry and sample structure. The QM contribution to the desorption process can be derived to $\left|\frac{d_1-d_2}{max(d_1,d_2)}\right|$. Desorption induced by femtosecond QM interaction occurs at non-equilibrium conditions, hence, before thermalisation and heating of the surrounding material have completed [272]. Therefore, the desorption rate attributed to QM desorption is typically larger than the respective rate for thermal desorption. The occurrence of two different rates is a clear indication of a QM process in addition to the always present thermal desorption.

113

In our model, the racemic film within the area of laser interaction is assumed as an ensemble of molecules with an initial number density of $2N_0$ including S-BINOL and R-BINOL molecules in equal amounts with a respective number density of N_0. The corresponding rate equations describe the decay of the number density of S-BINOL molecules $N_S^{\mathrm{LCP,RCP}}$ and R-BINOL molecules $N_R^{\mathrm{LCP,RCP}}$ with desorption time t_d upon interaction with LCP and RCP light:

$$N_S^{\mathrm{LCP}}(t_d) = \frac{N_0}{1 + C_1}(e^{-d_1 t_d} + C_1), \quad N_S^{\mathrm{RCP}}(t_d) = \frac{N_0}{1 + C_2}(e^{-d_2 t_d} + C_2),$$

$$N_R^{\mathrm{LCP}}(t_d) = \frac{N_0}{1 + C_2}(e^{-d_2 t_d} + C_2), \quad N_R^{\mathrm{RCP}}(t_d) = \frac{N_0}{1 + C_1}(e^{-d_1 t_d} + C_1). \tag{6.15}$$

The quantities C_1 and C_2 are either obtained from the fit or set to a constant value. In order to account for the saturation of Δg and the fact that I_{SHG} did not vanish for the examined time range, the expressions $\frac{C_i}{1+C_i}$, $i = 1, 2$, denote the fraction of S-BINOL and R-BINOL molecules, which can not be desorbed. M. A. Kriech and J. C. Conboy report a similar observation and assume that some molecules are too strongly bound, e.g. in surface traps of the substrate, to be desorbed [286]. The next step is the estimation of the relation between the number densities and the generated SSHG intensity. In general, the SSHG intensity is quadratically depending on the number density of molecules within the coherence length of SHG in the medium (see equations 2.73 and 2.67). Determination of the coherence length, however, requires further knowledge about the exact crystalline composition of our films. Therefore, we consider the empirically determined linear dependence of I_{SHG} on the film thickness (see figure 25), hence, a linear dependence on the number density of BINOL molecules.

Accordingly, the SSHG signals generated with LCP and RCP light, respectively, can be described as

$$I_{2\omega,\mathrm{j}}^{\mathrm{LCP}}(t_d) \propto N_S^j(t_d)(\chi_{SL}^{(2)})^2(I_\omega^{\mathrm{LCP}})^2 + N_R^j(t_d)(\chi_{RL}^{(2)})^2(I_\omega^{\mathrm{LCP}})^2, \quad j = \mathrm{LCP, RCP}, \tag{6.16}$$

and

$$I_{2\omega,\mathrm{j}}^{\mathrm{RCP}}(t_d) \propto N_S^j(t_d)(\chi_{SR}^{(2)})^2(I_\omega^{\mathrm{RCP}})^2 + N_R^j(t_d)(\chi_{RR}^{(2)})^2(I_\omega^{\mathrm{RCP}})^2, \quad j = \mathrm{LCP, RCP}. \tag{6.17}$$

Here, the index j = LCP, RCP represents the polarisation, which is used for desorption. I_ω^{LCP} and I_ω^{RCP} denote the intensities of the incoming LCP and RCP pulses for the g-value measurement (for the current experiments $I_\omega^{\mathrm{LCP}} = I_\omega^{\mathrm{RCP}} = I_\omega$), while $\chi_{SL}^{(2)}$ ($\chi_{RL}^{(2)}$) and $\chi_{SR}^{(2)}$ ($\chi_{RR}^{(2)}$) are the effective second order susceptibilities of S-BINOL (R-BINOL) for interaction with LCP and RCP light, respectively. Analogue to the desorption rates, we can assume that $\chi_{SL}^{(2)} = \chi_{RR}^{(2)} = \chi_1^{(2)}$ and $\chi_{SR}^{(2)} = \chi_{RL}^{(2)} = \chi_2^{(2)}$. Using these notations, the averaged SSHG signal is

$$I_{2\omega,\mathrm{j}}(t_d) = \frac{1}{2}(I_{2\omega,\mathrm{j}}^{\mathrm{LCP}} + I_{2\omega,\mathrm{j}}^{\mathrm{RCP}}) \propto \frac{1}{2}(N_S^j(t_d) + N_R^j(t_d))\left((\chi_1^{(2)})^2 + (\chi_2^{(2)})^2\right)I_\omega^2, \quad j = \mathrm{LCP, RCP}. \tag{6.18}$$

The desorption time dependent normalised SSHG signal can be written as

$$I_{\mathrm{SHG}}^{j}(t_d) = \frac{I_{2\omega,\mathrm{j}}(t_d)}{I_{2\omega,\mathrm{j}}(0)} = \frac{N_S^j(t_d) + N_R^j(t_d)}{N_S^j(0) + N_R^j(0)}, \quad j = \mathrm{LCP}, \mathrm{RCP}. \tag{6.19}$$

Accordingly, the induced change in anisotropy factor $\Delta g(t_d)$ is represented by

$$\Delta g^j(t_d) = 2\frac{I_{2\omega,\mathrm{j}}^{\mathrm{LCP}} - I_{2\omega,\mathrm{j}}^{\mathrm{RCP}}}{I_{2\omega,\mathrm{j}}^{\mathrm{LCP}} + I_{2\omega,\mathrm{j}}^{\mathrm{RCP}}} = 2g_p\frac{N_S^j(t_d) - N_R^j(t_d)}{N_S^j(t_d) + N_R^j(t_d)}, \quad j = \mathrm{LCP}, \mathrm{RCP}, \tag{6.20}$$

with the g-value g_p determined from enantiopure samples

$$g_p = 2\frac{(\chi_1^{(2)})^2 - (\chi_2^{(2)})^2}{(\chi_1^{(2)})^2 + (\chi_2^{(2)})^2}. \tag{6.21}$$

Using the rate equations 6.15, we can write equations 6.19 and 6.20 as follows:

$$I_{\mathrm{SHG}}^{\mathrm{LCP}}(t_d) = I_{\mathrm{SHG}}^{\mathrm{RCP}}(t_d) = I_{\mathrm{SHG}}(t_d) = \frac{1}{2}\left(\frac{1}{1+C_1}(e^{-d_1 t_d} + C_1) + \frac{1}{1+C_2}(e^{-d_2 t_d} + C_2)\right), \tag{6.22}$$

and

$$\Delta g^{\mathrm{j}}(t_d) = (\mp)2\frac{\frac{1}{1+C_1}(e^{-d_1 t_d} + C_1) - \frac{1}{1+C_2}(e^{-d_2 t_d} + C_2)}{\frac{1}{1+C_1}(e^{-d_1 t_d} + C_1)) + \frac{1}{1+C_2}(e^{-d_2 t_d} + C_2)}, \quad j = \mathrm{LCP}, \mathrm{RCP}. \tag{6.23}$$

whereas '-' and '+' account for the cases of LCP and RCP desorption, respectively. Initially, $I_{\mathrm{SHG}}^{\mathrm{j}}(0) = 1$, and $\Delta g^{\mathrm{j}}(0) = 0$. In the limit of large desorption times, I_{SHG} and Δg^{j} become

$$I_{\mathrm{SHG}}(t_d \to \infty) = \frac{1}{2}\left(\frac{C_1}{1+C_1} + \frac{C_2}{1+C_2}\right), \tag{6.24}$$

and

$$\Delta g^{\mathrm{j}}(t_d \to \infty) = (\mp)2\frac{\frac{C_1}{1+C_1} - \frac{C_2}{1+C_2}}{\frac{C_1}{1+C_1} + \frac{C_2}{1+C_2}}, \quad j = \mathrm{LCP}, \mathrm{RCP}. \tag{6.25}$$

Equations 6.22 and 6.23 are used to analyse the experimental data. We calculated the moving average of the data presented in figure 39, i.e. all data sets satisfying the requirement $|g(t_d = 0)| < 0.1$. Because the g-values were recorded after different time steps of the desorption time during the n different scans, the moving average of all $I_{\mathrm{SHG}}(t_d)$ and $\Delta g(t_d)$ was transformed to evenly spaced new time steps t_i and weighted with Gaussian functions according to

$$I_{\mathrm{SHG}}^{\mathrm{av}}(t_d) = \frac{\sum_n w_n(t_d) I_{\mathrm{SHG}}(t_d)}{\sum_n w_n(t_d)}, \quad \Delta g^{\mathrm{av}}(t_d) = \frac{\sum_n w_n(t_d) \Delta g(t_d)}{\sum_n w_n(t_d)}, \tag{6.26}$$

with the Gaussian weights for

$$w_n(t_d) = \sum_i \exp \frac{-4 \log 2 \cdot (t_d - t_i)^2}{100}. \tag{6.27}$$
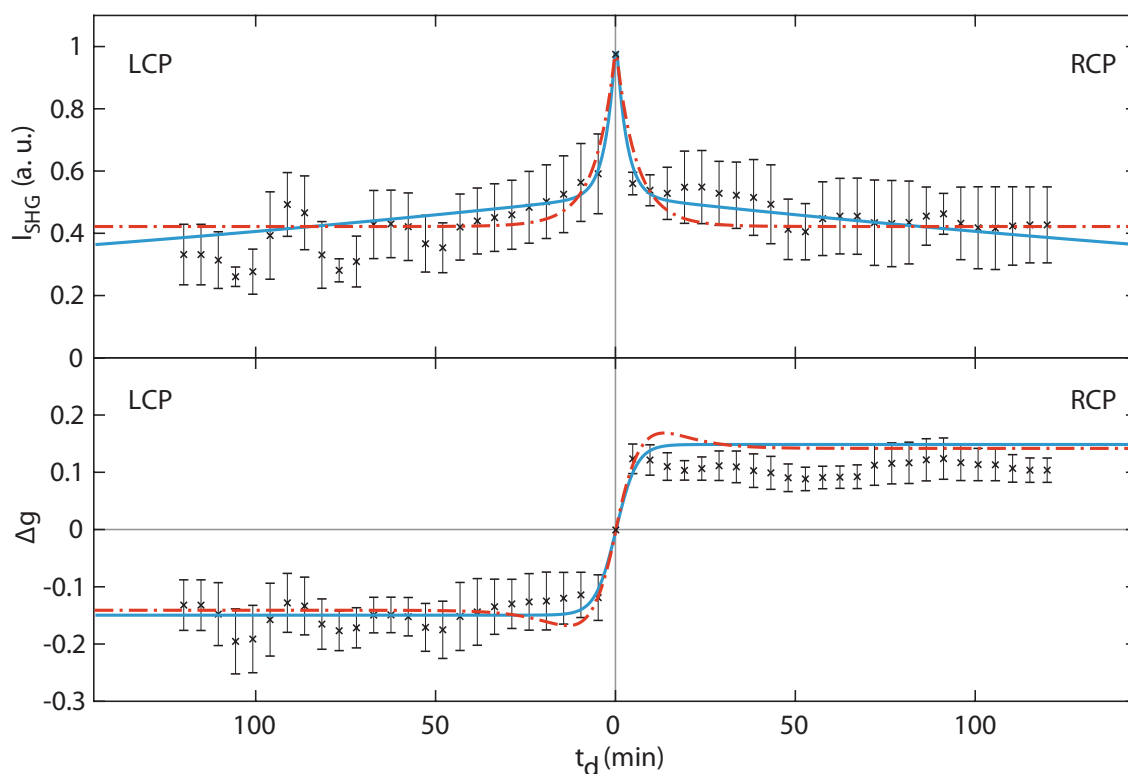

Figure 46 Moving average weighted with Gaussian functions of the data shown in figure 39. The data (black) is fitted according to a simple phenomenological rate equation model using different boundary conditions. Version 1: $C_1 = C_2 = 0$, blue solid line, version 2: $g_p = \pm 0.71$, red dot-dashed line.

Figure 46 depicts the corresponding results of $I_{\mathrm{SHG}}^{\mathrm{av}}(t_d)$ and $\Delta g^{\mathrm{av}}(t_d)$ fitted simultaneously according to equations 6.22 and 6.23. These bi-exponential functions include five fitting parameters: both desorption rates d_1 and d_2, the constants C_1 and C_2, and the anisotropy in the SSHG of the pure enantiomers g_p. In order to avoid overestimation, one of these parameters has to be fixed. The corresponding results for these parameters are summarised in table 9. In a first step, denoted as version 1, we set $C_1 = C_2 = 0$, hence, allowing all molecules to be desorbed. This necessarily results in the generation of complete enantio-purification, i.e. $ee = \frac{\Delta g_{\mathrm{max}}}{g_p} = 100\%$, as the fit approaches asymptotically the maximum possible value of $\Delta g_{max} = \pm 0.15$ (+ for RCP desorption, and - for LCP desorption) within less than 30 min. Assuming LCP desorption, the desorption rates d_1 = 0.13 h^{-1} and d_2 = 21 h^{-1} for the normalised number densities of S- and R-BINOL can be extracted from the fit. This leads to a relation of $d_2 = 162 \cdot d_1$. For RCP desorption, the rates are exchanged. In the second version (version 2), the parameter g_p is fixed to the value of ± 0.71 determined from enantiopure samples (see section 6.3). Hence, Δg_{max} of ± 0.15 corresponds to an enantiomeric excess of $\frac{\Delta g_{\mathrm{max}}}{g_p} = 21\%$.

Desorption rates of $d_1 = 8$ h^{-1} and $d_2 = 13$ h^{-1} can be obtained. For LCP desorption the remaining film contains fractions of 50% S-BINOL molecules and 35% R-BINOL molecules.

Fit model	g_p	$d_1(h^{-1})$	$d_2(h^{-1})$	$\frac{C_1}{1+C_1}(\%)$	$\frac{C_2}{1+C_2}(\%)$
Version 1	0.15 ± 0.03	0.13 ± 0.01	21 ± 7	0	0
Version 2	0.71	8 ± 3	13 ± 4	50 ± 2	35 ± 2

Table 9 Parameters extracted from the fitted data traces according to a biexponential model.

Although both versions of the fit describe the data well within the examined range of t_d, this simple rate equation model does not give a sufficient representation of the laser induced processes in the BINOL film. For long desorption times, both I_{SHG} and Δg^{j} approach zero in version 1. After long irradiation, all BINOL molecules must be desorbed, either quantum mechanically or thermally. However, a maximum ee of 100% and a QM contribution of 99% seems unrealistic. Nonetheless, we can set the corresponding relation of $d_2 = 140 \cdot d_1$ as upper limit for the relation of desorption rates. Fitting the data according to version 2, $d_2 = 1.6 \cdot d_1$, which we define as lower limit of the relation of desorption rates. The corresponding QM contribution can be deduced to 38%. The fit yields a saturation of the SSHG intensity to a constant value of 0.42. Assuming linear dependence of I_{SHG} on film thickness, this would represent a permanent remaining film thickness of 630 nm, which is not supported by our microscopy results. Besides, long-time desorption experiments show that the SSHG intensity still decreases continuously below values of 0.3 (see figure 41b).

It has to be noted that the model is limited to desorption effects, while neglecting effects like diffusion, racemisation or re-adsorption. Besides, the modelling of the BINOL film as an ensemble of molecules is too simplified to contribute for the fact that desorption can only occur from the upper layers of the film. Although it is not an adequate description of the processes underlying the observed phenomena, it serves as a simple tool for the estimation of the relation of the two desorption rates, which can be further applied in more elaborate simulations (see section 6.6).

6.4.5. Discussion

In the previous sections, we show the generation of a significantly antisymmetric evolution of the optical activity $\Delta g(t_d)$ in originally racemic crystalline BINOL films upon desorption triggered by CP pulses (section 6.4). This unambiguously demonstrates the creation of a well-defined substantial anisotropy or chirality in the remaining film in contrast to desorption with LPP pulses (section 6.4.3). Further confirmation is given by SHG-ORD measurements (see section 6.4.2), which indicate a controlled optical rotation during CPL desorption. Hence, our results strongly support the generation of a substantial enantiomeric excess in the remaining film as origin for the observed antisymmetry in the data. Comparison of figures 39 and 45 suggests the requirement of resonant electronic transitions for the occurrence of these effects. Our studies indicate no photodegradation of the BINOL molecules during irradiation within the chosen experimental conditions (see section 6.2.4). Therefore, we exclude photodestruction as a possible enantiospecific process. Furthermore, we conclude that laser-induced desorption (definition given in section 6.2.4) and thermal desorption to be the major processes causing material removal and neglect other processes such as ablation. Thus, principally two processes seem plausible for the generation of an enantiomeric excess in an initially racemic material triggered by CPL: partial photoresolution by enantiomerisation and enantiospecific desorption. Both processes require a quantum mechanical light-matter interaction and occur via the excited electronic state. The initiating question for these experiments was, whether we can generate an enantiomeric excess by enantiospecific desorption, i.e. by preferably desorbing one of the enantiomers from the BINOL film. For this reason, and because the enantioenrichment occurs during desorption, we first present a hypothetical model based on the feasibility of enantiospecific desorption. As (linear) absorption of CP pulses leads to enantiospecific effects, such as circular dichroism, enantiospecific photodestruction and photoresolution, it is expected that resonant photodesorption upon TPA of CP pulses can also be enantiospecific due to the enhanced cross-section of one enantiomer. According to this model, the ee is achieved by preferential desorption of one enantiomer. Negative Δg values indicate an enrichment of S-BINOL molecules in the remaining film. Thus, excitation with LCP pulses leads to a preferential desorption of R-BINOL molecules in agreement with the enhanced SSHG intensity (leading to $g > 0$) upon LCP excitation in enantiopure R-BINOL (see 6.3). Using RCP light, the film exhibits an ee of R-BINOL molecules as indicated by positive Δg. The estimation of the degree of enantioenrichment, however, is very difficult. The relation between Δg and ee can be obtained by measuring the anisotropy factor of enantiopure films with the same method. As shown in section 6.3, a reliable determination of this value is very tedious due to the occurrence of macroscopic chiral structures. Using the value of $g_p = 0.71$, we can estimate a mean ee of 21% ($ee = \Delta g_{\max}/g_p = 0.015/0.71$, see section 6.4.4). Incorporating the g-value of 10%-ee S-BINOL and R-BINOL samples, the mean enantiomeric excess is estimated to $0.10\cdot(\Delta g_{\max}/g_{10\%ee}) = 0.15/0.069$ = 22% in agreement with the value obtained from enantiopure samples. Accordingly, the strongest generated enantiomeric excess would be $|-0.260/0.7| = 37\%$ in one of our samples (cf. figure 39).

The exact mechanism of enantiospecific desorption of chiral molecules from a multilayered film is still under discussion. Interaction with the insulating substrate can be ruled out due to a film thickness of more than 2000 monolayers. For photodesorption with 600 nm and 650 nm light, we therefore assume direct TPA excitation by the laser as the dominant effect inducing desorption in a nonadiabatic process (see section 6.2.4). In crystals of racemic BINOL, the molecules are bonded with hydrogen bonds, which have to be broken for desorption. Excitation of BINOL in the pronounced absorption maximum at 230 nm causes a decrease of the dihedral angle between the 2-naphthol planes as was shown in sub-ps transient absorption CD measurements [67, 287]. We assume similar orientational changes in the BINOL molecule due to the modified electron configuration upon excitation by TPA of 600 nm and 650 nm. The induced distortions and shearing forces in the crystal structure could trigger the removal of the molecule from the film in a similar way as described for polar crystal lattices by R. Haglund [266]. In addition to this quantum mechanical process, thermal desorption contributes without preferation to the removal of both enantiomers from the film surface. Thus, the enantiospecific character of photodesorption is solely related to the larger TPA cross-section σ_{TPA} (equation 2.53) for CPL of one of the enantiomers. Applying a bi-exponential fit to the averaged data, we estimate a lower limit of 38% quantum mechanical contribution (see section 6.4.4). The exact contribution, however, depends on different parameters such as excitation intensity and temperature in the film.

As included in the phenomenological fitting model (see section 6.4.4), we assume simultaneous desorption of both enantiomers, but with different desorption rates. Desorption can only occur from the topmost few monolayers of the BINOL film and only in the inner part of the irradiated area, where the intensity of the Gaussian shaped intensity profile of the laser pulse exceeds the desorption threshold. The generation of ee is limited to the surface layers within this area on the film leading to a compositional gradient between surface and bulk. Excitation of molecules in the bulk leads to a heating of the material due to coupling to phonons and vibrational modes of the surrounding molecules during thermalisation. The increased temperature in the crystal lattice promotes thermal desorption as well as diffusion in the bulk facilitated by the compositional gradient. Although bulk diffusion in the crystalline material is presumably very low, it counteracts the depletion of the fast desorbing enantiomer in the surface layers. Diffusion on the surface by random walk is more pronounced than in the bulk film. In general, the energy barrier for this process is lower than for desorption. Hence, loose molecules are trapped in surface vacancies of racemic crystallites allowing a smooth material removal on the surface according to the Gaussian shaped intensity profile of the laser pulse.

The temperature in the irradiated material is a crucial parameter. When exciting the samples with femtosecond pulses at a repetition rate of 1 kHz, most thermalisation processes in the film have completed before the next laser pulse re-excites the material. Hence, the temperature of the crystal lattice is difficult to estimate. The heat is rapidly diffused to the surfaces (substrate

and air). Thus, we assume a medium temperature increase in the BINOL film to a temperature far below the melting point. The heating of the film further depends on its thickness. Because more energy can be deposited in a thicker film and conduction to the surfaces takes longer, we suppose that the temperature in the film decreases during desorption slowing down thermal desorption. Assuming the case that the temperature is close to the melting point, then not even the energy of a single laser pulse would be sufficient to melt the film. When exciting the 1.5 μm thick sample with a 1 μJ pulse corresponding to a fluence of 1.85 mJ/cm^2 (see section 6.2.4), a maximum energy density of 12.1 kJ/mol can be deposited in the material. This value is below the required enthalpy of melting $\Delta H =$32 kJ/mol (racemic crystal) [263]. Because BINOL and BK7 are transparent for visible light and cross sections for TPA are usually very low, we note that more than 90% of the incoming photons are either scattered or transmitted. Thus, we conclude that our BINOL films are not melt during the desorption experiments.

The assumption of two different desorption rates and diffusion is not sufficient for a model matching the $\Delta g(t_d)$ saturation effect in our data (see section 6.6), because every rate equation model based on two different desorption rates and diffusion necessarily leads to an ee of close to 100% after a certain amount of time (and subsequent decrease to zero as soon as all molecules are desorbed). Therefore, further thermodynamical and structural aspects have to be considered. Below the solidus temperature at 197°C, a binary mixture of S-BINOL and R-BINOL favours the formation of racemic crystals with respect to conglomerates [264, 277]. "Loose" excess molecules, which are not trapped in crystal vacancies, are presumably only weakly bound by electrostatic interactions with the surface. Thus, the energy barrier for desorption is probably lower, which contributes to an attenuation of enantioenrichment and $\Delta g(t_d)$. The excess molecules might also form enantiopure crystals enforced by the increased temperatures in the irradiated material. Similar to the difference in enthalpy of melting ΔH (racemic crystal: 32 kJ/mol, enantiopure crystal: 29 kJ/mol [263]), the energy barrier for desorption of enantiopure crystals is also assumed to be lower by approximately 10% than for the more stable racemic crystals, further contributing to attenuation of enantioenrichment.

Additional attenuation of enantioenrichment is caused by racemisation. An enantiopure solution is thermodynamically unstable. Hence, there exists a driving force for the generation of a racemic mixture in order to minimise the Gibbs free energy $\Delta G = \Delta H - T\Delta S$. Because the enthalpy change ΔH required for isomerisation is the same for both enantiomers, racemisation is only driven by entropy S [288]. It depends on temperature T [289] and counteracts the enrichment of one specific enantiomer. The half-life time for thermal racemisation of BINOL in melt at 220°C is 100 min [290]. Binaphthyl (1,1'-binaphthyl), which is very similar to BINOL in its structural and thermodynamical properties, exhibits a half-life time of 10 h at 25°C [284]. Hence, we assume that the rate of thermal racemisation in our irradiated films is low, but not neglectable. Moreover, the excitation with (un)polarised UV laser pulses can induce photoracemisation in chiral solutions [291]. When using CP pulses, the reverse process, photoresolution, also

called photo-deracemisation, leads to reversible enantioenrichment in racemic solutions of axially chiral molecules with kinetically stable enantiomers [288]. The CP laser pulse induces enhanced enantiomerisation, i.e. the interconversion of one enantiomer into the other, of the enantiomer with the larger absorption cross-section. This process generates an ee of the other enantiomer. As long as the total concentration of intact molecules is conserved, (partial) photoresolution is a reversible process. However, it is often accompanied by (preferential) photodestruction of the strongly absorbing enantiomer [223]. Photoresolution was described theoretically and demonstrated in numerous studies on different axially chiral molecules [230, 233, 288, 227, 291, 234]. The achievement of large ee in experiments on photoresolution in solution is, however, hindered by the competing process of thermal racemisation. Experimental results and simulations exhibit an exponential evolution of enantiomeric excess or optical activity, which resembles strongly our Δg evolution. Photoracemisation examinations on binaphthyl revealed that the interconversion to the other enantiomer occurs in the excited triplet state and is accompanied by changes of the dihedral angle between the two naphthyl planes and rotation along the C-C bond [292]. Taking into account the excited state dynamics of BINOL [67, 287], a similar process is expected to induce interconversion of BINOL enantiomers. Theoretical studies show that BINOL can exist in three different isomers exhibiting different dihedral angles close to 90°. Isomerisation and enantiomerisation, i.e. the interconversion from S-BINOL to R-BINOL or vice versa, can occur on a trans-path or a cis-path through the C-C inter-ring rotation [293]. The latter involves the rotation of the hydroxy groups around the CO-bond. The energy barrier for enantiomerisation depends on the respective isomer. The largest barrier of 2.78 eV exists for the trans-enantiomerisation of the most stable isomer. An energy of 2.78 eV can be provided by a 450 nm laser photon or by TPA of two visible photons. We assume a similar mechanism upon TPA of 600 nm and 650 nm laser pulses to be capable of inducing enantiomerisation of BINOL. Hence, two enantiospecific processes compete presumably upon resonant excitation by TPA of a racemic BINOL film with CP laser pulses, photoresolution and enantiospecific desorption. The respective contribution to enantioenrichment, however, is unclear. It depends mainly on the respective energy barrier (in particular in the crystalline state), which has to be overcome for the process to occur. Both processes occur in the excited electronic state and are presumably related to changes in the dihedral angle between the 2-naphthol planes indicative of possible coupling of these processes. In the crystalline structure, enantiospecific desorption intuitively seems to be more probable, because it does not require a rotation of more than 180° around the C-C bond. On the other hand, enantiomerisation would automatically cause a break of the hydrogen-bonds, which lowers the barrier for desorption. When taking into account loose molecules and re-adsorbed molecules, it may be different. Both processes cause an enantiomeric excess of the enantiomer with the lower absorption cross-section for the respective circular polarisation of the laser pulse. Thus, the observed evolution of $\Delta g(t_d)$ as well as $I_{\mathrm{SHG}}(t_d)$ could also be described by partial photoresolution in combination with thermal desorption or by a superposition of different contributions of partial photoresolution, enantiospecific desorption and thermal desorption. In all cases, thermal and photo-racemisation

attenuate enantioenrichment and lead to a saturation of $\Delta g(t_d)$.

Since SHG-CD is not only sensitive to molecular chirality, but also to the optical activity of macroscopic chiral structures (see section 2.2.7), the antisymmetric evolution of $\Delta g(t_d)$ might also have another origin. A controlled antisymmetric arrangement of the molecules in the remaining film in a macroscopic optical active structure is expected to generate similar results. Moreover, magnitude and sign of CD are depending on the dihedral angle between the 2-naphthol planes of BINOL [67]. However, anisotropy factors of racemic crystals are usually below the measured Δg (see section 6.3). Hence, the remaining film would have to consist at least partly of enantiopure crystals, which arrange in a macroscopic optical active structure (cf. section 6.3) with preferred chirality. Neither irradiation during the crystallisation process (see figure 58) nor irradiation at the desorption threshold (see figure 41a) generate a controlled handedness of the chiroptical response reflected by induced anisotropy factors around zero. Hence, desorption, i.e. the removal of material, which was proofed by the microscopy examinations (see section 6.2.4), is either essential or at least a concomitant effect for generating the observed antisymmetry. Therefore, either irradiation increases the temperature above the solidus temperature, where a conglomerate is more stable than the racemic phase, or enantiospecific desorption and enantiomerisation generate at least a small enrichment of one enantiomer, which then can form enantiopure chiral structures. In particular, the SHG-ORD results indicate a strong contribution of macroscopic effects to the generated optical activity (see sections 6.3 and 6.4.2). As we presumably do not melt the BINOL film, we conclude that irradiation with CPL above the desorption threshold generates an enantioenrichment. Variations of Δg magnitude during desorption (see figures 38c and d) can be an indication of processes including crystallisation and arrangement of enantiopure crystallites.

Moreover, irradiation during crystallisation (figure 58) suggests that the linear dependence of I_{SHG} on film thickness, which was measured during evaporation (see figure 25b), does not necessarily match the respective dependence in the completely crystallised film, in which the desorption series were recorded. In general, the SSHG intensity is quadratically depending on $\chi^{(2)}$ (equation 2.73), which is proportional to the number density of molecules (equation 2.67). This relation applies within the coherence length of SHG in the medium, which can be very small close to single- or multi-photon absorption resonances. However, our crystallised films presumably exhibit many crystallites or grains of different sizes. Without further knowledge about the exact crystalline composition of our films, the coherence length is difficult to estimate. Moreover, the SSHG intensity is depending on degree of order in a medium [75, 76] and also on particle or grain sizes [294, 295]. We assume that the crystallites in the film continue growing under irradiation, even beyond the period of 48 h after preparation, when most crystallisation processes at room temperature are completed [263]. This counteracts the decrease of the SSHG intensity during desorption similar as shown for the first 48 h in figure 58, but with lower rate. When generating an excess of one enantiomer, the composition of these crystallites or

grains may be different, i.e. racemic or enantiopure (see above). Besides, the two enantiomers contribute presumably differently to SSHG generation, i.e. the strongly absorbing enantiomer contributes stronger to I_{SHG}. Another crucial parameter is the temperature in the crystal lattice. As discussed earlier, the temperature may decrease during desorption. This would lead to a reduction of thermal desorption and could be an explanation for the exponential SSHG signal decay. Furthermore, we assume that the second-harmonic response of the boundary area of the irradiated spot, where the excitation intensity of the Gaussian shaped intensity profile of the laser pulse is below the desorption threshold, gives rise to a non-zero background contribution to the SSHG intensity. Taking into account the results from desorption series at the desorption threshold, this background signal is expected to exhibit $g = 0$ and $\Delta g = 0$ (see figure 41a). However, desorption for 9 h still exhibits decreasing SSHG intensity and non-zero Δg (see figure 41b). Thus, the presumed background signal is probably very low, i.e. far below the lowest observed values of 20% of initial SSHG intensity. Hence, further examinations are necessary for an exact determination of I_{SHG} on film thickness, structure and temperature in our crystallised BINOL samples.

In summary, our desorption experiments indicate enantioenrichment in a film of racemic BINOL with controlled handedness. However, the exact determination of the magnitude of the enantiomeric excess is not possible in multilayered crystallised BINOL films with SHG-CD and SHG-ORD in our setup. Moreover, the exact mechanism, which leads to the generation of a substantial enantiomeric excess, enantiospecific desorption, photoderacemisation or a combination of both, is still under discussion.

6.5. In situ and cooled SHG-CD for studying enantiospecific desorption

In order to enhance reproducibility of sample quality and measurements, we exchanged the simple SSHG setup by a high-vacuum chamber for a second set of experiments. The new setup provides in-situ sample preparation and SSHG spectroscopy in combination with the option of cooling the sample (see figure 47). Thereby, the evolution of the anisotropy factor can be measured before the crystallisation processes in the BINOL film have completed to thermal equilibrium.
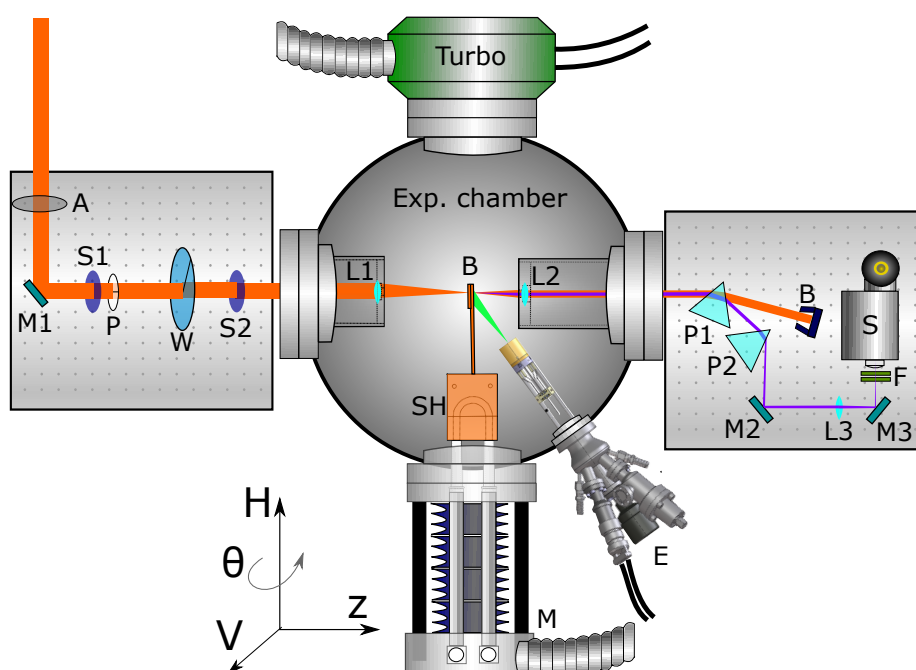

Figure 47 Top-view of the evaporation chamber setup. Two apertures (S1, S2) allow alignment of the NOPA output through an adjustable neutral density filter-wheel (A), a wire-grid polariser (P), a quarter-waveplate (W) and a lens (L1) onto the BINOL sample (B) in the vacuum chamber. Similar to the proof-of-principle setup, the co-propagating fundamental and SSHG pulses are re-collimated by lens L2 and separated by diffraction in two prisms (P1, P2). A third lens (L3) focuses the SSHG signal through UV bandpass filters (F) into the detector (S). The sample holder (SH) is connected to a manipulator (M) enabling 3D translation and rotation about the horizontal axis H. Evaporation of BINOL onto 0.2 mm thin glass substrates is realised by the OMBE (E), which is mounted from below. Adapted from [259].

A turbo-pump (TMU521P, Pfeiffer) together with pre-pumping by a diaphragm-pump (200 W, Infraserv) allow evacuation of the experimental chamber down to a pressure of 10^{-7} mbar. Femtosecond pulse generation, arrangement of optical elements and detection unit of the vacuum setup are very similar to the setup used for proof-of-principle experiments (see figure 24). The focusing and re-collimating lenses are glued on flanges, which are inserted into the chamber, and serve as entrance and exit windows for the beam. The copper sample holder is mounted onto a block of copper, which can be cooled to approximately -100°C by liquid

nitrogen pass-through. The mount is further connected to a manipulator, which allows 3D translation of the sample and rotation about its horizontal axis perpendicular to the z-axis (direction of beam propagation). Further cooling is achieved by a copper cryo-shield, which is also connected to a liquid nitrogen cooled copper block and encloses the sample holder. For sample preparation we use a temperature controlled molecular beam evaporator (OMBE-4C, DODECON nanotechnology). The thickness of the evaporated molecular film was measured with a pre-calibrated quartz micro balance similar as described in section 6.2.3. Evaporating a full crucible of BINOL at a set temperature of 210°C, close to the melting point of BINOL, provided a 7.5 μm thick film after 30 min. Already after 20 min a film thickness of 4 μm was measured. Hence the adsorption rate was larger than for the previous experiments (1.5 μm in 20 min). By slow evaporation at 150°C, homogeneous films of 1.5 μm thickness were deposited within 60 min. BINOL can be heated above the melting point without degradation [263, 277]. Therefore, effects caused by different evaporation temperatures (210°C and 150°C) can be deduced to effects caused by slower adsorption rates and final film thickness.

Figure 48 shows desorption series on racemic BINOL samples after evaporation at 210°C (a, c) and 150°C (b, d), respectively. Desorption series in figures 48a and c include data measured on 4 μm and 7.5 μm thick films. The films in figures 48b and d were 1.5 μm thick. In order to suppress or retard the formation of crystals, the sample holder was cooled during evaporation. Cooled in situ measurements are depicted in figures 48a and b, whereas figures 48c and d illustrate ex situ measurements after storing the samples for at least two days at room temperature, with the result that the main crystallisation processes in the BINOL films are completed. SSHG intensities $I_{\mathrm{SHG}}(t_d)$ evolve in a similar manner as in previous experiments, i.e. symmetrically with respect to LCP and RCP desorption, with a large spreading of the decay curves due to different excitation intensities. In situ, the SSHG signal amplitude was lower by about 3 orders of magnitude for similar excitation intensities than in the previous experiments on fully crystallised samples. Therefore, the errors are generally larger due to a lower signal-to-noise ratio. Earlier studies report a dependency of SSHG intensity on the degree of order in a medium and also on the size of particles or crystallites in a powder [294, 295]. We assume that due to suppressing the crystallisation by cooling, only a small fraction of the BINOL molecules are deposited in an ordered structure, and the majority of molecules in the film is randomly ordered, leading to the low signal intensity. Because of the low SSHG signal intensity, the excitation intensity was also adjusted to up to three-fold enhanced magnitudes.

The measured changes in anisotropy factor, $\Delta g(t_d)$, do not exhibit the clear antisymmetric evolution on samples, which are cooled during in situ preparation and desorption (see figures 48a and b, lower panels). We measure both positive and negative values for Δg on fast evaporated BINOL films (a) upon RCP desorption. The average deviates only slightly from zero to positive values. Only one desorption series was measured during LCP desorption. $\Delta g(t_d)$ increases quickly to -0.1, but changes to positive signs after 40 min. For slowly evaporated films (b), $\Delta g(t_d)$
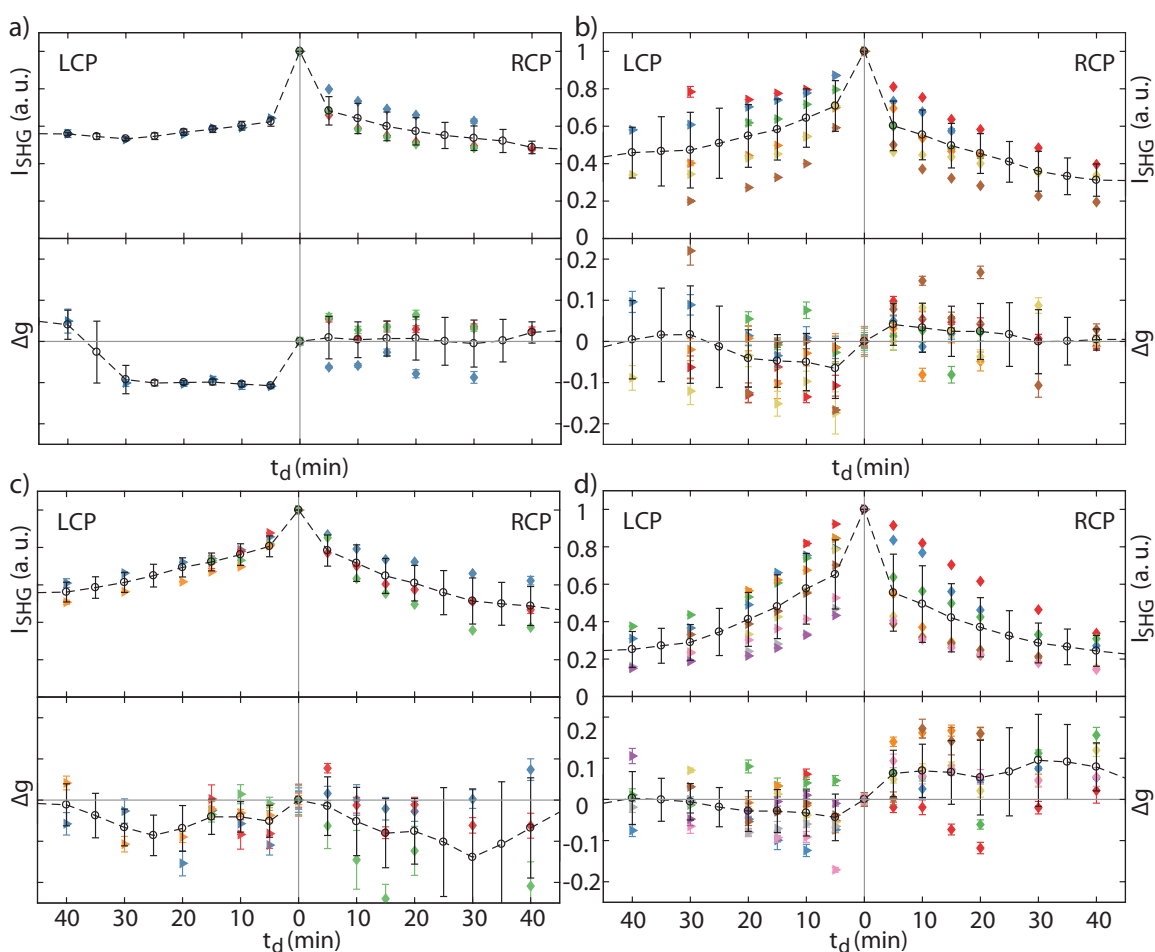
Figure 48 Desorption measurements in the vacuum chamber after evaporation of racemic BINOL at 210°C (a, c) and 150°C (b, d), respectively. The sample holder was cooled during evaporation. I_{SHG} and Δg upon irradiation with LCP (left panels) and RCP (right panels) pulses on spots satisfying the requirement $|g(t_d = 0)| < 0.1$ are plotted for desorption times t_d up to 40 min. a), b) In situ evaporation and measurement with cooling. a) and c) include data measured on 4 μm and 7.5 μm thick films. c), d) Ex situ measurements more than 2 days after cooled sample preparation. The black circles connected by a dashed line denote a moving average of the data.

evolves antisymmetrically with negative signs for LCP desorption and positive signs for RCP desorption at least for the first 30 min, but approaches zero for longer times. Moreover, both positive and negative values are observed for each desorption polarisation.

Crystallisation does not lead to a significant change of the Δg evolution on films evaporated onto cooled substrates (see figures 48c and d, lower panels). The average values of the fast evaporated films are both negative during the first 40 min desorption with LCP and RCP pulses (figure 48c). Crystallized films after slow evaporation reflect the antisymmetric evolution of $\Delta g(t_d)$ observed during in situ measurements (figure 48d). Again, negative as well as positive values are determined for both desorption polarisations.

Figure 49 shows all desorption series (in situ and crystallised) measured on a sample, which was
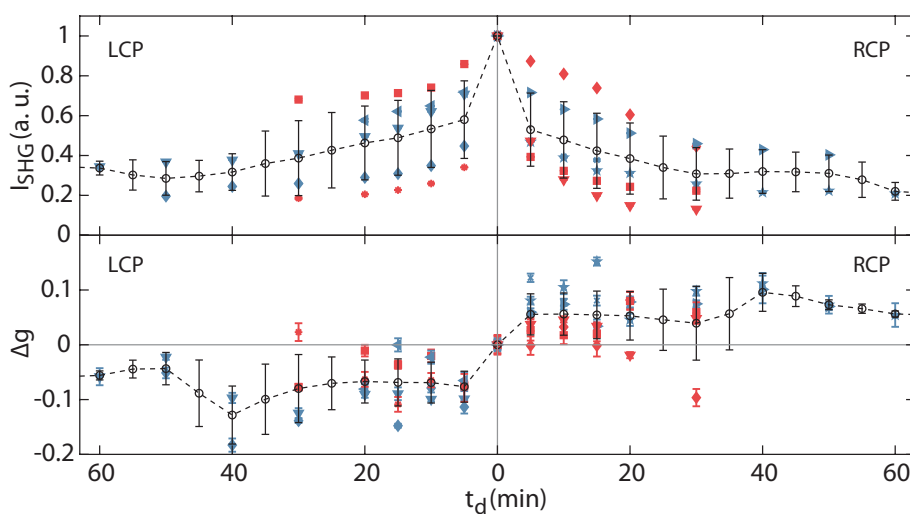
Figure 49 Desorption measurements in the vacuum chamber after slow evaporation of racemic BINOL (evaporator set to 150°C) without cooling. I_{SHG} and Δg upon irradiation with LCP (left panels) and RCP (right panels) pulses on spots satisfying the requirement $|g(t_d = 0)| < 0.1$ are plotted for desorption times t_d up to 60 min. Desorption series measured in situ and after > 2 d are shown in red and blue, respectively. The circles connected by a dashed line denote a moving average of the data.

slowly evaporated at 150°C, however without cooling the sample holder, i.e. at room temperature. The evolution of $I_{\mathrm{SHG}}(t_d)$ and $\Delta g(t_d)$, i.e. symmetric for I_{SHG} and antisymmetric for Δg with respect to CP desorption polarisation, clearly demonstrates that the previous results (see figure 39) can be principally reproduced with the new setup. Without cooling, crystallisation of BINOL molecules into small crystallites can already occur during the 60 min of evaporation, which develops further during the in situ measurements in vacuum directly after evaporation. The Δg evolution exhibits larger antisymmetry (blue data points) when measured on fully crystallised films than measured in situ directly after evaporation (red data points).

By comparison of the results from figures 48 and 49, it seems that sufficient progression of crystallisation during evaporation is required for the occurrence of generating antisymmetric Δg evolution during desorption with CPL. Slow evaporation of 1.5 μm thick films definitely seems to favour the antisymmetric effect. For films evaporated without cooling, completion of the crystallisation process further enhances the effect. The missing antisymmetry in figures 48a and c could also be caused by the much larger thickness of the film, i.e. 4 μm and 7.5 μm instead of 1.5 μm. Moreover, we can not exclude photodegradation anymore due to the larger excitation intensities. This might be another reason for the missing antisymmetry. For a complete understanding of the origin related to the observed phenomena, a high-resolution microscopic examination of the structural properties and changes during desorption and crystallisation of the films is required.

6.6. Numerical modelling

We developed a simple phenomenological model of the most important processes during irradiation of the racemic BINOL film with CP laser pulses, which were worked out in section 6.4.5. The predominant processes are desorption, surface diffusion and racemisation. Since photoresolution by enantiomerisation in combination with thermal desorption leads to the same microscopic composition of the film as enantiospecific desorption, we restrict the description to enantiospecific desorption. Bulk diffusion in the BINOL film is of minor relevance, particularly in the crystal phase. Due to the lack of explicit values of desorption and racemisation rates and diffusion constants other than phenomenological estimations, we try to keep the numerics as simple as possible.

Finite difference model

As a first step, we model the irradiated BINOL film as a 1D layered system and apply phenomenological rate equations. The temporal evolution of the number concentrations is calculated numerically by implementation of a finite difference method using a forward Euler algorithm. We limit the discussion to the case of desorption with RCP laser pulses.
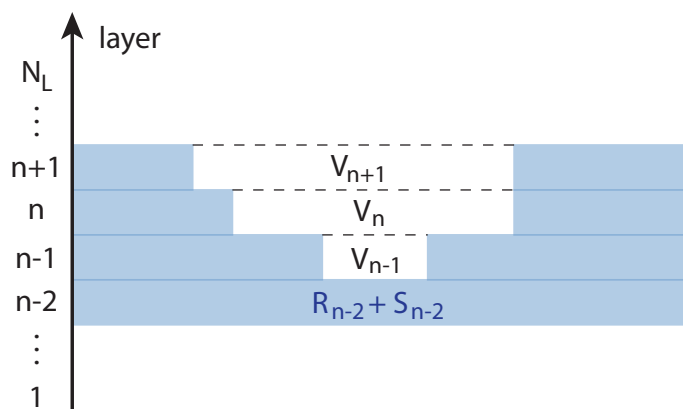

Figure 50 Numerical model of a system of N_L layers. Each layer n represents one volume cell containing normalised number concentrations of S-molecules S_n, R-molecules R_n and vacancies V_n.

The system consists of N_L layers. Each layer n represents exactly one volume cell, which initially contains equal normalised number concentrations $S_n = 0.5$ of S-BINOL and $R_n = 0.5$ of R-BINOL molecules. Desorption causes a decrease of S_n and R_n and creates vacancies $V_n = 1 - S_n - R_n$ (see figure 50). According to the bi-exponential decay of SSHG intensity during desorption, we implement rate equations using two different desorption rates $\delta_{1,2}$ for the two enantiomers. Both rates include quantum mechanical and thermal contributions. Similar to the fitting model (see section 6.4.4), δ_1 and δ_2 denote the desorption rates of S-BINOL and R-BINOL molecules upon interaction with RCP pulses, respectively. We restrict desorption to the top layer and exclude vacancies in this layer, which gives rise to the expression $-V_n$. In

lower layers, desorption is only possible, if the respective molecule is below a vacancy V_{n+1} in the next upper layer $n + 1$. Accordingly, desorption of S-BINOL and R-BINOL from the film surface is written as

$$\frac{d}{dt} S_n^{des} = -\delta_1 S_n (V_{n+1} - V_n) \tag{6.28}$$

and

$$\frac{d}{dt} R_n^{des} = -\delta_2 R_n (V_{n+1} - V_n), \tag{6.29}$$

respectively. Diffusion on the surface by random walk leads to a refilling of vacancies in the upper layers with rate γ. Hence, a gain in number concentration of S in layer n, which is equal to the concentration of vacancies in this layer multiplied by the concentration of S in the upper layer S_{n+1}, opposes a loss in S equal to V_{n-1} multiplied by S_n. The respective rate equation is written as

$$\frac{d}{dt} S_n^{surf} = \gamma (S_{n+1} V_n - S_n V_{n-1}). \tag{6.30}$$

Because this process is not enantiospecific, the respective rate equation of R is analogously represented by

$$\frac{d}{dt} R_n^{surf} = \gamma (R_{n+1} V_n - R_n V_{n-1}). \tag{6.31}$$

Racemisation denotes the interconversion of one enantiomer into the other enantiomer. For long times, this process produces a racemate. Thus, the effective loss or gain of S_n and R_n with rate ρ is proportional to the difference in S-BINOL and R-BINOL concentrations:

$$\frac{d}{dt} S_n^{rac} = \rho (R_n - S_n) \tag{6.32}$$

and

$$\frac{d}{dt} R_n^{rac} = \rho (S_n - R_n). \tag{6.33}$$

Enantiospecific desorption from the top layers generates a concentration gradient $\frac{\partial c}{\partial x}$ between the top and bottom layers. The concentration gradient induces diffusion in the bulk, which is generally described by the diffusion equation

$$\frac{d}{dt} c = \frac{\partial}{\partial x} \left(D \frac{\partial}{\partial x} c \right), \tag{6.34}$$

with the diffusion constant D. In our model, bulk diffusion is very weak. Therefore, we consider only the case of self-diffusion (often referred to as inter-diffusion), which describes the position exchange of two molecules driven by a concentration gradient in the binary S-BINOL and R-BINOL crystal or mixture. The self-diffusion constant is defined as [296, 297]

$$D_s = \alpha_S \cdot S + \alpha_R \cdot R = \alpha (S + R), \tag{6.35}$$

with the self-diffusion coefficients $\alpha_S \cong \alpha_R := \alpha$ for S-BINOL and R-BINOL molecules. Accordingly, the contribution of diffusion to the temporal evolution of S_n and R_n is written

as

$$\frac{d}{dt}S_n^{diff} = \alpha\frac{\partial}{\partial x}\left[(S_n + R_n)\frac{\partial}{\partial x}S_n\right] = \alpha\left[(\frac{\partial S_n}{\partial x})^2 + (S_n + R_n)\frac{\partial^2 S_n}{\partial x^2} + \frac{\partial R_n}{\partial x}\frac{\partial S_n}{\partial x}\right] \quad (6.36)$$

and

$$\frac{d}{dt}R_n^{diff} = \alpha\frac{\partial}{\partial x}\left[(S_n + R_n)\frac{\partial}{\partial x}R_n\right] = \alpha\left[(\frac{\partial R_n}{\partial x})^2 + (S_n + R_n)\frac{\partial^2 R_n}{\partial x^2} + \frac{\partial R_n}{\partial x}\frac{\partial S_n}{\partial x}\right]. \quad (6.37)$$

The temporal evolution upon irradiation with RCP pulses is calculated numerically for N_T finite time steps t_i ($i = 1...N_t$) for the complete equations

$$\frac{d}{dt}S_n = \frac{d}{dt}(S_n^{des} + S_n^{surf} + S_n^{rac} + S_n^{diff}) \quad (6.38)$$

and

$$\frac{d}{dt}R_n = \frac{d}{dt}(R_n^{des} + R_n^{surf} + R_n^{rac} + R_n^{diff}), \quad (6.39)$$

for all layers n. The enantiomeric excess for each layer n and time step t_i is defined as

$$ee_n(t_i) = \left|\frac{R_n(t_i) - S_n(t_i)}{R_n(t_i) + S_n(t_i)}\right|. \quad (6.40)$$

Moreover, the total number concentrations $S(t_i)$ and $R(t_i)$ for each time step are

$$S(t_i) = \frac{1}{2}\cdot\frac{\sum_n^{N_L} S_n(t_i)}{\sum_n^{N_L} S_n(t_1)} \quad (6.41)$$

and

$$R(t_i) = \frac{1}{2}\cdot\frac{\sum_n^{N_L} R_n(t_i)}{\sum_n^{N_L} R_n(t_1)}. \quad (6.42)$$

The total enantiomeric excess for each time step is defined as

$$ee(t_i) = \left|\frac{R(t_i) - S(t_i)}{R(t_i) + S(t_i)}\right|. \quad (6.43)$$

The relation of ee to the experimentally determined Δg is given by $ee(t_i) = \frac{\Delta g(t_i)}{g_p}$ (see section 6.4.4), and $I_{\mathrm{SHG}}(t_i)$ is given by $(R(t_i) + S(t_i))$. Before fitting the numerical model to the experimental data, we defined suitable start values and boundaries for the parameters δ_1, δ_2, γ, ρ and α (see table 12, appendix A.7).

Figure 51a shows the fit of a system of 100 layers to the moving average data set (see figure 46). The fit was performed for three different values of g_p, reflecting the maximum of the moving average ($g_p = 0.15$), the absolute value of the maximum measured Δg ($g_p = 0.26$), and the value obtained from enantiopure and 10%-ee S-BINOL and R-BINOL samples ($g_p = 0.7$). In
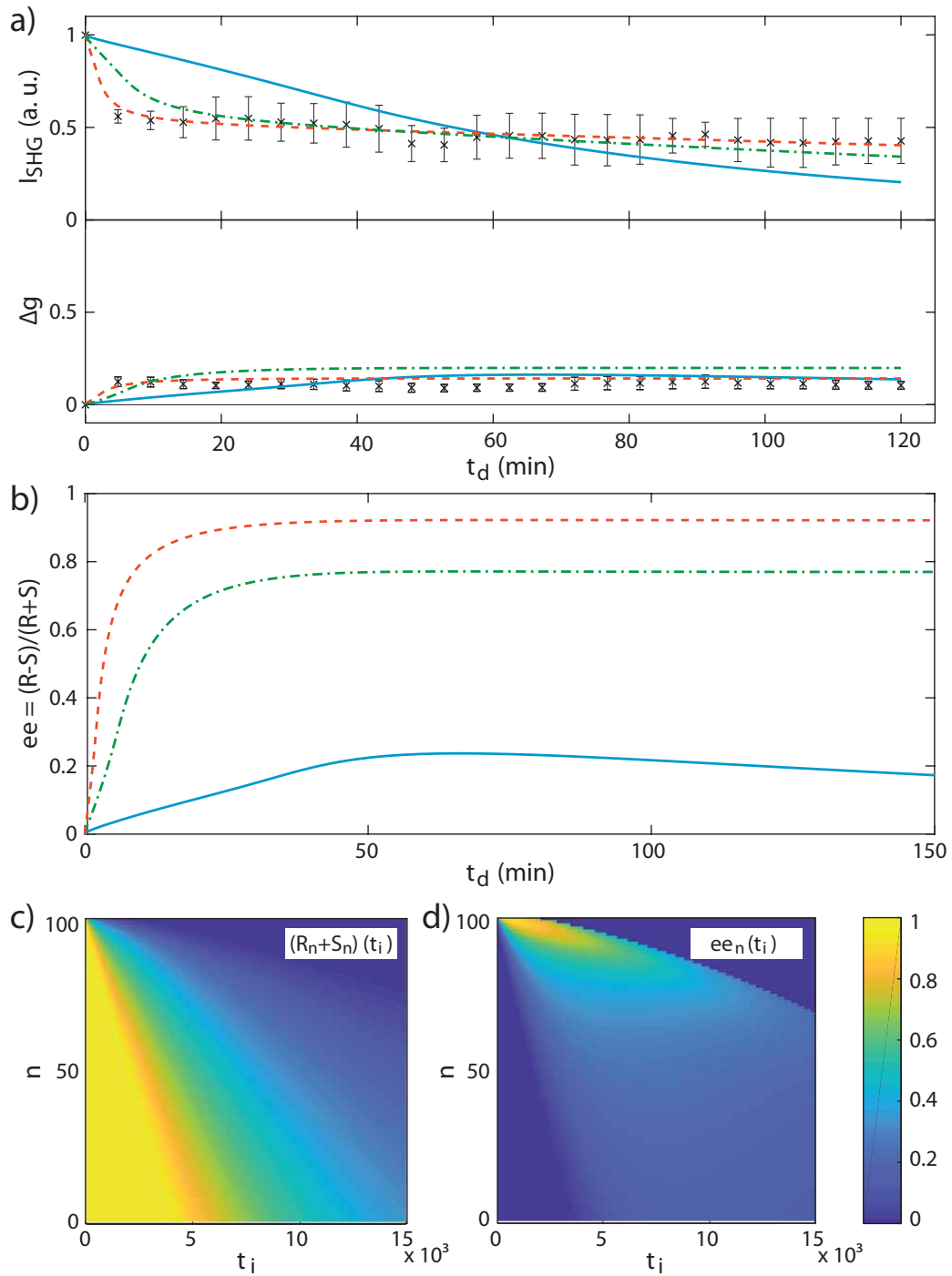
Figure 51 Numerical simulations and fit to experimental data. a) Results from a numerical simulation of a 1D system of 100 layers according to equations 6.39 fitted to a moving average of the experimental data (black crosses). Upper panel: I_{SHG}, lower panel: Δg. The fits were performed for different values of g_p: 0.7 (blue solid lines), 0.26 (green dot-dashed lines), 0.15 (red dashed lines). The fit parameters are listed in table 10. b) Corresponding simulated curves for ee using the fit parameters obtained from the 3 fits. c), d) Simulated temporal evolution of $R_n + S_n$ in number concentrations (c) and ee_n (d) for each layer n and time step t_i according to the parameters obtained from the fit using the spectroscopically determined g_p of 0.7: $\delta_1 = 5$ min^{-1}, $\delta_2 = 0.26$ min^{-1}, $\gamma = 0.2$ min^{-1}, $\rho = 0.2$ min^{-1} and $\alpha = 0$.

g_p	$\delta_1 (min^{-1})$	$\delta_2 (min^{-1})$	$\rho (min^{-1})$	$\gamma (min^{-1})$	$\alpha (m^2 s^{-1})$
0.15	89 ± 39	0.001 ± 0.278	0.001 ± 0.002	0.2	0
0.26	31 ± 18	0.001 ± 0.449	0.004 ± 0.004	0.2	0
0.7	4.9 ± 5.3	0.26 ± 1.7	0.03 ± 0.040	0.2	0

Table 10 Fit parameters extracted from the fitted data traces according to the 1D numerical simulation of a system of 100 layers for 150 min with time steps of 0.01 min: δ_1: desorption rate for S-BINOL, δ_2: desorption rate for R-BINOL, ρ: racemisation rate, γ: diffusion rate for refilling vacancies, α: self-diffusion constant. The errors denote 95% confidence intervals.

order to avoid overestimation, we fixed γ and α to pre-determined values (see table 10). Starting values and limits as well as the results from fitting γ and α are summarized in tables 12 and 13 (appendix A.7). Setting γ equal to zero generates weakly filled porous upper layers. Therefore, we set it to a suitable value of 0.2 for our simulation. Because diffusion in the bulk can not be larger than on the surface, we limited α to values below γ. For the parameter set applied for figures 51c and d, bulk diffusion appeared to be neglectable. Hence, α was set to zero for simplicity for the following discussion.

The complete set of above described rate equations was fitted simultaneously to I_{SHG} and Δg of our data (see figure 51a). The simulations of $ee(t)$, which correspond to the fits in figure 51a, are illustrated in figure 51b. Only the fits with g_p equal to 0.15 and 0.26 reflect the extremely fast decaying intensity and increasing Δg (figure 51a). The generation of an ee close to 1, however, seems too high. For a significant attenuation of the enantiomeric excess, racemisation has to be included. The growing fit values for ρ, when increasing g_p, indicate that ρ is the crucial parameter for the low ee and Δg. Although the fits using g_p equal to 0.15 and 0.26 match the data better, we set g_p to the spectroscopically determined value of 0.7 in the following for lack of evidence for the other values. Hence, the lowest ee-curve, corresponding to the fit with $g_p = 0.7$, exhibits a maximum at slightly above 0.2. Both simulated $I_{\mathrm{SHG}}(t) = (R+S)(t)$ and $ee(t)$ approach zero for longer desorption times.

Figure 51c depicts the evolution of the magnitudes $R_n(t_i) + S_n(t_i)$ and $ee_n(t_i)$ (equation 6.40) for the fit parameters obtained from fitting with $g_p = 0.7$. Initially, all layers are completely filled with S- and R-molecules indicated by number concentrations close to unity. After 15000 time steps corresponding to 150 min, the upper edge of partly filled layers has decreased to about layer number 75 due to the refilling terms S^{surf} and R^{surf}. Preferential desorption of S-molecules (due to $\delta_1 > \delta_2$) leads to fast generation of an enantiomeric excess close to unity in the upper layers and zero in the bottom layers. For proceeding time, the ee disperses to lower layers. The upper limit to layers with ee equal to zero corresponds to the lower edge of partly filled layers in figure 51c. When allowing bulk diffusion, these strong borders blur.

In this simplified model, the simulation parameters $\delta_{1,2}$, ρ, γ and α are not equal to the real physical rates and constants, however, indicate the relative contributions of the particular processes. Their exact values depend on the experimental conditions such as excitation intensity and the thickness of the film. When extending the system to 2000 layers, i.e. each layer represents a monolayer of the BINOL film, the evolution is qualitatively similar.
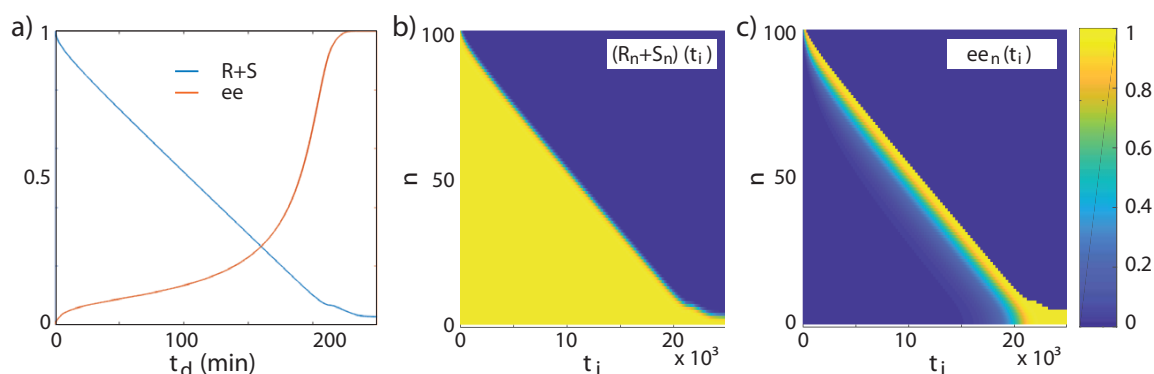

Figure 52 Numerical simulation illustrating the influence of surface and bulk diffusion for a total desorption time of 250 min. Desorption rates are set to the same values as for figures 51c and d ($\delta_1 = 5$ min^{-1}, $\delta_2 = 0.26$ min^{-1}), racemisation is excluded ($\rho = 0$), whereas large rates are chosen for surface and bulk diffusion: $\gamma = \delta_1 = 5$ min^{-1}, $\alpha \cdot (dx)^2 = \gamma/2$. dx denotes the thickness of one layer. a) Simulated curves of R+S (blue) and ee (orange). b) Simulated evolution of $(R_n + S_n)$, and c) ee_n per layer n and time step t_i.

It has to be noted that the generation of an ee greater than zero is solely caused by introducing two different desorption rates. A very similar result is expected for introducing photoderacemisation in the upper layers in combination with thermal desorption, or a combination of these processes with enantiospecific desorption. Keeping γ low and neglecting racemisation, the system necessarily evolves to an ee of close to 100% (see figure 51b, red and green curves). Excluding racemisation, the ee can only be attenuated for a certain time when setting γ to a large value. Figure 52c shows that setting of γ equal to δ_1 limits the generation of ee to the top layers due to nearly instantaneous refilling of vacancies as indicated by completely filled layers up to the film surface in figure 52b. In order to extend the number of layers, where enantioenrichment is possible, the contribution of bulk diffusion needs to be included. Hence, setting $\alpha \cdot (dx)^2 = \gamma/2$, with layer thickness $dx = 1.5$ μm/N_L, gives rise to a total ee which matches the experimental data more or less up to t_d = 120 min, but then rises fast to unity for longer times (figure 52a). This evolution, however disagrees our data, in particular the results for long-time desorption (see figure 41b). A comparison with figure 52c yields that the fast increase of ee occurs, when the number of layers approaches zero. For longer desorption times, all molecules are desorbed and the ee decreases rapidly to zero.

We conclude that only the introduction of racemisation leads to an evolution of ee and Δg, which reflects our experimental data. Using the parameter set obtained from the fit according to the spectroscopically determined g_p of 0.7, the simulated system evolves in agreement with our

phenomenological model derived in section 6.4.5. Particularly, the simulation of the enantiomeric excess matches the saturated evolution of the experimentally determined Δg. The deviation of the summed concentrations of R- and S-molecules from the measured SSHG intensity is an indication for further processes such as structural changes in the BINOL film, which contribute to the SSHG signal, but are not covered by this simplified model. As discussed in section 6.4.5, I_{SHG} does not necessarily depend linearly on film thickness in the completely crystallised film, and the two enantiomers may contribute differently to SSHG generation. Moreover, a possible decrease of the temperature in the film with decreasing film thickness is not incorporated. Besides, SSHG contributions of the film from the boundary area of the irradiated spot, where the intensity of the Gaussian shaped intensity profile of the laser pulse is below the desorption threshold, are not considered here. Hence, further information on the structural properties and further thermodynamical processes in the film during irradiation with fs-pulses is required for a better theoretical description and modelling.

Monte-Carlo model

Furthermore, we pursued a different approach on elucidating the processes in the film on a microscopic level with a 2D Monte-Carlo formalism. We implemented a 2D layered matrix of initially randomly distributed S-BINOL and R-BINOL molecules. The random distribution can represent a crystallised film consisting of many small crystallites as in the experiments in section 6.4, or a random conglomerate as it is assumed to be upon cooled evaporation (see section 6.5). The Monte-Carlo implementation is suitable for the description of statistical processes such as surface diffusion, desorption and racemisation, which are further restricted by different boundary conditions. Thus, we assume distinct probabilities for the occurrence of these processes according to their respective rates. The temporal evolution of the system was numerically calculated. Although desisting from an exponential ansatz, the evolution of the sum of S-BINOL and R-BINOL molecules resembles the blue curve for $g_p = 0.7$ in figure 51a. The calculated enantiomeric excess increases rapidly to values below 0.01, then grows very slowly, but continuously, depending on the difference between the two desorption probabilities. When the number of molecules decreases below approximately 20%, the ee increases fast to a maximum, which is limited by the probability for racemisation, before approaching zero. This continuously increasing evolution with decreasing number of molecules seems plausible, however does not agree with the experimentally observed Δg evolution. The deviation could indicate that the measured SSHG intensity and Δg do not represent the microscopic composition of the film, but rather comprise the nonlinear chiroptical response of both macroscopic structure and microscopic composition. However, without further investigations the estimation of the relation between measured values of I_{SHG} and Δg and the simulation of the composition of the film is too speculative. Therefore, we desisted from presenting more details. Further information presupposed, the Monte-Carlo model can easily be extended to a 3D implementation, which incorporates the Gaussian shaped intensity profile of the laser pulse.

6.7. Conclusion and outlook

In conclusion, we demonstrate the reproducible generation of a well-defined antisymmetric evolution of the optical activity in a film of racemic BINOL upon irradiation with circularly polarised femtosecond pulses. The antisymmetric evolution of induced changes in the anisotropy factor Δg and the rotation angle $\Delta \delta$ was examined by resonant SHG-CD and SHG-ORD spectroscopy using pulses at a central wavelength of 600 nm and 650 nm. From comparison with experiments using off-resonant excitation and linearly polarised pulses we conclude that a quantum mechanical light-matter interaction leads to this evolution. The observed effect is closely connected with desorption of BINOL molecules from the film surface induced by the laser pulses. We assume that in addition to thermal desorption direct TPA excitation by the laser pulses triggers the desorption in a nonadiabatic process. The removal of material from spots with more than 200 μm diameter was confirmed by microscopy. Our results strongly support the generation of an enantiomeric excess in the remaining BINOL film as source for the antisymmetric evolution. Excluding enantiospecific photodestruction, two potential enantiospecific processes can be identified, which can lead to enantioenrichment: enantiospecific desorption and photoresolution by preferential enantiomerisation. Their particular contributions mainly depend on the respective energy barriers and have to be unravelled by theoretical calculations and further experiments. Moreover, an entanglement of both processes is imaginable, since both involve changes in the dihedral angle in the excited state. Because the feasibility of enantiomerisation is limited to axially chiral molecules, experiments on molecules, which exhibit other types of chirality such as planar chirality, can help to confirm photodesorption as an enantiospecific effect.

Based on these results, we developed a simple phenomenological model and identify desorption (thermal and quantum mechanical), surface diffusion and enantiomerisation (photoresolution and racemisation) as the predominant processes in the irradiated film. Assuming enantiospecific desorption as feasible, circularly polarised laser pulses induce desorption of both enantiomers from the film surface, but with significantly different rates due to the different TPA cross-sections. Vacancies are quickly refilled by random walk of BINOL molecules on the surface in order to minimise the total energy of the system. Thermal heating caused by the absorbed laser pulses is in our estimation too low for melting, however, facilitates thermal desorption, thermal racemisation and diffusion. Although bulk diffusion is expected to be very weak in the crystalline film, it counteracts the depletion of the fast desorbing enantiomer in the top layers. We identify racemisation as main process leading to saturation and attenuation of the antisymmetric evolution of optical activity, similar to earlier photoresolution experiments.

The numerical finite difference implementation of the predominant processes, which are triggered by circularly polarised fs-pulses, exhibits good agreement with the experimental data. In particular, the introduction of racemisation proved essential for the description of the saturation and attenuation of the enantiomeric excess. Although the decay of the number concentration of

S-BINOL and R-BINOL molecules in the system was modelled with an exponential function in order to reflect the bi-exponential decay of the measured SSHG intensity, a fit of the numerical model to the experimental data exhibits a significant deviation in its early evolution. Moreover, exponential decay of film thickness, i.e. the total number of molecules, is not trivial. Describing laser-induced desorption as a statistical process with certain probabilities does not necessarily lead to an exponential decrease of the number of molecules. One reason can be that the relation of SSHG intensity and film thickness, and thus the number of molecules, in the crystalline film may be different from the measured linear dependence during evaporation. SHG-ORD results indicate structural contributions to the SSHG response and the optical activity of the film. Changes in molecular composition and growth of the crystallites in the film during irradiation presumably give rise to further structural contributions. Besides, the eventually different contribution of the enantiomers to the SSHG signal and contributions from molecules of the boundary area of the irradiated spot, which can not be desorbed, have to be elucidated. In-situ experiments with cooling reveal that a slow evaporation rate is essential for the observation of an antisymmetric evolution of optical activity Δg. Thus, we conclude that a certain orientation and arrangement of the molecules is required for the antisymmetry. Hence, further investigations of the structural and thermodynamical processes and of the dependence of SSHG intensity on film thickness, structure and temperature in the crystallised film are required for a complete understanding of the observed evolution.

Our results indicate that statistical averaging over many measurement spots on the film is essential in order to obtain convincing and reproducible results. Therefore, the irradiation parameters should be adjusted in order to desorb and measure on spots as large as possible allowing to average over structural inhomogeneities. This entails the use of a high energy pulsed laser system. Furthermore, a faster motor driving the quarter-wave plate would allow a randomised order of LCP and RCP measurements leading to diminishing measurement errors err_{des} and err_{surf}.

The generation of a chiral surface, as we produce in our irradiated and not completely desorbed spots, would be of great relevance for heterogeneous asymmetric catalysis, when extended to larger dimensions. The exact determination of the generated enantiomeric excess, however, remains challenging with SHG-CD and SHG-ORD. Microscopy studies on enantiopure films revealed the formation of large crystals with a macroscopic optical activity. Thus, the measurement of reliable anisotropy factors on enantiopure films turned out to be difficult. Incorporation of films exhibiting 10% ee, allowed to estimate an anisotropy factor of approximately 0.7 in enantiopure films. Hence, average maximum desorption-induced Δg of ± 0.15 would reflect an enantiomeric excess of 21%. Particularly SHG-ORD experiments indicated that we cannot exclude structural contributions to the SSHG intensity and generated optical activity. Other methods, which are not sensitive to macroscopic chirality, such as SFG spectroscopy (see section 2.2.7), could improve this examination. Adjusting the irradiation parameters in order to enable desorption

from larger spots would allow examination of the composition and the enantiomeric excess with FTIR (Fourier transform infrared) spectroscopy [277], or even with (linear) CD after dissolving the irradiated material. The desorbed molecules may also be condensed at a second substrate, which can be mounted above the film, prospective of an enantioseparation method. As soon as the ee can be reliably determined, this method opens new ways in enantioseparation and -purification without the risk of contamination by chemical adducts.

The detailed dynamics of photodesorption of single BINOL molecules from a film consisting of the same material still has to be elucidated. We assume that orientational changes in the BINOL molecule due to the modified electron configuration in the excited state, similar to the decrease of the dihedral angle upon UV excitation, causes distortions, which can trigger the removal of the molecule from the film. Femtosecond transient absorption or fluorescence measurements on BINOL films with different excitation wavelengths together with TDDFT calculations can help to unravel the electron dynamics in the excited state. Applied to surfaces, these methods allow to elucidate the evetually different steps of the desorption mechanism. The change of the dihedral angle can be examined by applying femtosecond transient absorption circular dichroism spectroscopy in solution and on films. UV-pump-IR-probe spectroscopy gives further insight into structural changes. Furthermore, repeating the desorption experiment with weak UV pulses can give information on the requirement of TPA for the desired effect. The nonlinear, and in case of TPA, resonant, nature of the process can further be examined by testing, whether intensity or fluence is the crucial parameter, which desorption yield and generated change in optical activity depend on. Performing experiments using different pulse durations (at constant fluence) would be a simple method to determine, whether the desorption occurs in one step or in two steps in order to further elucidate the mechanism. Intactness of desorbed molecules can be verified by mass spectrometry during in-situ desorption experiments in the vacuum chamber. Repetition of desorption series on films of 2-naphthol, the achiral component of BINOL, could further confirm enantiospecific desorption.

Part V

Summary and outlook

Summary and outlook

This thesis presents two different approaches to utilise femtosecond spectroscopy. As a first step, broadband transient absorption spectroscopy was applied to unravel complex photophysical and photochemical processes in pharmaceutically and technically relevant organic molecules. In combination with TDDFT calculations we elucidated the origins of an anomalous heavy-atom effect upon 6-substitution of 3-diethylphosphonocoumarins and coumarin-3-phosphonic acid with the halogens Cl and Br. Strongly enhanced singlet lifetimes and fluorescence quantum yields of the Cl-compound were related to an enhanced change of dipole moments due to a partial charge transfer from the halogen lone pair orbitals to the coumarin π^*-orbitals. On the other hand, the impact of the heavy-atom effect, which gives rise to increased intersystem crossing rates and triplet yields in both halogen substituted compounds, quenches fluorescence and lifetime particularly in the Br-compound. From a multi-exponential fit we could extract singlet lifetimes between 16 ps and 160 ps, depending on 6-substitution and solvent. Br-substitution enabled to double the triplet yield with respect to the unsubstituted compound. The complex interplay of two different effects allows the individual control of singlet lifetime and triplet yield by different 6-substitutions, which is of great interest for pharmaceutical applications. In a second project, we disentangled the excited state dynamics during the photochemical transformation of a chromone compound, which is an interesting candidate for the application as organic WORM-type information storage. The photochemical transformation involves a ring-opening process and the subsequent formation of a new ring. Broadband transient absorption spectroscopy reveals strong indication for an ultrafast two-step process via an intermediate state (with a lifetime of 3 - 5 ps), which can be attributed to the open-ring isomer. These examinations are an important first step towards optimising the molecular structure towards larger switching efficiency and quantum yield of the photoproduct. Prospective pump-repump-fluorescence and UV-pump-IR-probe measurements in combination with TDDFT calculations will help to completely describe the photochemical process. The obtained results emphasise further the relevance of femtosecond transient spectroscopy for the understanding and the resultant optimisation of photophysical and photochemical properties with respect to the desired applications. Femtosecond spectroscopy, hence, can serve as a bridge between chemical synthesis and in vitro studies.

Furthermore, we applied fluorescence upconversion spectroscopy with a femtosecond-long-cavitiy-oscillator on naphthalimide-isoquinoline derivatives in solution. These molecules exhibit dual fluorescence from different excited states with strong dependency on solvent polarity. Because a detailed presentation of the obtained results would extend the scope of this work, I would like to refer to Julia Frisch's Master's thesis [298].

In the second experimental part, we used circularly polarised femtosecond pulses to investigate the optical activity and its evolution during laser-induced desorption of BINOL films. The

optical activity of enantiopure and racemic films was determined using SHG-CD and SHG-ORD spectroscopy. Therefore, a surface second-harmonic spectroscopy setup, including a Czerny-Turner spectrometer and a liquid nitrogen cooled CCD camera as spectrograph, was developed and characterised. The experiments yielded reproducible generation of significant and well-defined optical activity in a crystalline BINOL film upon resonant TPA and simultaneous desorption triggered by visible circularly polarised laser pulses. The decrease of the film thickness and its intactness were confirmed by microscopy. Through a thorough analysis of our data and comparison with earlier studies on the structural properties of BINOL, we conclude a substantial enantiomeric excess in the remaining BINOL film as origin for the generated optical activity. Enantioenrichment is presumably achieved by preferential direct desorption of one of the two enantiomers due to an enhanced cross-section for TPA of circularly polarised laser pulses. However, a contribution of laser-induced isomerisation leading to partial photoresolution and following thermal desorption upon TPA can not be ruled out without further investigations. The enhanced temperature in the film due to TPA in the bulk facilitates thermal desorption, surface and bulk diffusion, and thermal racemisation. We assume the latter process as reason for the saturation of generated optical activity to a maximum degree during a desorption experiment. This simplified model was qualitatively confirmed by a 1D numerical simulation. The exact determination of the associated enantiomeric excess revealed to be difficult. By comparison with enantiopure and 10%ee samples, we could attribute average maximum desorption-induced anisotropy factors of ± 0.15 to an enantiomeric excess of 21%. However, macroscopic chiral structures on enantiopure films hindered the reliable measurement of their microscopic optical activity. Hence, this value still needs verification by applying different methods such as conventional CD spectroscopy in solution. Nonetheless, this is the first demonstration of a defined laser-stimulated enantioenrichment of a racemic film, which is deposited on an achiral substrate. Implying the extension of the desorbed spots from sub-mm diameter to larger dimensions and eventual condensation of the desorbed molecules provides unprecedented ways of contaminant-free enantioseparation. The resultant production of a chiral surface opens up new opportunities for absolute asymmetric catalysis. The idea for this new method for enantioenrichment was granted with a patent [299].

As a further step, utilisation of the methods presented in the first experimental part of this thesis to BINOL surfaces allows to get a deeper insight into the exact enantiospecific mechanism which leads to the enantioenrichment. Combination of various methods, involving transient absorption circular dichroism spectroscopy, structural investigation by different microscopy techniques, infrared spectroscopy, and quantum chemical calculations constitutes a holistic approach to understanding and further development of the invention.

Part VI

Appendix

A. Nonlinear studies on enantioenrichment - supplementary information

A.1. Pulse duration
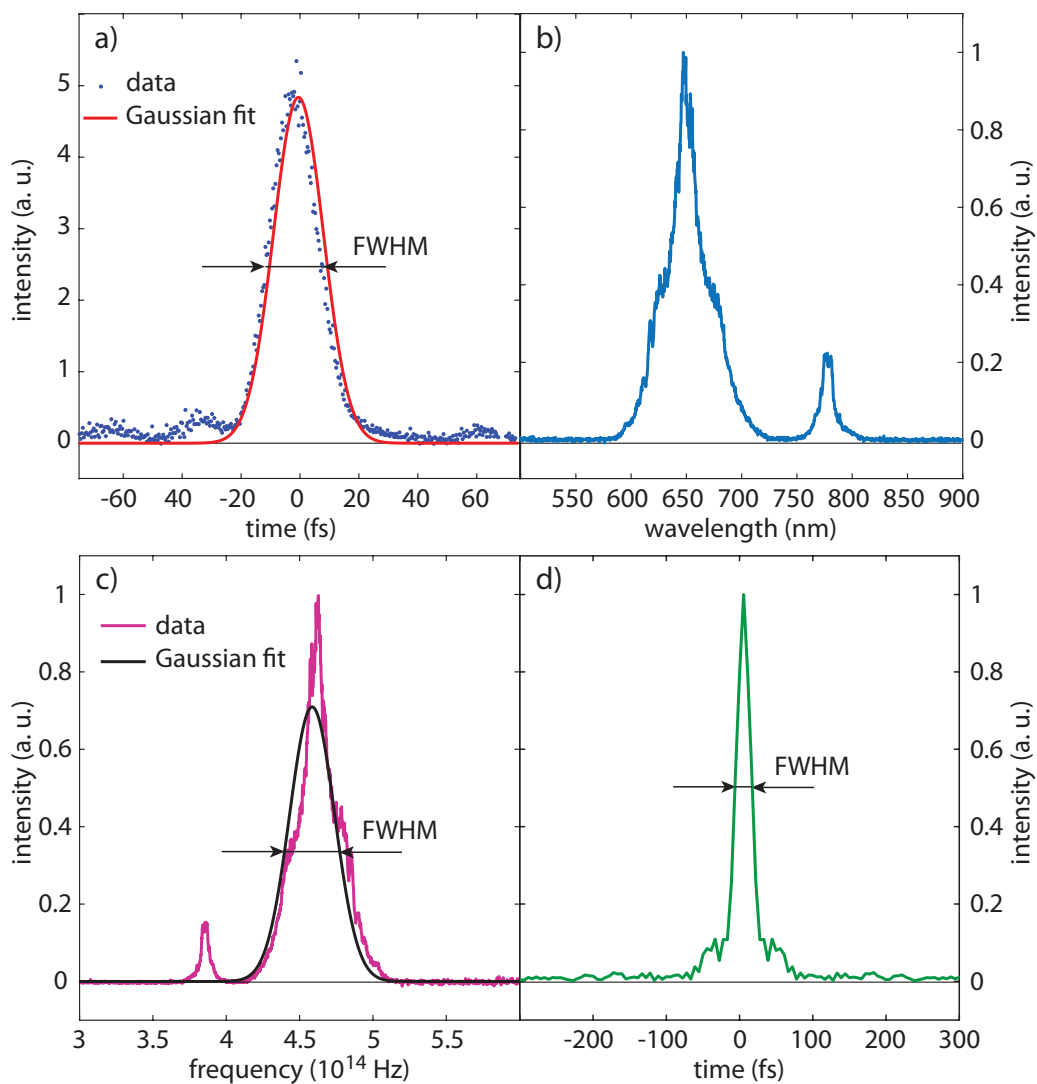
Figure 53 Pulse characterisation of the NOPA output tuned to 650 nm, which are used as excitation pulses. a) SHG-autocorrelation curve. By dividing the FWHM by $\sqrt{2}$, a pulse duration of 13.8 fs can be obtained. b) NOPA spectrum tuned to a central wavelength of 650 nm. Incomplete conversion of the laser fundamental gives rise to a small peak centered at 775 nm. c) NOPA spectrum in frequency domain with FWHM bandwidth of 36.08 THz. d) Fast-Fourier-Transformation of c).

The output pulses of the noncollinear optical parametric amplifier used for excitation of the samples (NOPA I, see secitons 3.2 and 6.2.1) were characterised by SHG autocorrelation measurements. Figure 53 shows the results from the NOPA output pulses tuned to 650 nm.

The corresponding autocorrelation trace of the second-harmonic is depicted in figure 53a. A pulse duration of 13.8 fs can be determined by dividing the FWHM of the measured curve by $\sqrt{2}$. The original spectrum of the fundamental 650 nm-pulse is illustrated in figure 53b. The small peak centred at 775 nm is remaining fundamental laser light due to incomplete conversion to 650 nm. In the frequency domain (see section 2.4.1), we determine a FWHM bandwidth of 36.08 THz. Using the time-bandwidth product for a Gaussian shaped pulse, a pulse duration of 12.22 fs can be obtained for a Fourier limited pulse (see figure 53c). Fast-Fourier-Transformation of the spectral intensity yields a pulse duration of 15.56 fs, which further confirms that the pulses used for our experiments are close to Fourier-limited.

A.2. Generation of circularly polarised pulses

A.2.1. Definitions regarding polarisation and sample orientation

Figure 54 illustrates the alignment of the quarter-wave plate (achromatic retarder, 460-680 nm, B. Halle) for generation of circularly polarised laser pulses, which we define as right circularly polarised (RCP), left circularly polarised (LCP) or linearly polarised parallel to the plane of incidence on the sample surface (LPP). Moreover, the respective alignment of the sample holder for an angle of incidence of 20° is shown. When measuring SHG-ORD, a UV-polariser is mounted directly after the recollimating lens. The respective direction of rotation by the azimuthal angle φ is depicted in figure 54c.

A.2.2. Characterisation of the quarter-wave plate

After passing the quarter-wave plate aligned to generate LCP, RCP and LPP light, we measured pulse energies of 9.3 μJ, 9.2 μJ, and 9.5 μJ, respectively, with our powermeter (LabMax, Coherent). According to equation 2.106, the degree of circular polarisation is given by the Stokes parameter P_3. Hence, we obtain a Stokes parameter P_3 of -0.005 for our CPL.

In order to characterise the ellipticity of circular polarisation generated by the quarter-wave plate, we measured the transmitted pulse energy after a wire-grid polariser, which was rotated stepwise in angles of 45° (see figures 55 and 56a). The LPP data was fitted according to equation 6.6 (dipole fit) and yielded a rotation angle $\delta = 1.5°$ (see figure 56b). For LCP and RCP light we fitted the data according to the polar form of an ellipse (equation 6.5) (see figure 56c, d). The extracted rotation angles δ and ellipticities b/a are given in table 11.

	$\delta(deg)$	b/a
LCP	22.2	0.81
RCP	27.3	0.83

Table 11 Rotation angles δ and ellipticity b/a of LCP and RCP light.

It has to be noted that the mirror between waveplate and polariser (see figure 55) can lead to distortions of the circular polarisation.
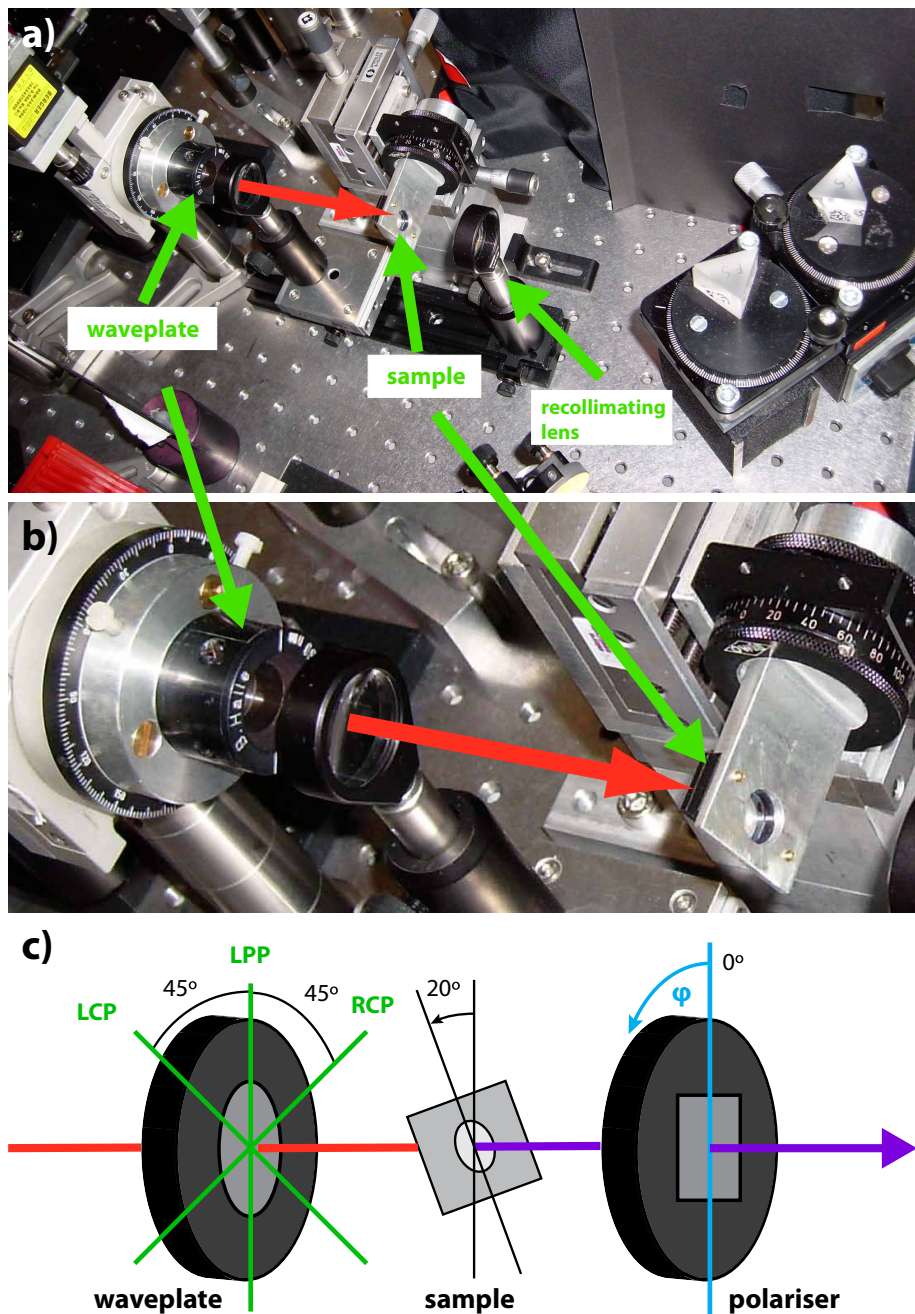
Figure 54 a) Arrangement of optical elements in the SSHG-setup. Quarter-wave plate, sample in sample holder, and recollimating lens are marked with green arrows. The red arrow represents the direction of beam propagation. b) Magnification of quarter-wave plate and sample holder. CPL generated by the quarter-wave plate with the illustrated position of its fast axis is defined as RCP within this work, and the alignment of the sample holder denotes 20° incidence of the incoming laser beam with respect to the surface normal of the sample. c) Sketch of quarter-wave plate (left) with the respective fast-axis alignment: LCP, LPP, and RCP (green). Sample holder (middle) aligned at an angle of 20°. Polariser (right), which is placed directly after the recollimating lens for SHG-ORD, and direction of rotation with respect to 0° (blue). Lenses are not shown. Red and purple arrows represent the direction of beam propagation.
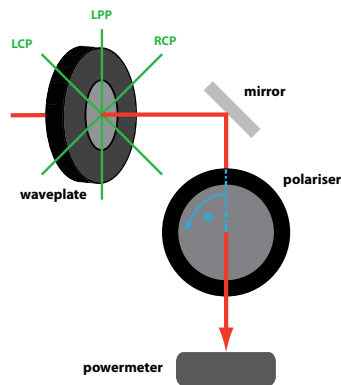
Figure 55 Arrangement of optical elements for characterisation of the quarter-wave plate and definition of rotation angle φ.
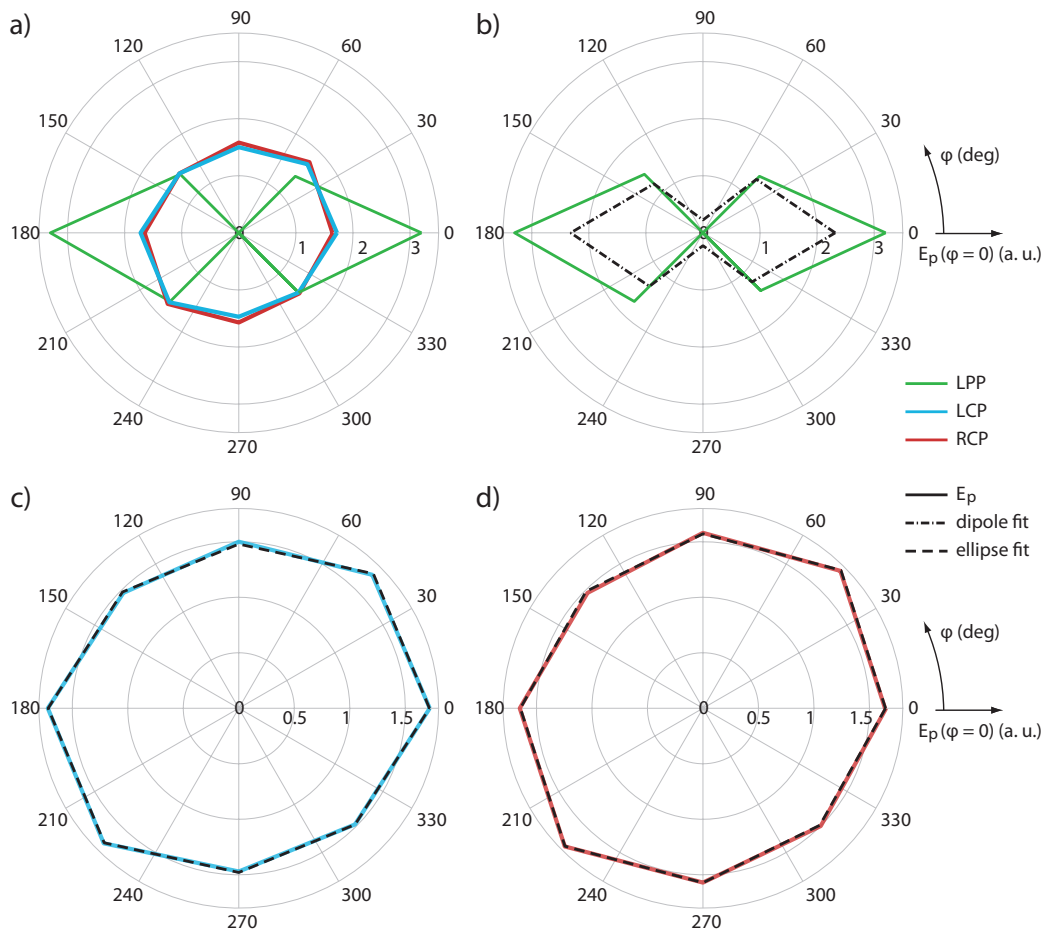

Figure 56 Characterisation of the quarter-wave plate. Pulse energy E_p measured as a function of azimuthal angle φ of the polariser. a) $E_p(\varphi)$ for LPP (green), LCP (blue) and RCP (red) light. b) $E_p(\varphi)$ for LPP (green solid) light fitted according to equation 6.6 (black dot-dashed). c) $E_p(\varphi)$ for LCP (blue solid) light fitted according to equation 6.5 (black dashed). d) $E_p(\varphi)$ for RCP (red solid) light fitted according to equation 6.5 (black dashed).

# A.3. Estimation of measurement errors in SHG-CD and SHG-ORD results
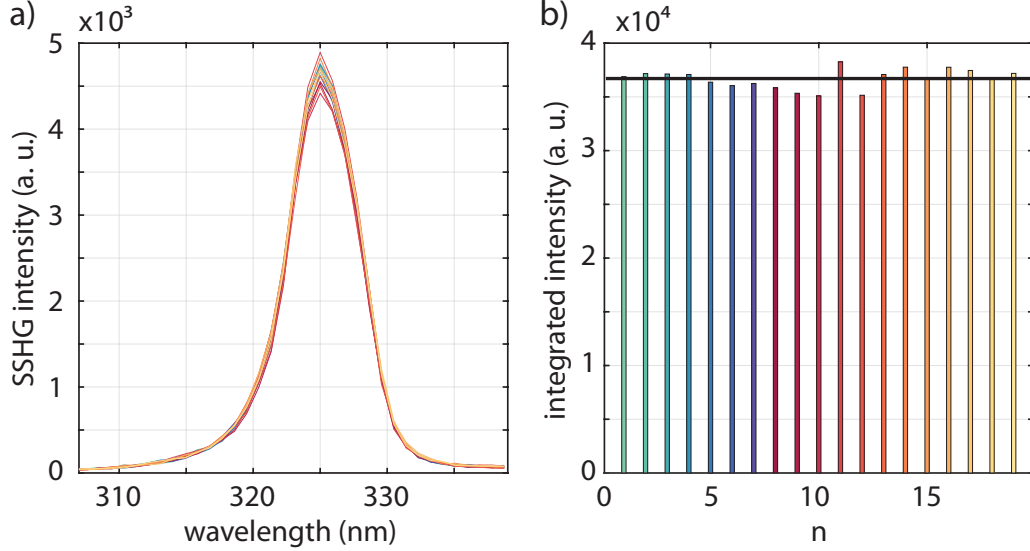
Figure 57 Estimation of measurement errors err_{stat} and err_{des}. a) First ($t_d = 0$) set of n = 19 SSHG spectra $S_k^{RCP}(\lambda)$, $k = 1...19$ measured upon RCP excitation extracted from the desorption series shown in figure 38b. b) Corresponding integrated intensities I_k^{RCP}. The black horizontal line denotes the mean intensity, which is equal to $3.67 \cdot 10^4$. err_{stat} is derived from the standard deviation of I_k^{RCP} and the corresponding intensities I_k^{LCP}. The difference of the mean of the first and last pair of intensities serves as a basis for estimation of err_{des}.

The measurment errors of the data shown in section 6.4 consist of three contributions:

$$err(t_d) = err_{\text{stat}}(t_d) + err_{\text{des}}(t_d) + err_{\text{surf}}(t_d) \tag{A.1}$$

The errors $err_{\text{stat}}(t_d)$ and $err_{\text{des}}(t_d)$ appear both in anisotropy factors $g(t_d)$ and induced changes in anisotropy factor $\Delta g(t_d)$ for each time step t_d. Estimation of these errors is performed using the integrated intensities $I_{\text{SHG}}^{\text{LCP/RCP}}$ and their normalised values, respectively. The error $err_{\text{surf}}(t_d)$ is given by the inhomogeneity of the BINOL films and contributes only to $g(t_d)$. Because an exact determination is difficult, we set it equal to the standard standard deviation of 0.090, which is extracted from the g-value distribution in figure 35c.

The random error $err_{\text{stat}}(t_d)$ is calculated from the standard deviation of $I_{\text{SHG}}^{\text{LCP/RCP}}$ for each time step t_d upon excitation with LCP and RCP pulses. Figure 57 illustrates the first ($t_d = 0$) set of n = 19 SSHG spectra $S_k^{RCP}(\lambda)$, $k = 1...19$ (see section 6.2.2), measured upon RCP excitation. The spectra belong to the desorption series shown in figure 38b. The corresponding intensities integrated over the spectral range I_k^{RCP} are depicted in figure 57b. The black horizontal line denotes the mean intensity, which is equal to $3.67 \cdot 10^4$. Hence, a standard deviation of 39.9 is calculated. Applying error propagation, the standard deviation of the normalised intensity $I_{\text{SHG}}^{\text{n,R}}(0)$

can be calculated to 0.0015. Taking into account the value obtained from the corresponding normalised LCP-spectra $I_{\mathrm{SHG}}^{\mathrm{n,L}}(0)$, the propagated error of $\Delta g(0)$ can be estimated to 0.0019.

Desorption occurring during the 19 s duration of recording the 19 spectra gives rise to the small systematic error err_{des}. The difference

$$DI^{RCP} = (I_{18}^{RCP} + I_{19}^{RCP})/2 - (I_1^{RCP} + I_2^{RCP})/2 = 44.3, \tag{A.2}$$

and the corresponding value for LCP excitation (DI^{LCP}) are used for estimation of err_{des}. Error propagation yields are value of 0.0012 for this case.

Standard deviations are calculted according to

$$\sigma = \sqrt{\frac{1}{n} \sum_{i=1}^{n} (x_i - \bar{x})^2}, \tag{A.3}$$

with x_i denoting a single measurement value and $\bar{x} = \frac{1}{n} \sum_{i=1}^{n} x_i$ the mean of all measurement values. For propagation of errors of x_i in a quantity derived by $f(x_i)$, we use the formula

$$\Delta y = \sqrt{\left(\frac{\partial f}{\partial x_i}\right)^2 \sigma_i^2}, \tag{A.4}$$

with Δy denoting the propagated error.

# A.4. SHG-CD during crystallisation
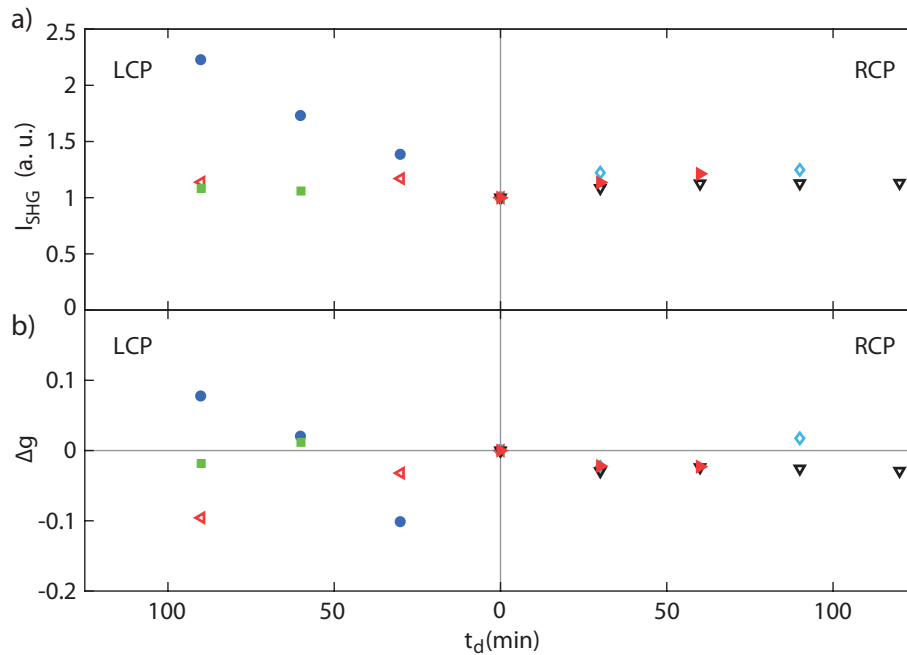
Figure 58 Ex-situ SHG-CD during crystallisation. a) I_{SHG} grows during irradiation with LCP (left) and RCP (right) pulses. b) Corresponding evolution of Δg with desorption time t_d.

Ex-situ SHG-CD spectroscopy on samples within the first two days after preparation show clearly increasing SSHG intensity with desorption time (see figure 58a). Because the major crystallisation processes are not completed before approximately 48 h at room temperature [263], we assume that the laser pulses or the enhanced temperature in the film facilitates the completion of crystallisation processes. Hence, the increased degree of orientation in the film is probably the origin for this signal growth. Visual observation of the surface after irradiation revealed small white spots similar to desorption spots of desorption series with exponential decay of SSHG intensity indicative of significant material removal. However, we can not disentangle the two contributions to the evolution of SSHG intensity.

The corresponding curves of Δg do not reflect the antisymmetric evolution of similar measurements on completely crystallised samples.

# A.5. Mass spectrometry of desorbed BINOL
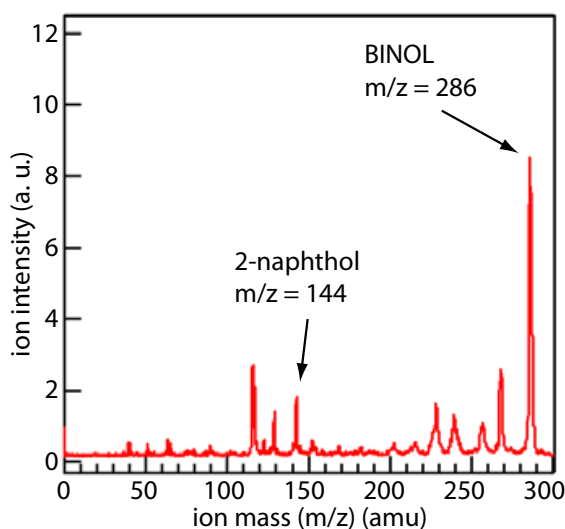
Figure 59 Mass spectrum of BINOL desorbed with 10 ns pulses (607 nm, 5 mJ, 30 Hz), which were focused to a spot of 2 mm diameter. Detection was performed by time-of-flight upon 1+1 ionisation at 267.5 nm. Adapted and modified from [281]. Copyright Wiley-VCH Verlag GmbH & Co. KGaA. Reproduced with permission.

The mass spectrum of BINOL molecules, which were desorbed from an identical sample using a nanosecond-laser (607 nm, 5 mJ, 30 Hz), is depicted in figure 59. The largest peak appears at m/z = 286 corresponding to the mass of BINOL. The small peak at m/z = 144 can be assigned to 2-naphthol, a possible fragment of BINOL. The peaks between 230 and 280 can presumably be related to fragments of BINOL caused by the loss of -H_2O (m/z = 268), the loss of -CO and -H (m/z = 257), and the loss of -OH_2, -CO and -H (m/z = 239). The peaks below m/z = 144 refer to fragments of 2-naphthol [250]. None of the fragmentation peaks is larger than 30% of the BINOL mother peak. Hence, the spectrum confirms that desorption of intact and neutral BINOL molecules is generally favoured.

A.6. Photodegradation test
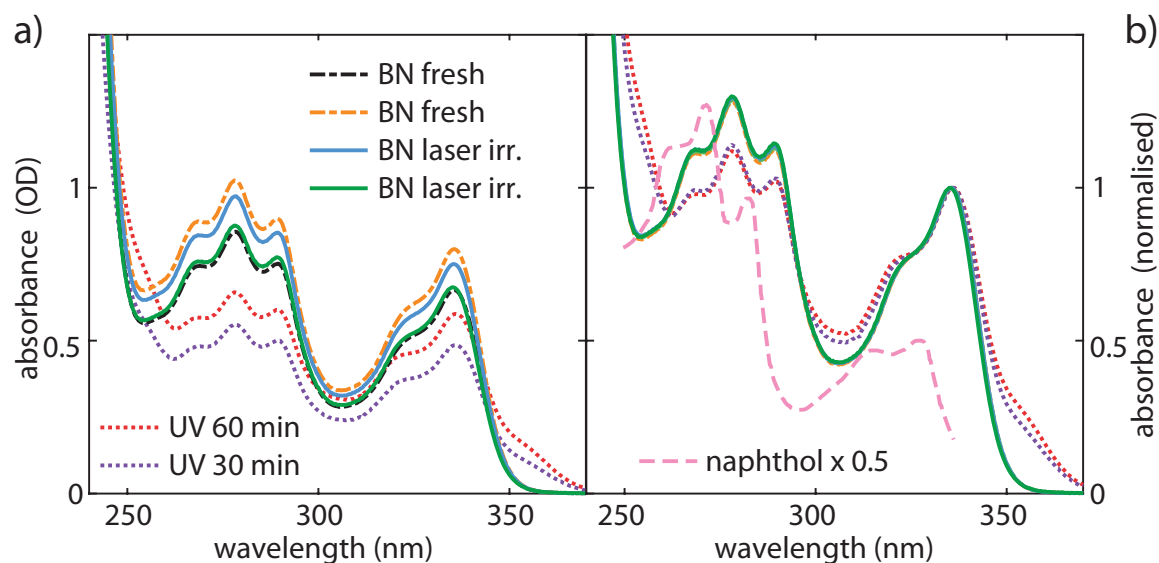
Figure 60 Photodegradation test: 30 μl racemic BINOL solution was irradiated with focused laser pulses for 120 min. After dilution absorption spectra were recorded (BN laser irr., blue and green solid lines) and compared to a freshly prepared solution (BN fresh, black and orange dashed lines). Red and purple dotted lines represent absorption spectra of BINOL solutions of the same concentration after irradiation with a UV lamp for 60 min (UV 60 min) and 30 min (UV 30 min). a) Absorbance in units of OD. b) Absorbance normalised to the OD at 335 nm. The pink dashed line denotes the normalised spectrum of 2-naphthol (divided by 2 for clarity).

In order to test whether irradiation with the 650 nm laser pulses causes photodegradation during a desorption series, we irradiated a small volume (30 μl) of a highly concentrated racemic BINOL (C = 0.01 mol/l in ethanol) solution. Similar to the desorption experiments, the laser beam was focused by a lens (f = 100 mm) into the centre of the volume. The pulse energy was tuned to 3.3 μJ, hence, twice as large as usually. A total of eight "spots" was illuminated for 10-30 min. Thus, the intensively irradiated volume is larger than 13% of the total volume. In addition, the laser beam was scanned slowly over the complete volume to ensure that the whole volume was irradiated at least for 1 s. Subsequently, the solution was diluted by adding 270 μl ethanol. Absorption spectra of the diluted samples were recorded with a commercial absorption spectrometer (Lambda 19, Perkin-Elmer) and compared to freshly prepared BINOL solutions of the same concentration (see figure 60a). We estimate an error of approximately 10% in optical density due to variations in amount of BINOL and ethanol during the preparation process. Changes in OD between the samples are all within the error. Figure 60b shows the normalised spectra. Hence, the spectra of the irradiated samples do not deviate significantly from the fresh samples. Subsequently, we irradiated the fresh samples in 1 mm x 2 cm glass cuvettes by a commercial UV lamp (UV lamp, Bioblock Scientific, Model VL6MC, 6 W, 1.7 W/cm^2) at a wavelength of 285 nm for 30 min and 60 min and recorded the absorbance again. This leads to strongly reduced OD. Additionally, the emergence of a shoulder on the red side of both the primary absorption band and the band below wavelengths of 260 nm is observed indicative of

significant photodegradation. A decomposition to 2-naphthol can be ruled out due to insufficient spectral overlap (see figure 60b). Thus, we conclude that irradiation of 13% of a small volume of BINOL solution with focused 3.3 μJ laser pulses at a central wavelength of 650 nm does not lead to observable photodegradation.

A.7. Numerical finite difference model: fit parameters and limits

parameter	$\delta_1(min^{-1})$	$\delta_2(min^{-1})$	$\rho(min^{-1})$	$\gamma(min^{-1})$	$\alpha \cdot (dx)^2(min^{-1})$
start value	12	0.01	0.03	0.2	0.01
limits	$1-100$	$0.001-1$	$0.001-10$	$0.001-0.9$	$0.001-0.2$

Table 12 Fit to 1-dim numerical simulation: start values and limits for the fits presented in table 10 and 13: δ_1: desorption rate for S-BINOL, δ_2: desorption rate for R-BINOL, ρ: racemisation rate, γ: diffusion rate for refilling vacancies, α: self-diffusion constant. dx: thickness of one layer.

version	g_p	$\delta_1(min^{-1})$	$\delta_2(min^{-1})$	$\rho(min^{-1})$	$\gamma(min^{-1})$	$\alpha \cdot (dx)^2(min^{-1})$
v1	0.15	89 ± 39	0.001 ± 0.278	0.001 ± 0.002	0.2	0
	0.26	31 ± 18	0.001 ± 0.449	0.004 ± 0.004	0.2	0
	0.7	4.9 ± 5.3	0.26 ± 1.7	0.03 ± 0.040	0.2	0
v2	0.15	92 ± 35	0.01	0.002 ± 0.002	0.001 ± 0.44	0
	0.26	32 ± 14	0.01	0.005 ± 0.004	0.001 ± 0.55	0
	0.7	6.5 ± 2.0	0.01	0.03 ± 0.002	0.001 ± 0.50	0
v3	0.15	89 ± 35	0.01	0.001 ± 0.001	0.2	0.001 ± 2.5
	0.26	31 ± 15	0.01	0.004 ± 0.004	0.2	0.001 ± 6.3
	0.7	5.9 ± 4.0	0.01	0.03 ± 0.016	0.2	0.2 ± 27.8
v4	0.15	70 ± 32	0.26	0.005 ± 0.001	0.2	0.001 ± 5.5
	0.26	25 ± 14	0.26	0.002 ± 0.002	0.2	0.001 ± 3.1
	0.7	4.9 ± 1.9	0.26	0.03 ± 0.017	0.2	0.2 ± 16.4

Table 13 Fit parameters of the 1D numerical simulation of a system of 100 layers for 150 min with time steps of 0.01 min: δ_1: desorption rate for S-BINOL, δ_2: desorption rate for R-BINOL, ρ: racemisation rate, γ: rate for surface diffusion, α: self-diffusion constant, dx: layer thickness. The errors denote 95% confidence intervals. Version v1 is copied from table 10.

Bibliography

[1] Daniel I. Arnon. The light reactions of photosynthesis. *Proc. Nat. Acad. Sci.*, 68(11):2883–2892, 1971.

[2] P. Candau, C. Manzano, and M. Losada. Bioconversion of light energy into chemical energy through reduction with water of nitrate to ammonia. *Nature*, 262:715–717, 1976.

[3] C. V. Shank and E. P. Ippen. Sub-picosecond, Kilowatt Pulses from a Mode-Locked CW Dye Laser. *Applied Physics Letters*, 24(8):373, 1974.

[4] W. H. Knox, R. L. Fork, M. C. Downer, R. H. Stolen, C. V. Shank, and J. A. Valdmanis. Optical pulse compression to 8 fs at a 5-kHz repetition rate. *Applied Physics Letters*, 46(12):1120–1121, 1985.

[5] Ahmed H. Zewail. Femtochemistry: Atomic-Scale Dynamics of the Chemical Bond Using Ultrafast Lasers (Nobel Lecture). *Angewandte Chemie - International Edition*, 39:2586–2631, 2000.

[6] M. Hentschel, R. Kienberger, Ch Spielmann, G. A. Reider, N. Milosevic, T. Brabec, P. Corkum, U. Heinzmann, M. Drescher, and F. Krausz. Attosecond metrology. *Nature*, 414(6863):509–513, 2001.

[7] M. Ossiander, J. Riemensberger, S. Neppl, M. Mittermair, M. Schäffer, A. Duensing, M. S. Wagner, R. Heider, M. Wurzer, M. Gerl, M. Schnitzenbaumer, J. V. Barth, F. Libisch, C. Lemell, J. Burgdörfer, P. Feulner, and R. Kienberger. Absolute timing of the photoelectric effect. *Nature*, 561(7723):374–377, 2018.

[8] Charles V. Shank. Investigation of Ultrafast Phenomena in the Femtosecond Time Domain. *Science*, 233(4770):1276–1280, 1986.

[9] M. C. Nuss, W. Zinth, W. Kaiser, E. Kölling, and D. Oesterhelt. Femtosecond spectroscopy of the first events of the photochemical cycle in bacteriorhodopsin. *Chemical Physics Letters*, 117(1):1–7, 1985.

[10] N. F. Scherer, J. L. Knee, D. D. Smith, and A. H. Zewail. Femtosecond photofragment spectroscopy: The reaction ICN - CN + I. *Journal of Physical Chemistry*, 89(24):5141–5143, 1985.

[11] W. Thomas Pollard and Richard A. Mathies. Analysis of femtosecond dynamic absorption spectra of nonstationary states. *Annual review of physical chemistry*, 43(1):497–523, 1992.

[12] H. Iglev, M. Schmeisser, K. Simeonidis, A. Thaller, and A. Laubereau. Ultrafast superheating and melting of bulk ice. *Nature*, 439(7073):183–6, jan 2006.

[13] Andrei Tokmakoff. Shining light on the rapidly evolving structure of water. *Science*, 317(5834):54–55, 2007.

[14] Eberhard Riedle, Maximilian Bradler, Matthias Wenninger, Christian F Sailer, and Igor Pugliesi. Electronic transient spectroscopy from the deep UV to the NIR: unambiguous disentanglement of complex processes. *Faraday Discussions*, 163(0):139–158, 2013.

[15] Carlos E. Crespo-Hernández, Boiko Cohen, and Bern Kohler. Base stacking controls excited-state dynamics in A·T DNA. *Nature*, 436(7054):1141–1144, 2005.

[16] Nicolas Renaud, Michelle A. Harris, Arunoday P.N. Singh, Yuri A. Berlin, Mark A. Ratner, Michael R. Wasielewski, Frederick D. Lewis, and Ferdinand C. Grozema. Deep-hole transfer leads to ultrafast charge migration in DNA hairpins. *Nature Chemistry*, 8(11):1015–1021, 2016.

[17] Malte Oppermann, Jasmin Spekowius, Benjamin Bauer, Rolf Pfister, Majed Chergui, and Jan Helbing. Broad-Band Ultraviolet CD Spectroscopy of Ultrafast Peptide Backbone Conformational Dynamics. *Journal of Physical Chemistry Letters*, pages 2700–2705, 2019.

[18] Majed Chergui. Ultrafast molecular photophysics in the deep-ultraviolet. *Journal of Chemical Physics*, 150(7), 2019.

[19] Imran Ali, Hassan Aboul-Enein, and Ashraf Ghanem. Enantioselective Toxicity and Carcinogenesis. *Current Pharmaceutical Analysis*, 1(1):109–125, 2005.

[20] Silas W. Smith. Chiral toxicology: It's the same thing only different. *Toxicological Sciences*, 110(1):4–30, 2009.

[21] Klaus Dieter Thomann. Die Contergan-Katastrophe: Die trügerische Sicherheit der "harten" Daten. *Deutsches Aerzteblatt*, 104(41), 2007.

[22] Kesavan Meganathan, Smita Jagtap, Vilas Wagh, Johannes Winkler, John Antonydas

Gaspar, Diana Hildebrand, Maria Trusch, Karola Lehmann, Jürgen Hescheler, Hartmut Schlüter, and Agapios Sachinidis. Identification of Thalidomide-Specific Transcriptomics and Proteomics Signatures during Differentiation of Human Embryonic Stem Cells. *PLoS ONE*, 7(8), 2012.

[23] Etsuko Tokunaga, Takeshi Yamamoto, Emi Ito, and Norio Shibata. Understanding the Thalidomide Chirality in Biological Processes by the Self-disproportionation of Enantiomers. *Scientific Reports*, 8(1):6–12, 2018.

[24] John David Jackson. *Classical Electrodynamics*. John Wiley & Sons, Inc., 3rd edition, 1999.

[25] Robert W. Boyd. *Nonlinear Optics*. Elsevier Inc., 3rd edition.

[26] P.N. Butcher and D. Cotter. *The Elements of Nonlinear Optics*. Cambridge University Press, 1990.

[27] D. A. Kleinman. Nonlinear dielectric polarization in optical media. *Physical Review*, 126(6):1977–1979, 1962.

[28] R. J. W. Le Fevre. Molecular Refractivity and Polarizability. *Advances in Physical Organic Chemistry*, 3:1–90, 1965.

[29] Jacob B. Khurgin, A. Obeidat, S. J. Lee, and Yujie J. Ding. Cascaded optical nonlinearities: Microscopic understanding as a collective effect. *Journal of the Optical Society of America B*, 14(8):1977, 1977.

[30] P. S. Pershan. Nonlinear optical properties of solids: energy considerations. *Physical Review*, 130(3):919–929, 1963.

[31] Eric Adler. Nonlinear optical frequency polarization in a dielectric. *Physical Review*, 134(3A):728–733, 1964.

[32] N. Bloembergen, R. K. Chang, S. S. Jha, and C. H. Lee. Optical second-harmonic generation in reflection from media with inversion symmetry. *Physical Review*, 174(3), 1968.

[33] J. M. Chen, J. R. Bower, C. S. Wang, and C. H. Lee. Optical second-harmonic generation from submonolayer Na-covered Ge surfaces. *Optics Communications*, 9(2):132–134, 1973.

[34] Maria Goeppert-Mayer. Über Elementarakte mit zwei Quantensprüngen. *Ann. Physik*, 9:273–294, 1931.

[35] Christian W. Freudiger, Wei Min, Brian G. Saar, Sijia Lu, Gary R. Holtom, Chengwei He, Jason C. Tsai, Jing X. Kang, and X. Sunney Xie. Label-Free Biomedical Imaging with High Sensitivity by Stimulated Raman Scattering Microscopy. *Science*, 322(5909):1857–1861, 2008.

[36] Minbiao Ji, Daniel A. Orringer, Christian W. Freudiger, Shakti Ramkissoon, Xiaohui Liu, Darryl Lau, Alexandra J. Golby, Isaiah Norton, Marika Hayashi, Nathalie Y.R. Agar, Geoffrey S. Young, Cathie Spino, Sandro Santagata, Sandra Camelo-Piragua, Keith L. Ligon, Oren Sagher, and X. Sunney Xie. Rapid, label-free detection of brain tumors with stimulated raman scattering microscopy. *Science Translational Medicine*, 5(201), 2013.

[37] Andrew J. Moad and Garth J. Simpson. A Unified Treatment of Selection Rules and Symmetry Relations for Sum-Frequency and Second Harmonic Spectroscopies. *The Journal of Physical Chemistry B*, 108(11):3548–3562, 2004.

[38] Georg Hohlneicher and Bernhard Dick. Two-photon spectroscopy of dipole-forbidden transitions. II. Calculation of two-photon cross sections by the CNDO-CI method. *The Journal of Chemical Physics*, 70(12):5427–5437, 1979.

[39] A. D. Buckingham and M. B. Dunn. Optical Activity of Oriented Molecules. *J. Chem. Soc. (A): Inorg. Phys. Theory*, pages 1988–1991, 1971.

[40] Peer Fischer and François Hache. Nonlinear optical spectroscopy of chiral molecules. *Chirality*, 17(8):421–437, 2005.

[41] Sonja Sioncke, Thierry Verbiest, and André Persoons. Second-order nonlinear optical properties of chiral materials. *Materials Science and Engineering R: Reports*, 42(5-6):115–155, 2003.

[42] Martti Kauranen, Thierry Verbiest, Jeffery J. Maki, and André Persoons. Second-harmonic generation from chiral surfaces. *The Journal of Chemical Physics*, 101(9):8193–8199, 1994.

[43] L. Rosenfeld. Quantenmechanische Theorie der natürlichen optischen Aktivität von Flüssigkeiten und Gasen. *Zeitschrift für Physik*, 52(3-4):161–174, 1929.

[44] E. U. Condon. Theories of Optical Rotatory Power. *Reviews of Modern Physics*, 9:432–457, 1937.

[45] E. A. Power and T. Thirunamachandran. Circular dichroism: A general theory based on quantum electrodynamics. *The Journal of Chemical Physics*, 60(9):3695–3701, 1974.

[46] A. D. McNaught and A. Wilkinson. *IUPAC. Compendium of Chemical Terminology, 2nd ed. (the "Gold Book")*. Blackwell Scientific Publications, Oxford, 1997.

[47] T. Petralli-Mallow, T. M. Wong, J. D. Byers, H. I. Yee, and J. M. Hicks. Circular dichroism spectroscopy at interfaces: A surface second harmonic generation study. *Journal of Physical Chemistry*, 97(7):1383–1388, 1993.

[48] N. A. Cherepkov and V. V. Kuznetsov. Optical activity of oriented molecules. *J. Chem. Phys.*, 95(5):3046–3052, 1991.

[49] Ying Nan Chiu. Temperature-dependent optical activity due to quantized molecular rotation and optical rotation by oriented molecules. *The Journal of Chemical Physics*, 52(3):1042–1053, 1970.

[50] M. A. Belkin, S. H. Han, X. Wei, and Y. R. Shen. Sum-frequency generation in chiral liquids near electronic resonance. *Physical Review Letters*, 87(11):113001–113001–4, 2001.

[51] T. Petralli-Mallow, T. M. Wong, J. D. Byers, H. I. Yee, and J. M. Hicks. Circular dichroism spectroscopy at interfaces: A surface second harmonic generation study. *Journal of Physical Chemistry*, 97(7):1383–1388, 1993.

[52] J D Byers, H I Yee, T Petralli-Mallow, and J M Hicks. Second-harmonic generation circular-dichroism spectroscopy from chiral monolayers. *Physical Review B*, 49(20):643–648, 1994.

[53] J. D. Byers, H. I. Yee, and J. M. Hicks. A second harmonic generation analog of optical rotatory dispersion for the study of chiral monolayers. *The Journal of Chemical Physics*, 101(7):6233, 1994.

[54] J. A. Giordmaine. Nonlinear Optical Properties of Liquids. *Phys.Rev.A*, 138(6):1599–1606, 1965.

[55] Pao-keng Yang and Jung Y Huang. Sum-frequency generation from an isotropic chiral medium. *J. Opt. Soc. Am. B*, 15(6):1698–1706, 1998.

[56] Na Ji and Yuen-Ron Shen. A Novel Spectroscopic Probe For Molecular Chirality. *Chirality*, 18:146–158, 2006.

[57] Garth J. Simpson. Molecular origins of the remarkable chiral sensitivity of second-order nonlinear optic. *ChemPhysChem*, 5(9):1301–1310, 2004.

[58] Y R Shen. Surface properties probed by second-harmonic and sum-frequency generation. *Nature*, 337(9):519–525, 1989.

[59] Mikko J. Huttunen, Miro Erkintalo, and Martti Kauranen. Absolute nonlinear optical probes of surface chirality. *Journal of Optics A: Pure and Applied Optics*, 11(3), 2009.

[60] F. Hache, H. Mesnil, and M. C. Schanne-Klein. Application of classical models of chirality to surface second harmonic generation. *Journal of Chemical Physics*, 115(14):6707–6715, 2001.

[61] Jeffery J. Maki, Thierry Verbiest, Martti Kauranen, Sven Van Elshocht, and André Persoons. Comparison of linearly and circularly polarized probes of second-order optical activity of chiral surfaces. *Journal of Chemical Physics*, 105(2):767–772, 1996.

[62] Sven Van Elshocht, Thierry Verbiest, Martti Kauranen, André Persoons, B. M.W. Langeveld-Voss, and E. W. Meijer. Direct evidence of the failure of electric-dipole approximation in second-harmonic generation from a chiral polymer film. *Journal of Chemical Physics*, 107(19):8201–8203, 1997.

[63] M. C. Schanne-Klein, F. Hache, T. Brotin, C. Andraud, and A. Collet. Magnetic chiroptical effects in surface second harmonic reflection. *Chemical Physics Letters*, 338(2-3):159–166, 2001.

[64] G. Wagnière. Optical activity of higher order in a medium of randomly oriented molecules. *The Journal of Chemical Physics*, 77(6):2786–2792, 1982.

[65] Jeffery J. Maki and André Persoons. One-electron second-order optical activity of a helix. *Journal of Chemical Physics*, 104(23):9340–9348, 1996.

[66] Levi M. Haupert and Garth J. Simpson. Chirality in Nonlinear Optics. *Annual Review of Physical Chemistry*, 60(1):345–365, 2009.

[67] Claire Niezborala and François Hache. Conformational Changes in Photoexcited (R)-(+)-1,1'-Bi-2-naphthol Studied by Time-Resolved Circular Dichroism. *Journal of the American Chemical Society*, 130(38):12783–12786, 2008.

[68] T. Verbiest, S. Van Elshocht, M. Kauranen, C. Nuckolls, T.J. Katz, and A. Persoons. Strong Enhancement of nonlinear optical properties through supramolecular chirality. *Science*, 282(October):913–915, 1998.

[69] Victor Ostroverkhov, Kenneth D. Singer, and Rolfe G. Petschek. Second-harmonic generation in nonpolar chiral materials: relationship between molecular and macroscopic properties. *Journal of the Optical Society of America B*, 18(12):1858, 2001.

[70] Brian J. Burke, Andrew J. Moad, Mark A. Polizzi, and Garth J. Simpson. Experimental confirmation of the importance of orientation in the anomalous chiral sensitivity of second harmonic generation. *Journal of the American Chemical Society*, 125(30):9111–9115, 2003.

[71] Ulrich Gubler and Christian Bosshard. A new twist for nonlinear optics. *Nature Materials*, 1(December):209–210, 2002.

[72] Thierry Verbiest, Martti Kauranen, Yves Van Rompaey, and André Persoons. Optical Activity of Anisotropic Achiral Surfaces. *Physical Review Letters*, 77(8):1456–1459, 1996.

[73] P. Fischer and A. D. Buckingham. Surface second-order nonlinear optical activity. *Journal of the Optical Society of America B*, 15(12):2951, 1998.

[74] Roman Fasel, Manfred Parschau, and Karl Heinz Ernst. Amplification of chirality in two-dimensional enantiomorphous lattices. *Nature*, 439(7075):449–452, 2006.

[75] T. F. Heinz, H. W K Tom, and Y. R. Shen. Determination of molecular orientation of monolayer adsorbates by optical second-harmonic generation. *Physical Review A*, 28(3):1883–1885, 1983.

[76] S. H. Han, N. Ji, M. A. Belkin, and Y. R. Shen. Sum-frequency spectroscopy of electronic resonances on a chiral surface monolayer of bi-naphthol. *Physical Review B - Condensed Matter and Materials Physics*, 66(16):1–6, 2002.

[77] P Heister, T Lunskens, M Thamer, A Kartouzian, S Gerlach, T Verbiest, and U Heiz. Orientational changes of supported chiral 2,2 '-dihydroxy-1,1 ' binaphthyl molecules. *Phys. Chem. Chem. Phys.*, 16(16):7299–7306, 2014.

[78] Martti Kauranen, Thierry Verbiest, Sven van Elshocht, and André Persoons. Chirality in surface nonlinear optics. *Optical Materials*, 9(1-4):286–294, 1998.

[79] Jeffery J. Maki, Martti Kauranen, and André Persoons. Surface second-harmonic generation from chiral materials. *Physical Review B*, 51(3):1425–1434, 1995.

[80] Wolfgang Demtröder. *Molekülphysik*. Oldenbourg Verlag München Wien, 2003.

[81] M. Born and R. Oppenheimer. Zur Quantentheorie der Molekeln. *Annalen der Physik*, 389(20):457–484, 1927.

[82] Ingolf V. Hertel and C.-P. Schulz. *Atome, Moleküle und optische Physik 2*. Springer-Lehrbuch. Springer Berlin Heidelberg, Berlin, Heidelberg, 2010.

[83] Hermann Haken and Hans Christoph Wolf. *Molekülphysik und Quantenchemie*. Springer Verlag Berlin Heidelberg, 2nd edition, 1994.

[84] Maurizio Persico and Giovanni Granucci. *Photochemistry - A Modern Theoretical Perspective*. Springer International Publishing AG, 2018.

[85] Joseph R. Lakowicz. *Principles of Fluorescence Spectroscopy*. Springer Science+Business Media, LLC, 3rd edition, 2006.

[86] Vincenzo Balzani, Paola Ceroni, and Alberto Juris. *Photochemistry and Photophysics*. Wiley-VCH Verlag GmbH & Co. KGaA., 1st edition, 2014.

[87] Nicholas J. Turro, V. Ramamurthy, and J. C. Scaiano. *Principles of Molecular Photochemistry*. University Science Books, 2009.

[88] J Franck. Elementary processes of photochemical reactions. *Trans. Faraday Soc.*, (21):0536–0542, 1926.

[89] Edward U. Condon. Nuclear motions associated with electron transitions in diatomic molecules. *Physical Review*, 32(6):858–872, 1928.

[90] S. J. Strickler and Robert a. Berg. Relationship between Absorption Intensity and Fluorescence Lifetime of Molecules. *The Journal of Chemical Physics*, 37(4):814, 1962.

[91] J.B. Birks. Fluorescence quantum yield measurements. *Journal of Research of the National Bureau of Standards Section A: Physics and Chemistry*, 80A(3):389, 1976.

[92] Michael Kasha. Characterization of electronic transitions in complex molecules. *Discussions of the Faraday Society*, 9(c):14, 1950.

[93] Bernard Smaller. Role of triplet state in photoreactions. *Nature*, 195(4841):593–594, 1962.

[94] D. Wöhrle, M. W. Tausch, and W. D. Stohrer. *Photochemie: Konzepte, Methoden, Experimente*. Wiley-VCH Verlag GmbH & Co. KGaA., 2002.

[95] John B. Birks. *Photophysics of aromatic molecules*. Wiley Interscience, London and New York, 1970.

[96] M.A. El-Sayed. Theoretical Considerations Concerning the Intramolecular Heavy-Atom Effect on the Phosphorescence Process: C_2v Symmetric Dihalonaphthalene. *Journal of Chemical Physics*, 43(8), 1965.

[97] Konstantin N. Solovyov and Elena A. Borisevich. Intramolecular heavy-atom effect in the photophysics of organic molecules. *Uspekhi Fizicheskih Nauk*, 175(3):247, 2005.

[98] M.A. El-Sayed. Spin - Orbit Coupling and the Radiationless Processes in Nitrogen. *Journal of Chemical Physics*, 38(12):2834–2838, 1963.

[99] Donald S. McClure. Triplet-Singlet Transitions in Organic Molecules. Lifetime Measurements of the Triplet State. *J. Chem. Phys.*, 17(905), 2004.

[100] T. Pavlopoulos and M. A. El-Sayed. Spectroscopic investigation of the mechanism of the intramolecular heavy atom effect on the phosphorescence process. I. Naphthalene emission. *The Journal of Chemical Physics*, 41(4):1082–1092, 1964.

[101] M. A. El-Sayed and T. Pavlopoulos. Intramolecular heavy-atom effect on the polarization of naphthalene phosphorescence. *The Journal of Chemical Physics*, 39(7):1899–1900, 1963.

[102] Michael Kasha. Collisional Perturbation of Spin-Orbital Coupling and the Mechanism of Fluorescence Quenching. A Visual Demonstration of the Perturbation. *J. Chem. Phys.*, 20(1):7174, 1952.

[103] a. Kearvell and F. Wilkinson. Fluorescence Quenching and External Spin-Orbit Coupling Effects. *Molecular Crystals*, 4(1-4):69–81, 1968.

[104] S. P. McGlynn, R. Sltnseri, and N. Christodouleas. External heavy-atom spin-orbital coupling effect. I. The nature of the interaction. *The Journal of Chemical Physics*, 37(8):1818–1824, 1962.

[105] A. C. Albrecht. Vibronic-spin-orbit perturbations and the assignment of the lowest triplet state of benzene. *The Journal of Chemical Physics*, 38(2):354–365, 1963.

[106] Karen J. Latas and A. M. Nishimura. Heavy atom effects on the phosphorescent triplet states of several aromatic molecules. *Journal of Physical Chemistry*, 82(4):491–495, 1978.

[107] I Najbar, W. Jarzeba, and R. M. Hochstrasser. NON-RADIATIVE DECAY OF THE T1-SATES OF CHLORONAPHTHALENES AND PROTONATED CHLOROQUINOLINES AT 77 K. *Chemical Physics*, 95:1–8, 1985.

[108] Joseph W. Perry, Daniel Alvarez, Ingrid Choong, Kamjou Mansour, Seth R. Marder, and Kelly J. Perry. Enhanced reverse saturable absorption and optical limiting in heavy-atom-substituted phthalocyanines. *Optics Letters*, 19(9):625, 1994.

[109] Weijie Su, Thomas M. Cooper, and Mark C. Brant. Investigation of Reverse-Saturable Absorption in Brominated Porphyrins. *Chemistry of Materials*, 10(5):1212–1213, 1998.

[110] J.C. Koziar and O. Cowan. Photochemical Heavy-Atom Effects. *Accounts of chemical research*, 71(9):334–341, 1977.

[111] Hikaru Takano, Tetsuo Narumi, Wataru Nomura, Toshiaki Furuta, and Hirokazu Tamamura. Utilization of the Heavy Atom Effect for the Development of a Photosensitive 8-Azacoumarin-Type Photolabile Protecting Group. *Organic Letters*, 17(21):5372–5375, 2015.

[112] Longwei He, Qiuyan Xu, Yong Liu, Haipeng Wei, Yonghe Tang, and Weiying Lin. Coumarin-Based Turn-On Fluorescence Probe for Specific Detection of Glutathione over Cysteine and Homocysteine. *ACS Applied Materials & Interfaces*, 7(23):12809–12813, 2015.

[113] Martin Wörle. *Optimierung eines Anrege-Abfrage-Spektroskopie Experiments mit sub-50-fs Zeitauflösung und erste Messungen an CeO2-Nanopartikel*. Masterarbeit, Technische Universität München, 2015.

[114] Donna Strickland and Gerard Mourou. COMPRESSION OF AMPLIFIED CHIRPED OPTICAL PULSES. *Optics Communications*, 55(6):447–449, 1985.

[115] T Wilhelm, J Piel, and E Riedle. Sub-20-fs pulses tunable across the visible from a blue-pumped single-pass noncollinear parametric converter. *Optics letters*, 22(19):1494–6, oct 1997.

[116] J. Piel, M. Beutter, and E. Riedle. 20–50-Fs Pulses Tunable Across the Near Infrared From a Blue-Pumped Noncollinear Parametric Amplifier. *Optics Letters*, 25(3):180, 2000.

[117] U. Megerle, I. Pugliesi, C. Schriever, C. F. Sailer, and E. Riedle. Sub-50 fs broadband absorption spectroscopy with tunable excitation: putting the analysis of ultrafast molecular dynamics on solid ground. *Applied Physics B: Lasers and Optics*, 96(2-3):215–231, 2009.

[118] Marcus Rasmusson, Alexander N. Tarnovsky, Eva Åkesson, and Villy Sundström. On the use of two-photon absorption for determination of femtosecond pump-probe cross-correlation functions. *Chemical Physics Letters*, 335(3-4):201–208, 2001.

[119] S a Kovalenko, a L Dobryakov, J Ruthmann, and N P Ernsting. Femtosecond spectroscopy of condensed phases with supercontinuum probing. *Phys.Rev.A*, 59(3):35–37, 1998.

[120] Shaul Mukamel. *Principles of Nonlinear Optical Spectroscopy*. Oxford University Press, 1999.

[121] Jean-Claude Diels and Wolfgang Rudoplh. *Ultrashort Laser Pulse Phenomena*. Academic Press, Inc., 1996.

[122] R. R. Alfano, Q. X. Li, T. Jimbo, J. T. Manassah, and P. P. Ho. Induced spectral broadening of a weak picosecond pulse in glass produced by an intense picosecond pulse. *Optics Letters*, 11(10):626, 1986.

[123] Bastian Baudisch. *Time resolved broadband spectroscopy from UV to NIR: beneficial use of the coherent artifact and pyrene dynamics*. Dissertation, LMU München, 2018.

[124] Sergey A. Kovalenko, Nikolaus P. Ernsting, and J. Ruthmann. Femtosecond hole-burning spectroscopy of the dye DCM in solution: the transition from the locally excited to a charge-transfer state. *Chemical Physics Letters*, 258(3-4):445–454, 1996.

[125] I. H M Van Stokkum, Delmar S. Larsen, and Rienk Van Grondelle. Global and target analysis of time-resolved spectra. *Biochimica et Biophysica Acta - Bioenergetics*, 1657(2-3):82–104, 2004.

[126] P. Fita, E. Luzina, T. Dziembowska, Cz Radzewicz, and A. Grabowska. Chemistry,

photophysics, and ultrafast kinetics of two structurally related Schiff bases containing the naphthalene or quinoline ring. *Journal of Chemical Physics*, 125(18), 2006.

[127] Andreas Brodschelm. *Amplituden- und phasenaufgelöste Femtosekundenspektroskopie im mittleren Infrarot: Hochfeldtransport in Galliumarsenid und Silizium*. PhD thesis, Technische Universität München, 2003.

[128] Andy Thaller. *Dynamik solvatisierter Elektronen in Methanol und Wasser: Neue Erkenntnisse aus der Femtosekunden-Spektroskopie*. PhD thesis, Technische Universität München, 2003.

[129] Katrin E. Oberhofer, Mikayel Musheghyan, Sebastian Wegscheider, Martin Wörle, Eleonora D. Iglev, Rositca D. Nikolova, Reinhard Kienberger, Petko St. Petkov, and Hristo Iglev. Individual control of singlet lifetime and triplet yield in halogen-substituted coumarin derivatives. *RSC Advances*, 10:27096–27102, 2020.

[130] D Egan, R O'Kennedy, E Moran, D Cox, E Prosser, and R D Thornes. The pharmacology, metabolism, analysis, and applications of coumarin and coumarin-related compounds. *Drug metabolism reviews*, 22(5):503–529, 1990.

[131] Yang Yang, Qing Wen Liu, Ye Shi, Zhi Guang Song, Ying Hua Jin, and Zai Qun Liu. Design and synthesis of coumarin-3-acylamino derivatives to scavenge radicals and to protect DNA. *European Journal of Medicinal Chemistry*, 84(2519):1–7, 2014.

[132] Pravin O. Patil, Sanjay B. Bari, Sandip D. Firke, Prashant K. Deshmukh, Shailesh T. Donda, and Dilip A. Patil. A comprehensive review on synthesis and designing aspects of coumarin derivatives as monoamine oxidase inhibitors for depression and Alzheimer's disease. *Bioorganic and Medicinal Chemistry*, 21(9):2434–2450, 2013.

[133] Preet Anand, Baldev Singh, and Nirmal Singh. A review on coumarins as acetylcholinesterase inhibitors for Alzheimer's disease. *Bioorganic and Medicinal Chemistry*, 20(3):1175–1180, 2012.

[134] Raffaele De Caterina, Steen Husted, Lars Wallentin, Felicita Andreotti, Harald Arnesen, Fedor Bachmann, Colin Baigent, Kurt Huber, Joergen Jespersen, Steen Dalby Kristensen, Gregory Y H Lip, Joao Morais, Lars Hvilsted Rasmussen, Agneta Siegbahn, Freek W A Verheugt, and Jeffrey I. Weitz. Vitamin K antagonists in heart disease: Current status and perspectives (Section III): Position paper of the ESC working group on thrombosis - Task force on anticoagulants in heart disease. *Thrombosis and Haemostasis*, 110(6):1087–1107, 2013.

[135] Xiuyu Yi, Caishun Zhang, Song Guo, Jie Ma, and Jianzhang Zhao. Strongly emissive long-lived 3IL excited state of coumarins in cyclometalated Ir(iii) complexes used as triplet photosensitizers and application in triplet–triplet annihilation upconversion. *Dalton Trans.*, 43(4):1672–1683, 2014.

[136] Haiyang Sun, Huimin Guo, Wenting Wu, Xin Liu, and Jianzhang Zhao. Coumarin phosphorescence observed with NˆN Pt(ii) bisacetylide complex and its applications for luminescent oxygen sensing and triplet–triplet-annihilation based upconversion. *Dalton Transactions*, 40(31):7834, 2011.

[137] Daiki Hara, Hirokazu Komatsu, Aoi Son, Sei Ichi Nishimoto, and Kazuhito Tanabe. Water-soluble phosphorescent ruthenium complex with a fluorescent coumarin unit for ratiometric sensing of oxygen levels in living cells. *Bioconjugate Chemistry*, 26(4):645–649, 2015.

[138] Isabelle Leray, Zouhair Asfari, Jacques Vicens, and Bernard Valeur. Photophysics of calix[4]biscrown-based ditopic receptors of caesium containing one or two dioxocoumarin fluorophores. *Journal of Fluorescence*, 14(4):451–458, 2004.

[139] Naoko Senda, Atsuya Momotake, Yoshinobu Nishimura, and Tatsuo Arai. Synthesis and photochemical properties of a new water-soluble coumarin, designed as a chromophore for highly water-soluble and photolabile protecting group. *Bulletin of the Chemical Society of Japan*, 79(11):1753–1757, 2006.

[140] Qianli Zou, Yanyan Fang, Yuxia Zhao, Hongyou Zhao, Ying Wang, Ying Gu, and Feipeng Wu. Synthesis and in vitro photocytotoxicity of coumarin derivatives for one- and two-photon excited photodynamic therapy. *Journal of Medicinal Chemistry*, 56(13):5288–5294, 2013.

[141] Raju Nomula, Xueyan Wu, Jianzhang Zhao, and Nagegownivari R. Munirathnam. Photodynamic effect of light-harvesting, long-lived triplet excited state Ruthenium(II)-polyimine-coumarin complexes: DNA binding, photocleavage and anticancer studies. *Materials Science and Engineering C*, 79:710–719, 2017.

[142] Richard Brimioulle, Andreas Bauer, and Thorsten Bach. Enantioselective Lewis Acid Catalysis in Intramolecular [2 + 2] Photocycloaddition Reactions: A Mechanistic Comparison between Representative Coumarin and Enone Substrates. *Journal of the American Chemical Society*, 137(15):5170–5176, 2015.

[143] T Furuta, S S Wang, J L Dantzker, T M Dore, W J Bybee, E M Callaway, W Denk, and R Y Tsien. Brominated 7-hydroxycoumarin-4-ylmethyls: photolabile protecting groups with

biologically useful cross-sections for two photon photolysis. *Proceedings of the National Academy of Sciences of the United States of America*, 96(4):1193–1200, 1999.

[144] J. Sérgio Seixas de Melo, R. S. Becker, and A. L. Macanita. Photophysical Behavior of Coumarins As a Function of Substitution and Solvent - Experimental-Evidence for the Existence of a Lowest Lying 1(n,pi*) State. *Journal Of Physical Chemistry*, 98(24):6054–6058, 1994.

[145] J. Seixas de Melo, Ralph S. Becker, Fausto Elisei, and a. L. Maçanita. The photophysical behavior of 3-chloro-7-methoxy-4-methylcoumarin related to the energy separation of the two lowest-lying singlet excited states. *The Journal of Chemical Physics*, 107(16):6062–6069, 1997.

[146] Y. Jiang, P. K. McCarthy, and G. J. Blanchard. The role of multiple electronic states in the dissipative energy dynamics of coumarin 153. *Chemical Physics*, 183(2-3):249–267, 1994.

[147] B.R. Henry and R.V. Hunt. Triplet-Triplet Absorption Studies on Coumarin and Related Molecules. *Journal of Molecular Spectroscopy*, 39:466–470, 1971.

[148] Bryan R. Henry and Edward A. Lawler. Substituent effects on the triplet-triplet absorption spectra of coumarin and its derivatives. *Journal of Molecular Spectroscopy*, 48(1):117–123, 1973.

[149] Theodore G. Pavlopoulos. Tbe auxochromic group in the triplet manifold. *Spectrochimica Acta*, 1985.

[150] Kacem Khemakhem, Marine Soulié, Rémy Brousses, Houcine Ammar, Souhir Abid, and Suzanne Fery-Forgues. Small iminocoumarin derivatives as red emitters: From biological imaging to highly photoluminescent non-doped micro- and nanofibres. *Chemistry - A European Journal*, 21(21):7927–7937, 2015.

[151] M. S. Wagner, E. D. Ilieva, P. St. Petkov, R. D. Nikolova, R. Kienberger, and H. Iglev. Ultrafast hydrogen bond dynamics and partial electron transfer after photoexcitation of diethyl ester of 7-(diethylamino)-coumarin-3-phosphonic acid and its benzoxaphosphorin analog. *Phys. Chem. Chem. Phys.*, 17:9919–9926, 2015.

[152] Hui Zhang, Tianzhi Yu, Yuling Zhao, Duowang Fan, Yangjun Xia, and Peng Zhang. Synthesis, crystal structure, photo- and electro-luminescence of 3-(4-(anthracen-10-

yl)phenyl)-7-(N,N-diethylamino)coumarin. *Synthetic Metals*, 160(15-16):1642–1647, 2010.

[153] Guilford Jones, William R. Jackson, Chol Yoo Choi, and William R. Bergmark. Solvent effects on emission yield and lifetime for coumarin laser dyes. Requirements for a rotatory decay mechanism. *Journal of Physical Chemistry*, 89(2):294–300, 1985.

[154] G. A. Reynolds and K. H. Drexhage. New coumarin dyes with rigidized structure for flashlamp-pumped dye lasers. *Optics Communications*, 13(3):222–225, 1975.

[155] E. J. Schimitschek, J. A. Trias, P. R. Hammond, R. A. Henry, and R. L. Atkins. New laser dyes with blue-green emission. *Optics Communications*, 16(3):313–316, 1976.

[156] Guilford Jones and Mohammad A. Rahman. Fluorescence properties of coumarin laser dyes in aqueous polymer media. Chromophore isolation in poly(methacrylic acid) hypercoils. *Journal of Physical Chemistry*, 98(49):13028–13037, 1994.

[157] Elias Stathatos, Panagiotis Lianos, Urska Lavrencic Stangar, and Boris Orel. Study of laser action of Coumarine-153 incorporated in sol-gel made silica/poly(propylene oxide) nanocomposite gels. *Chemical Physics Letters*, 345(5-6):381–385, 2001.

[158] Tianzhi Yu, Peng Zhang, Yuling Zhao, Hui Zhang, Jing Meng, and Duowang Fan. Synthesis, characterization and high-efficiency blue electroluminescence based on coumarin derivatives of 7-diethylamino-coumarin-3-carboxamide. *Organic Electronics: physics, materials, applications*, 10(4):653–660, 2009.

[159] Scott R. Trenor, Allan R. Shultz, Brian J. Love, and Timothy E. Long. Coumarins in polymers: From light harvesting to photo-cross-linkable tissue scaffolds. *Chemical Reviews*, 104(6):3059–3077, 2004.

[160] Tomas Cihlar, Gong-Xin He, Xiaohong Liu, James M. Chen, Marcos Hatada, Swami Swaminathan, Martin J. McDermott, Zheng-Yu Yang, Andrew S. Mulato, Xiaowu Chen, Stephanie A. Leavitt, Kirsten M. Stray, and William A. Lee. Suppression of HIV-1 Protease Inhibitor Resistance by Phosphonate-mediated Solvent Anchoring. *Journal of Molecular Biology*, 363(3):635–647, oct 2006.

[161] Jay Parrish, Leah Tong, Michael Wang, Xiaowu Chen, Eric B. Lansdon, Carina Cannizzaro, Xubin Zheng, Manoj C. Desai, and Lianhong Xu. Synthesis and biological evaluation of phosphonate analogues of nevirapine. *Bioorganic and Medicinal Chemistry Letters*, 23(5):1493–1497, 2013.

[162] Jérémy M. Boilevin and Jean Louis Reymond. Synthesis of Lipid-Linked Oligosaccharides (LLOs) and Their Phosphonate Analogues as Probes to Study Protein Glycosylation Enzymes. *Synthesis (Germany)*, 50(14):2631–2654, 2018.

[163] Sebastian Wegscheider. *Transient Absorption Spectroscopy of Halogen Substituted Coumarin Derivatives*. Master of science, Technical University of Munich, 2016.

[164] Mikayel Musheghyan. *Photochemical Properties of Halogenated Coumarin Derivatives Studied by Femtosecond Spectroscopy*. Master of science, Technical University of Munich, 2015.

[165] Anka Bojilova, R. Nikolova, Christo Ivanov, Nestor a. Rodios, a. Terzis, and C. P. Raptopoulou. A comparative study of the interaction of salicylaldehydes with phosphonoacetates under Knoevenagel reaction conditions. Synthesis of 1,2-benzoxaphosphorines and their dimers. *Tetrahedron*, 52(38):12597–12612, 1996.

[166] Albert M. Brouwer. Standards for photoluminescence quantum yield measurements in solution (IUPAC Technical Report). *Pure and Applied Chemistry*, 83(12):2213–2228, 2011.

[167] Haridas Pal, Sanjukta Nad, and Manoj Kumbhakar. Photophysical properties of coumarin-120: Unusual behavior in nonpolar solvents. *Journal of Chemical Physics*, 119(1):443–452, 2003.

[168] Michael J.S. Dewar and Patrick J. Grisdale. Substituent Effects. I. Introduction. *Journal of the American Chemical Society*, 84(18):3539–3541, 1962.

[169] M. L. Horng, J. A. Gardecki, A. Papazyan, and M. Maroncelli. Subpicosecond measurements of polar solvation dynamics: Coumarin 153 revisited. *Journal of Physical Chemistry*, 99(48):17311–17337, 1995.

[170] M S Zakerhamidi, a Ghanadzadeh, H Tajalli, M Moghadam, M Jassas, and R Hosseini nia. Substituent and solvent effects on the photo-physical properties of some coumarin dyes. *Spectrochimica acta. Part A, Molecular and biomolecular spectroscopy*, 77(2):337–41, oct 2010.

[171] Hermann Haken and Hans Christoph Wolf. *Molekülphysik und Quantenchemie*. Springer Verlag Berlin Heidelberg, 2nd edition.

[172] Uli Schmidhammer, Uwe Megerle, Stefan Lochbrunner, Eberhard Riedle, and Jerzy

Karpiuk. The key role of solvation dynamics in intramolecular electron transfer: Time-resolved photophysics of crystal violet lactone. *Journal of Physical Chemistry A*, 112(37):8487–8496, 2008.

[173] Noboru Edward T. Harrigan, Asok Chakrabarti, Hirota. Single Crystal EPR, Zero-Field ODMR, and Phosphorescence Studies of the T1 State of Coumarin. *J. Am. Chem. Soc.*, 3460(6):3460–3465, 1975.

[174] Anatolio Pigliucci and Eric Vauthey. Vibrational Relaxation Dynamics of Polyatomic Molecules in Solution. *CHIMIA International Journal for Chemistry*, 57(4):200–203, 2003.

[175] Jian Yong Liu, Wen Hui Fan, Ke Li Han, Wei Qiao Deng, Da Li Xu, and Nan Quan Lou. Ultrafast Vibrational and Thermal Relaxation of Dye Molecules in Solutions. *Journal of Physical Chemistry A*, 107(50):10857–10861, 2003.

[176] M. J. Frisch, G. W. Trucks, H. B. Schlegel, G. E. Scuseria, M. A. Robb, J. R. Cheeseman, D. J. Fox, and ... Gaussian 09, Revision B.01. Technical report, 2009.

[177] Riidiger Bauernschmitt and Reinhart Ahlrichs. Treatment of electronic excitations within the adiabatic approximation of time dependent density functional theory. *Chemical Physics Letters*, 256:454–464, 1996.

[178] Mark E. Casida, Christine Jamorski, Kim C. Casida, and Dennis R. Salahub. Molecular excitation energies to high-lying bound states from time-dependent density-functional response theory: Characterization and correction of the time-dependent local density approximation ionization threshold. *Journal of Chemical Physics*, 108(11):4439–4449, 1998.

[179] Filipp Furche and Reinhart Ahlrichs. Adiabatic time-dependent density functional methods for excited state properties. *Journal of Chemical Physics*, 117(16):7433–7447, 2002.

[180] Takeshi Yanai, David P. Tew, and Nicholas C. Handy. A new hybrid exchange-correlation functional using the Coulomb-attenuating method (CAM-B3LYP). *Chemical Physics Letters*, 393(1-3):51–57, 2004.

[181] Alfonso Pedone. Role of solvent on charge transfer in 7-aminocoumarin dyes: New hints from TD-CAM-B3LYP and state specific PCM calculations. *Journal of Chemical Theory and Computation*, 9(9):4087–4096, 2013.

[182] Giovanni Scalmani, Michael J. Frisch, Benedetta Mennucci, Jacopo Tomasi, Roberto

Cammi, and Vincenzo Barone. Geometries and properties of excited states in the gas phase and in solution: Theory and application of a time-dependent density functional theory polarizable continuum model. *Journal of Chemical Physics*, 124(9), 2006.

[183] Jacopo Tomasi, Benedetta Mennucci, and Roberto Cammi. Quantum mechanical continuum solvation models. *Chemical Reviews*, 105(8):2999–3093, 2005.

[184] Yihui Bai, Fang Zhang, Jin Ying, and Yingzi Wu. Theoretical investigation of the substituent effects on the electronic and optical properties of 6-substituted coumarin derivatives. *Journal of Molecular Structure*, 1089:53–58, 2015.

[185] Smritakshi Phukan, Mithu Saha, Amarta Kumar Pal, A. C. Bhasikuttan, and Sivaprasad Mitra. Intramolecular charge transfer in coumarin based donor-acceptor systems: Formation of a new product through planar intermediate. *Journal of Photochemistry and Photobiology A: Chemistry*, 303-304:67–79, 2015.

[186] Marie Humbert-Droz, Claude Piguet, and Tomasz A. Wesolowski. Fluorescence quantum yield rationalized by the magnitude of the charge transfer in π-conjugated terpyridine derivatives. *Physical Chemistry Chemical Physics*, 18(42):29387–29394, 2016.

[187] Xiaobo Ni, Yuan Guo, Huaiyu Bu, Jing An, and Da En. Effect of structure and conformation on fluorescence properties in novel coumarin-based mannich base dyes. *Journal of the Chinese Chemical Society*, 59(11):1439–1445, 2012.

[188] Fritz Weigert. Über die spezifische Wirkung der polarisierten Strahlung. *Annalen der Physik*, 1920.

[189] Fritz Weigert. Über einen neuen Effekt der Strahlung. *Zeitschrift für Physik*, 5(5-6):410–427, 1921.

[190] Valery A. Barachevsky. Photoanisotropic polymeric media and their application in optical devices. *SPIE Photopolymer Device Physics, Chemistry, and Applications II*, 1559:184–193, 1991.

[191] V. A. Barachevsky, M. M. Krayushkin, V. V. Kyiko, and E. P. Grebennikov. Light-sensitive organic recording media for 3D optical memory. *Physica Status Solidi (C) Current Topics in Solid State Physics*, 8(9):2841–2845, 2011.

[192] I. Yu Martynov, V. A. Barachevsky, A. O. Ayt, O. I. Kobeleva, T. M. Valova, K. S. Levchenko, V. N. Yarovenko, and M. M. Krayushkin. Fluorescence properties of light-sensitive

chromones used in archival polymer recording media. *Optical Materials*, 37(C):488–492, 2014.

[193] Kenneth Robert. Huffman, C. E. Kuhn, and Arnold. Zweig. Photoisomerization of 3-aroyl-2-(2-furyl)chromones. Example of quenching of a photochemical reaction by a product. *Journal of the American Chemical Society*, 92(3):599–605, 1970.

[194] Mikhail M. Krayushkin, Konstantin S. Levchenko, Vladimir N. Yarovenko, Igor V. Zavarzin, Valery A. Barachevsky, Yury A. Puankov, Tatyana M. Valova, and Olga I. Kobeleva. Synthesis and study of photosensitive chromone derivatives for recording media of archival three-dimensional optical memory. *Arkivoc*, 9(5):269–283, 2009.

[195] HENRI BOUAS-LAURENT and HEINZ DÜRR. Organic photochromism (IUPAC Technical Report). *Pure and Applied Chemistry*, 73(4):639–665, 2001.

[196] A. S. Dvornikov, E. P. Walker, and P. M. Rentzepis. Two-photon three-dimensional optical storage memory. *Journal of Physical Chemistry A*, 113(49):13633–13644, 2009.

[197] Veniaminovich Vadim Kiyko. United States Patent US 8455079 B2. 2013.

[198] S Hunter, F Kiamilev, S Esener, D a Parthenopoulos, and P M Rentzepis. Potentials of two-photon based 3-D optical memories for high performance computing. *Applied optics*, 29(14):2058–66, 1990.

[199] A. O. Ayt, V. A. Barachevsky, A. Duensing, Ya Yu Fomicheva, S. V. Gagarskiy, H. Iglev, V. V. Kiyko, M. M. Krayushkin, A. N. Sergeev, A. V. Veniaminov, and V. V. Zakharov. Thresholds for nonlinear recording of fluorescent centers in chromone-doped polymer films. *Optical and Quantum Electronics*, 49(2):1–8, 2017.

[200] Cassandra L. Ward and Christopher G. Elles. Controlling the Excited-State Reaction Dynamics of a Photochromic Molecular Switch with Sequential Two-Photon Excitation. *The Journal of Physical Chemistry Letters*, 3(20):2995–3000, 2012.

[201] Cassandra L. Ward and Christopher G. Elles. Cycloreversion Dynamics of a Photochromic Molecular Switch via One-Photon and Sequential Two-Photon Excitation. *The Journal of Physical Chemistry A*, 118(43):10011–10019, 2014.

[202] Pascal Tobias Scigalla. *Spektroskopische Untersuchungen an organischen Materialien in Vorbereitung für Femtosekunden Transient-Absorption-Spektroskopie*. Bachelor of science, Technical University of Munich, 2016.

[203] S. V. Gagarskiy, E. P. Grebennikov, V. V. Kiyko, K. S. Levchenko, A. N. Sergeev, Ya. Yu. Fomicheva, K. Oberhofer, and H. Iglev. Investigation of Transient State and Dynamics of Photochemical Transformations of Chromone Molecules. *Optics and Spectroscopy*, 125(4):482–486, 2018.

[204] A. O. Ayt, V. A. Barachevsky, S. V. Gagarskiy, K. Oberhofer, Ch Brunner, Ya Yu Fomicheva, H. Iglev, V. V. Kiyko, and A. N. Sergeev. Ultrafast dynamics of Chromone phototransformation by means of transient absorption spectroscopy. *Proceedings - International Conference Laser Optics 2018, ICLO 2018*, 49:377, 2018.

[205] Simone Draxler, Thomas Brust, Stephan Malkmus, Florian O. Koller, Björn Heinz, Stefan Laimgruber, Christine Schulz, Steffen Dietrich, Karola Rück-Braun, Wolfgang Zinth, and Markus Braun. Ultrafast reaction dynamics of the complete photo cycle of an indolylfulgimide studied by absorption, fluorescence and vibrational spectroscopy. *Journal of Molecular Liquids*, 141(3):130–136, 2008.

[206] Roland Wilcken, Monika Schildhauer, Florian Rott, Ludwig Alexander Huber, Manuel Guentner, Stefan Thumser, Kerstin Hoffmann, Sven Oesterling, Regina De Vivie-Riedle, Eberhard Riedle, and Henry Dube. Complete Mechanism of Hemithioindigo Motor Rotation. *Journal of the American Chemical Society*, 140(15):5311–5318, 2018.

[207] Simone Draxler, Thomas Brust, Stephan Malkmus, Jessica A. DiGirolamo, Watson J. Lees, Wolfgang Zinth, and Markus Braun. Ring-opening reaction of a trifluorinated indolylfulgide: Mode-specific photochemistry after pre-excitation. *Physical Chemistry Chemical Physics*, 11(25):5019–5027, 2009.

[208] Jay R. Knutson, Dana G. Walbridge, and Ludwig Brand. Decay-Associated Fluorescence Spectra and the Heterogeneous Emission of Alcohol Dehydrogenase. *Biochemistry*, 21(19):4671–4679, 1982.

[209] C. Ruckebusch, M. Sliwa, P. Pernot, A. de Juan, and R. Tauler. Comprehensive data analysis of femtosecond transient absorption spectra: A review. *Journal of Photochemistry and Photobiology C: Photochemistry Reviews*, 13(1):1–27, 2012.

[210] Jan Erik Loefroth. Time-resolved emission spectra, decay-associated spectra, and species-associated spectra. *The Journal of Physical Chemistry*, 90(6):1160–1168, 1986.

[211] J. E. Loefroth. Deconvolution of single photon counting data with a reference method and global analysis. *European Biophysics Journal*, 13(1):45–58, 1985.

[212] Florian O. Koller, Wolfgang J. Schreier, Tobias E. Schrader, Arne Sieg, Stephan Malkmus, Christine Schulz, Steffen Dietrich, Karola Rück-Braun, Wolfgang Zinth, and Markus Braun. Ultrafast structural dynamics of photochromic indolylfulgimides studied by vibrational spectroscopy and DFT calculations. *Journal of Physical Chemistry A*, 110(47):12769–12776, 2006.

[213] Sebastian Carl Tassilo Roth. *Vibrational Characterization of Photoswitches with DFT-Simulations and FTIR Spectroscopy*. Bachelor of science, Technical University of Munich, 2018.

[214] Simone Draxler. *Ultraschnelle photochrome Reaktionen eines Indolylfulgids und deren Steuerung durch Schwingungsanregung*. Phd thesis, Ludwig-Maximilians-Universität München, 2009.

[215] Sandra Wiedbrauk, Benjamin Maerz, Elena Samoylova, Anne Reiner, Florian Trommer, Peter Mayer, Wolfgang Zinth, and Henry Dube. Twisted Hemithioindigo Photoswitches: Solvent Polarity Determines the Type of Light-Induced Rotations. *Journal of the American Chemical Society*, 138(37):12219–12227, 2016.

[216] Jean-Babtiste Biot. Memoire sur la Polarisation Circulaire et sur les Applications a la Chimie Organique. *Mém. Acad. Sci. Inst. Fr.*, 13:39–175, 1835.

[217] Louis Pasteur. Sur les relations qui peuvent exister entre la forme crystalline, la composition chimique et le sens de la polarization rotatoire. *Annales Chimie Phys.*, 24:442–459, 1848.

[218] Joseph Gal. Pasteur and the art of chirality. *Nature Chemistry*, 9(7):604–605, 2017.

[219] Lien Ai Nguyen, Hua He, and Chuong Pham-Huy. Chiral drugs: an overview. *International journal of biomedical science : IJBS*, 2(2):85–100, 2006.

[220] Al Arsh Basheer. Chemical chiral pollution: Impact on the society and science and need of the regulations in the 21stcentury. *Chirality*, 30(4):402–406, 2018.

[221] Xiangming He, Xiaowu Dong, Dehong Zou, Yang Yu, Qunying Fang, Quan Zhang, and Meirong Zhao. Enantioselective Effects of o,p-DDT on Cell Invasion and Adhesion of Breast Cancer Cells: Chirality in Cancer Development. *Environmental Science and Technology*, 49(16):10028–10037, 2015.

[222] Eric R. Francotte. Enantioselective chromatography as a powerful alternative for the preparation of drug enantiomers. *Journal of Chromatography A*, 906(1-2):379–397, 2001.

[223] Ben L. Feringa and Richard A. Van Delden. Absolute asymmetric synthesis: The origin, control, and amplification of chirality. *Angewandte Chemie - International Edition*, 38(23):3418–3438, 1999.

[224] Farinaz Mortaheb, Katrin Oberhofer, Johann Riemensberger, Florian Ristow, Reinhard Kienberger, Ulrich Heiz, Hristo Iglev, and Aras Kartouzian. Enantiospecific Desorption Triggered by Circularly Polarized Light. *Angewandte Chemie International Edition*, 58(44):15685–15689, oct 2019.

[225] K. Oberhofer, F. Mortaheb, J. Riemensberger, F. Ristow, R. Kienberger, U. Heiz, H. Iglev, and A. Kartouzian. Enantio-enrichment of Racemic Films Using Circularly Polarized Femtosecond Pulses. In *Conference on Lasers and Electro-Optics, OSA Technical Digest*, volume SF2G.1, Washington, D.C., 2019. OSA.

[226] Moshe Shapiro and Paul Brumer. Controlled photon induced symmetry breaking: Chiral molecular products from achiral precursors. *Journal of Chemical Physics*, 95(11):8658–8661, 1991.

[227] Yoshihisa Inoue. Asymmetric Photochemical Reactions in Solution. *Chemical Reviews*, 92(5):741–770, 1992.

[228] A. Moradpour, J. F. Nicoud, G. Balavoine, H. Kagan, and G. Tsoucaris. Photochemistry with Circularly Polarized Light. The Synthesis of Optically Active Hexahehcene. *Journal of the American Chemical Society*, 93(9):2353–2354, 1971.

[229] William J. Bernstein, Melvin Calvin, and Ole Buchardt. Absolute Asymmetric Synthesis. I. On the Mechanism of the Photochemical Synthesis of Nonracemic Helicenes with Circularly Polarized Light. Wavelength Dependence of the Optical Yield of Octahelicene. *Journal of the American Chemical Society*, 94(2):494–498, 1972.

[230] Werner Kuhn and E. Braun. Photochemische Erzeugung optisch aktiver Stoffe. *Die Naturwissenschaften*, 14:227–228, 1929.

[231] G. Balavoine, A. Moradpour, and H. B. Kagan. Preparation of Chiral Compounds with High Optical Purity by Irradiation with Circularly Polarized Light, a Model Reaction for the Prebiotic Generation of Optical Activity. *Journal of the American Chemical Society*, 96(16):5152–5158, 1974.

[232] Andreas Steinbacher, Patrick Nuernberger, and Tobias Brixner. Optical discrimination of racemic from achiral solutions. *Physical Chemistry Chemical Physics*, 17(9):6340–6346, 2015.

[233] Kenneth L. Stevenson and James F. Verdieck. Partial photoresolution. Preliminary studies on some oxalato complexes of chromium(III). *Journal of the American Chemical Society*, 90(11):2974–2975, 1968.

[234] Mauricio Suarez and Gary B Schuster. Photoresolution of an Axially Chiral Bicyclo[3.3.0]octan-3-one: Phototriggers for a Liquid-Crystal-Based Optical Switch. *J. Am. Chem. Soc.*, 117:6732–6738, 1995.

[235] Nina P M Huck, Wolter F Jager, Ben De Lange, and Ben L Feringa. Dynamic Control and Amplification of Molecular Chirality by Circular Polarized Light. *Science*, 273(5282):1686–1688, 1996.

[236] Yoshiki Nakata, Masataka Yoshida, and Noriaki Miyanaga. Parallel fabrication of spiral surface structures by interference pattern of circularly polarized beams. *Scientific Reports*, 8(1):2–6, 2018.

[237] Georgiy Tkachenko and Etienne Brasselet. Optofluidic sorting of material chirality by chiral light. *Nature Communications*, 5:1–7, 2014.

[238] Nina Kravets, Artur Aleksanyan, and Etienne Brasselet. Chiral Optical Stern-Gerlach Newtonian Experiment. *Physical Review Letters*, 122(2):24301, 2019.

[239] J P Cowin, D J Auerbach, and C Becker. MEASUREMENT OF FAST DESORPTION KINETICS OF D2 FROM TUNGSTEN BY LASER INDUCED THERMAL DESORI'TION J.P. COWIN, D J. AUERBACH * , C. BECKER and L, WHARTON. 78:545–564, 1978.

[240] R B Hall. Pulsed-Laser-Induced Desorption Studies of the Kinetics of Surface Reactions. *J. Phys. Chem.*, 91(22):1007–1015, 1987.

[241] Dietrich Menzel. Electronically induced surface reactions : Evolution , concepts , and perspectives. *The Journal of chemical physics*, 137(091702), 2012.

[242] Hendrik Spieker and Thorsten Klüner. Photoinduced desorption of CO from rutile TiO2: elucidation of a new desorption mechanism using first principles. *Physical chemistry chemical physics : PCCP*, 16(35):18743–8, 2014.

[243] M. Karas, D. Bachmann, U. Bahr, and F. Hillenkamp. Matrix-assisted ultraviolet laser desorption of non-volatile compounds. *International Journal of Mass Spectrometry and Ion Processes*, 78(C):53–68, 1987.

[244] V. N. Varakin, A. D. Lozovskii, and A. P. Simonov. Multiphoton UV laser desorption of physisorbed molecules. *High Energy Chemistry*, 34(6):414–415, 2000.

[245] Hiroyuki Saigusa, Azusa Tomioka, Takumi Katayama, and Eijiro Iwase. A matrix-free laser desorption method for production of nucleobase clusters and their hydrates. *Chemical Physics Letters*, 418(1-3):119–125, 2006.

[246] Jürgen Grotemeyer, Ulrich Boesl, Klaus Walter, and Edward W. Schlag. A general soft ionization method for mass spectrometry: Resonance-enhanced multi-photon ionization of biomolecules. *Organic Mass Spectrometry*, 21(10):645–653, 1986.

[247] Ronald C. Beavis, Brian T. Chait, and K. G. Standing. Factors affecting the ultraviolet laser desorption of proteins. *Rapid Communications in Mass Spectrometry*, 3(7):233–237, 1989.

[248] Katharina Titze, Tilo Zollitsch, Ulrich Heiz, and Ulrich Boesl. Laser Mass Spectrometry with Circularly Polarized Light: Circular Dichroism of Cold Molecules in a Supersonic Gas Beam. *ChemPhysChem*, 15(13):2762–2767, 2014.

[249] Fabrizio Santoro, Farinaz Mortaheb, Joern Lepelmeier, Ulrich Boesl, and Ulrich Heiz. High-Resolution Absorption and Electronic Circular Dichroism Spectra of (R)-(+)-1-Phenylethanol . Confident Interpretation Based on the Synergy between Experiments and Computations. *ChemPhysChem*, 19:715–723, 2018.

[250] Farinaz Mortaheb. *Linear and nonlinear chiroptical activity in the gas phase and at surfaces*. Phd-thesis, TU München, 2019.

[251] N. Böwering, T. Lischke, B. Schmidtke, N. Müller, T. Khalil, and U. Heinzmann. Asymmetry in photoelectron emission from chiral molecules induced by circularly polarized light. *Physical Review Letters*, 86(7):1187–1190, 2001.

[252] Martin Pitzer, Maksim Kunitski, Allan S. Johnson, Till Jahnke, Hendrik Sann, Felix Sturm, Lothar Ph. H. Schmidt, Horst Schmidt-Böcking, Reinhard Dörner, Jürgen Stohner, Julia Kiedrowski, Michael Reggelin, Sebastian Marquardt, Alexander Schießer, Robert Berger, and Markus S. Schöffler. Direct Determination of Absolute Molecular Stereochemistry in Gas Phase by Coulomb Explosion Imaging. *Science*, 341(6150):1096–1100, 2013.

[253] David Patterson, Melanie Schnell, and John M. Doyle. Enantiomer-specific detection of chiral molecules via microwave spectroscopy. *Nature*, 497(7450):475–477, 2013.

[254] Dietrich Menzel. Desorption induced by electronic transitions. Some recent progress. *Nuclear Inst. and Methods in Physics Research, B*, 13(1-3):507–517, 1986.

[255] M. S. Slutsky and Thomas F. George. Quantum Theory of Laser-Stimulated Desorption. *Chemical Physics Letters*, 57(3):474–476, 1978.

[256] Gerhard Bringmann, Rainer Walter, and Ralf Weirich. The Directed Synthesis of Biaryl Compounds: Modern Concepts and Strategies. *Angewandte Chemie International Edition in English*, 29(9):977–991, 1990.

[257] Qiao-Sheng Hu, Dilrukshi Vitharana, and Lin Pu. An efficient and practical direct resolution of racemic 1,1-bi-2-naphthol to both of its pure enantiomers. *Tetrahedron: Asymmetry*, 6(9):2123–2126, 1995.

[258] J. D. Horvath and A. J. Gellman. Enantiospecific desorption of R- and S-propylene oxide from a chiral Cu(643) surface. *Journal of the American Chemical Society*, 123(32):7953–7954, 2001.

[259] Florian Ristow. *High-Vacuum Evaporation Chamber Setup for In-Situ SHG-CD Spectroscopy and Enantiospecific Laser Desorption*. Master of science, TU Muenchen, 2018.

[260] Aras Kartouzian, Philipp Heister, Martin Thämer, Sabine Gerlach, and Ulrich Heiz. In-line reference measurement for surface second harmonic generation spectroscopy. *Journal of the Optical Society of America B*, 30(3):541, 2013.

[261] J J Yeh and I Lindau. ATOMIC SUBSHELL PHOTOIONIZATION ASYMMETRY CROSS SECTIONS AND PARAMETERS: 1 < Z < 103. *Atomic Data and Nuclear Data Tables*, 32(1):1–155, 1985.

[262] Alexander von Weber, Matthias Jakob, Eva Kratzer, Aras Kartouzian, and Ueli Heiz. In situ Second-Harmonic Generation Circular Dichroism with Submonolayer Sensitivity. *ChemPhysChem*, 20(1):134–141, jan 2019.

[263] Fumio Toda, Koichi Tanaka, Hisakazu Miyamoto, Hideko Koshima, Ikuko Miyahara, and Ken Hirotsu. Formation of racemic compound crystals by mixing of two enantiomeric

crystals in the solid state. Liquid transport of molecules from crystal to crystal. *Journal of the Chemical Society, Perkin Transactions 2*, 5(9):1877–1886, 1997.

[264] K. Mori, Y. Masuda, and S. Kashino. (+)-(R)- and racemic forms of 2,2'-dihydroxy-1,1'-binaphthyl. *Acta Crystallographica Section C*, 49(6):1224–1227, 1993.

[265] Peter Saalfrank. Quantum dynamical approach to ultrafast molecular desorption from surfaces. *Chemical Reviews*, 106(10):4116–4159, 2006.

[266] Richard F. Haglund. Microscopic and mesoscopic aspects of laser-induced desorption and ablation. *Applied Surface Science*, 96-98:1–13, 1996.

[267] Thorsten Klüner. Photodesorption of diatomic molecules from surfaces: A theoretical approach based on first principles. *Progress in Surface Science*, 85(5-8):279–345, 2010.

[268] Dietrich Menzel and Robert Gomer. Desorption from Metal Surfaces by Low-Energy Electrons. *The Journal of Chemical Physics*, 41(11):3311–3328, 1964.

[269] P. a. Redhead. Interaction of Slow Electrons With Chemisorbed Oxygen. *Canadian Journal of Physics*, 42(5):886–905, 1964.

[270] R. O. Adams and E. E. Donaldson. Photodesorption. *Journal of Chemical Information and Modeling*, 42(2):770–774, 1965.

[271] Peter R Antoniewicz. Model for electron- and photon-stimulated desorption. *Physical Review B*, 21(9):3811–3815, 1980.

[272] F. Budde, T. F. Heinz, M. M.T. Loy, J. A. Misewich, F. De Rougemont, and H. Zacharias. Femtosecond time-resolved measurement of desorption. *Physical Review Letters*, 66(23):3024–3027, 1991.

[273] G. W. Fabel, S. M. Cox, and D. Lichtman. Photodesorption from 304 stainless steel. *Surface Science*, 40:571–582, 1973.

[274] Grégory Taupier, Alex Boeglin, Olivier Crégut, Loïc Mager, Alberto Barsella, Katarzyna Gąsior, Jean Luc Rehspringer, and Kokou D. Dorkenoo. Beating photo-degradation in sum-frequency imaging of chiral organic media. *Optical Materials*, 45:22–27, 2015.

[275] F. J. Kao, D. G. Busch, D. Gomes Da Costa, and W. Ho. Femtosecond versus

nanosecond surface photochemistry: O2+CO on Pt(111) at 80 K. *Physical Review Letters*, 70(26):4098–4101, 1993.

[276] D. G. Busch and W. Ho. Direct observation of the crossover from single to multiple excitations in femtosecond surface photochemistry. *Physical Review Letters*, 77(7):1338–1341, 1996.

[277] Teresa M.R. Maria, Fábio A. Marins, J. Bianca S. Costa, M. Ramos Silva, Rui M.B. Carrilho, Carlos J.P. Monteiro, Mariette M. Pereira, and M. Ermelinda S. Eusébio. Solid state investigation of BINOL and BINOL derivatives: A contribution to enantioselective symmetry breaking by crystallization. *Thermochimica Acta*, 648:32–43, 2017.

[278] Jeffrey D. Byers and Janice M. Hicks. Electronic spectral effects on chiral surface second harmonic generation. *Chemical Physics Letters*, 231(2-3):216–224, 1994.

[279] Stefan Bienz. *Spektroskopische Methoden in der organischen Chemie*. New York, Georg Thieme Verlag, Stuttgart, 9., überar edition, 2016.

[280] CARLOS TORO, LEONARDO DE BONI, NA LIN, FABRIZIO SANTORO, ANTONIO RIZO, and FLORENCIO E. HERNANDEZ. Two-Photon Absorption Circular-Linear Dichroism on Axial Enantiomers. *Chirality*, 22, 2010.

[281] Farinaz Mortaheb, Katrin Oberhofer, Johann Riemensberger, Florian Ristow, Reinhard Kienberger, and Ulrich Heiz. Supporting Information: Enantiospecific Desorption Triggered by Circularly Polarized Light. *Angewandte Chemie - International Edition*, 58, 2019.

[282] Alexander von Weber, David C. Hooper, Matthias Jakob, Ventsislav K. Valev, Aras Kartouzian, and Ueli Heiz. Circular Dichroism and Isotropy – Polarity Reversal of Ellipticity in Molecular Films of 1,1'-Bi-2-Naphtol. *ChemPhysChem*, 20(1):62–69, 2019.

[283] Richard E. Pincock, Robert R. Perkins, Alan S. Ma, and Keith R. Wilson. Probability Distribution of Enantiomorphous Forms in Spontaneous Generation of Optically Active Substances. *Science*, 174(4013), 1971.

[284] Keith R. Wilson and Richard E. Pincock. Thermally Induced Resolution of Racemic 1,1-Binaphthyl in the Solid State. *Journal of the American Chemical Society*, 97(6):1474–1478, 1975.

[285] Sigma Aldrich Data Sheet S-BINOL, 2019.

[286] Matthew A. Kriech and John C. Conboy. Using the intrinsic chirality of a molecule as a label-free probe to detect molecular adsorption to a surface by second harmonic generation. *Applied Spectroscopy*, 59(6):746–753, 2005.

[287] Marco Schmid, Lara Martinez-Fernandez, Dimitra Markovitsi, Fabrizio Santoro, François Hache, Roberto Improta, and Pascale Changenet. Unveiling Excited-State Chirality of Binaphthols by Femtosecond Circular Dichroism and Quantum Chemical Calculations. *The Journal of Physical Chemistry Letters*, 10(14):4089–4094, jul 2019.

[288] Hermann Rau. Asymmetric Photochemistry in Solution. *Chemical Reviews*, 83(5):535–547, 1983.

[289] Darshan C. Patel, Ross M. Woods, Zachary S. Breitbach, Alain Berthod, and Daniel W. Armstrong. Thermal racemization of biaryl atropisomers. *Tetrahedron Asymmetry*, 28(11):1557–1561, 2017.

[290] Jia-Hui Tay and Pavel Nagorny. 31P NMR Based Method for Determining Enantiopurity of Chiral Phosphoric Acids and Its Application to the BINOL- and H8-BINOL-Based Chiral Phosphoric Acid Thermal Racemization Studies. *Synlett*, 27(04):551–554, nov 2015.

[291] Robert P. Lemieux and Gary B. Schuster. Photochemistry of Axially Chiral (Arylmethylene)cycloalkanes: A Search for Suitable Photoswitchable Liquid Crystalline Materials. *Journal of Organic Chemistry*, 58(1):100–110, 1993.

[292] Masahiro Irie, Kikuo Yoshida, and Koichiro Hayashi. Laser photolysis study of the photoracemization of 1,1'-binaphthyl. *Journal of Physical Chemistry*, 81(10):969–972, 1977.

[293] Riadh Sahnoun, Shiro Koseki, and Yuichi Fujimura. Theoretical investigation of 1,1'-bi-2-naphthol isomerization. *Journal of Molecular Structure*, 735-736(SPEC. ISS.):315–324, 2005.

[294] Ya Nan Li, Yang Chi, Zong Dong Sun, Huaiguo Xue, Nian Tzu Suen, and Sheng Ping Guo. Partial substitution induced centrosymmetric to noncentrosymmetric structure transformation and promising second-order nonlinear optical properties of (K0.38Ba0.81)Ga2Se4. *Chemical communications (Cambridge, England)*, 55(91):13701–13704, 2019.

[295] Susanne Lisinski, Lorenz Ratke, Dominik Schaniel, Tobias Jungk, Elisabeth Soergel, Hans Boysen, and Theo Woike. Second-harmonic generation in nano-structured LiTaO3- and

LiNbO3-xerogels with randomly oriented ferroelectric grains. *Optical Materials*, 32(4):504–509, 2010.

[296] J. Crank. Diffusion. Coefficients in solids, their measurement and significance. *Discussions of the Faraday Society*, 23:99–104, 1957.

[297] C. E. Birchenall. The mechanism of diffusion in the solid state. *Metallurgical Reviews*, 3(1):235–277, 1958.

[298] Julia Frisch. *Femtosecond Fluorescence Spectroscopy on Naphthalimide Derivatives with Isoquinoline Backbone*. Master of science, Technical University of Munich, 2015.

[299] A. Kartouzian, U. Heiz, F. Mortaheb, K. Oberhofer, J. Riemensberger, H. Iglev, and R. Kienberger. Verfahren zur Enantiomerenanreicherung, DE 10 2018 117 346, 2018.

Danksagung

zu dürfen.

Natürlich möchte ich mich auch für die gute Zusammenarbeit im Rahmen unserer Kooperation bei den Experimenten zur Enantiomerenanreicherung bei Dr. habil. Aras Kartouzian, Dr. Farinaz Mortaheb, Prof. Ulrich Heiz und Dr. Alexander von Weber bedanken. Außerdem danke ich Dr. Sergey Gagarskiy, Dr. Andrey Sergeev und Yana Fomicheva für die Zusammenarbeit im Rahmen des Chromon-Projekts und für Ihre wunderbare Gastfreundschaft bei meinem Aufenthalt in St. Petersburg. Mein Dank gilt weiterhin Dr. Eleonora Iglev und Dr. Petko Petkov für ihre Beiträge zum Cumarin-Projekt.

Größter Dank gilt nicht zuletzt auch meinen Eltern, insbesondere meiner Mutter, ihrem Lebensgefährten, meinem Bruder, meinen engsten Freunden und natürlich meinem Freund Johann, für sein Vertrauen in mich und meine Arbeit, für das Korrekturlesen meiner Doktorarbeit und dafür, dass die letzten Jahre meiner Promotion ganz besonders schön waren.